DEVELOPMENT AND VALIDATION OF A KNEE-THIGH-HIP LSDYNA MODEL OF A 50th PERCENTILE MALE

by

Chiara Silvestri

A Dissertation

Submitted to the Faculty

of the

WORCESTER POLYTECHNIC INSTITUTE

In partial fulfillment of the requirements for the

Degree of Doctor of Philosophy

in

Civil engineering

April 24, 2008

APPROVED:

Dr. Malcolm H. Ray, ~~Major~~ Advisor

Dr. Kristen L. Billiar, Committee Member

Dr. Roberto Pietroforte, Committee Member

Dr. Ali O. Atahan, Committee Member

Dr. Tahar El-Korchi, Department Head

ABSTRACT

With the introduction of air bags, occupant safety in frontal car crashes has been improved for upper regions of the body, such as the head and thorax. These improvements, however, have not helped improve the safety for the lower extremities, increasing their percentage of injuries in car crashes. Though lower extremity injuries are usually not life threatening, they can have long lasting physical and psychosocial consequences. An LSDYNA finite element model of the knee-thigh-hip (KTH) of a 50th percentile adult male was developed for exploring the mechanics of injuries to the KTH during frontal crash crashes. The model includes a detailed geometry of the bones, the mass of the soft tissue, and a discrete element representation of the ligaments and muscles of the KTH. The bones were validated using physical tests obtained from the National Highway Traffic and Safety Administration's (NHTSA) test database. The geometry, the material properties and the failure mechanisms of bone materials were verified. A validation was also performed against a whole-body cadaver test to verify contributions of passive muscle and ligament forces. Failure mechanisms in the tests and simulations were compared to ensure that the model provides a useful tool for exploring fractures and dislocations in the KTH resulting from frontal vehicle crashes.

The validated model was then used to investigate injury mechanisms during a frontal car crash at different occupant positions. The role of muscle forces on these fracture mechanisms was explored and simulations of frontal impacts were then reproduced with the KTH complex at different angles of thigh flexion, adduction and abduction. Results show that the failure mechanism of the lower limb can significantly depend on the occupant position prior to impact. Failure mechanisms in the simulations were compared to results found in literature to ensure the model provides a useful tool for predicting fractures in the lower limb resulting from out-of-position frontal vehicle crashes. The FE model replicate injury criteria developed for ligament failure and suggested lowering the actual used axial femur force threshold for KTH injures both in neutral and out-of-position KTH axial impacts.

ACKNOWLEDGEMENTS

My first thought goes to Professor Malcolm Ray, who gave me this wonderful life opportunity. Thanks for being more than only an advisor for me, for helping me anytime I had problems even outside school, and for making me feel part of your big family more than once.

A special thank to Dr. Rolf Eppinger , Dr. Eric Takhounts, Dr. Shashi Kuppa from NHTSA for supporting this project: without you, I would not had the chance to learn more about bones and muscles! Many thanks also to Dr. Rupp from UMTRI, for his availability and kindness when we asked his help, and for having conducted so many cadaver component tests on which I based my research!

Thanks to three special people on the other side of the Ocean: thanks mum and dad for all your complete sustaining during this four-year adventure in the States and thanks to Elena for your advice and support and for the hours you spent on the phone listening to me. Thanks to Mario for the help you gave me anytime I needed that, for your advice about LsDyna, for all the French fries you prepared for me and for the "caffelatte" every morning. Thanks for sharing your time with me.

A special thank to someone who I had the privilege and the luck to meet here: Marlyn Myers; all the strawberry shortcakes were just an excuse to find time to share with one of the best friends I've ever had in my all life!

How could I forget to thank a wonderful person like Agata? With your smile and your kindness, the entire civil engineering department shines every day… thanks for everything you have done in these years, and for supporting me every time I felt discouraged. And thanks to my officemate Christine for sharing the office with me for more than a year!

I am also grateful to Professors El-Korchi, Billiar, Pietroforte and Atahan for being my committee members.

To my Mum, Dad,
my sister Elena and my boyfriend Mario

TABLE OF CONTENTS

LIST OF FIGURES

LIST OF TABLES

I. Introduction

In the last decades many efforts were made in research and in the automotive industry in order to design safer cars. Until recent times the main goal was protecting vital parts of the human body: head, neck and thorax. Lately, increased use of safety belts and air bags in vehicles has changed the distribution and severity of injuries in frontal car crashes. Better protection of the head and thorax has reduced the severity of injuries in this region but these improved safety systems do not address prevention of injuries in other body regions like the lower extremities. (Figure 1.1) Now that great steps forward were done in this direction thanks to devices such as seat belts and airbags, more attention is paid to non-fatal injuries of lower limbs: pelvis, femur, knee, tibia, ankle and foot. Even with a major research effort to model the knee, still little is known about the behaviour of the femoral-pelvic system in case of impact, although femur fractures together with femur dislocation from the pelvis turned out to be one of the most common injuries in severe car collisions, regardless the safety equipment (e.g., seat belts, airbags) of the cars.

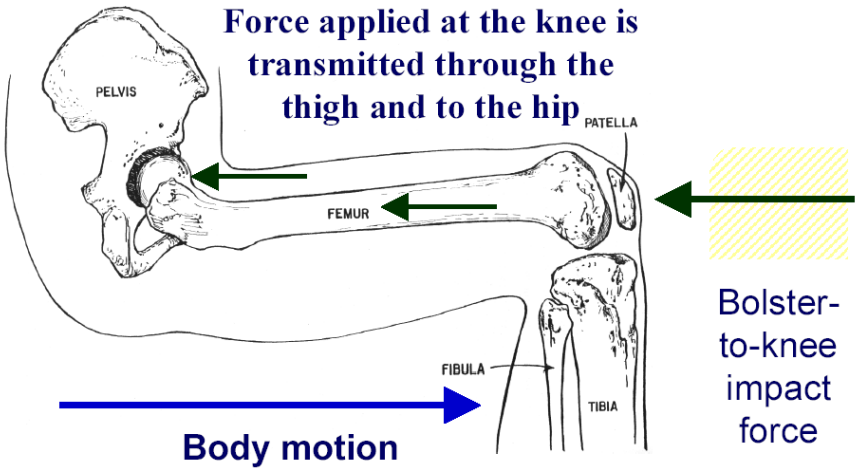

Figure 1.1. Force transmission on the KTH in a frontal impact crash. (Kuppa, 2002)

Injuries to the pelvis, to the pelvic-femoral joint and to the femur are the most clinically expensive KTH injuries because of the instability of this weight-bearing region. The computation of such costs includes direct costs (e.g., clinical treatment, rehabilitation, "property damages"), indirect costs (e.g., productivity loss, wages lost, etc.) and intangible costs (e.g., depression and suffering). Various indices have been created in an attempt to quantify injuries. The AIS (Abbreviated Injury Scale), FCI (Functional Capacity Index) and LLI (Life-years Lost to Injuries) are several used in the case of lower limb injuries. Lower limb injuries usually correspond to a two or greater value on the AIS scale. The FCI quantifies the level of functional capacity loss one year after the accident. A FCI equal to zero implies no functional capacity loss whereas a FCI equal to unity corresponds to a total functional capacity loss. LLI is FCI times the life expectancy of the injured person (e.g., if an individual's life expectancy was 20 years and the FCI 0.5, 10 years of life-function would have been lost).

Kuppa *et al* in an examination of the 1993 through 1999 National Automotive Sampling System/Crashworthiness Data System (NASS/CDS) found that more AIS level two or greater injuries occurred in the lower extremities than any other body region for out-board seated occupants of vehicles. (Kuppa *et al*, 2001). About half of these lower extremity injuries involve the knee-thigh-hip (KTH) region. (Figure 1.2)

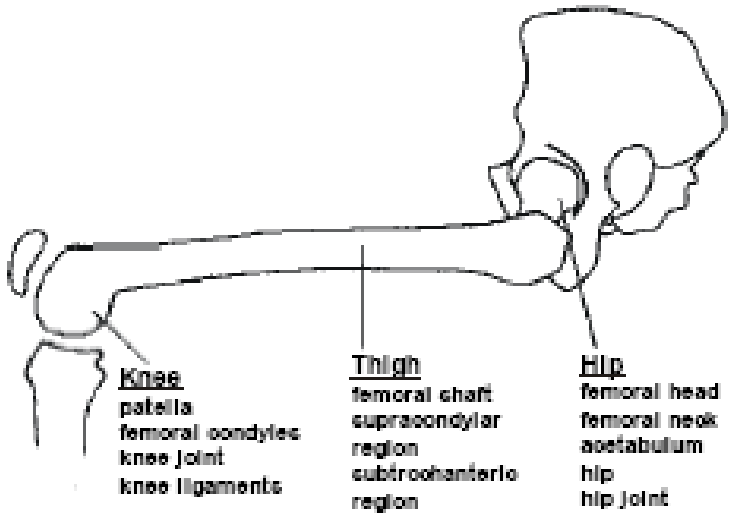

Figure 1.2. KTH complex with its most common injuries. (Kuppa, 2003)

Common types of KTH injuries in frontal crashes include mid-shaft femur fractures, fracture of the femoral head, splitting fractures of the femoral condyles, acetabular fractures and hip dislocations.

Kuppa *et al* estimated that the comprehensive annual cost of KTH injuries in the U.S. is on the order of $4 billion (i.e., values in US Dollars in the year 2000) (Kuppa *et al*, 2001). Lower limbs are the most struck part of the human body in frontal and offset frontal crashes. Thirty-six percent of all AIS 2+ injuries concern lower limbs, half of which (i.e., eighteen percent) involve the KTH. The index that best displays the social consequences of the phenomenon is LLI: the life-years lost due to KTH AIS 2+ injuries account for 60,000 years annually, 23 percent of all LLI associated with AIS 2+ injuries in frontal collisions. In particular, hip injuries represent 65 percent of the LLI caused by KTH AIS 2+ injuries, which, compared to the fact that they account for only 46 percent of all KTH AIS 2+ injuries, shows how severe disabilities induced by pelvis impairments are. In fact, they are known for causing long-lasting mobility loss because of the high load-bearing nature of the joints involved. Clinical inquiries have shown that only 58 percent of the individuals who sustained lower extremity injuries were able to work one year after the accident. In addition, the risk of AIS 2+ injuries have increased in air-bag equipped cars as shown in Figure 1.3. While the airbag is very effective in limiting thorax and head injuries, it is not effective in limiting or preventing lower extremity injuries. Thus, as the number of head and thorax injuries decreases, the importance of KTH injuries increases.

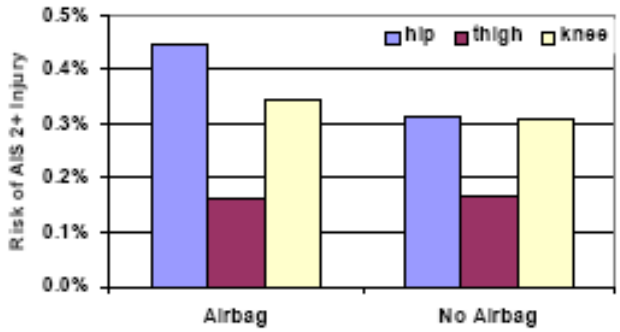

Figure 1.3. Increase of the AIS 2+ Risk for the KTH complex in air-bag equipped cars. (Kuppa, 2003)

Some previous studies of lower limb injuries in car crashes have highlighted axial loads (Dischinger *et al.* 1994), driver anthropometrics (Dischinger *et al.* 1995) and foot placement (Pilkey *et al.* 1994) being key parameters in lower limbs injury events. Designing vehicle safety systems to minimize these debilitating injuries requires an understanding the mechanics of these different types of KTH failures and the role of occupant position during braking. The finite element model described herein is one tool that can be used to explore injury mechanisms to the KTH in frontal crashes.

Generally, the KTH is loaded through the knee bolster in a frontal crash. The structural performance of the KTH is likely dependent on a variety of factors such as the specific seating posture and muscle forces as well as the material or design of the knee-bolster. For example, an occupant seated in an abducted position (i.e., legs spread apart) is probably more likely to suffer an acetabular fracture since the positions of the bones will tend to drive the femoral head into the acetabular cup and cause the pelvis to fracture. On the other end of the spectrum, an occupant in an adducted seating posture (i.e., legs together or even crossed) is more likely to experience a hip dislocation because the orientation of the bones will promote the femur head coming out the acetabular cup. If an occupant is either pressing on the brake pedal or bracing against the crash, the muscle forces tend to pre-load the KTH. This may make a mid-shaft fractures more likely and the forces in the hip muscles may work against hip dislocation. The point of these examples is that understanding how these injuries occur in real-world crashes requires a detailed examination of the geometry, loading, positions and material properties of the KTH. Obtaining such understanding is not possible using volunteers or cadaver tests, so finite element simulations provide one of the few methods for examining injury causation in frontal crashes involving the KTH. The need to model the muscles comes from the hypothesis that their contraction can develop large compressive loads on the bones they are attached to. These muscle forces act as a pre-load to the bones they are connected to and can increase and complicate the state of stress of the bones in the KTH. An experimental proof of this was provided by Tencer *et al.* who found a discrepancy between real data from low velocity frontal car impacts and measurements obtained from testing. Crash investigations reported femur fractures at a mean collision velocity of 40.7

km/h, whereas cadaver sled tests run in similar conditions at a mean impact velocity of 56.3 km/h resulted in no femur fractures. The different behaviour may have been due to muscle contraction and bracing of the occupant pushing on the brake pedal before the impact. Such contraction causes an increase in axial load on the femur which, once added to the one due to collision between the knee and the dashboard, may induce fracture of the femur, dislocation of the hip or fracture of the acetabulum.

A research program was initiated by NHTSA several years ago to better understand injury mechanisms to the knee-thigh-hip complex. (Kuppa *et al.*, 2001) The research program involved axial knee impacts to isolated cadaveric knee-thigh-hip specimens as well as knee impacts to whole body cadaveric specimens. The outcome of this research was an injury prediction model that describes the tolerances of the knee and femur, and the tolerance of the hip as a function of posture under frontal knee impact loading. (Kuppa *et al.*, 2001)

There are, however, some aspects of human response that were not accounted for in this human injury prediction model.

1. The effect of muscle tension on knee-thigh-hip force response and injury tolerance is unknown. The change in human response to knee impacts due to muscle tension such as during braking in a crash scenario is unknown.
2. Changes in the femur-to-tibia angle results in changes in the tolerance of the knee due to changes in patella positioning and kinematics but the amount of this change is not known.
3. The current injury prediction model provides separate tolerances of the femur in axial compression and pure bending. The femur, however, simultaneously experiences axial compression and bending in a typical vehicle crash (i.e., it is in a state of bi-axial stress). The changes in femur tolerance under combined compression and bending loads have not been examined.

In order to address these issues, this research is aimed to build a finite element (FE) model of the 50th percentile KTH to parametrically explore variations in seating

posture, loading conditions and muscle activation in frontal crash scenarios and thereby examine failure mechanisms in the KTH. The model will be conceived to be mainly focused on the phenomenon of dislocation of the femur from the hip and fractures in the trochanteric femoral region.

II. LITERATURE REVIEW

This chapter reviews the available literature in the areas of motor vehicle crashes in the United States, biomechanical modeling of human body, bone and soft tissue anatomical and mechanical properties, and fracture mode of bones.

2.1. Motor Vehicle Crash Facts in the United States

The National Safety Council (NSC) reported approximately that there were 12.5 million traffic crashes in the US in 2001, 2.3 million of which were disabling injuries. (NHTSA, 2002a) In 2000, according to the U.S. Department of Transportation (DOT), about 5.3 million injuries were caused by car crashes and it was estimated that 20% of injuries were not reported. (NHTSA, 2002b)

According to Holden, every American has the risk of being involved in a collision event of some type every six years. (Holden, 1986)

2.1.1 Motor Vehicle Collisions in the USA: Costs

Blincoe et al. reported that the societal costs of motor vehicle crashes for the year 2000 was estimated to be around $230.6 billion, which meant about $820 per person per year living in the United States: out of this $230.6 billion, $32.6 billion was spent in medical costs, $1.4 billion on emergency services, $61 billion on lost workplace productivity. (Blincoe *et al.*, 2002)

2.1.2 Injury Risk

For a better understanding and prediction of injuries during a car crash, crash thresholds were derived from experimental data in order to theoretically define values at which injuries potentially occur. Injury thresholds have the ultimate purpose of guiding designers in the design of safer vehicles.

The AIS. The Abbreviated Injury Scale (AIS) was first used by National Highway Traffic Safety Administration (NHTSA) in 1971: it is in use in all U.S. Federal studies to rank injuries in various anatomical parts of the body with respect to the risk of fatality. The AIS system considers nine regions of the body: head, face, neck, thorax, abdomen and pelvic, spine, the upper extremity and the lower extremity. Table 2.1 shows the AIS ranking for degree of Injury and table 2.2 shows AIS ranks for extremity injuries.

Table 2.1. AIS Ranking for Degree of Injury (Nordhoff, 2004)

AIS 1	Mild Injury	0% Risk of Death
AIS 2	Moderate Injury	0.1% to 0.4% Risk of Death
AIS 3	Serious Injury	0.8% to 2.3% Risk of Death
AIS 4	Severe Injury	10% Risk of Death
AIS 5	Critical Injury	50% Risk of Death
AIS 6	Maximum Injury	Virtually Unsurvivable

Table 2.2. AIS Ranking for Upper and Lower Extremity Injuries (Nordhoff, 2004)

AIS 1	Includes minor lacerations, contusions, and abrasion that are superficial. Tendon tears or lacerations and strain/sprain injuries. Finger and toe fractures.
AIS 2	Degloving injury to arm, forearm, fingers, toes, thigh, and calf. Includes muscle and joint capsule lacerations, tears, avulsions, and ruptures. Achilles and patellar tendon and collateral/cruciate ligament tears, etc.
AIS 3	Massive destruction, amputation, or crush to part or entire arm or leg. Blood loss >20% and tissue loss >25 cm. Includes injury to major artteries or veins. Includes fractures with nerve laceration.
AIS 4	Amputation above knee or major laceration of femoral artery. Substantial fracture and deformation of pelvis with associated vascular disruption or with major retroperitoneal hematoma and blood loss of <20% by volume.
AIS 5	Includes AIS 4 description with blood loss > 20% by volume.
AIS 6	N/A

The FCI. The Functional Capacity Index (FCI) was defined to quantify the long-term individual and societal consequences of non-fatal injuries. (MacKenzie et al., 1996) Its

values vary from 0 to 1.0 where zero stands for no loss, while unity represents a complete loss of function.

The LLI. The Life years Lost to Injury is a scale developed by Luchter which represents the years lived at a reduced level of functioning. (Luchter, 1995) It is defined as the product of its FCI and the life expectancy of the injured individual, determined from standard life tables.

2.1.3 Knee-Thigh-Hip Injuries in Frontal Crashes in the USA: Costs, Frequency and Risk

In fact, though lower extremity injuries are usually not life threatening, they can have long lasting physical and psychosocial consequences. (Read *et al*., 2002) With the introduction of air bags, safety has been increased for the upper region of the body, such as head and thorax. However, this has not helped safety for the lower part of the body, pelvic region and legs, increasing the percentage of lower extremity injuries in car crashes.

Ore reported that fifty percent of lower extremity injuries are to the knee-thigh-hip and this accounts for 45 percent of the life years lost (Ore *et al.,* 1993; Kuppa *et al.,* 2001) After a detailed examination of the UK CCIS database, it was found that for unrestrained occupants, 51% of skeletal injuries involved the hip-pelvis region. (Pattimore, 1991) In 1991, Huelke found that, of all lower extremity injuries, the hip accounts for 15%, thigh for 18%, while knee for 22%. (Huelke, 1991)

Kuppa examined the National Accident Sampling System (NASS) data file for the years 1993-2001 with the purpose of estimate the frequency and risk of KTH in real world frontal crashes. (Kuppa, 2002) Kuppa found that injuries to the KTH accounted for 18% of all injuries categorized as AIS Level 2+ and for 23% of the associated Lost-years Lost to Injury (LLI). Annually, the cost of lower extremity injuries was found to be around $7.64 billion and 52% of this cost was due to KTH injuries. The risk and frequency of

injury were also evaluated with respect to different parameters, such as age of the occupant, restraint conditions, and impact angle and vehicle type.

2.2. Fracture Modes of Bones

The most common car crash KTH injury occurs when the knee strikes the dashboard or the steering column. In the latter case, the load can be very concentrated, with the knee striking a small area: this can cause fracture of the patella, which is generally comminuted and stellate as a shape.

In the case of a dashboard, the knee may not be significantly injured. In high energy crashes, however, fracture of the femur or fracture/dislocation of the hip could occur when the knee is trapped under the dashboard, the tibial plateau may experience fractures due to axial load because of buckling of the floorboard as shown in Figure 2.1.

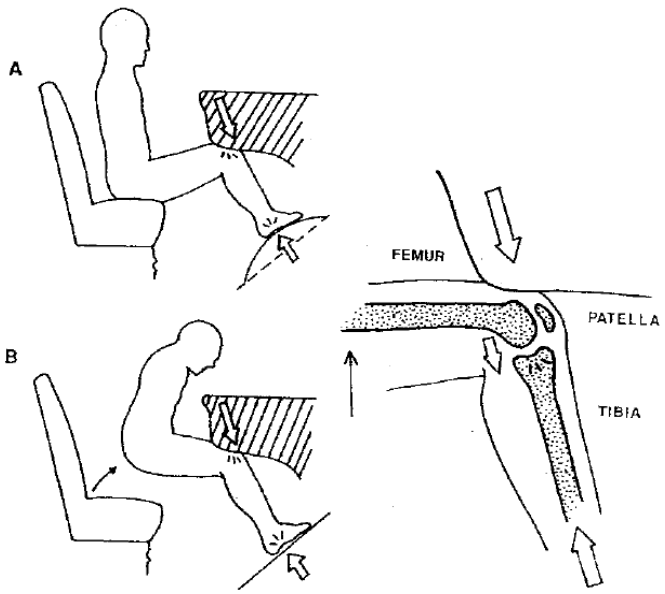

Figure 2.1. Knee striking the dashboard and possible tibial axial load due to buckling of the floorboard. (Teresinski, 2002)

Because of this axial load, the tibia bone can be "pushed" against the femur, causing fractures to the femur condyles.

Rich et al. reported in his book four main scenarios to be considered when studying injury mechanism in the lower limbs as consequence of a frontal car crashes (Figure 2.2). (Teresinski, 2005) A considerable parameter to be taken into account is the exact geometry of the dashboard and car interior. In fact, according to the different heights of the knee-bolster, the area of impact between the interior of the car and the lower limb can vary: the impact can affect mainly the condyle region of the knee (Figure 2.2 (1)), or it can be directed to the tibia bone (Figure 2.2 (3)). There can be also the case in which the impact is mainly coming from the pedal region and this could lead to a compression of the tibia between the pedal itself and a too-high dashboard with respect to the stature of the occupant (Figure 2.2 (2)). Figure 2.2 illustrates the influence of vehicle dimensions and characteristics of the occupant on the type and severity of leg injury mechanisms during a crash.

With this research project, the particular scenario reported in Figure 2.3 will be considered. Fractures directed to the patella bone (a) and condyle region of the knee (b), the shaft (c) and the head-trochanters (d and e) of the femur bone and the acetabular and wing parts of the pelvis (f) will be more likely to experience bone failures occurring during a frontal impact.

Later in this chapter, fracture modes of KTH bones are reviewed, giving particular attention to the femur and the pelvis. Out-of-position injuries are also considered and investigated at different combination angles of flexion with adduction and abduction.

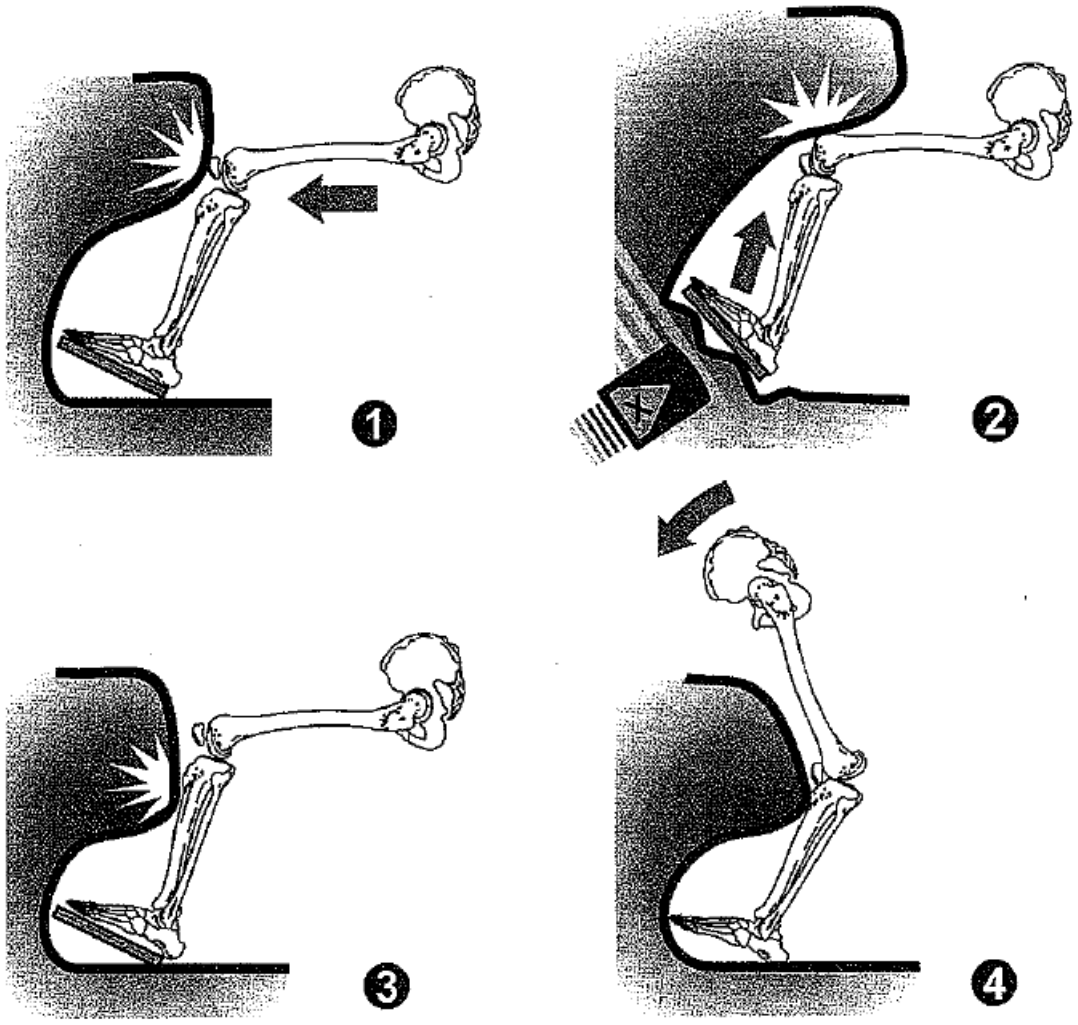

Figure 2.2. Different possible scenarios for leg injury mechanism during a frontal crash. (Teresinski, 2005)

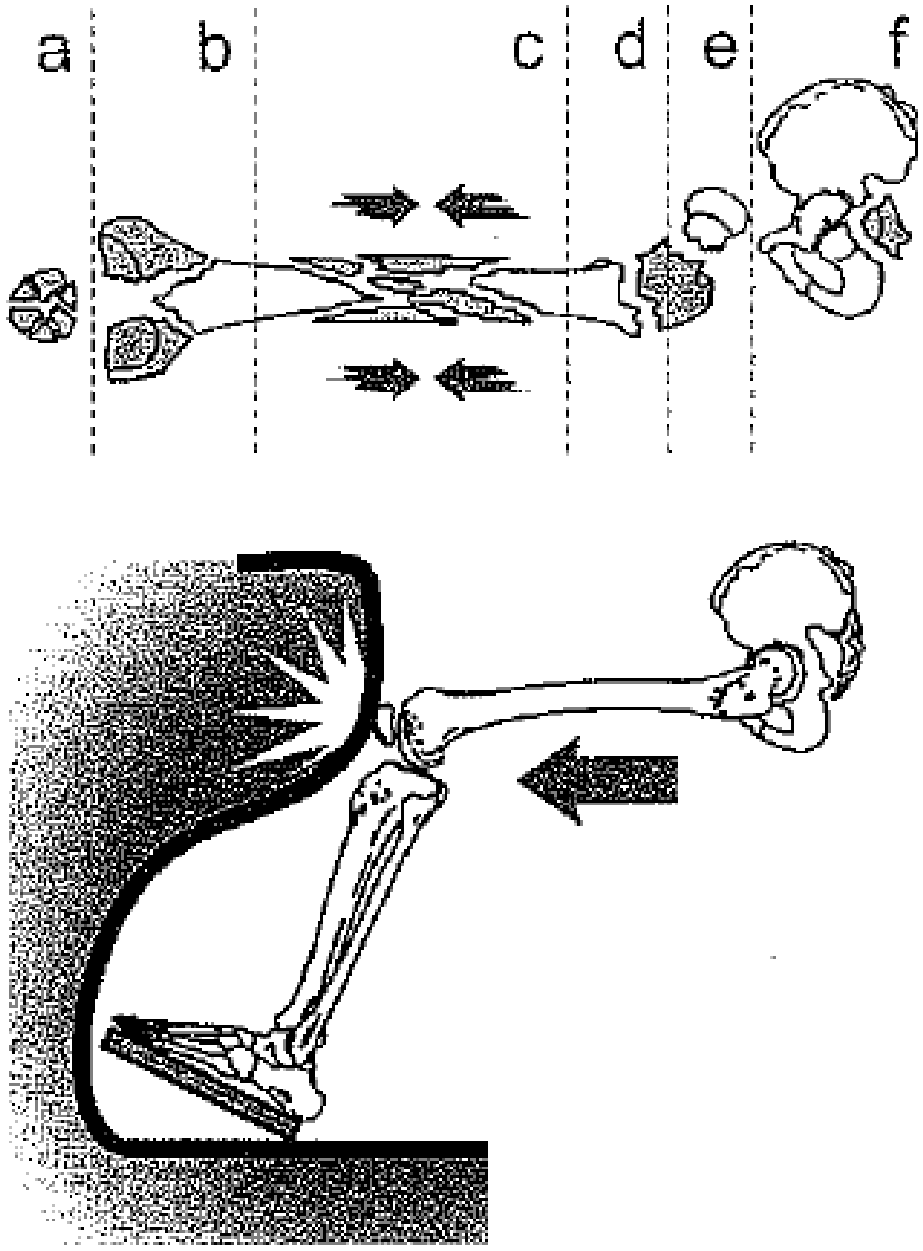

Figure 2.3. Scenarios considered in this research for investigation of KTH injury mechanism during a frontal crash. (Teresinski, 2005)

Several studies have been conducted in the past to develop a more complete understanding of the distribution of lower extremity injuries after impact and to relate these fracture modes with posture.

Lewis et al. analyzed data from the National Accident Sampling System (NASS) concluding that 53% of all pelvic injuries happened in frontal crashes. Sixtytwo percent were ranked as AIS 2 and 38% as AIS 3. 22% of AIS ≥2 pelvic injuries occurred in the 16 to 20 mph change in velocity range and 78% occurred with changes if velocity less than 30 mph. (Lewis *et al*, 1996)

Sochor et al. examined CIREN database and concluded that the initial angle of legs prior to impact can influence the risk and the location of injury. It was also determined that a 10-kN limit on femur loads is not adequate to represent real-world car crashes. (Sochor, 2003) Sochor also concluded that hip, thigh and knee injuries are more likely to occur when occupants are restrained by a three-point belt system and airbag system. Occupant compartment intrusion was not found to be an important factor for hip injuries. (Sochor, 2003)

Yoganandan et al. found that the initial position of the lower extremity prior to collision plays a considerable role also in hip injuries, after having performed unembalmed cadaver frontal crash tests with pendulum impacting knees at 4.3 to 7.6 m/s velocities. (Yoganandan *et al*., 2001)

Rupp et al. tested 22 cadavers in frontal impacts with the lower extremities positions in neutral position, (i.e, 10 degrees of adduction and 30 degrees of flexion). It was found out that hip fracture tolerance in the neutral posture was 6.1 ± 1.5 kN, with 30 degrees flexion the tolerance was reduced by 34 ± 4% and in 10 degrees adduction it was reduced by 18 ± 8% with respect to the neutral position. (Rupp, 2003a)

Monma and Sugita concluded that the action of braking can cause a slight flexion, adduction and internally rotation of hip leading to possible posterior hip dislocations. (Monma and Sugita, 2001)

Tests have also been conducted also to verify the consequences of frontal impacts on soft tissue, such as ligaments. As an example, Pike concluded that the location of the impact can play a significant role for fracture of knee ligaments: if the impact load is

directed to the anterosuperior tibial area rather then the knee joint, the tibia is displaced posteriorly with respect to the knee. This causes straining of the posterior cruciate ligament and eventually leads to its failure. (Pike, 1990)

Nordhoff offers a wider literature review on lower extremities impact tests and a more complete review of car crashes injuries analysis. (Nordhoff, 2005)

2.2.1 Injury Mechanisms for the Knee-joint

The condyles at the distal end of the femur are thin wedge shaped sesamoid bones which articulate with the tibial plateau forming the so-called knee-joint. During movements, the patella bone, also called knee-cap, travels in between these condyles according to the angle of knee extension/flexion. For movements from full extension to 90 degree flexion, the patella travels in the intercondylar groove, articulating with both condyles. Beyond 90 degree flexion, the knee-cap externally rotates and it articulates only with one condyle, the medial one, also called the medial facet.

As consequence, during an impact between the knee and the dashboard, two different types of fracture can be expected according to the angle of extension of the knee itself. In the case of flexion up to 90 degree, a fracture of both knee femoral condyles can be experienced because the patella bone is pushing against the intercondylar groove. If the knee is flexed more than 90 degrees, a split of the medial condyle is more likely to occur because the patella has rotated externally and is positioned on the medial facet. (Table 2.3)

Table 2.3. Femoral condyle fracture modes with respect to the angle of flexion of the knee

Flexed Knee 90 degrees Position

Intercondylar Groove Patella Position

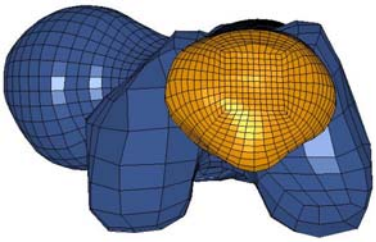

Intercondylar Fracture Femoral Condyles

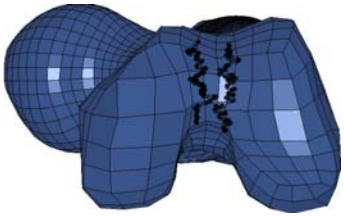

Flexed Knee >90 degrees Position

Medial Facet Patella Position

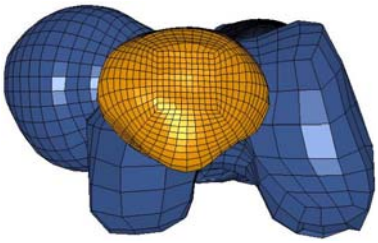

Medial Condyle Fracture

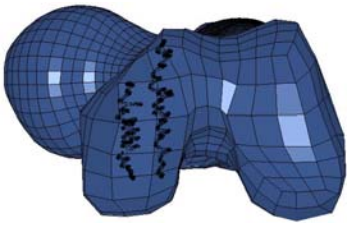

2.2.2 Injury Mechanisms for the Femur Bone

During the impact of the knee with the dashboard, a considerable amount of impact energy can be transmitted to the femoral shaft causing shaft fractures and/or fracture-dislocation of the proximal femur as well as acetabular fractures of the hip.

Fractures of the proximal femur can be extracapsular or intracapsular according to whether or not the fracture is within or without the hip joint capsule (Figure 2.4) (OrthoMeditec. Our Joint Success, 2008*)*:

- **Extracapsular**: fractures either between the greater and lesser trochanters or through them (intertrochanteric region fracture);
- **Intracapsular**: fractures at femoral neck and head.

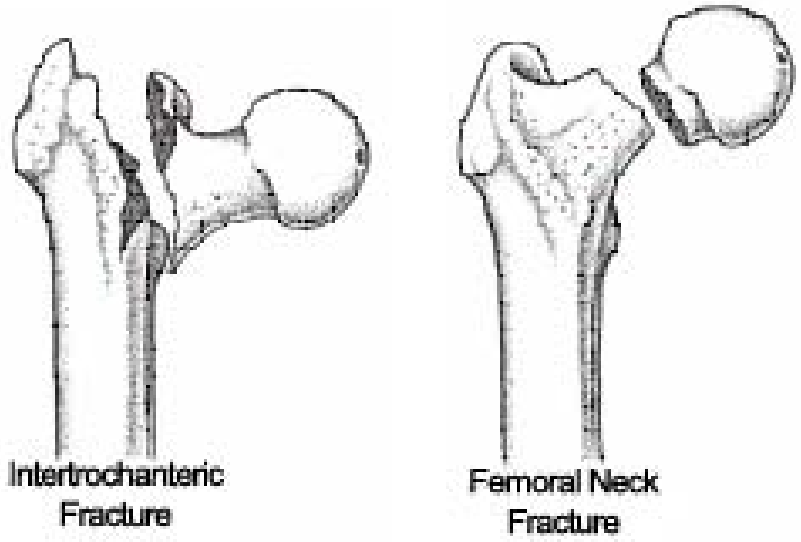

Figure 2.4. Extracapsular (left) and intracapsular femoral fractures (right). (OrthoMeditec. Our Joint Success, 2008*)*

Figure 2.5 shows different types of femur shaft fracture mechanisms (Merk Manuals. Online Medical Library, 2008). A fracture of the shaft femur is considered transverse if it is perpendicular to the long axis of the bone, while it is called oblique when it occurs at an angle. A rotatory mechanism could produce a spiral fracture. If the bone is broken in more than two bone fragments, the failure is called comminuted fracture. Comminuted fractures include segmental fractures, which are two separate breaks in the bone.
Torus fractures are typically found in childhood, when it is more likely to have a buckling of the bone cortex. Another childhood fracture is the greenstick one, when the cracks are only in one side of the cortex.

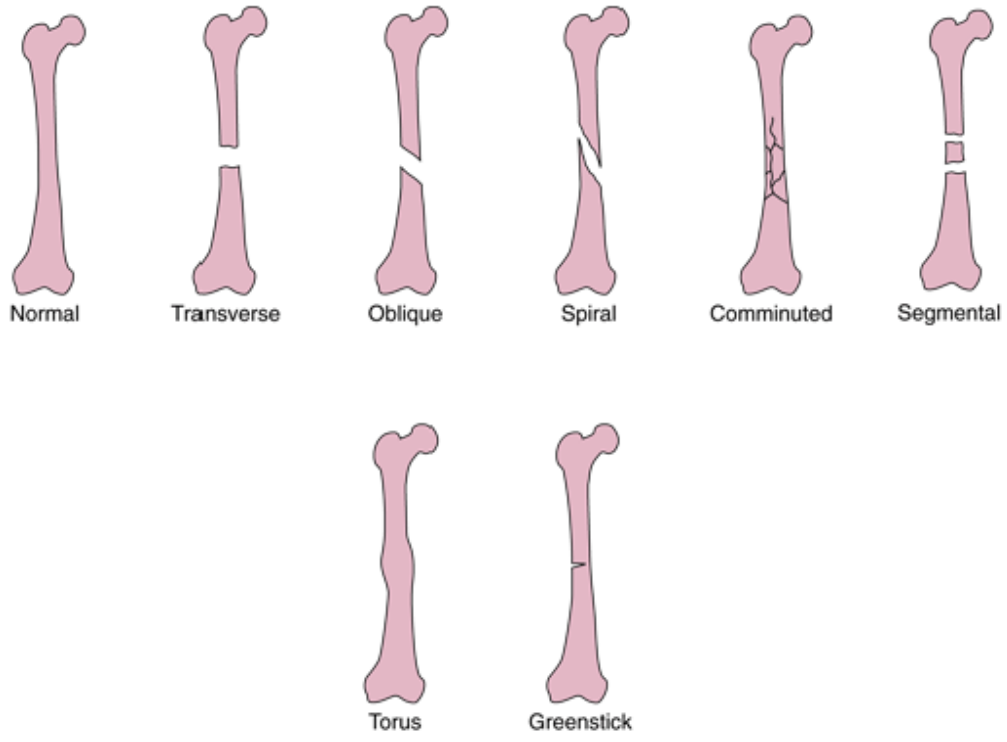

Figure 2.5. Common types of fracture lines for the femoral shaft. (Merk Manuals. Online Medical Library, 2008)

2.2.3 Injury Mechanisms for the Pelvis Bone

The pelvis is a very strong bone which requires a great force to fracture. Since high impacts are necessary to cause damage, it is understandable that car crashes are the most responsible for pelvic fractures.

As shown in Figure 2.6, fractures of the pelvic ring due to anterior-to-posterior compression could either cause:

- **"Straddle Fracture"**: all or some of the four rami are fractured off the ring or
- **"Open Book"** or **"Hinge Fracture"**: the pelvic ring separates at the area of the symphysis and opens up like a book.

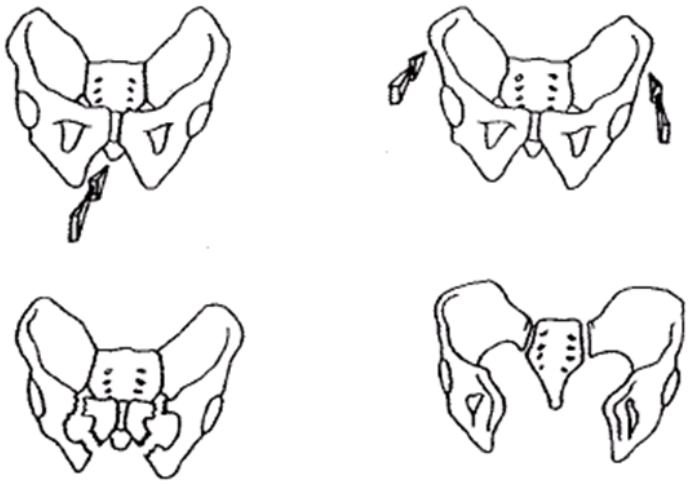

a) Straddle Fracture **b) Open Book (Hinge) Fracture**

Figure 2.6. Front-to-back compression of the pelvic ring (Hyde, 2002)

Acetabular fractures are also possible for the pelvis bone: the manner of fracture depends on the different angles of abduction and adduction of a flexed thigh (Figure 2.6).

2.2.4 Injury Mechanisms of the Femur and Acetabulum in Frontal Crashes depending on the Angle of Flexion, Adduction and Abduction

Point C in Figure 2.7 shows the neutral position of the femur (i.e., where the thigh shows neither abduction nor adduction).

In the seated position at points A and B (i.e., thigh flexed and abducted), a frontal crash would cause the knee to strike the dashboard, resulting in possible fractures of the femoral condyles, shaft or head (either intracapsular or extracapsular). If the thigh is flexed and adducted, the potential injuries from a frontal impact are acetabular fractures and/or posterior dislocation of the femur, as shown at points C and D. When the thigh is flexed and in neutral position, either A, B, C or D may occur with frontal impact.

Pure frontal impacts are rare, so even the neutral position could yield some adduction/abduction effect depending upon the direction of the eccentricity of the impact in relation to a pure frontal one. (Hyde, 2002)

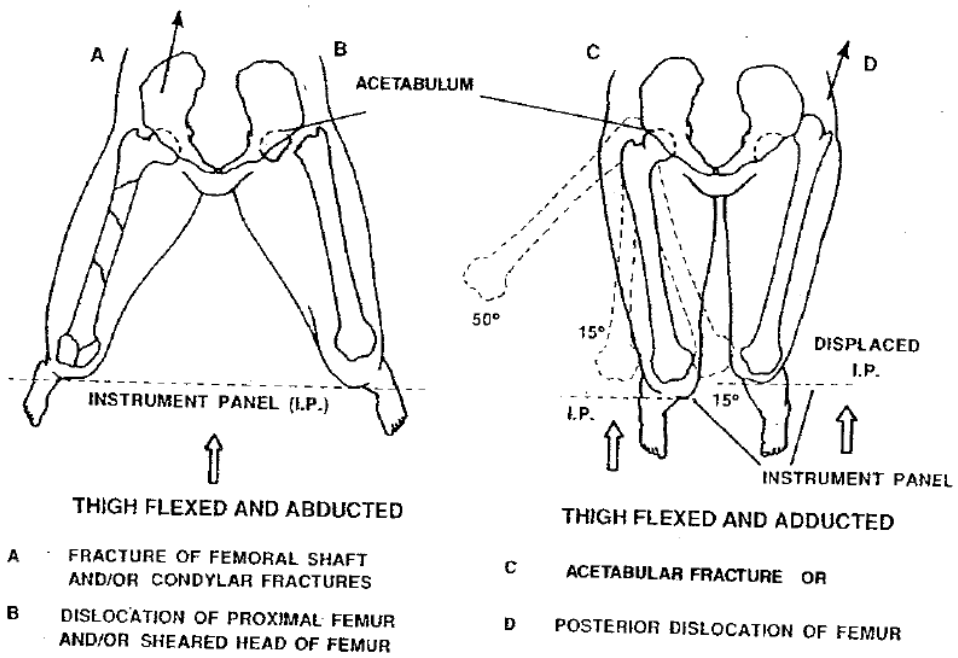

Figure 2.7. Injuries of the femur and the acetabulum in frontal crashes depending on the angles of thigh flexion, adduction and abduction. (Hyde, 2002)

Correlation between adduction/abduction angles of the leg prior to the impact and the more likely consequent injury mechanism for the lower limb are reported also by Teresinski (Teresinski, 2005). Figures 2.8 and 2.9 suggest that there is a relatively high probability for a hip joint dislocation when the leg is either flexed-adducted or abducted at a high angle, for certain direction of the impact load. Of particular interest could be Figure 2.8, because it reports probability of hip dislocation in case of a frontal impact of the knee for and abducted thigh.

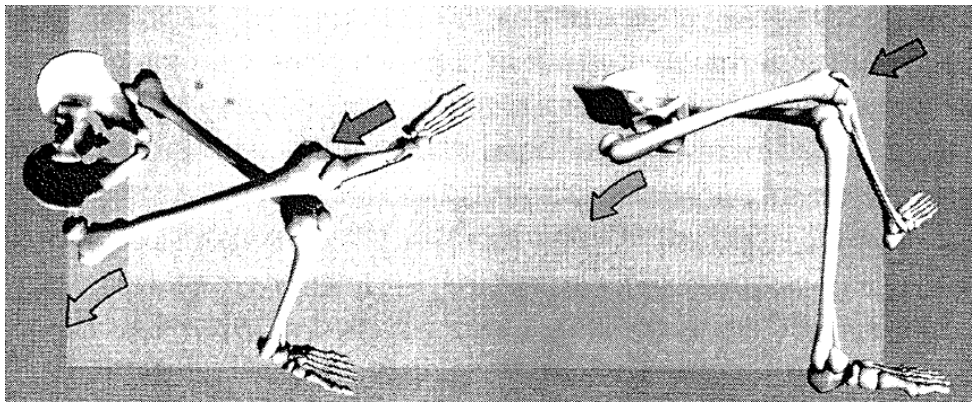

Figure 2.8. Possible hip joint dislocation occurring at adduction position of the lower limb, with a adducted femur-axial direction for the impact load. (Teresinski, 2005)

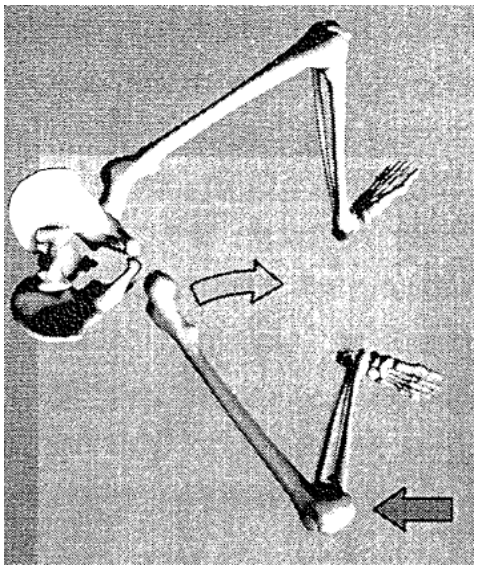

Figure 2.9. Possible hip joint dislocation occurring at high angle of abduction position of the lower limb, during a frontal impact of the knee during a car crash. (Teresinski, 2005)

2.3. Biomechanical Modeling

The use of computer simulations in passive safety area has greatly increased in the last decade: mathematical models have been used and are still under development in human impact biomechanics research, reconstruction of crashes and design of vehicle structures, safety device and roadside facilities.

2.3.1 The Need for Mathematical Modeling

Safety regulations are currently defined using crash tests of different types and conditions. Cadavers or anthropometric test devices (i.e., ATD, commonly also called "dummies") are normally used for testing human impact thresholds, at which fractures of bones or failure of soft tissue such as ligaments occur. (Figures 2.10 and 2.11) The response of a cadaver, however, can not be the same of a living person for two important reasons: (1) muscle activation cannot be taken into consideration with cadavers, while it can play a relevant role in living humans and (2) soft tissue and bones have different mechanical properties and responses "in vivo" and "in vitro" which can lead to different fracture dynamics.

Figure 2.10. Cadaver used for a sled test. (UMTRI, 2002)

On the other hand, ATDs are made of materials which are very different from the living tissues. Although they are constructed with biofidelic dimensions, masses and mass-distribution, they are made of metal, plastic and foam. Their responses to the different type of impacts can be considered just as an approximation of those that a living human would experience at the same load conditions.

Another important point is that cadavers can be used generally only once for impact tests, while ATDs need maintenance and eventually replacement of parts after each test, requiring, as consequence, a considerable amount of money.

Figure 2.11. ATDs of different sizes to be used in car crash tests. (edmunds.com, 2007)

Biofidelic mathematical models of human body, or regions of it, can be a good solution for the problems listed above. An accurate model could become part of safety regulations like standard crash tests. Several techniques, such as computer tomography (CT) scans, mechanical slicing and also detailed human anatomy books, help reproduce the exact geometry, dimensions and mass-distribution of a human model. Plus, thanks to computer modeling, it is possible to replicate mechanical responses of living tissue with adequate constitutive models.

2.3.2 The Finite Element Method

The finite element method (FEM) represents an optimal tool for modeling complicated materials such as bones and soft tissue and understanding their response to unusual loading conditions like impacts. With this method, the continuum is discretised in elements with finite dimension and interpolation functions are selected for assembling element properties to get global properties. System equations are solved for obtaining nodal unknowns and then, using the nodal values, additional calculations are made to obtain other results such as stresses, strains, moments, etc.

With classical methods, exact equations are used for defining a problem; exact solutions, however, are available in a few realistic cases. Finite element analysis leads to approximate solutions, which are possible to obtain for any problem setting. Moreover, classical methods need to simplify shapes, boundary and loading conditions of the problem considered in order to produce a solution. FEM does not require any simplification of the problem: it is just treated as it is presented. Material and geometric non-linearities can not be treated by classical methods while they can be handled by FEM.

Though FEM seems to be a very easy and powerful method with lots of advantages with respect to the use of other methods, it represents also a potentially "dangerous" tool if used by a user without knowledge about it.

For a proper use of FEA package, Bhavikati describes the basic knowledge that a user must have (Bhavikati , 2004), for example, he must know which types of elements are to be used for solving the particular problem, how to discretise to get good results, which are the limitations of the element properties considered and how the displays are developed in pre and post processors for understanding of their limitations.

2.3.3 Biomechanical Modeling of Human Body

In 1975, King and Chou presented an interesting review of biomechanical modeling activities. (King and Chou, 1976) From that time, finite element analysis techniques have been developed, helping refining and detailing anatomical finite element models of human body. Nowadays, there are biofidelic finite element model representations of several parts of the human body, such as human skull, brain, head, chest and leg. (Figure 2.12)

Just to list some of the finite element models that have been developed: DiMasi et al. proposed a model of the human brain, published a finite element representation of the human head, while Plank and Eppinger worked on the development of a human chest mathematical model. (DiMasi et al., 1991; Ruan et al., 1993; Plank, 1989) Kleinberger developed a human cervical spine model and Renaudin et al. proposed a finite element model of the human pelvis. (Kleinberger, 1993; Renaudin et al., 1993) Also, a lot of effort has been made to produce models of the long bones in upper and lower extremities.

These models of human body regions could be integrated to develop a finite element model of the whole human body to be used with vehicle crash models in virtual testing. These models could also be scaled to obtain models of different size and dimensions, in order to reproduce different types of vehicle occupants. Once the model is ready and integrated with vehicle structure and roadside facilities, virtual testing requires just a few hours (up to a few days) of simulations, according to the type of computers and the number of cpus in use. However, this leads to a considerable difference in terms of money and time-costs from conventional hardware testing.

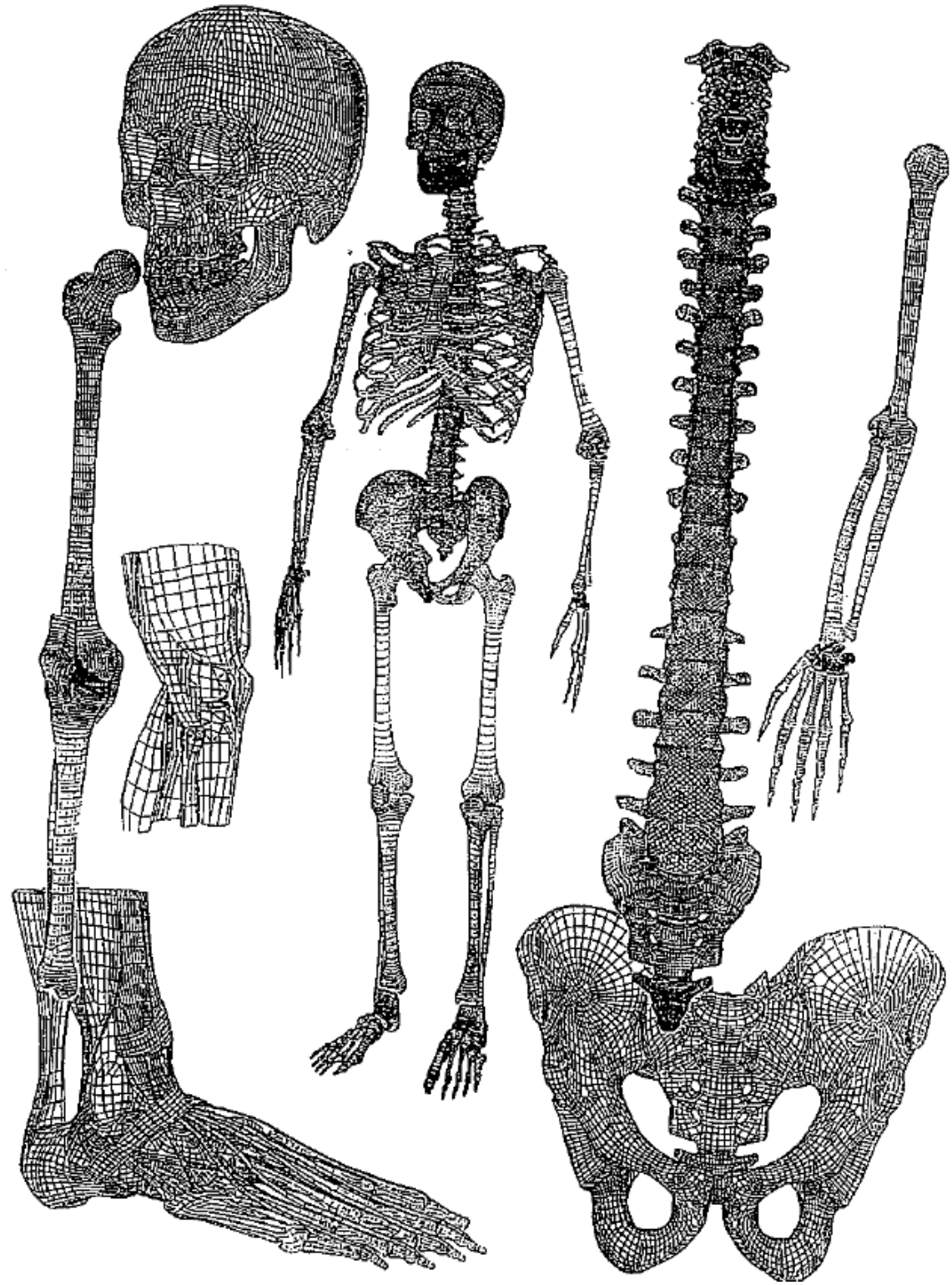

Figure 2.12. Examples of biomechanical modeling with finite element analysis. (Nordhoff, 2005)

2.4. Anatomy and Mechanical Properties of the KTH Bones

KTH bones have very complex geometry and their material behavior is complicated to define and reproduce. A few steps were needed in order to develop a bio-fidelic and reliable model:

- Inclusion of both cortical and trabecular bones because of their different properties and behavior;
- Refinement of bone meshes for avoiding unrealistically numerical errors;
- Choice of a material model which closest represents bones behavior in reality and
- Addition of failure material properties to investigate rupture modes at different loadings.

2.4.1 Geometrical and Mechanical Representation of Cortical and Trabecular bones

2.4.1.1 Bone Material

Human bones consist of two types of material: cortical and trabecular bone. Although chemical, molecular and cellular components of both types are similar, they show ultrastructural and microstructural differences that cause the two bone types to have very different mechanical properties. *(*Turner, 1993*)*

Figure 2.13 shows the structural difference between these two types of bone.

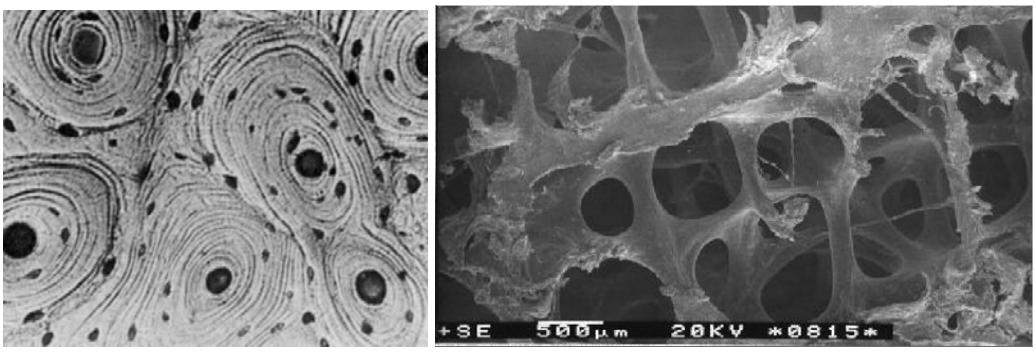

Figure 2.13. Cortical (left) and Trabecular (right) bone structures. (ICB Dent, 2008)

Cortical bone is organized in cylindrical shaped elements called osteons composed of concentric lamellae. Variations in the mechanical properties of cortical bone can be influenced by the number, orientation and size of the osteons. Similarly, the structure of individual lamellae changes orientation in different regions of the bone. This variation gives the bone its orthotropic material properties and allows the bone to respond to optimizing the usual load paths through the structure. (Turner, 1993)

Trabecular bone is quite porous and it is organized in trabecules oriented according to the direction of the physiological load (ICB Dent, 2008). It is a highly anisotropic structure composed of a large number of interconnected rods, plates or beams. Moreover, the configuration of the trabecular structures is highly variable and it depends on the anatomical site. The role of trabecular bone is to absorb and dissipate energy much like a structural foam.

With a porosity varying from five to 30 percent, cortical bone represents approximately four times the mass of trabecular bone in any long bone. In fact, in the trabecular bone porosity varies from 30 to 90. As a result, trabecular bone is much more susceptible to the morphologic alterations that accompany advancing age, metabolic diseases, and other pathologic processes. (Turner, 1993) From a structural point of view, trabecular material behaves like a foam core providing stability and volumetric support to the cortical bone which represents a stronger and denser structural shell.

2.4.1.2 Structural and Mechanical Properties of Bones

Bone is a nonlinear, viscoelastic, anisotropic and inhomogeneous material. (Turner, 1993) In fact, cortical and trabecular bone differ also for their mechanical properties.

Cortical bone properties. Due to its higher stiffness, the cortical part of a bone has a greater yield stress and a smaller plastic region than trabecular bone. It is a brittle material whose ultimate strain is on the order of magnitude of only two percent. Because of the orientation of the osteons along the major axis of the bone, it can be considered

transversely isotropic for long bones. A transversely isotropic material has the same properties in one plane (e.g. the x-y plane) and different properties in the direction normal to this plane (e.g. the z-axis).

Trabecular bone properties. In vivo, trabecular bone can sustain strains on the order of 75 percent before failure. It has a greater capacity to store energy than the cortical bone and it can be treated as an anisotropic material having no planes of material symmetry.

Mechanical properties can also vary between specific bones. This is especially true for cortical bone, in fact the orientation of the osteons varies with the kind of forces applied. In the femur shaft, for example, the osteons are aligned with the direction of the typically applied compression forces. The pelvis, on the other hand, is subjected to different systems of forces and the directions of the osteons are much more complex since the load paths in the pelvis are more complex.

Both types of bones exhibit viscoelastic behavior. This means that the material is rate-sensitive: its stiffness increases with strain rate and that the plastic region shrinks as shown in Figure 2.14. *(*Hall, 1992*)* This effect is particularly important since the strain rates typical for car crashes are in the order of five – 10 (velocities around 5 m/s – 10 m/s). *(*Turner, 1993*)*

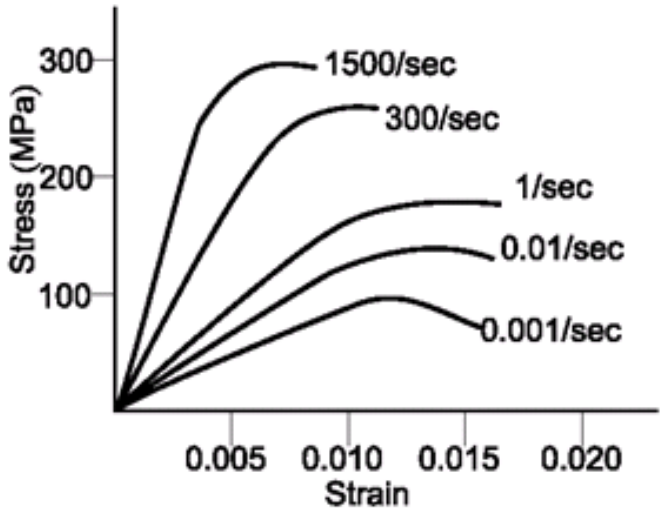

Figure 2.14. Strain rate effects on bone material. *(*Kennedy, 2004*)*

There are other parameters influencing the mechanical properties of bones, such as age, disease, preservation and bone hydration.

Studies showed that from the third to the ninth decades of life, the ultimate tensile strength of cortical bone of the femur decreases from approximately 130 MPa to 110 MPa and the corresponding elastic moduli reduces from 17 GPa to 15.6 GPa. The slope of the stress-strain curve decreases by 8 percent per decade. (Hall, 1992)

Some diseases, like osteoporosis, can greatly decrease the ultimate stress of the bone material.

The best way to preserve bones for mechanical testing is to freeze the specimen at -20°C in saline soaked gauze. Tests have shown that mechanical properties do not change even after some weeks when bone materials are stored in this way. (Kennedy, 2004)

When the bone is dried, the Young's modulus and ultimate stress tend to increase significantly while the toughness decreases. Femurs, for example, show an increase of 17 percent in the Young's modulus, a 31 percent increase in the ultimate tensile stress but a 55 percent decrease in toughness after drying. (Kennedy, 2004)

2.4.1.3 Material Modeling

Cortical bone is a nonlinear orthotropic material, however, it has often been considered a linear elastic material in finite element simulations. For a more correct prediction of the bone fracture sites and failure modes, a more realistic and biofidelic material model should be used. LSDYNA has several composite material models that may be useful in representing the nonlinear orthotropic behavior of cortical bone. Trabecular bones are also nonlinear but they function more like a foam core which suggests that a foam material model could be used. LSDYNA has several material models that describe a variety of foams.

Hooke's law, in the case of the elastic model, describes the stress – strain relationship:

$$\sigma_{ij} = C_{ijkl}\varepsilon_{kl} \tag{2.1}$$

In general, C is a tensor with 81 coefficients. Symmetry, however, can reduce the number of independent variables to nine independent constants for an orthotropic material, five for a transversely isotropic (TI) material, and only two for a completely isotropic material. A TI material is one which has a principal direction (longitudinal) and a transverse direction. Properties in all the transverse directions are constant. A TI model is a good assumption for the material behavior of cortical bone, especially long bones like the femur that have a dominant structural axis. The inverted form of the coefficient tensor (i.e., flexibility), relates the engineering constants to the more general ones.

$$C^{-1} = \begin{bmatrix} \frac{1}{E_1} & -\frac{\upsilon_{21}}{E_2} & -\frac{\upsilon_{13}}{E_3} & 0 & 0 & 0 \\ -\frac{\upsilon_{21}}{E_2} & \frac{1}{E_2} & -\frac{\upsilon_{13}}{E_3} & 0 & 0 & 0 \\ -\frac{\upsilon_{13}}{E_1} & -\frac{\upsilon_{23}}{E_2} & \frac{1}{E_3} & 0 & 0 & 0 \\ 0 & 0 & 0 & \frac{1}{G_{13}} & 0 & 0 \\ 0 & 0 & 0 & 0 & \frac{1}{G_{23}} & 0 \\ 0 & 0 & 0 & 0 & 0 & \frac{1}{G_{12}} \end{bmatrix} \qquad (2.2)$$

The three directions (i.e., 1, 2 and 3) correspond to the principal axis. Additional restrictions are that:

$$G_{12} = \frac{E_1}{2 \cdot (1 + \upsilon_{21})} \qquad \frac{\upsilon_{13}}{E_1} = \frac{\upsilon_{31}}{E_3} \qquad (2.3)$$

which reduces the unknowns to five, E1, E3, v12, v13, G13. Equation (2.2) can then be inverted to give Hooke's law for a TI solid in terms of the engineering constants. (Niebur, 2002) Experimental tests can be used to find the values for these fives variables.

Tests on trabecular bone material can be used to determine the type behavior and the appropriate type of constitutive model (i.e., linear or nonlinear, anisotropic or with

some symmetry). Good candidates to describe trabecular bone behavior are (1) open cell foams since there is no internal pressure and (2) crushable.

From a finite element modeling point of view it is preferable to attempt to model "typical" mechanical properties rather than those at the extremes. (i.e., a healthy middle aged male, for example, rather than an elderly woman with osteoporosis). However, most of the test results used for comparison with KTH model simulations were obtained from bones of older humans with osteoporosis problems.

2.4.2 Anatomy of the KTH Bones

There are three bones in the knee-thigh-hip region: the pelvis, femur and patella. The following sections describe the basic anatomy of each of these bones. A complete and detailed description of the anatomy of these bones can be found in Gray, 1918.

2.4.2.1 Pelvis

The pelvis is a bone with an irregular shape, large and flattened. It is symmetric about the midsaggital plane. Three main parts can be identified, which are the ilium, the ischium, and the pubis. While in younger age, these three parts are not united, around the twenty-fifth year they come into fusion. The place where these parts unified is called acetabulum. The acetabular cup is also the socket where the femoral head fits. The thicker parts of the pelvis consist of trabecular tissue, enclosed between two layers of cortical tissue. The thinner parts, as at the bottom of the acetabulum and center of the iliac fossa, are composed entirely of compact tissue. (Gray, 1918) A sketch of the pelvis with its major features is shown in Figure 2.15.

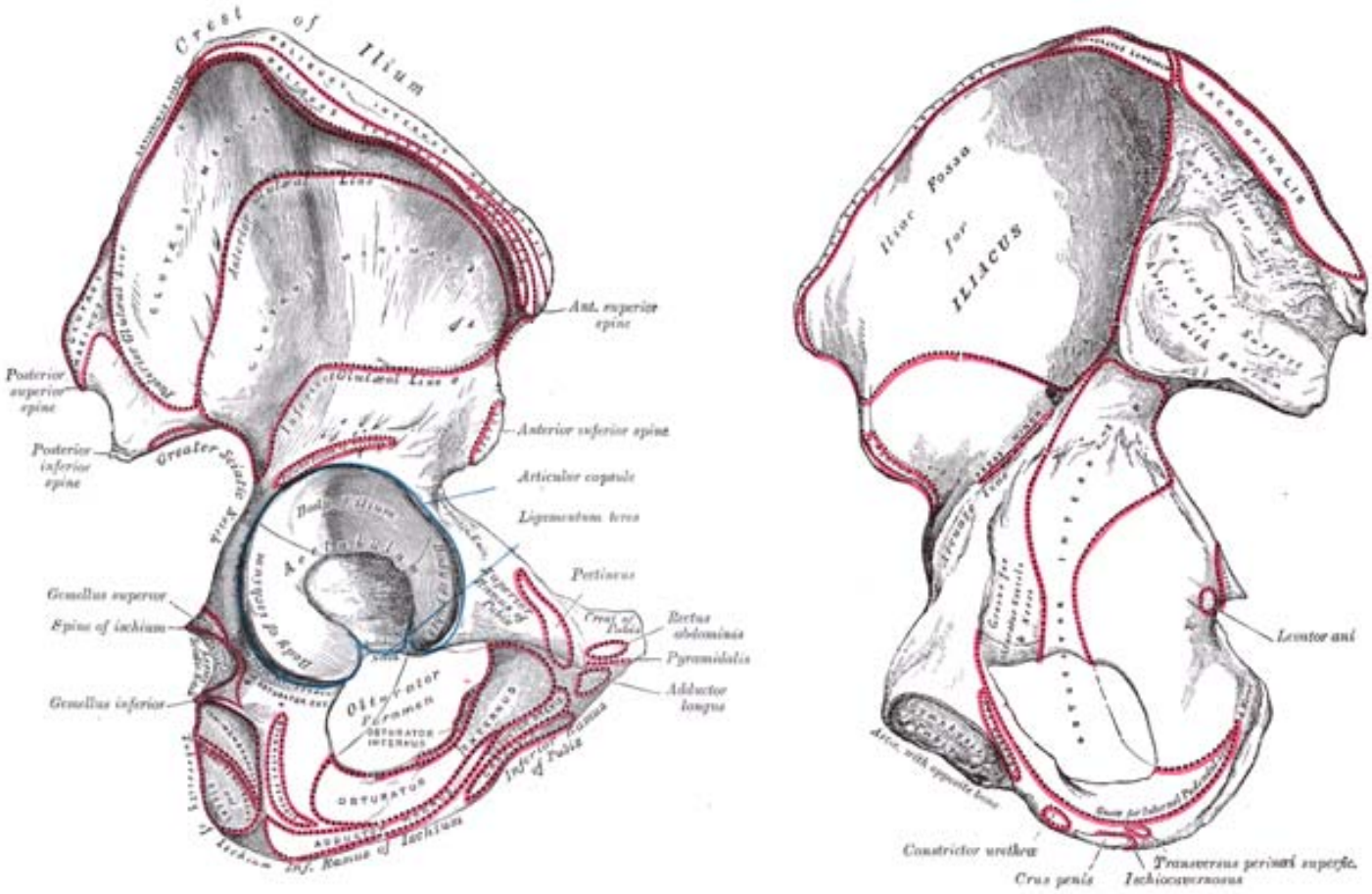

Figure 2.15. External (left) and internal (right) surfaces of the pelvis. (Gray, 1918)

2.4.2.2 Femur

Cortical Part. The femur is the longest and strongest bone of the human body. As other long bones, it can be divided into a body and upper and lower extremities parts. The body part is also called femoral shaft and has almost a cylindrical shape for all its length (Figure 2.17). The upper extremity is composed of the femoral head fitting into the acetabular cup, a neck connecting the head with the body and a greater and a lesser trochanter providing leverage to muscles for rotation of the thigh. (Gray, 1918) Figure 2.16 shows the important parts of the proximal femur.

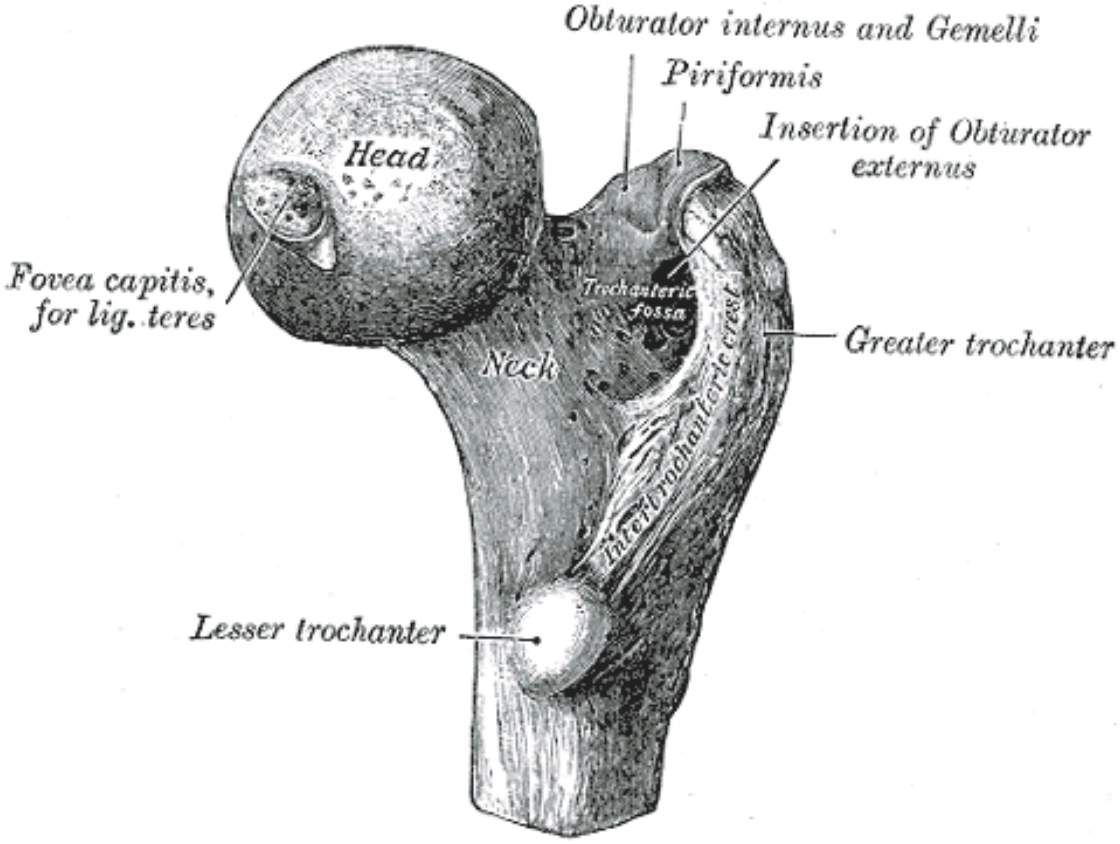

Figure 2.16. Upper extremity of the femur. (Gray, 1918)

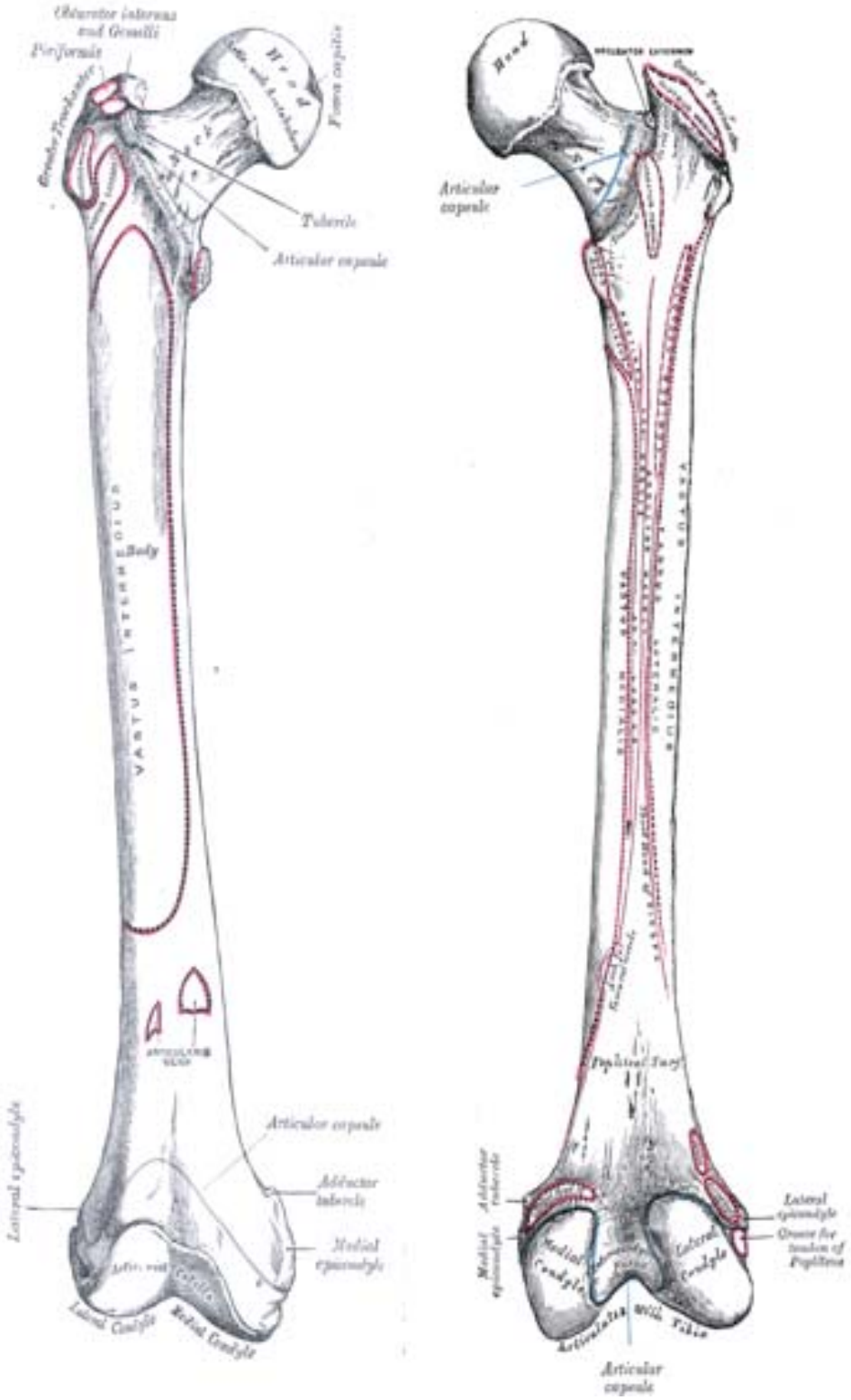

Figure 2.17. Anterior (left) and posterior (right) surfaces of the femur. (Gray, 1918)

Figure 2.18 shows the condyles of the femur.

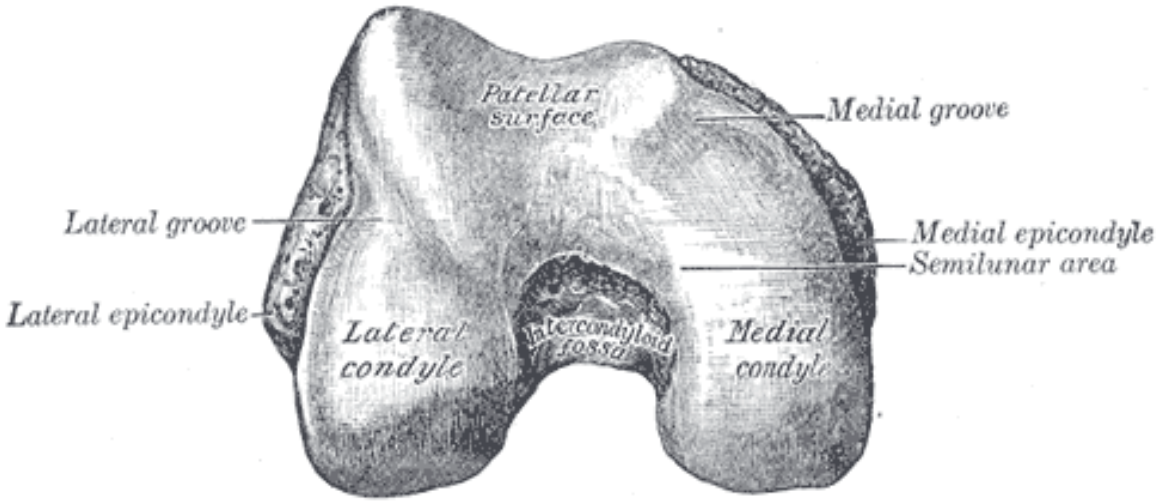

Figure 2.18. Condyles of the femur. (Gray, 1918)

Bones adapt their structure in response to long-term loading. The femur is constituted in such a way that it transmits the loads from the acetabulum to the tibia in the most economical and structurally efficient way. Throughout the femur the bony material is arranged in the paths of the maximum internal stresses in order to resist the applied loads with the greatest possible efficiency and economy of material. (Koch, 1917)

Trabecular Part. Trabecular part is present in the upper and lower extremities of the femur. In the upper femur, this cancellous part is composed of two distinct systems of trabeculae arranged in curved paths which intersect each other at right angles. This system is related with the lines of maximum compressive stress, as shown in the Figures 2.19, 2.20 and 2.21. (Gray, 1918)

Under normal conditions, the trabeculæ are arranged in two general systems: compressive and tensile, which correspond in position with the lines of maximum and

minimum stresses in the femur determined as a mechanical structure. The thickness and spacing of the trabeculæ vary with the intensity of the maximum stresses at various points in the upper femur, being thickest and most closely spaced in the regions where the greatest stresses occur. The amount of bony material in the spongy bone of the upper femur varies in proportion to the intensity of the shearing force at the various sections. The arrangement of the trabeculæ in the positions of maximum stresses is such that the greatest strength is secured with a minimum of material. (Gray, 1918) The same pattern can be found in the whole femur. The bone material of the femur, therefore, is orthotropic and its principal axes change continuously throughout its length, especially in the proximal portion of the femur. This presents some interesting mesh generation and material selection issues that will be discussed in a later section.

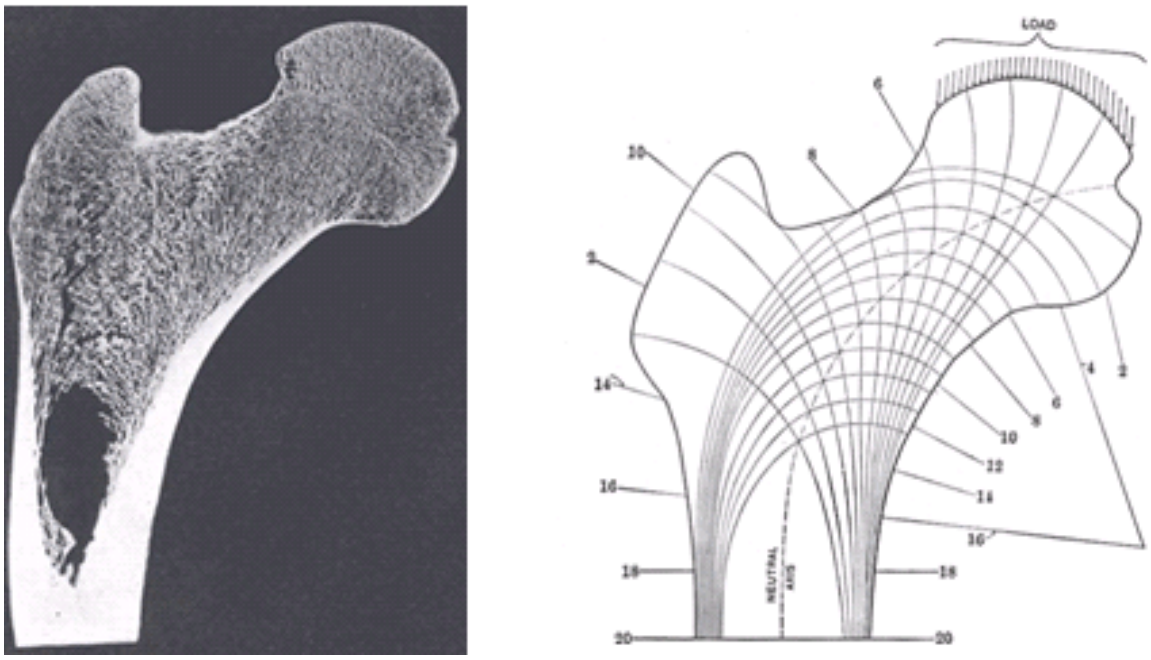

Figure 2.19. Section of the femoral head with visible trabecular pattern (left) and representation of lines of maximum compressive stresses (right). (Gray, 1918)

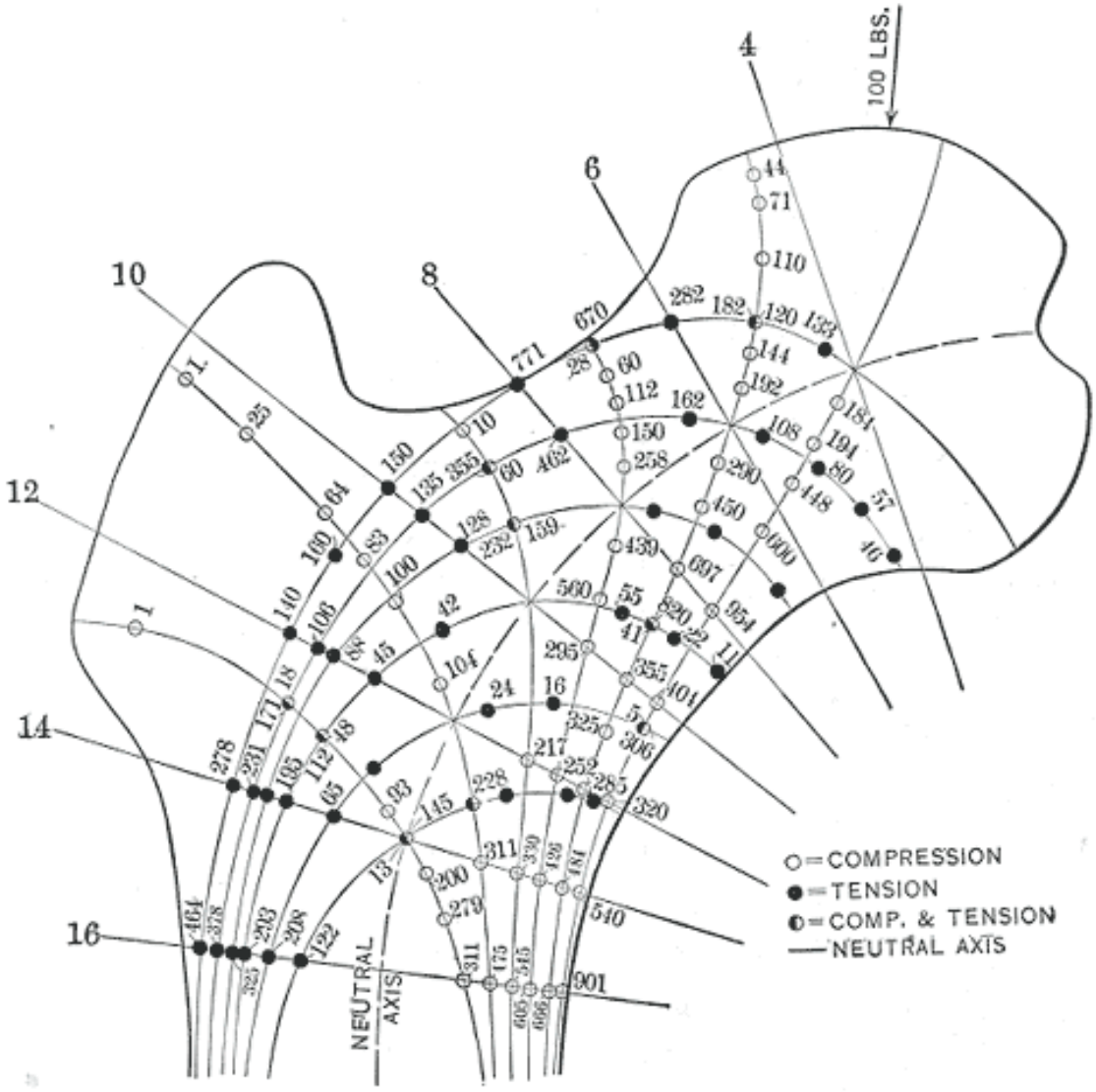

Figure 2.20. Intensity of the maximum tensile and compressive stresses in the upper femur. Computed for the load of 100 pounds on the right femur. (Gray, 1918)

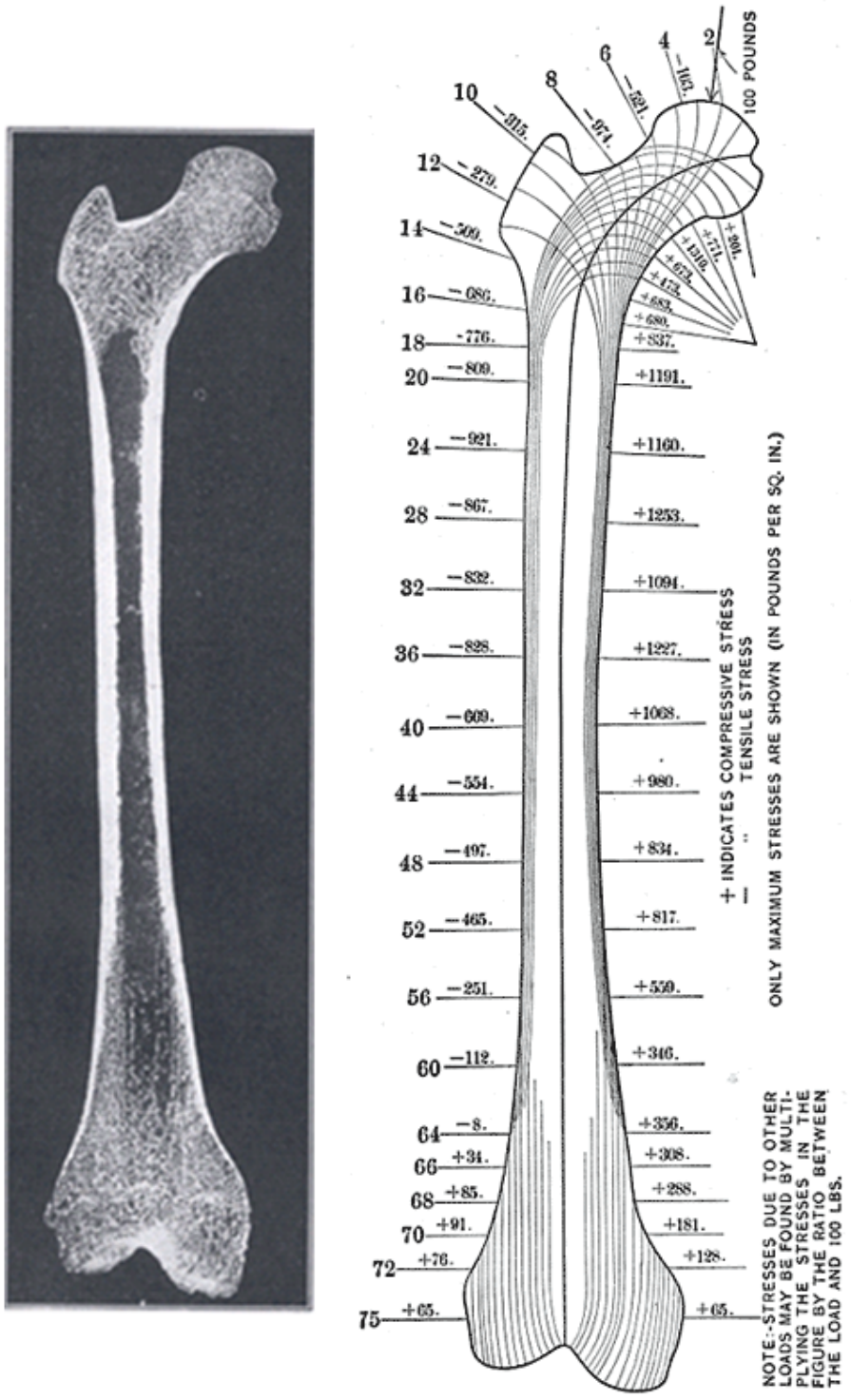

Figure 2.21. Frontal longitudinal midsection of left femur (left) and diagram of the computed lines of maximum stress in the normal femur (right). (Gray, 1918)

2.4.2.3 Patella

The patella is a small bone located in front of the knee joint. It covers the junction between the lower femur and the upper tibia. Their main functions are protecting the front of the joint and increasing the leverage of the quadriceps femoris. The patella is essentially composed by dense trabecular tissue. (Gray, 1918) This cancellous part is covered by a thin cortical surface. The basic geometry of the patella is shown in Figure 2.22.

Figure 2.22. Anterior (right) and posterior (left) surfaces of the patella. (Gray, 1918)

2.4.3 Mechanical Testing of Bones

A wide variety of data exists in literature regarding testing of bones. Unfortunately, there is a wide variability in the kinds of test performed (i.e., tension, compression, whole bone, specimen, age of bone, etc.) and a corresponding wide variation in the results. Many tests give results without specifying the type of preservation for the bone, others do not specify if the bone was wet or dry, others use compressive tests to find mechanical properties of the bone without taking into account the geometry of the test setup. (Garnier, 1999) The result is that there are a large number of tests and results but their usefulness and accuracy for finite element modeling are uncertain. Moreover, the interest of this study are the mechanical properties of bones in automobile crashes. Since the material is rate sensitive knowledge of the strain rate used in the tests is important although all the tests in the literature are presumed to be quasi-static.

Test specimens must be obtained from different parts of the whole bone and from different kind of bones (e.g., femur, pelvis, etc.). The preparation of the specimen must carefully controlled to obtain good results. Usually is it possible to obtain specimens of about 7 to 10 mm cubes for trabecular bones and 15-to 20-mm long, 4-to 8-mm wide specimens of cortical bone. During machining into coupons the specimens must be hydrated to ensure that they do not dry out. (Kennedy, 2004) The specimens must be small enough to avoid structural inhomogeneity but large enough to satisfy the continuum assumption. (Turner, 1993) The dimensions of the specimens are so small that their production and testing can be very difficult. Moreover, the measure of strain cannot be achieved by typical mechanical tools and require more precise instrumentations.

Two types of tests can be used for measuring the Young's and shear moduli: mechanical or acoustic.

- Acoustic testing has several advantages. Acoustic test do not require expensive testing machines and they are nondestructive so the same test can be repeated several times on the same specimen. For this reason ultrasonic methods can achieve much greater precision than mechanical tests in the calculation of the Young's modulus and shear

modulus; this is important if an experimental design requires small treatment groups. The disadvantage is that force must be inferred because it cannot be measured directly;

- Mechanical tests, shown schematically in Figure 2.23, are more common but require more attention to the setup of the test and the preparation of the specimen. The main advantage is that a direct measure of the force applied to the specimen is obtained allowing for direct computation of parameters like the yield and ultimate stress. Different kinds of tests can be performed: tensile, compression, bending, torsion and pure shear tests. Tensile and compression tests are most commonly performed since they are easier to do and involve more standard equipment. Tensile tests usually give better results than compressive tests. (Kennedy, 2004)

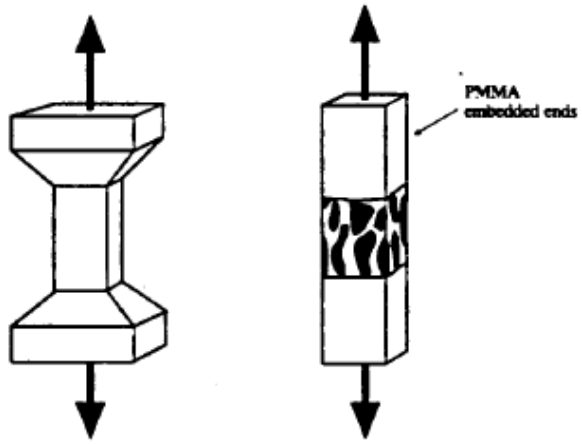

Figure 2.23. Tensile tests for cortical (left) and trabecular (right) bone. (Kennedy, 2004)

Data about material and mechanical properties for both trabecular and cortical bones were searched through a peculiar and meticulous literature review. Next section will give a more detailed explanation about the literature data which have been chosen for modeling bones in the KTH finite element model.

2.5. Anatomy and Mechanical Properties of the KTH Ligaments and Tendons

Ligaments and tendons are soft tissues with the role of connecting two bones and muscles to bones respectively.

A few steps are needed in order to develop a bio-fidelic and reliable model:

- Inclusion of ligaments of the pelvic region and more precise and anatomical location of those in the knee area;
- Choice of a material model which closest represents ligaments behavior in reality; and
- Addition of failure material properties to investigate rupture modes at different loadings.

2.5.1 Geometrical and Mechanical Representation of Ligaments

2.5.1.1 Structural and Mechanical Properties of Ligaments

The main function of ligaments is to allow smooth and effortless joint motions while restricting abnormal motions. Ligaments are composite structures made of fibers of collagen and elastin embedded in a ground substance matrix. Collagen constitutes 70 to 80 percent of the total weight and is responsible for the tensile properties of the ligaments, while the ground substance, made up primarily of water, provides lubrication and spacing that aid in the sliding of fibers. Organization of the collagen is shown in Figure 2.24. (Frisen, 1969)

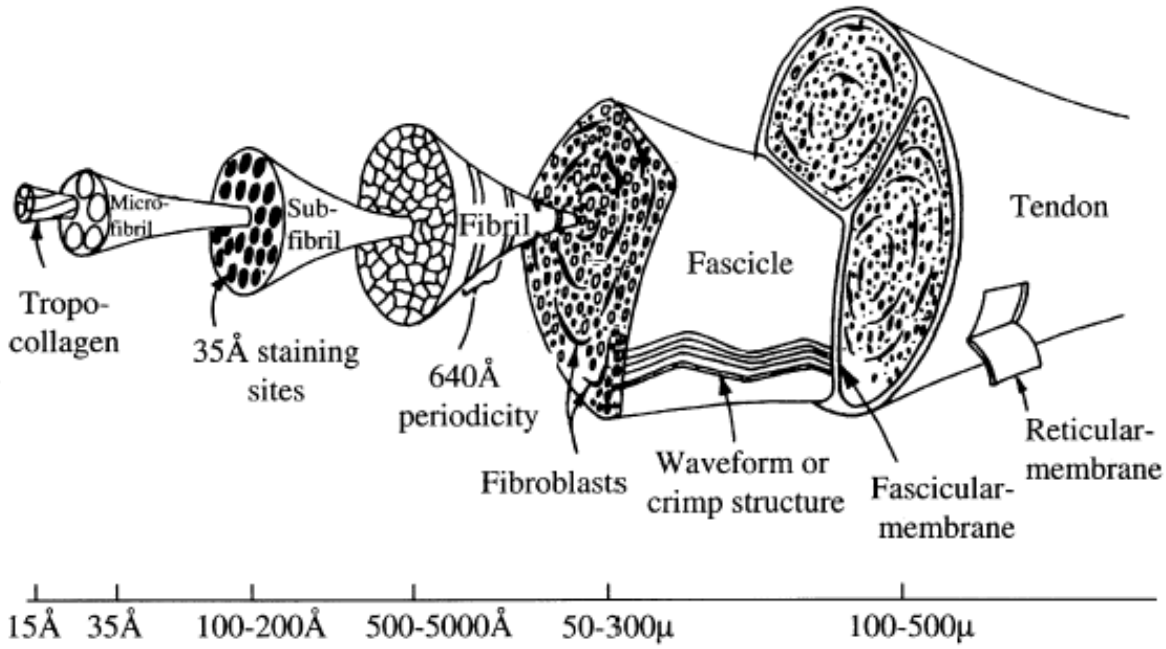

Figure 2.24. Structural hierarchy of ligaments and tendons. (Frisen, 1969)

The interaction of elastic, reticular, and collagen fibers are critical for normal joint mobility. These features allow ligaments to have a limited range of strains over which they produce minimal resistance to movement. As a result of this, joints may easily be moved in certain directions and over certain ranges.

Ligaments and tendons share very similar material and mechanical properties. They are inhomogeneous organic materials with anisotropic behaviour and show a great dependence on constitution, age, level of exercise, diseases and contingent factors. However, average material properties can be summarized in the Table 2.4. (Anderson, 2002)

Table 2.4. Average material properties of Ligaments. (Anderson, 2002)

Elastic Modulus:	1-2 GPa
Ultimate Strength:	50-150 Mpa
Toe Region (Strain):	1.5-3 %
Strain without damages:	5-7 %
Maximum Strain before failure:	9-18 %

Figure 2.25 (a and b) shows a typical load-elongation curve and a stress-strain curve for ligaments tested in tension. With initial lengthening of ligament tissue, the curve concavity is directed upward as the collagen crimp pattern is straightened. This portion of the stress-strain curve is known as the "toe" region and is often described as having the shape of an exponential or polynomial relationship. The toe region typically extends to a strain of 1.5 percent to 3 percent although there can be considerable inter-specimen variability. (Viidik, 1968a)

At the end of the toe region, there is a gradual transition into the linear region of the stress-strain curve as the collagen is straightened. This portion of the curve is dominated by the material behaviour of the straightened collagen. The uniaxial stress-strain curve remains essentially linear until failure. The peak stress value is the tensile strength and the corresponding strain is the ultimate strain. Continued straining beyond this point results in catastrophic failure of collagen fibres. (Woo, 1994)

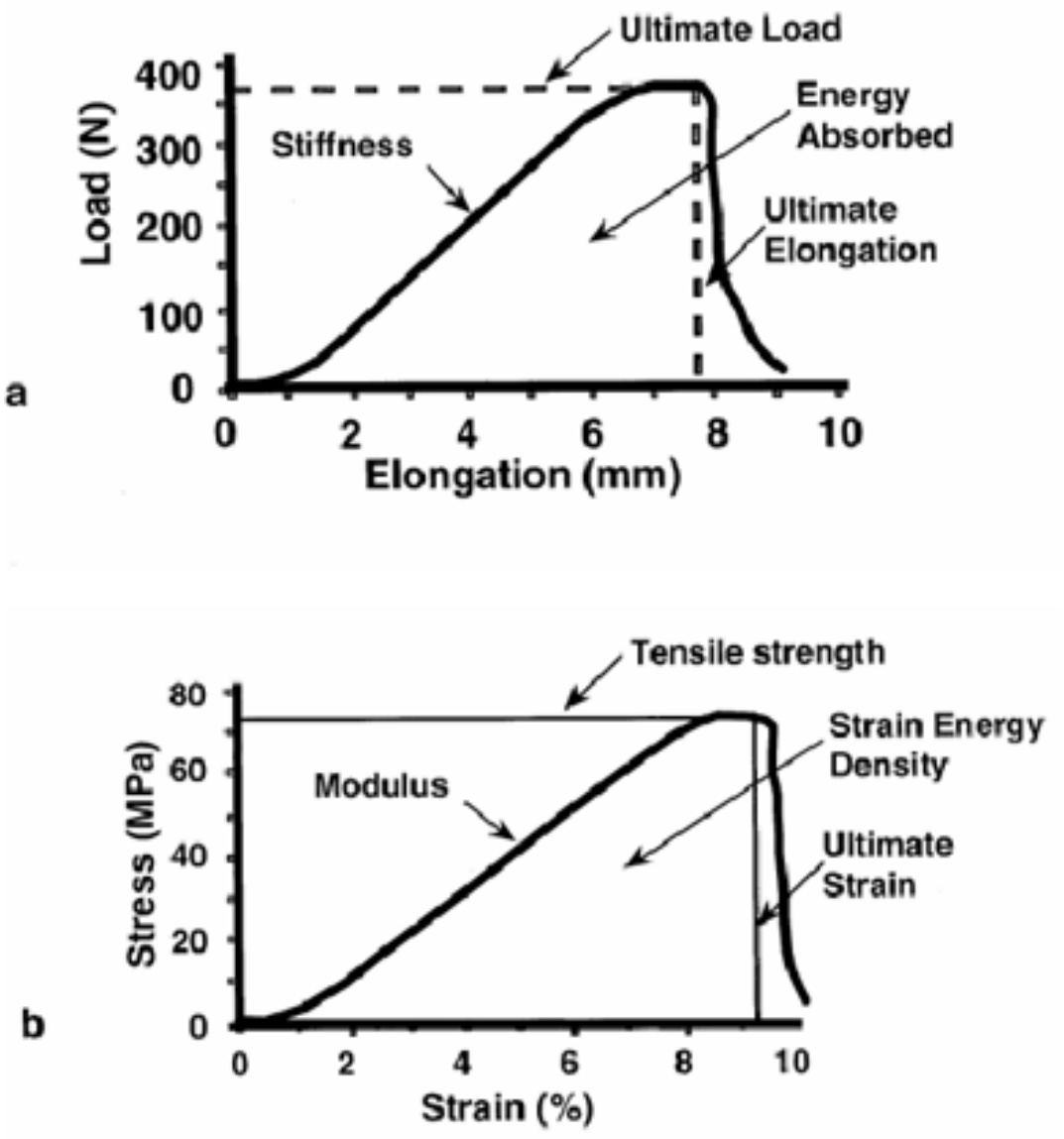

Figure 2.25. Typical load-elongation curve of a bone-ligament-bone complex (a) and typical stress-strain curve describing the mechanical properties of the ligament substance. (b) (Savio, 2000)

2.5.1.2 Material Modeling

According to Weiss, ligament material models can be divided into microstructural or phenomenological models depending on the scale on which the representation is carried out. (Weiss, 2001) Ligaments and tendons tissues are extremely nonlinear, anisotropic, inhomogeneous and viscoelastic, and can undergo large deformations. To deal with these complexities, some viscoelastic models have been formulated using either microstructural (i.e. spring and dashpots, including nonlinearity of the elastic response (Viidik, 1968b; Frisen, 1969; Lanir, 1980; Decraemer, 1980) or phenomenological approaches. (Barbenel, 1973; Dehoff, 1978; Bingham, 1979; Pioletti, 2000)

Fung developed the most widely used theory in soft tissue mechanics, named quasi-linear viscoelasticity (QLV) (Fung, 1993) The basis of this theory is that the stress at a given time can be described by a convolution integral, separating the elastic response and the relaxation function, and the relaxation function has a specific continuous spectrum. The formulation of QLV theory is similar to finite linear viscoelasticity. It is assumed that the stress relaxation function can be expressed as a convolution of a relaxation function with an elastic response:

$$S(t) = G(t) * S^e(E) \tag{2.4}$$

where $S^e(E)$ is the elastic response and G(t) is the reduced relaxation function. In general, G(t) is a fourth order tensor providing direction-dependent relaxation phenomena. Using the superposition principle and representing the strain history as a series of infinitesimal step strains, the overall stress relaxation function can be expressed as the sum of all individual relaxations. For a general strain history, the stress at time t, S(t), is given by the strain history and the convolution integral over time of G(t):

$$S(t) = \int_{-\infty}^{t} G(t-\tau) : \frac{\partial S^e(E)}{\partial E} : \frac{\partial E}{\partial \tau} d\tau \tag{2.5}$$

For biological soft tissues, Fung proposed a continuous relaxation representation for G(t). It was assumed that the relaxation function was the same in all directions which reduced G(t) to a scalar, G(t):

$$G(t) = \frac{\left\{1 + c\left[E_1(t/\tau_2) - E_2(t/\tau_1)\right]\right\}}{1 + c\ln(\tau_2/\tau_1)} \tag{2.6}$$

where $E_1(t)$ was the exponential integral function,

$$E_1(t) = \int_z^\infty \frac{e^{-t}}{t} dt \tag{2.7}$$

This relaxation function provides a smooth, linear decrease from short to long relaxation times. The stiffness (real part of complex modulus) increases with increasing frequency, whereas the damping (imaginary part) is relatively constant over a wide range of frequencies. (Tschoegl, 1989) This yields a hysteretic loop that is relatively insensitive to strain rate over several decades of change, a feature often observed for soft tissues. The three viscoelastic material coefficients, $\tau 1$, $\tau 2$, and c, can be determined from the analysis of a stress relaxation experiment. $\tau 1$ and $\tau 2$ represent time constants that bind the lower and upper limits of the constant damping range of the relaxation function and c is a dimensionless constant that scales the degree to which viscous effects are present. One of the advantages of QLV theory is that it decouples the elastic contribution to the stress from the time- and rate-dependent contributions. This makes it relatively easy to use any hyperelastic model for the elastic contribution since the viscoelastic portion will remain unaffected.

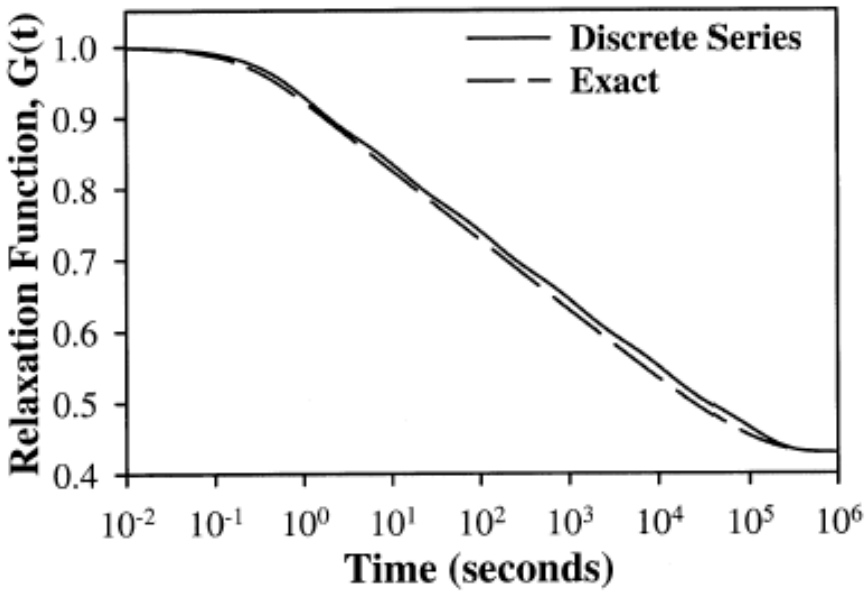

Figure 2.26. Relaxation functions G(t) given by the quasi-linear viscoelastic function and the discrete spectrum approximation. (Puso, 1997)

For all these models, however, the computational effort required is significant and numerous limitations of this technique have been documented (Lakes, 1999). To allow efficient and easy computational implementation, a discrete spectrum approximation was developed for the QLV relaxation function. This approximation provided a graphical means to fit experimental data with an exponential series. (Figure 2.26) (Puso, 1997) The response of many tissues shows a frequency-dependent damping and the QLV theory is not able to represent this behaviour. The most complete theoretical framework was introduced by Pioletti *et al*. and consists of a non-linear viscoelastic model based on the constitutive equations described by Truesdell and Noll. (Pioletti, 1998; Truesdell, 1992) This model assumes incompressibility and takes into account the contribution of elastic, short time and long time terms together with some thermodynamic constraints, in a single constitutive equation:

$$S = S^e(C(t)) + S^v(\dot{C}(t); C(t)) + \int_{\delta}^{\infty} \sum (G(t-s), s; C(t))ds, \tag{2.8}$$

where the successive terms of the right-hand side of (A) are the different contributions based on the time scale of their effects. This original description has the advantage of separating the different mechanical behaviours which facilitates the parameter identification process. This theory, however, does not include the frequency response of the tissue, and still assumes an isotropic material while a transversely isotropic material would better describe ligaments and tendons response. (Pioletti, 2000) A recent study from Bonifasi-Lista suggests that the viscoelastic mechanisms are unaffected by strain level and the change in dynamic stiffness with strain level are due to the elastic behaviour of the tissue. (Bonifasi Lista, 2003)

2.5.2 Anatomy of the KTH Ligaments

2.5.2.1 Hip Joint Ligaments

The hip joint, shown in Figure 2.27, is made up of the articular capsule, which is a membrane that covers the bone and the following six ligaments:

- The pubofemoral ligament,
- The iliofemoral ligament,
- The teres femoris (also ligamentum capitis femoris),
- The ischiofemoral ligament,
- The acetabular labrum and
- The transverse acetabular.

The articular capsule and ligaments stabilize the hip joint, especially the iliofemoral ligament which tightens in extension and enables the hip to assume a stable close-packed position. Contrary to what happens in other joints, the role of ligaments on determining the hip joint motion and range of motion is less significant. Generally, ligaments are responsible in large extent to the range of motion of a joint, but in the specific case of the hip, the ligament only limits motion in hyperextension. In fact, in this joint, the ligaments primarily work to keep the femur head inside the acetabular cup.

Besides the well known mechanical resistance provided by this tissue in the other joints, in the hip capsule the ligaments creates a kind of vacuum effect that increases several times the force necessary to dislocate the joint. (Anderson, 2002)

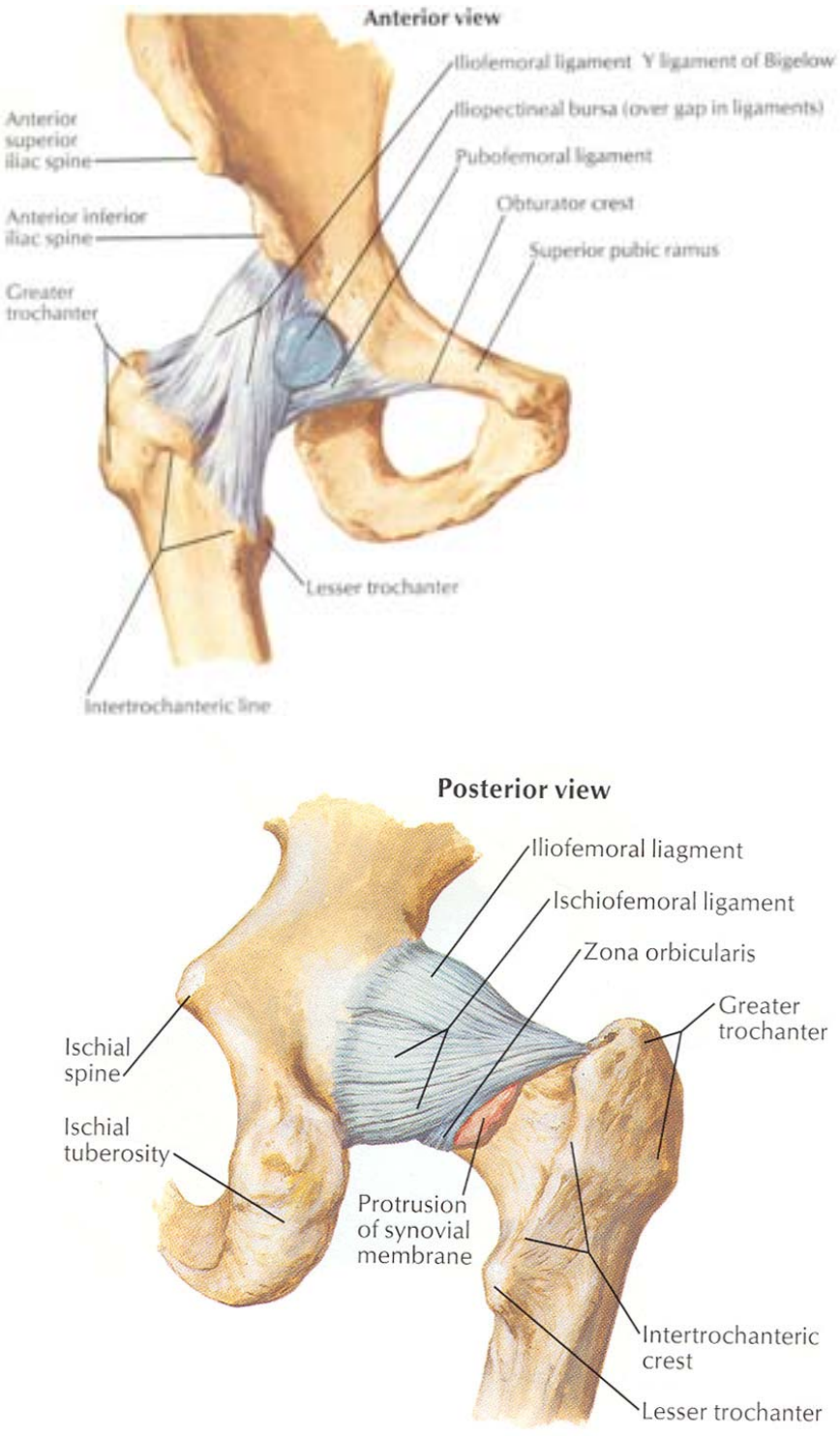

Figure 2.27. Anterior (top) and posterior (bottom) view of hip joint capsule. (Netter, 1997)

2.5.2.2 Knee Ligaments

There are four major ligaments in the knee area, which connect the femur bone to the tibia (Figure 2.28):

- The Anterior Cruciate Ligament (ACL),
- The Posterior Cruciate Ligament (PCL),
- The Medial Collateral Ligament (MCL) and
- The Lateral Collateral Ligament (LCL).

The ACL, located in the center of the knee, controls rotation and forwards movement of the tibia, while the PCL, always located in the center of the knee, controls backward movements of the tibia. The MCL and the LCL, both located laterally to the knee, give stability to the inner and outer knee respectively.

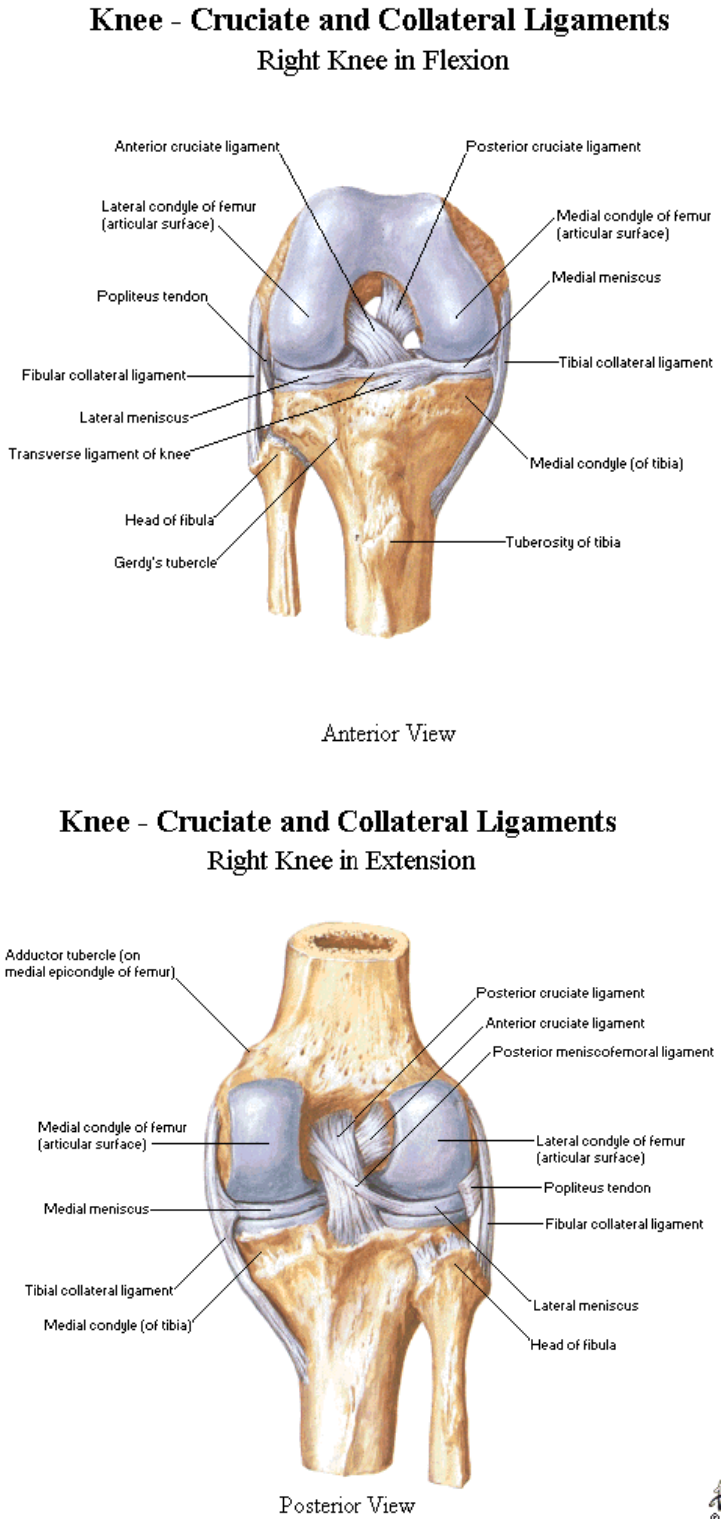

Figure 2.28. Anterior (top) and Posterior (bottom) Views of the four major ligaments in the Knee. (Anatomy, 2008)

2.5.2.3 Patellar Tendon

The Patellar Tendon is a tendon which extends from the quadriceps muscle in the thigh down into the patella bone and attaches to the tibia. It provides extension at the knee joint. Because of this role of connecting two bones, the patella and the tibia, it is frequently called also Patellar Ligament (Figure 2.29). (MedicineNet.com, 2008)

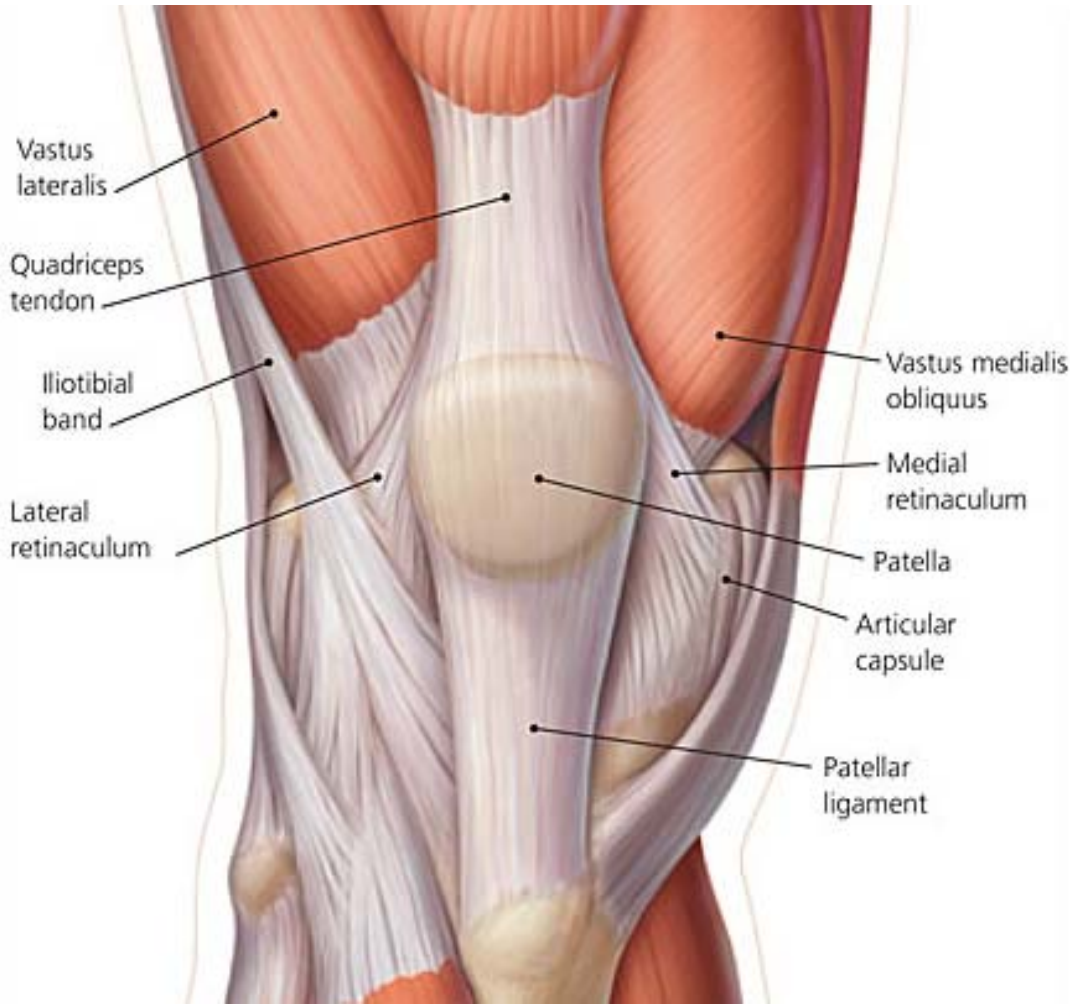

Figure 2.29. Patellar Tendon representation (AAFP, 2008)

2.6. Anatomy and Mechanical Properties of the KTH Muscles

2.6.1 Geometrical and Mechanical Representation of the KTH Muscles

2.6.1.1 Structural and Mechanical Properties of Muscles

The structural unit of muscles is a muscle fibre (Figure 2.30). Movement is provided by motor units, functional units consisting of one or more fibres controlled by a motor neuron. When a given movement is required, an electrical signal is sent through the nervous system to the concerned motor neuron located in the spinal cord. Once this impulse has reached the motor neuron, the latter generates a new signal that causes the muscle fibres it controls to contract simultaneously.

From a functional point of view muscles belong to three different groups (Bach, 1983):

- Skeletal muscles, which move bones and other structures;
- Cardiac muscles, that form the walls of heart and other large arteries;
- Smooth muscles that form the walls of most blood vessels and hollow organs. Smooth muscles move substances through viscera such as intestine and control movements through blood vessels.

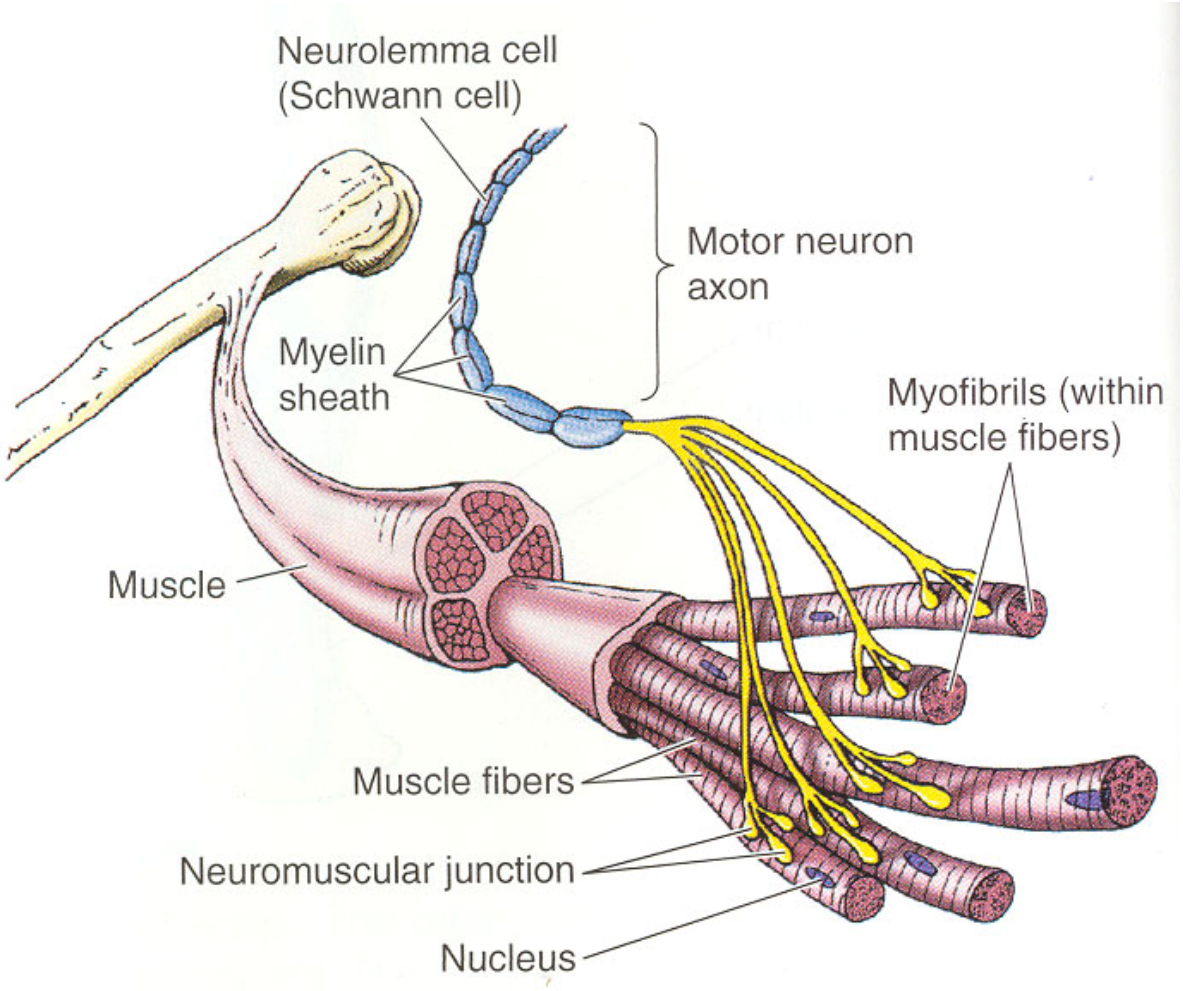

Figure 2.30. General structure of a muscle. (Bagley, 1987)

The model described in this research will focus on those muscles bridging between the hip and the femur, which are all skeletal muscles.

Skeletal muscles transmit movement by means of tendons, which are attached to bones, cartilage, ligaments, other muscles or some combination of these structures. Skeletal muscles can be classified by shape into five categories (Figure 2.31 and 2.32):

- Flat muscles;
- Pennate muscles (the way the fibres are laid recalls feathers. They are divided in unipennate, bipennate, multipennate);
- Fusiform muscles (they display the spindle shape that is commonly associated with muscles);
- Quadrate muscles - square-shaped muscles - and
- Circular or sphincteral muscle - round shaped muscles that control the width of orifices.

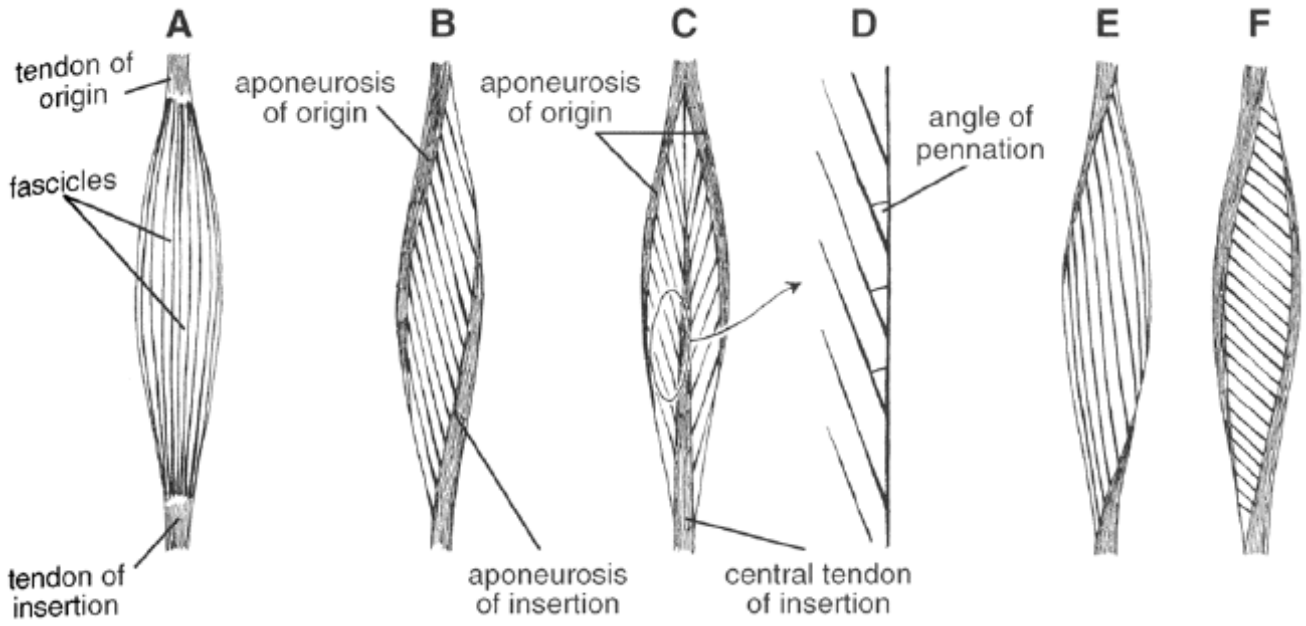

Figure 2.31. The internal architecture of skeletal muscles: (A) nonpennate; (B, E, F) unipennate; (C) bipennate. (Mc Gowan 1999)

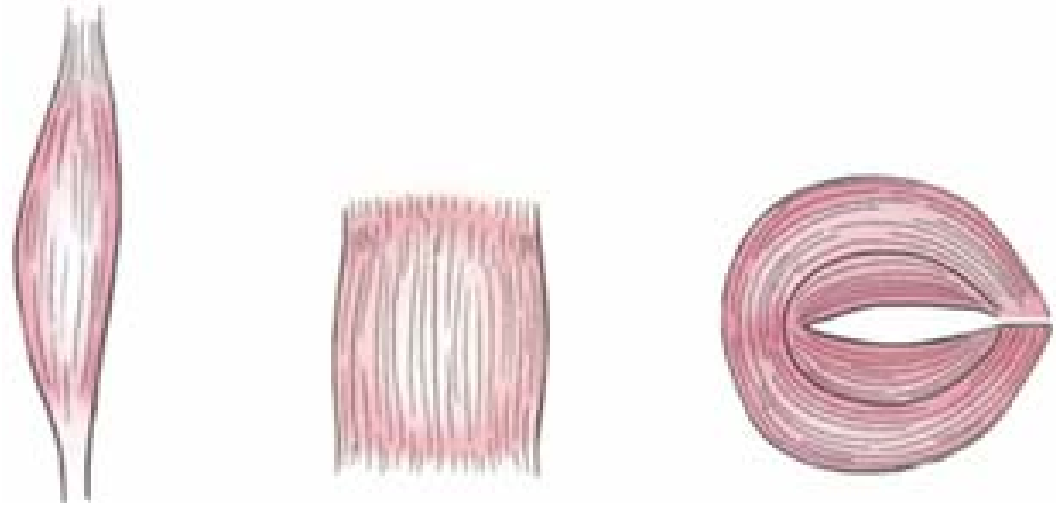

Figure 2.32. Example of a fusiform (left) quadrate (middle) and sphincteral (right) muscle. (Bach, 1983)

In providing movement, skeletal muscles carry out different kinematic tasks, so they can also be classified into the following categories:

- Agonists: in charge of activating a certain movement,
- Antagonists: contrasting the movement activated by the agonists,
- Synergists: assisting the task of the agonists by blocking the involved joints when the agonists pass over more than one joint, and
- Fixators: "freezing" the movement of the proximal part of an articulated limb, when movements take place in the peripheral parts.

Movements are the outcome of the activation of an increasing number of fibres in the agonist and the relaxation of progressively increasing number of fibres in the antagonists. This agonist-antagonist duet provides a controlled and smooth movement.

For a detailed explanation of muscle geometry and structures, see (Olivetti, 2006).

2.6.2.2 Material Modeling

There are two main models of the muscles, each following a different approach to the problem: a phenomenological/systemic macroscopic model, Hill's model, which assumes the muscle to be a one-dimensional entity and is based on a mechanical approach reducing the muscle to a set of springs, dashpots and other mechanical elements; a microscopic model, Huxley's model, which starts from very basic phenomena taking place at biochemical level. Through the years (Hill's model dates up to 1938 (Aidely, 1971) and Huxley's one to 1957 (Alexander, 1977) both models were subjected to several changes and improvements (Winters, 1988), also leading to an intermediate model, called the distribution moment (DM) model, which reinterprets Hill's macroscopic variables by means of the cross-bridges theory.

2.6.2 Anatomy of the KTH Muscles

There are four groups of muscles connecting the pelvis to the femur or to the upper part of the tibia: the anterior, medial and posterior thigh compartments and the gluteal muscles.

2.5.2.1 Anterior Thigh Muscles

These muscles are flexors of the hip and the extensors of the knee (Figure 2.33):

- Pectineus, a flat quadrangular muscle;
- Iliopsoas, which is the chief flexor of the thigh and also plays a role as a postural muscle by preventing hyperextension of the hip joint. The Iliopsoas, in turn, consists of three muscles: Iliacus, Psoas major and Psoas minor;
- Tensor of fascia lata, true to its name, tenses the fascia lata and the iliotibial tract with the result of supporting the femur on the tibia while standing. It is therefore a flexor of the thigh, producing flexion by acting together with the Iliopsoas;
- Sartorius is the longest muscle in the body. It bridges between two joints.

- Quadriceps femoris is the great extensor of the leg. It is composed of four muscles converging on the tendon attaching to the tibia. The four muscles are: Rectus femoris, Vastus lateralis, Vastus intermedius, Vastus medialis

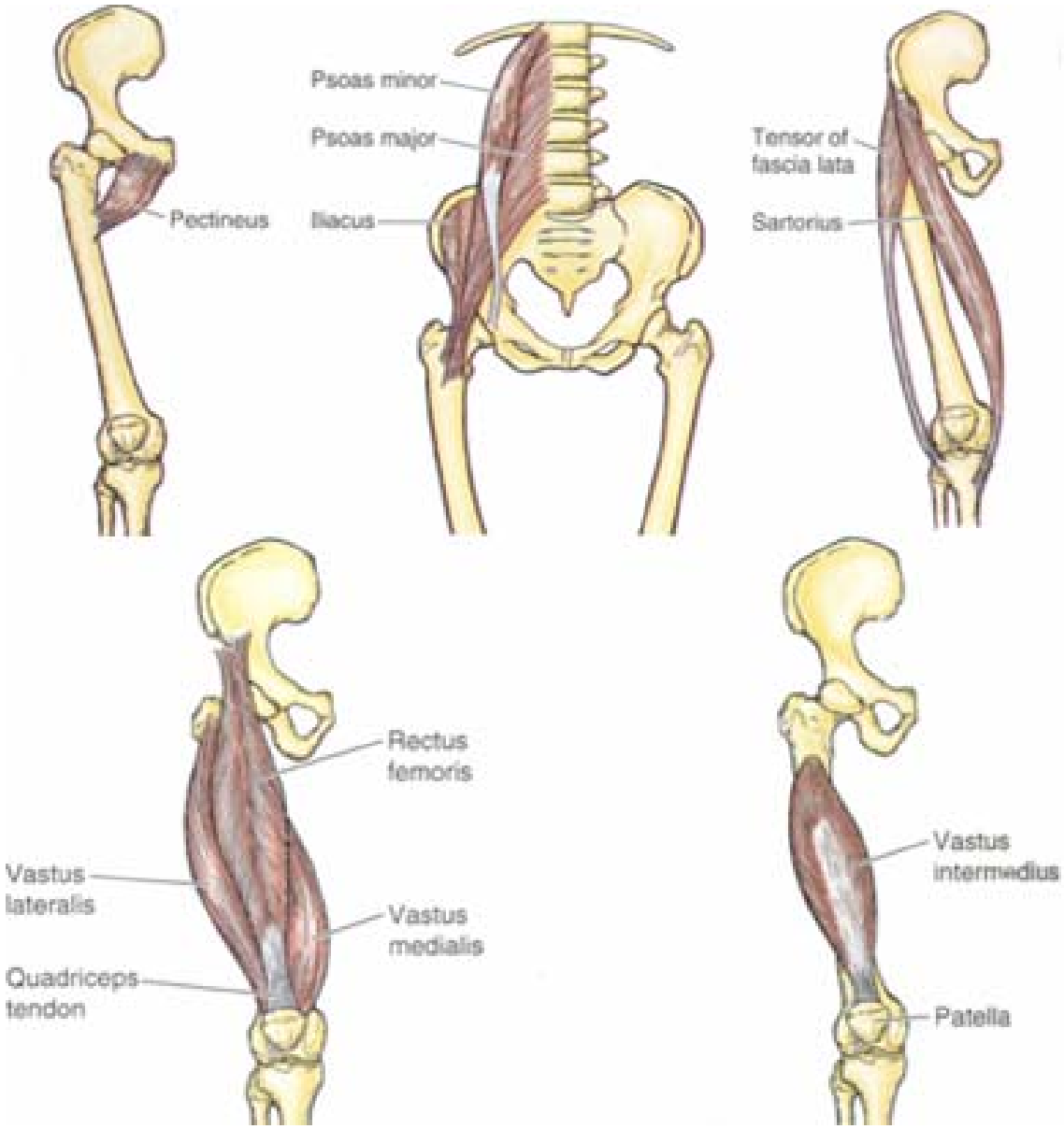

Figure 2.33. Anterior thigh muscles. (Agarwal, 1977)

2.5.2.2 Medial Thigh Muscles

They exert an adductive action on the thigh (Figure 2.34). This group consists of:

- Adductor longus,
- Adductor brevis,
- Adductor magnus,
- Gracilis,
- Obturator externus.

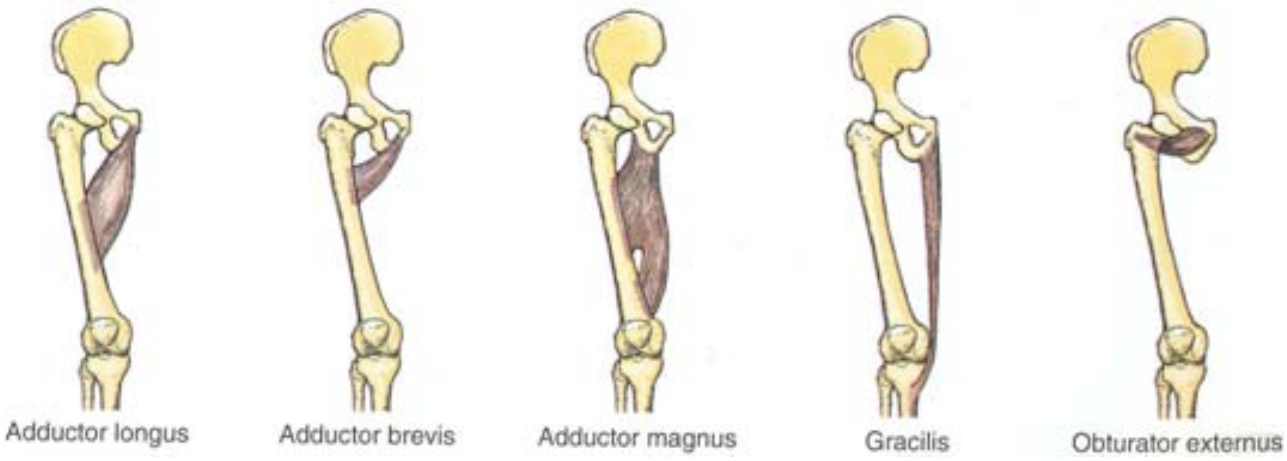

Figure 2.34. Medial thigh muscles. (Agarwal, 1977)

2.5.2.3 Posterior Thigh Muscles

They are also called “hamstring muscles” and are extensors of the thigh and flexors of the leg, especially during walking (Figure 2.35). This group consists of:

- Semitendinosus,
- Semimembranosus,
- Biceps femoris (long head).

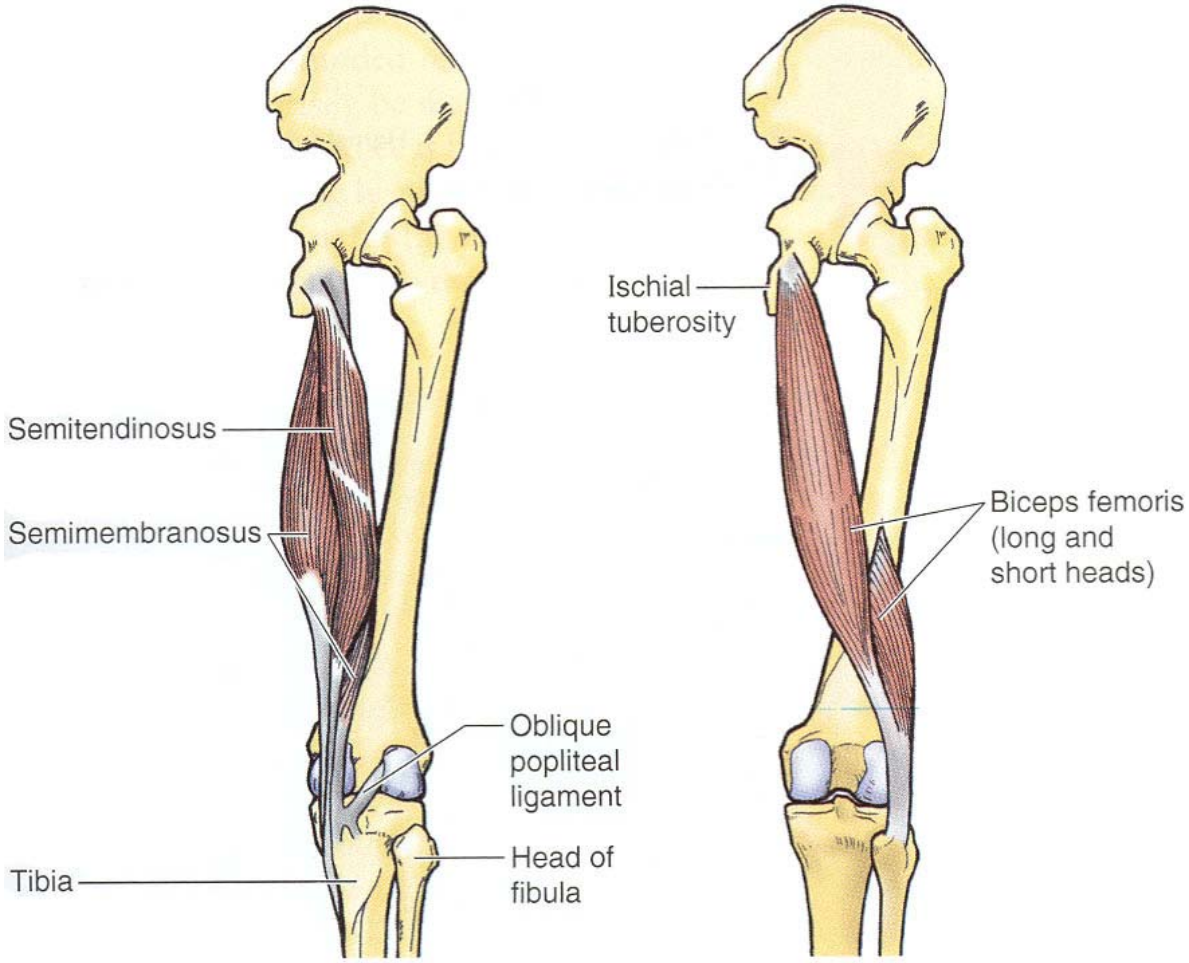

Figure 2.35. Posterior thigh muscles. (Agarwal, 1977)

2.5.2.4 Gluteal Thigh Muscles

This group consists of the gluteal group responsible for preventing sagging on the unsupported side of the pelvis during walking, and a smaller group of muscles lateral rotators of the thigh which play a role in stabilizing the femoral-pelvic joint by steadying the femoral head in the acetabulum (Figure 2.36). Muscles in these groups include:

- Gluteal group:
  - Gluteus maximus,
  - Gluteus medius,
  - Gluteus minimus.
- Smaller group of muscles:
  - Piriformis,
  - Obturator (internus, externus, gemelli)
  - Quadratus Femoris

Some of these muscles are more important than others in modelling frontal crash injuries. For example, some of the muscles function mainly to stabilize posture while standing and have little role in bracing in a seated position or exerting braking forces on the brake pedal prior to a crash.

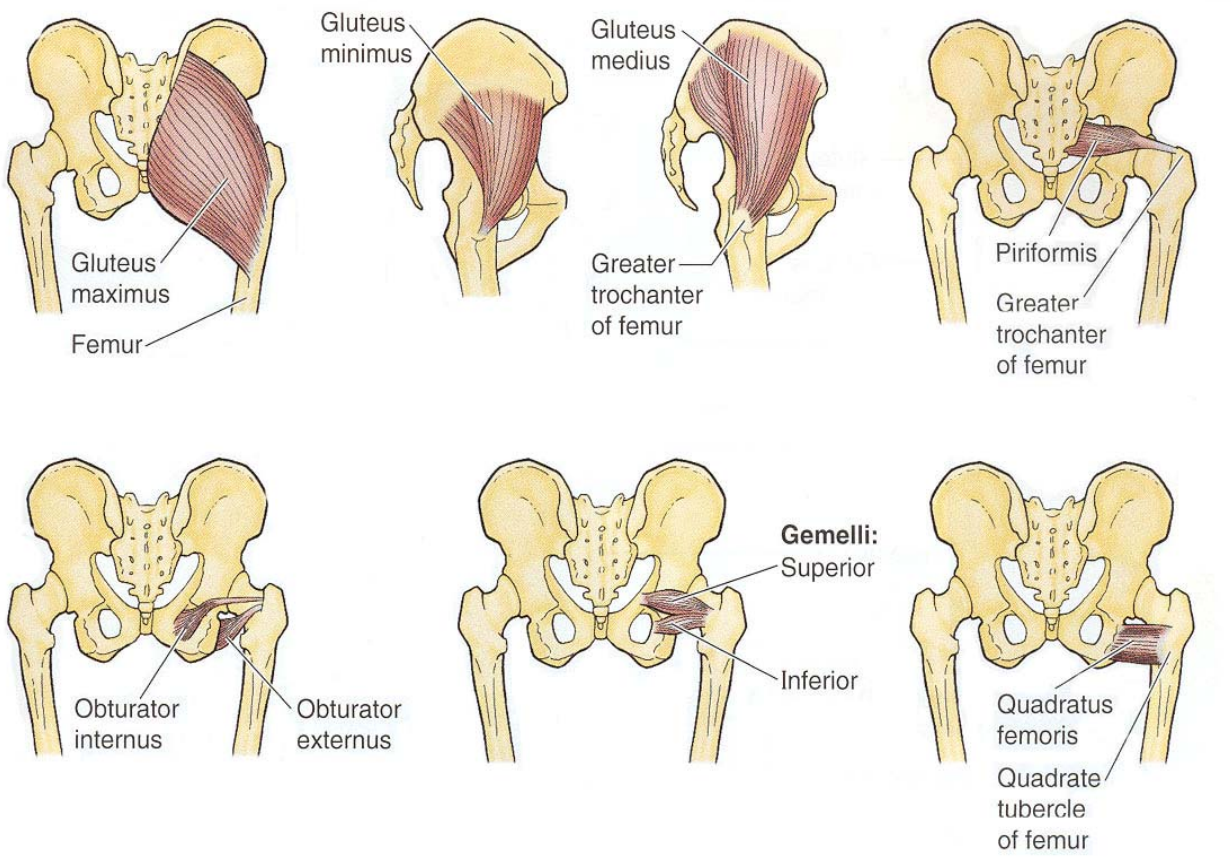

Figure 2.36. Gluteal muscles. (Agarwal, 1977)

III. OBJECTIVE AND METHODOLOGY

3.1. Objective

The objective of this research is to develop an accurate finite element model of the Knee-Thigh-Hip of a 50th percentile male including the structural properties of soft tissue. Dynamic failure properties will be considered for modeling the main ligaments and tendons and the main muscles of the lower limb will be taken into account with both their passive and active forces.

A parametric evaluation of the seating posture, loading conditions and muscle activation in frontal crash scenarios will be explored to examine failure mechanisms in the KTH complex.

3.1.1 Methodology

The following tasks explain, in detail, the methodology considered to pursue objectives mentioned above.

3.1.1.1 Integration of Prior Research into a Single Model

Prior research on KTH geometry and properties of bones, muscles and ligaments are considered and integrated into a single model of the KTH.

3.1.1.1.1 Skeletal KTH Geometry

An accurate and detailed representation of the femur, pelvis and patella bones by Valle is incorporated in the KTH model. (Valle, 2005) Valle improved a model of the human anatomic pelvis and leg that the Lawrence Livermore National Laboratory (LLNL) developed in 1997. (Perfect, 1997) The LLNL lower extremity model included a pelvis, femur, knee, ankle and foot.

A refined mesh of the femur, patella and pelvis was necessary. Patella and pelvis bones were consequently both re-meshed to capture smaller gradients and to closely match their geometry.

A new, more anatomical femur geometry and mesh were also proposed: new surfaces that closely match the femur geometry were chosen and a finer mesh was developed. This helped to avoid hourglass problems, which are unrealistic distortions of the geometry due to material energy distribution problems.

3.1.1.1.2 Bone Material Properties including Failure

The mechanical behavior of the bones of the lower extremities was investigated in order to determine material and failure properties of bones for use in LS-DYNA simulations.

A new model for bones is incorporated into the KTH model in order to be able to accurately predict fractures in actual crashes.

With this model, cortical tissue of bones was modeled using LSDYNA material 59 (i.e., the *MAT_COMPOSITE_FAILURE_SOLID_MODEL) to reproduce its transversely isotropic behavior. Trabecular tissue was modeled using material type 3 (i.e., *MAT_PLASTIC_KINEMATIC) that is homogeneous and isotropic.

3.1.1.1.3 Ligament Material Model including Failure

The FE model for human knee and hip ligaments presented by Farnese is considered and integrated into the KTH model. (Farnese, 2004) This model includes failure and is able to represent the correct ligament behaviour during loading-unloading cycles. The ligaments are modelled in LSDYNA as non linear springs. This material allows an unloading curve to be defined in order to model the behaviour of the ligaments in compression, after yielding or failure occurred. The springs are given a small pre-load to keep the joint in place.

3.1.1.1.4 Discrete Element Muscle Model

Olivetti developed a Hill's-type finite element model of the musculo-skeletal femoral-pelvic joint in order to gain an understanding of its behaviour when the main muscle groups of the region contract while the occupant is bracing before a frontal car impact. (Olivetti, 2006) Muscles were represented by discrete elements and both their passive and active properties were considered. The model was conceived to be mainly focused on the phenomenon of dislocation of the femur from the hip and fractures in the trochanteric femoral region. For these reasons, Olivetti's work is incorporated into the KTH model.

3.1.1.2 Finite Element Model Validation

This task more systematically performed both component-level and assembly-level validations. There are numerous cadaver tests in NHTSA's database that were used to assess the validity of the FE model. Some tests are component level tests where, for example, an impactor strikes the femoral condyles where the proximal femur is fully restrained. Such tests provide important information about the validity of the bone material model and mesh. Other tests involve whole-body sled tests that are used to assess the over-all validity of the model. Improvements obtained during these validations are then incorporated into the FE model.

3.1.1.3 Improvements to the Model

A further step, a more detailed and realistic representation of geometry and material properties of ligaments and muscles is required. This would more closely reproduce the dynamics of the lower limb and the interaction between its components. A representation of dynamic failure properties for both ligaments and tendons will help in the process of exploring and understanding failure mechanisms in the KTH during a crash scenario. Injury criteria for knee ligament injuries proposed by Viano and Mertz will be considered and used for validation of the ligament model. (Viano et al., 1978; Mertz et al., 1989) A new model for the patellar tendon made of parallel and serial springs is

introduced. This allows for a more bio-fidelic representation of the patella movement behaviors. Another objective is to determine the muscles involved and the level of muscle activation for particular KTH motions of interest such as pressing on a brake pedal. A parametric evaluation of muscle forces will be then investigated at various lower limb positions, considering adduction, abduction and flexion movements.

3.1.1.3.1 Ligament and Tendon Dynamic Failure Properties

Peck developed failure properties for ligaments that could be used in an LSDYNA FE model of the human lower extremities to estimate human response in high speed frontal automotive collisions. (Peck, 2007) Ligaments demonstrate viscoelastic behavior and the material properties are therefore rate dependant. Because of this, it is possible that the failure properties of ligaments also depend on the rate at which the load is applied. This failure predictive model proposed by Peck was chosen to be integrated into the KTH model to implement a new ligament material model which could incorporate dynamic failure.

3.1.1.3.2 Validation of Ligament and Tendon Model using Injury Criteria

Viano conducted dynamic tolerance tests on isolated cadaver tests joints. (Viano *et al*., 1978) He observed that, when flexed knee and tibia are impacted, posterior cruciate ligament tears occurred at 14.4 mm relative translation between the femur and the tibia. Complete failure of the ligament occurred at 22.6 mm relative translation. Following this data, in 1990, Mertz proposed for a 50^{th} percentile male an injury threshold level of 15 mm for relative translation between the femur and tibia at the knee joint to minimize rupture of the posterior cruciate ligament. (Mertz *et al.*, 1989)

FE simulations will be run reproducing the impact of the flexed knee and tibia. Data on involved ligament failures will be collected and compared with the proposed criteria of Viano and Mertz.

3.1.1.3.3 New Model of Patellar Tendon

A new version of the patellar tendon will be developed, for a more bio-fidelic representation of the patella movement using a series of springs with *MAT_SEATBELT card.

3.1.1.3.4 Modeling Active Muscles to Perform different Movements

With this task activation of muscles is considered. An activation level already included in the Hill-based muscle model used in LSDYNA is used. At first, displacements are imposed to the KTH group to reproduce movements of the lower limb for certain degrees of adduction, abduction and flexion. At each position, changes in length of the muscles are recorded, with an understanding of which muscles are involved in each type of movement. Their level of activation is recorded and used to perform pure movements of thigh flexion, adduction, abduction and knee extension.

3.1.1.4 Performing Impacts Including Muscle Activation

The objective of this task is to integrate all improvements obtained in modeling the geometry and the dynamics of the KTH and simulate a frontal impact between the KTH and a knee-bolster at different lower limb positions.

Failure modes of the main KTH bones are collected and analyzed and simulation results are compared with an existing KTH injury criteria developed by Kuppa for the National Highway Traffic Safety Administration (NHTSA). (Kuppa *et al*, 2001)

3.1.1.4.1 Parametric Runs in Different Positions

All improvements obtained in modeling the geometry and the dynamics of the KTH will be integrated into the previous model. A frontal impact of the KTH with a knee-bolster representation will be run with the lower limb at different positions, including angles of pure adduction/abduction, flexion or a combination of them for the thigh.

3.1.1.4.2 Find Failure Modes for Bones in the KTH Complex

For each considered position of the KTH, after the frontal impact simulations, failure modes or dislocations of the main bones of the KTH (i.e., femur, pelvis and patella) will be collected and analyzed. Possible ligament or tendon KTH failures will be also investigated.

3.1.1.4.3 Compare FE Injury Results with Existing KTH Injury Criteria

Kuppa presented injury criteria for the Knee-Thigh-Hip. (Kuppa *et al*, 2001) The aim is to apply these criteria to the FE injury results and compare the results obtained from the simulations with those proposed by Kuppa. A flowchart showing the methodology followed for this research is shown in Figure 3.1.

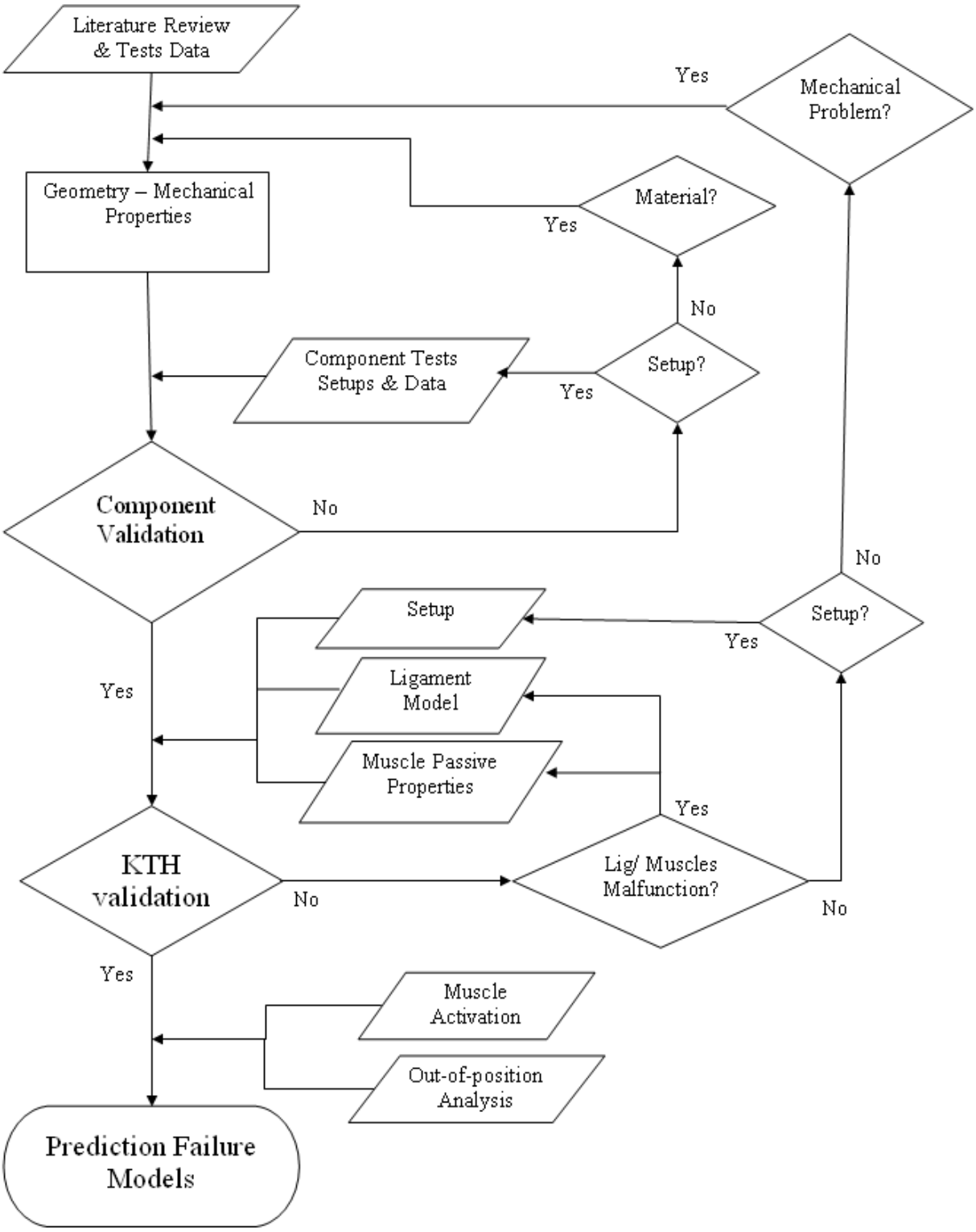

Figure 3.1. Flowchart of methodology.

3.1.2 FEM Characteristics

The LSDYNA solver, version 971 was chosen for running all the simulations. The computers used for the simulations are “Sunfire X2200M series” with two dual core AMD Opteron 2220 2.8GHZ CPUs and 12 GB of RAM. Simulation time varied with respect to the model scenario considered and the time of integration chosen. Models needed a simulation time of around two hours. The initial time-step was 4.50e-7 seconds.

IV. MODEL DEFINITION

4.1. The LLNL Model of the KTH

The National Highway Traffic Safety Administration (NHTSA) sponsored a research activity to develop a KTH finite element model with the Lawrence Livermore National Laboratory (LLNL). (Perfect, 1997) The LLNL KTH model is a finite element model of human lower extremities of an "average sized" adult male (i.e., 50th percentile male). It includes a pelvis, femur, knee, ankle and foot. Bones and a few particular ligaments are represented in the model. The model is detailed enough to be used as a simulation tool to investigate complex dynamic loadings that would be difficult to reproduce in a crash test. The model was implemented using LLNL DYNA3D and the mesh of the bones was generated from the Viewpoint Database International database using the finite element preprocessor Truegrid and is shown in Figure 4.1.

Figure 4.1. The LLNL KTH model of the lower extremity. (Perfect, 1997)

4.1.1 Principal Characteristics of the LLNL Model

Principal characteristics of the LLNL model are summarized below:

- The mesh consists of 14,126 elements and 18,800 nodes. The mesh experiences hourglassing problems for some impact conditions.
- The bones are assumed to be solid, homogeneous and isotropic. They are modeled as elastic-plastic with bilinear stress-strain response. The bone material models do not include failure.
- The soft tissue mass was included in the model as discreet masses attached to the bones at selected locations.
- Nonlinear springs were used to model selected ligaments, tendons and muscles. Only one ligament of the hip joint was modeled for joint stability. Only selected muscles were incorporated and muscles activation was not exploited.

While the model was a significant advancement at the time, it could not be used to investigate failure conditions and more complicated loadings since the model simply did not include all the necessary features. The purpose of this work was to build on the LLNL model and develop a model that could be used to perform parametric analyses of various impact scenarios to determine likely KTH failure mechanisms.

4.1.2 Main Changes Needed for the LLNL Model

Several relatively straight-forward changes were required to make the LLNL model more useful in the current research context. The following are the main changes that were applied to the LLNL model:

- **Conversion of the model to the SI system**. The model was originally developed in U.S. customary units (USCU) (i.e., English units of lbs, in, sec) so it was converted to the SI system (i.e., Mg, mm and sec).

- **Conversion of the LLNL model for use with LSDYNA Finite Element Processor**. The model was initially developed for use with the LLNL DYNA-3D analysis code whereas the research team and NHTSA more commonly use LSDYNA, the commercial successor of DYNA-3D. There are a number of features in LSDYNA that are not available in DYNA-3D and these additional features were deemed to be important to the research effort. For example there have been several improvements and additions of material models in LSDYNA.
- **Inclusion of trabecular bone and finer mesh in some areas**. The original model did not include any interior geometry of the bones so voids and trabecular bone are not included. It was also found to be relatively coarse in some important areas like the pelvis and the trochanter and condyle regions of the femur. The result of the coarser mesh was mesh stability problems like hourglassing and negative volumes. Some bones were re-meshed to overcome these problems.
- **Modeling anisotropic behavior and failure mechanism of bones**. The LLNL model used a linear isotropic material model which did not adequately represent the true material behavior of bones. In order to improve the bone material models, some physical testing was performed to obtain material properties of cortical bone and more realistic and complicated material models were used to capture the anisotropic material behavior and failure mechanism of cortical bone.
- **Re-distribution of the soft tissues mass**. The LLNL model concentrated soft tissue masses on 35 nodes. This concentration lead to mesh behavior problems since a lot of mass was concentrated on relatively few nodes. The improved model spread the soft tissue mass uniformly across all the external nodes of pelvis, femur, tibia and fibula. This was accomplished using the "mass D" command in LSPREPOST, the LSDYNA pre and postprocessor. For the calculation of the nodal soft tissue mass, a 100-kg man was considered. It was calculated that, as a percentage of the total body weight, the pelvis represents the 30 percent, a single foot the 1.24 percent, the shank (tibia + fibula) the 4.18 percent, the thigh the 14.42 percent.
- **More accurate reproduction of a bio-fidelic representation of the KTH ligaments and their insertion sites**. In order for the KTH structure to stay together when

subjected to an impact loading, the bones must be connected to one another. Bone-to-bone connections are made using ligaments. The LLNL model represented some of the ligaments, particularly the knee ligaments (i.e., the anterior cruciate ligament (ACL), posterior cruciate ligament (PCL), medial collateral ligament and the lateral collateral ligament (LCL), the foot ligaments and a preloaded artificial pelvis ligament used to maintain the position of the head of the femur in the acetabulum). All these soft tissues were modeled as discrete elements with non-linear springs. The whole structure of the ligaments was redone in order to more accurately reproduce a more bio-fidelic representation of the KTH ligaments.

- **Representation of all major muscles of the KTH region**. In the LLNL model, only selected muscles were incorporated and muscles activation was not exploited All the major muscles and tendons of the KTH were added to the model and passive and active muscle forces were represented.

The new WPI KTH model consists of 50,338 nodes and 40,138 elements and it is represented in Figure 4.2.

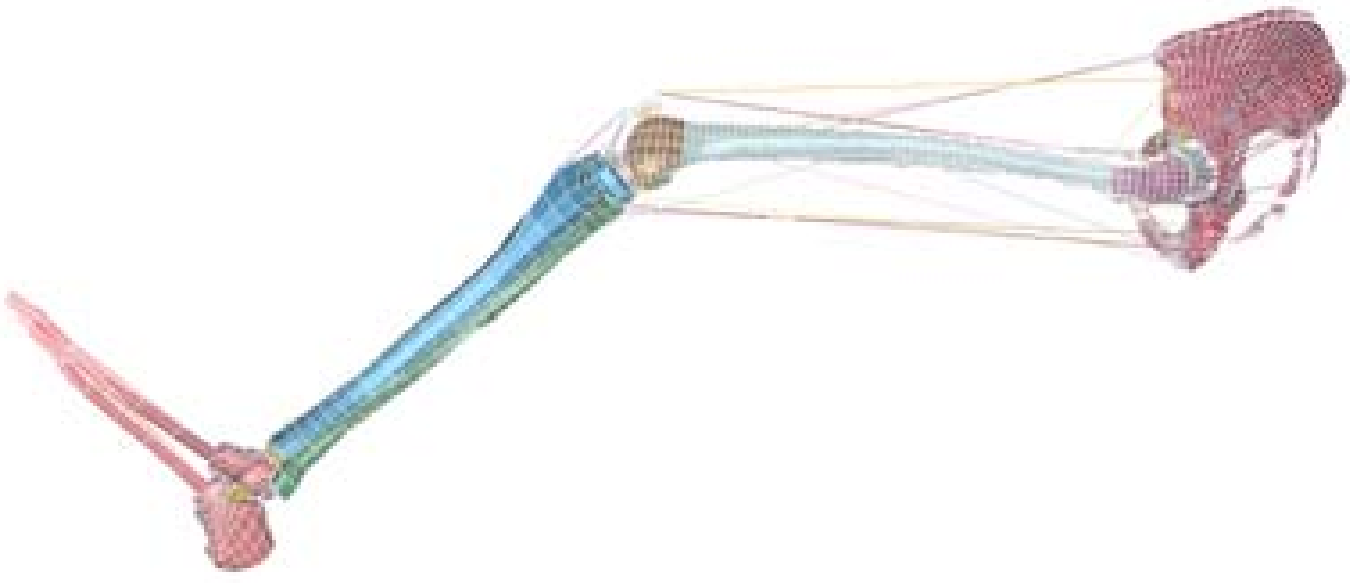

Figure 4.2. Improved model of the lower extremities.

Tables 4.1 and 4.2 summarize the main changes and refinements applied to the LLNL model, as matter of representation of bone, ligaments and muscles. More details on the geometry definition and mesh refinement for the KTH bones and further explanation about the material models used for bones and soft tissues are reported in the next paragraphs.

Table 4.1. Comparisons between representation of bones in the LLNL and in the WPI KTH model

LLNL MODEL	WPI MODEL	IMPROVEMENTS
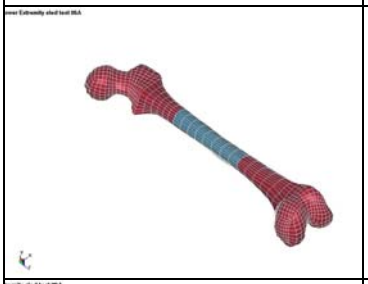	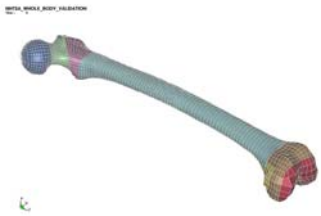	Modeling of more accurate geometry, femoral cortical and trabecular bone properties.
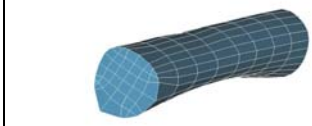		Reproduced hollow femoral cortical shaft.
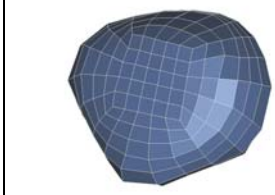	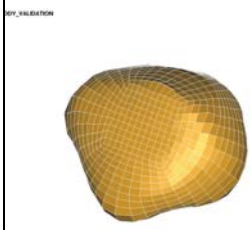	Represented more accurate and bio-fidelic geometry, finer mesh and new material properties for the patella.
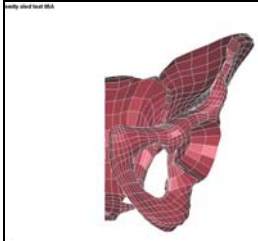		Modeled the pelvis with a more accurate geometry especially in the acetabular cup, finer mesh and new material properties.

Table 4.2. Comparisons between the representation of ligaments and muscles in the LLNL and in the WPI KTH model

LLNL MODEL	WPI KTH MODEL	IMPROVEMENTS
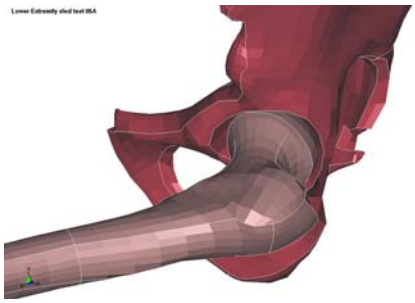	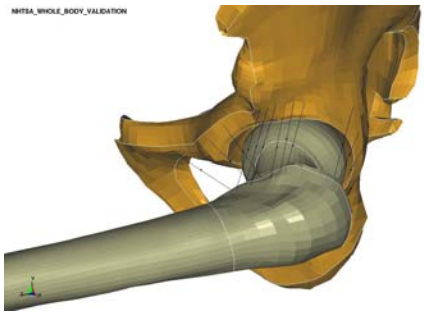	Included hip-ligaments with failure properties: - Ischiofemural - Iliofemural - Pubofemural - Capitis-femoris
	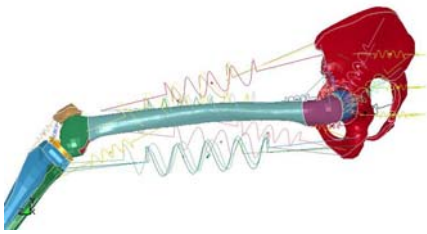	Modeled muscles with springs based on the Hill's model.
No mass representation	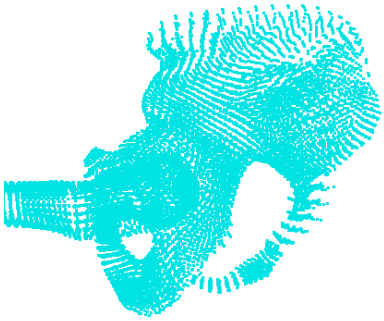	Represented and redistributed nodal mass for each bone.
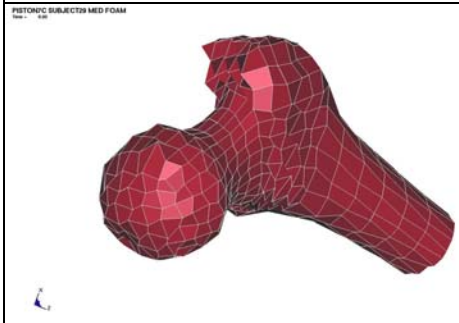	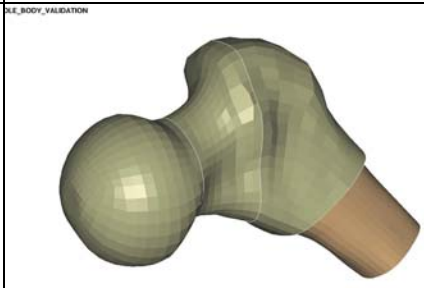	Avoided hourglassing problems with a finer mesh.

4.2. Finite Element Modeling of the KTH Bones

In the LLNL model, the femur was simply modeled as a whole type of bone without differentiation between trabecular and cortical parts. However, as explained before, a detailed representation of its geometry and characteristics is necessary to replicate its mechanical behavior and to investigate the rupture modes of the bone under different kinds of loadings.

This section briefly explains the procedure followed in order to develop a detailed mesh of the femur bone. The model was developed using the TrueGrid preprocessor and analyzed using LSDYNA. The output files were post-processed using LS-PREPOST. The model was validated by comparing the numerical simulations to experimental tests. (Valle, 2005)

4.2.1 Surface Definition and Element Formulation

The Viewpoint Premier Library contains the NURBS surface definition of an entire series of human lower extremities bones based on a 50^{th} percentile male skeleton. (Viceconti et al., 1996) However, these Viewpoint surfaces describe only the external surface of the bones and, therefore, they can not be used when the finite element model has to represent both the trabecular and the cortical tissues as was required for this project. As a consequence, the femur mesh was developed using NURBS surfaces which were obtained using the Visible Human Dataset. In this case, both internal and external surfaces were reconstructed from transverse CT, MRI and cross-section images of a representative 95^{th} percentile male cadaver at an average of one millimeter intervals. The geometry was then scaled down to a 50^{th} percentile male for use in this project. A more detailed explanation regarding model generation and validation can be found in Valle (Valle, 2005).

Linear or parabolic formulations can be used to perform element calculations of stress and strain. Polgar *et al.* investigated the computational accuracy obtained with

different kind of elements for the 'standardized femur' by testing the T4 tetrahedron (linear shape function) and the T10 tetrahedron (quadratic shape function). (Polgar et al., 2000,) His results showed that only if the model contains more than 50,000 elements, the solution for a T4 mesh elements takes up to 2.08 times longer than the solution for a T10 mesh with the same accuracy. At the same time, principal stress error computed for the T4 mesh has significantly higher value than for the T10 elements mesh.

The average edge of the element that results is 4 mm. Beillas *et al.* suggests that an element size of 3mm (brick linear elements) is suitable to study the kinematics and global response of the whole lower limb at the joint level and to guarantee a good compromise between computational effort and accuracy. (Beillas, 2004) However, the study of highly localized phenomena would require further refinement.

Information from the literature review was used to set the characteristics of the femur mesh as follows:

- Average dimension of the elements: 3 mm.
- Formulation of the elements: linear bricks (SOLID elements).
- Element formulation: linear under-integrated (ELFOR 1).

It was decided to switch the elements of the upper trochanter zone of the model to the fully-integrated elements (ELFOR 3) because they were experiencing strong bending moments and the under-integrated elements were not able to deform correctly showing numerical instabilities. Further simulations showed that the fully-integrated elements were able to model correctly the deformation and eventually the rupture mode of the femur.

The meshes of the tibia and fibula bones together with the finer ones of the patella and pelvis from the LLNL model were then combined with the newly meshed geometry of the femur developed to obtain the validation KTH model for this project.

4.2.2 Material Modeling

Cortical tissue of femur bone was modeled using LSDYNA material 59 (i.e., the *MAT_COMPOSITE_FAILURE_SOLID_MODEL). This material model was chosen because it allows for defining shear, compressive and tensile ultimate strength in longitudinal, transverse and normal directions. The LSDYNA control card *CONTROL_ACCURACY was included to define control parameters that could improve the accuracy of the calculation. Invariant node numbering for solid elements was switched on for solid elements. This option is recommended when solid elements of anisotropic material undergo significant deformation. "In spite of its higher costs (<5%), the invariant local system is recommended for several reasons. First, element forces are nearly independent of node sequencing; secondly, the hourglass modes will not substantially affect the material directions; and, finally, stable calculations over long time periods are achievable. This option has no effect on solid elements of isotropic material, and it is available only for anisotropic materials." (LSTC, 2007a)

The locally orthotropic material axes option was chosen, in a cylindrical coordinate system with the material axes determined by a vector v, and an originating point, P, which define the centerline axis as shown in Figure 4.3.

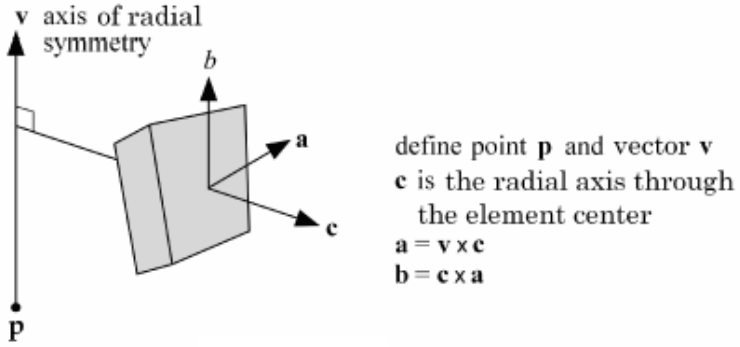

Figure 4.3. Locally orthotropic material axes option in cylindrical coordinate system chosen for cortical bone. (LSTC, 2007a

For this type of coordinate system it is necessary to provide the following input values: in plane and transverse shear strength, longitudinal, transverse and normal compressive

strength, longitudinal, transverse and normal tensile strength. A great deal of information can be found in the literature about mechanical and ultimate properties for cortical bones. Nahum and Melvin, in 2002, summarized many different research projects that have been conducted on this subject (Nahum, 2002). Tables from 4.3 to 4.5 summarize and compare ultimate stresses results for cortical femur bone obtained from these past researches.

Table 4.3. Femur: cortical-bone tensile properties. (Nahum, 2002)

Author	Comment	Ultimate stress (Mpa)
Sedlin and Hirsch (1966)	Longitudinal	86.5
Ko (1953)	Longitudinal	122±1.1
Burstein et al (1976)	Longitudinal	151±18
Reilly and Burstein (1975)	Longitudinal	133
Reilly and Burstein (1975)	Transverse	51
Gillet and Cescotto (2008)	Transverse	50
Evans and Lebow (1951)	Wet	77-84
	Dry	99-111
Yamada (1970)	Wet	122
	Dry	151
	10-79 years	86-113

Table 4.4. Femur: cortical-bone compressive properties. (Nahum, 2002)

Author	Comment	Ultimate stress (Mpa)
Reilly and Burstein (1975)	Longitudinal	193
Reilly and Burstein (1975)	Transverse	133
Burstein et al (1976)	20-89 years	179-209
McElhaney et al. (1970)		140
Yamada (1970)	Female 20-69 years	145-167
Yokoo (1952)		159

Table 4.5. Femur: cortical-bone shear properties. (Nahum, 2002)

Author	Comment	Ultimate stress (Mpa)
Yamada (1970)	Shear	82
http://silver.neep.wisc.edu	Shear	65-71

Parametric simulations were run for validating bone materials. From these runs, we chose the following values to be used as ultimate cortical bone strength further simulations (Table 4.6).

Table 4.6. Ultimate strength inputs used in FE simulations for cortical femur bone.

Variable	Description	Ultimate stress (Mpa)
SBA	In plane shear	60
SCA	Transverse shear	60
SCB	Transverse shear	60
XXC	Longitudinal compressive a-axis	130
YYC	Transverse compressive b-axis	190
ZZC	Normal compressive c-axis	130
XXT	Longitudinal tensile a-axis	50
YYT	Transverse tensile b-axis	50
ZZT	Normal tensile c-axis	50

The trabecular tissue for the femur bone has not been studied as intensely as the cortical so that the values of Young's moduli and ultimate strengths in different directions are not available. It was modeled using material type 3 (i.e., *MAT_PLASTIC_KINEMATIC) that is homogeneous and isotropic.

Tibia, fibula and foot were modeled as cortical bones either, by using LSDYNA material type 3.

For the patella material type 20 (i.e., *MAT_RIGID) was used to avoid numerical problems which arose when modeling this bone with material composite 59.

The menisci were modeled with material plastic kinematic type 3.

The pelvis bone was first modeled only as trabecular bone with plastic kinematic material properties; then it was overlaid with shell elements to reproduce the cortical part of the bone. The thickness of the pelvis shell elements was chosen to be 0.5 mm. (Anderson et al., 2005)

Table 4.7 summarizes the numerical values of each parameter needed to define the LSDYNA cards for each bone presented in the model, and eventually its parts.

Table 4.7. Material Properties for Cortical and Trabecular Bone used in the KTH Model

Cortical Pelvis	Properties Cortical Pelvis
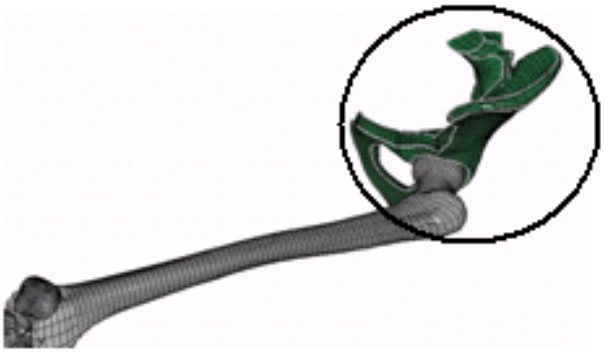	MAT: Piecewise Linear Plasticity (# 24) Density: 1.9E-9 ton/mm^3 Young Mod.: 23800 Mpa Poisson: 0.33 SigY: 11.9 N/nn^2 Tangent Mod.: 1200 Mpa Failure Strain: 3.30%
Trabecular Pelvis	**Properties Trabecular Pelvis**
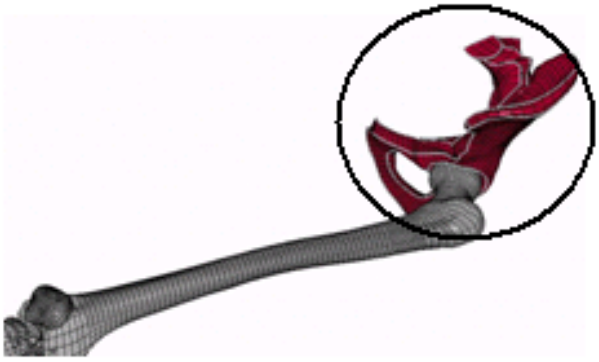	MAT: Plastic Kinematic (#3) Density: 5.0E-10 ton/mm^3 Young Mod.: 2470 Mpa Poisson: 0.33 SigY: 3.8 N/nn^2 Tangent Mod.: 124 Mpa Failure Strain: 5.50%
Femoral Head	**Properties Femoral Head**
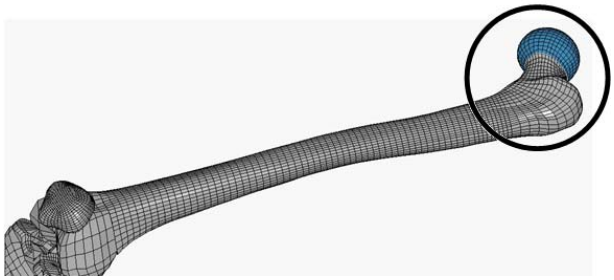	MAT: Composite Failure Model (# 59) Density: 1.9E-9 ton/mm^3 EA: 17000 Mpa EB - EC: 11500 Mpa PR: 0.3 SBA: 60 Mpa SCA: 60 Mpa SCB: 60 Mpa XXC: 130 Mpa YYC: 190 Mpa ZZC: 130 Mpa XXT: 50 Mpa YYT: 50 Mpa ZZT: 50 Mpa

Table 4.7. Material Properties for Cortical and Trabecular Bone used in the KTH Model (continued)

Femur Trochanters	Properties Femur Trochanters
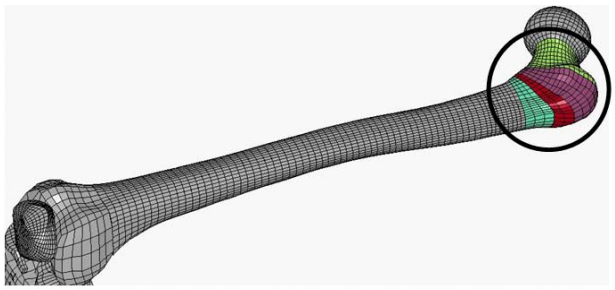	MAT: Composite Failure Model (# 59) Density: 1.9E-9 ton/mm^3 EA: 17000 Mpa EB - EC: 11500 Mpa PR: 0.3 SBA: 60 Mpa SCA: 60 Mpa SCB: 60 Mpa XXC: 130 Mpa YYC: 190 Mpa ZZC: 130 Mpa XXT: 50 Mpa YYT: 50 Mpa ZZT: 50 Mpa
Cortical Shaft	**Properties Cortical Shaft**
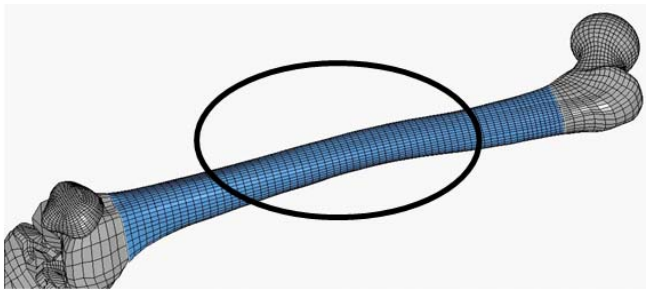	MAT: Composite Failure Model (# 59) Density: 1.9E-9 ton/mm^3 EA: 21900 Mpa EB: 14600 Mpa EC: 11600 Mpa PR: 0.3 SBA - SCA - SCB: 600 Mpa XXC - YYC - ZZC: 600 Mpa XXT - YYT - ZZT: 600 Mpa
Femur Condyles	**Properties Femur Condyles**
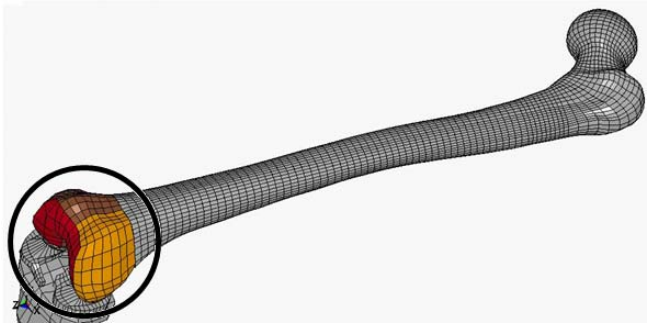	MAT: Composite Failure Model (# 59) Density: 1.9E-9 ton/mm^3 EA: 17000 Mpa EB - EC: 11500 Mpa PR: 0.3 SBA: 60 Mpa SCA: 60 Mpa SCB: 60 Mpa XXC: 130 Mpa YYC: 190 Mpa ZZC: 130 Mpa XXT: 50 Mpa YYT: 50 Mpa ZZT: 50 Mpa

Table 4.7. Material Properties for Cortical and Trabecular Bone used in the KTH Model (continued)

Trabecular Femur	Properties Trabecular Femur
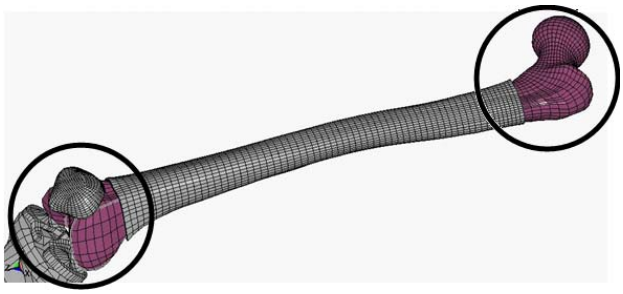	MAT: Plastic Kinematic (#3) Density: 5.0E-10 ton/mm^3 Young Mod.: 456 Mpa Poisson: 0.33 SigY: 3.8 N/nn^2 Tangent Mod.: 23 Mpa Failure Strain: 10.00% Erosion: 6.5 Mpa
Patella	**Properties Patella**
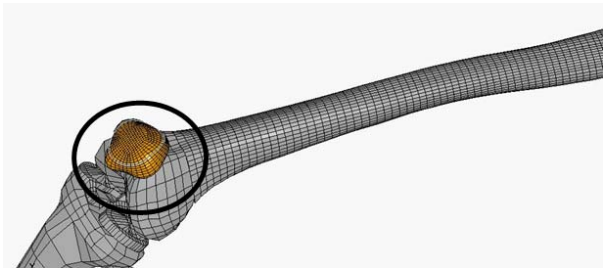	MAT: Rigid (#20) Density: 1.9E-9 ton/mm^3 Young Mod.: 17000 Mpa Poisson: 0.36
Tibia	**Properties Tibia**
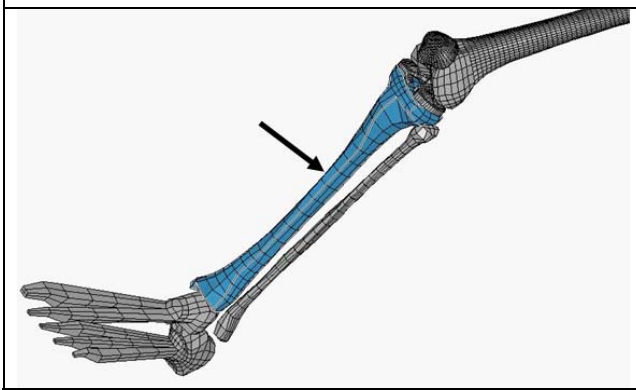	MAT: Plastic Kinematic (#3) Density: 1.9E-9 ton/mm^3 Young Mod.: 23800 Mpa Poisson: 0.33 SigY: 11.90 N/nn^2 Tangent Mod.: 1200 Mpa

Table 4.7. Material Properties for Cortical and Trabecular Bone used in the KTH Model (continued)

Fibula	Properties Fibula
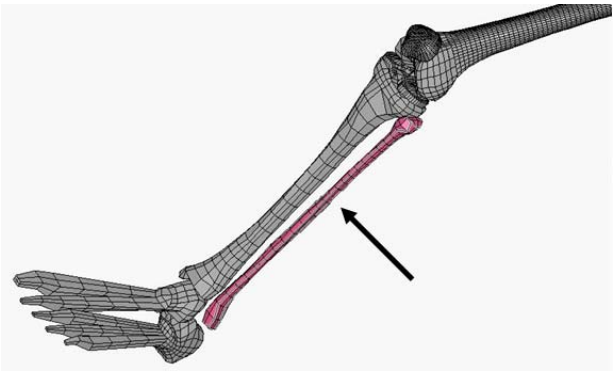	MAT: Plastic Kinematic (#3) Density: 1.9E-9 ton/mm^3 Young Mod.: 23800 Mpa Poisson: 0.33 SigY: 11.90 N/nn^2 Tangent Mod.: 1200 Mpa
Foot	**Properties Foot**
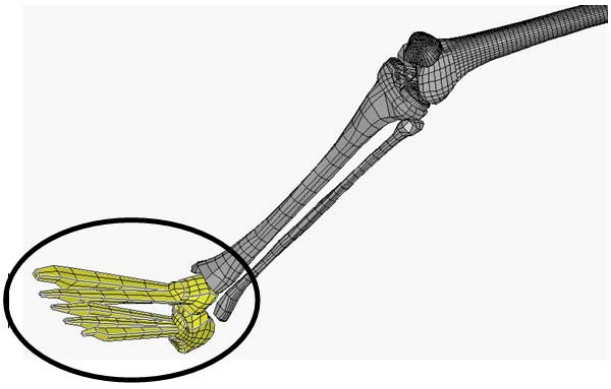	MAT: Plastic Kinematic (#3) Density: 1.9E-9 ton/mm^3 Young Mod.: 23800 Mpa Poisson: 0.33 SigY: 11.90 N/nn^2 Tangent Mod.: 1200 Mpa
Menisci	**Properties Menisci**
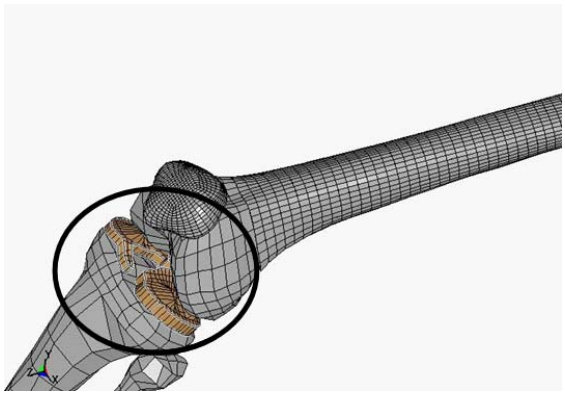	MAT: Plastic Kinematic (#3) Density: 5.0E-10 ton/mm^3 Young Mod.: 240 Mpa Poisson: 0.33 SigY: 15 N/nn^2 Tangent Mod.: 24 Mpa

4.3. Finite Element Modeling of the KTH Muscles

There are two main approaches reported in the literature regarding the mathematical representation of the mechanical behaviour of muscles:

- Hill's models are phenomenological/systematic macroscopic models which assume the muscles to be one-dimensional entities (i.e., springs and dash-pots) and reduce them to a set of springs and dashpots to represent the mechanical behaviour of the muscles. (Aigner, 1999)
- Huxley models are microscopic models which start from very basic phenomena occurring at the biochemical level. (Aigner, 1999)

The LSDYNA muscle model used in this research is built with Hill's type spring discrete elements since it is easy to implement in a finite element model.

4.3.1 LSDYNA Hill-based Muscle Model

*MAT_SPRING_MUSCLE is a Hill-based muscle model that is included in LSDYNA 970. (LSTC, 2007a) Its basic configuration consists of a passive element (PE) in parallel with an active one (SEE), the contractile element (CE). (Figure 4.4)

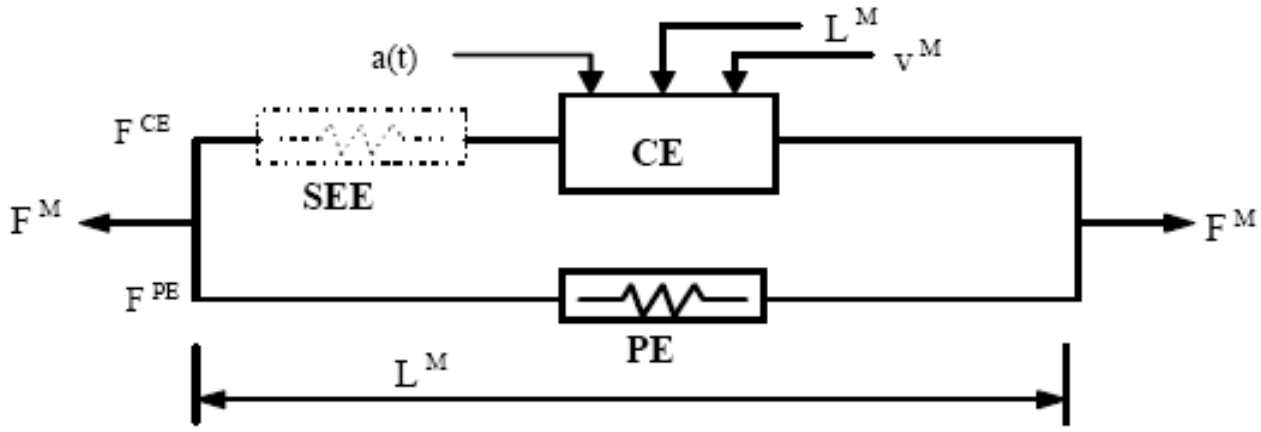

Figure 4.4. Muscle parameters in the *MAT_SPRING_MUSCLE material of LSDYNA. (LSTC, 2007a)

The total force developed by the muscle is represented as the sum of the passive force F^{PE} and the active force F^{CE}. The passive element PE represents energy storage due to muscle elastic properties while the contractive element CE represents the force generated by muscle during activation. This active force depends on three parameters: the function activation level a(t), the length of the muscle L^M and the shortening velocity of the muscle v^M.

4.3.2 Material Modeling

In the first part of this research, only the passive force of muscles were considered. (In section six, activation of muscles will be included for more complete and realistic investigation of fracture modes in frontal car crashes). In the case of only passive muscle properties, the total force is simply equal to the passive force, thus: $F_M=F_{PE}$. (Figure 4.5) In this case, the entire resistance to elongation is provided by the PE element.

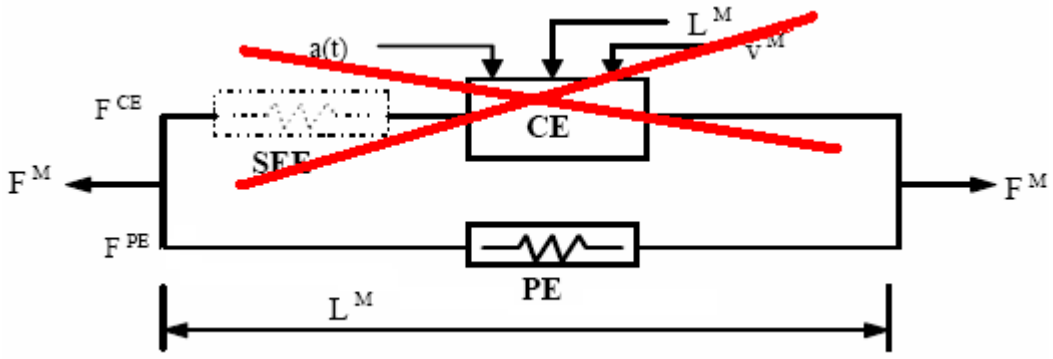

Figure 4.5. Hill-type model for a passive muscle. (LSTC, 2007a)

The force PE is determined directly from the current length of the muscle and can be adequately approximated by an exponential function of the following form:

$$\frac{F_{PE}}{F_{\max}} = \frac{1}{e^{Ksh} - 1}\left[e^{Ksh / L\max*(L-1)} - 1\right] \tag{4.1}$$

where:

- K_{sh} is a dimensionless shape parameter controlling the rate of rise of the exponential curve,
- L_{max} is the relative length (i.e. L/L_0) corresponding to F_{max} and
- F_{max} is the isometric peak force.

In fact, L_{max}, K_{sh} and F_{max} are all input parameters of the *MAT_SPRING_MUSCLE card for a passive muscle, together with L_0, muscle initial length. A value of $K_{sh} = 4$ was chosen (Olivetti, 2006). L_{max} values used in the model are reported in Table 4.8. Table 4.9 shows pictures of the KTH muscles with their insertion sites, main functions and pennation angles.

Table 4.8. L_{max} calculation and LSDYNA input parameters for the KTH muscles. (Olivetti, 2006)

Muscle name	Muscle length (mm)		L_{max}
	Driving position	Standing position	
Anterior Thigh Muscles			
Pectineus	111	138	1.49
Iliacus	181	205	1.35
Tensor fasciae latae	443	538	1.45
Sartorius	456	560	1.47
Rectus femoris	395	469	1.42
Vastus lateralis	387	369	1.25
Vastus intermedius	294	276	1.27
Vastus medialis	370	353	1.25
Medial Thigh Muscles			
Adductor longus	187	219	1.40
Adductor brevis	106	120	1.35
Adductor magnus (superior)	116	52	2.66
Adductor magnus (middle)	245	162	1.81
Adductor magnus (inferior)	364	289	1.51
Gracilis	455	412	1.32
Gluteal Muscles			
Gluteus Maximus (superior)	195	170	1.37
Gluteus Maximus (middle)	218	178	1.46
Gluteus Maximus (inferior)	225	155	1.74
Gluteus Medius (anterior)	101	113	1.34
Gluteus Medius (middle)	173	158	1.31
Gluteus Medius (posterior)	191	163	1.40
Gluteus Minimus (anterior)	73	74	1.22
Gluteus Minimus (middle)	116	110	1.26
Gluteus Minimus (posterior)	147	133	1.329
Piriformis	146	124	1.41
Gemelli	72	73	1.22
Quadratus femoris	85	60	1.69
Posterior Thigh Muscles			
Semitendinosus	460	408	1.35
Semimembranosus	464	397	1.40
Biceps Femoris (short head)	175	196	1.34

Table 4.9. KTH Muscles: characteristics and models (Muscle Atlas, 2008)

<table>
<tr><td colspan="2">Anterior thigh Muscles: Pectineus</td><td colspan="2">Pennation Angle: 0 degrees</td></tr>
<tr><td> 
</td><td> 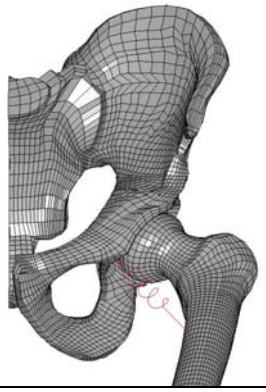 </td><td>Origin
Pecten pubis and pectineal surface of the pubis

Insertion
Pectineal line of femur</td><td>Functions
• Adducts thigh
• Flexes hip joint</td></tr>
<tr><td colspan="2">Anterior thigh M.: Iliacus</td><td colspan="2">Pennation Angle: 7 degrees</td></tr>
<tr><td>  </td><td> 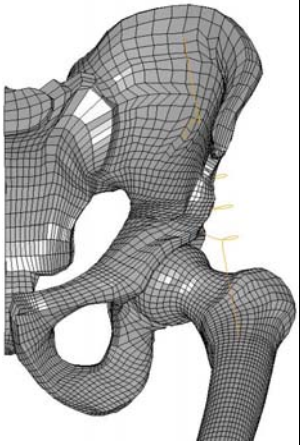 </td><td>Origin
Upper 2/3 of iliac fossa of ilium, internal lip of iliac crest, lateral aspect of sacrum, ventral sacroiliac ligament, and lower portion of iliolumbar ligament

Insertion
Lesser trochanter</td><td>Functions
• Flexes torso and thigh with respect to each other</td></tr>
<tr><td colspan="2">Anterior thigh M.: Tensor Fascia Latae</td><td colspan="2">Pennation Angle: 3 degrees</td></tr>
<tr><td> 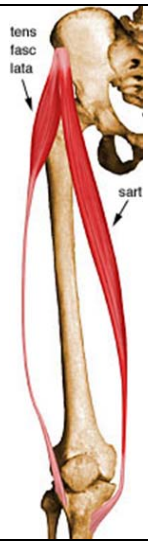
</td><td> 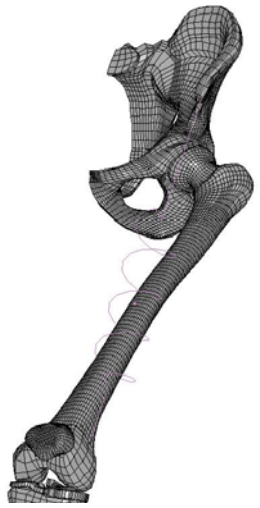 </td><td>Origin
Anterior superior iliac spine, outer lip of anterior iliac crest and fascia lata

Insertion
Iliotibial band</td><td>Functions
• Stabilizes hip
• Stabilizes knee joints</td></tr>
</table>

Table 4.9. KTH Muscles: characteristics and models (Muscle Atlas, 2008)

<table>
<tr><td colspan="2">Anterior thigh Muscles: Sartorius</td><td colspan="2">Pennation Angle: 0 degrees</td></tr>
<tr><td> 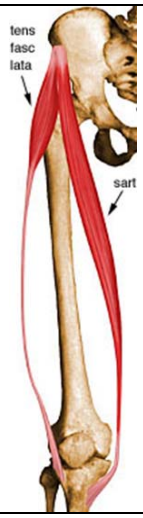
</td><td> 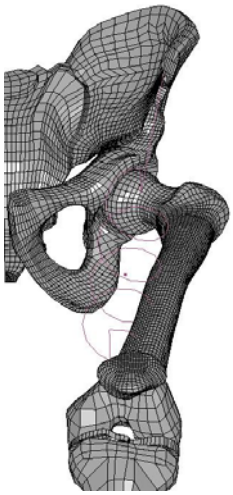 </td><td>Origin
Anterior superior iliac spine

Insertion
Superior aspect of the medial surface of the tibial shaft near the tibial tuberosity</td><td>Functions
• Flexes hip joint
• Laterally rotates hip joint
• Flexes knee</td></tr>
<tr><td colspan="2">Anterior thigh M.: Rectus Femoris</td><td colspan="2">Pennation Angle: 5 degrees</td></tr>
<tr><td>  </td><td> 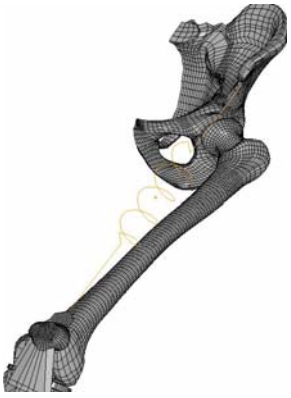 </td><td>Origin
Straight head from anterior inferior iliac spine; reflected head from groove just above acetabulum

Insertion
Base of patella to form the more central portion of the quadriceps femoris tendon</td><td>Functions
• Extends knee</td></tr>
<tr><td colspan="2">Anterior thigh M.: Vastus Lateralis</td><td colspan="2">Pennation Angle: 5 degrees</td></tr>
<tr><td> 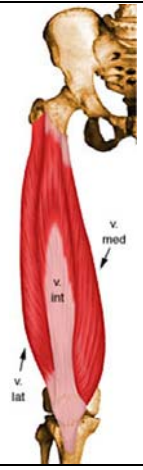
</td><td>  </td><td>Origin
Superior portion of intertrochanteric line, anterior and inferior borders of greater trochanter, superior portion of lateral lip of linea aspera and lateral portion of gluteal tuberosity of femur

Insertion
Lateral base and border of patella; also forms the lateral patellar retinaculum and lateral side of quadriceps femoris tendon</td><td>Functions
• Extends knee</td></tr>
</table>

Table 4.9. KTH Muscles: characteristics and models (Muscle Atlas, 2008)

<table>
<tr><td colspan="2">Anterior thigh Muscles: Vastus Intermedius</td><td colspan="2">Pennation Angle: 5 degrees</td></tr>
<tr>
<td> 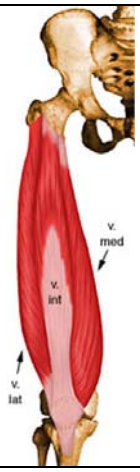
</td>
<td>  </td>
<td>Origin
Superior 2/3 of anterior and lateral surfaces of femur; also from lateral intermuscular septum of thigh

Insertion
Lateral border of patella; also forms the deep portion of the quadriceps tendon</td>
<td>Functions
• Extends knee</td>
</tr>
<tr><td colspan="2">Anterior thigh M.: Vastus Medialis</td><td colspan="2">Pennation Angle: 5 degrees</td></tr>
<tr>
<td> 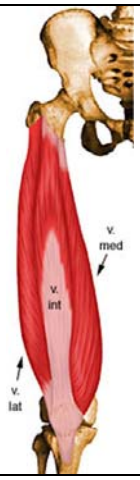
</td>
<td> 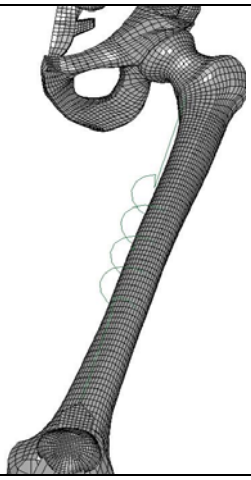 </td>
<td>Origin
Interior portion of intertrochanteric line, spiral line, medial lip of linea aspera, superior part of medial supracondylar ridge of femur, and medial intermuscular septum

Insertion
Medial base and border of patella; also forms the medial patellar retinaculum and medial side of quadriceps femoris tendon</td>
<td>Functions
• Extends knee</td>
</tr>
<tr><td colspan="2">Medial thigh M.: Adductor Longus</td><td colspan="2">Pennation Angle: 6 degrees</td></tr>
<tr>
<td>  </td>
<td> 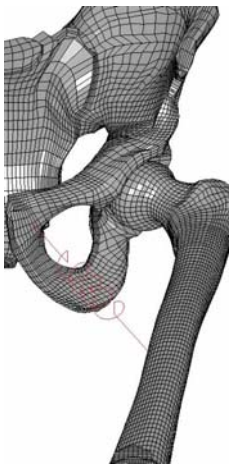 </td>
<td>Origin
Anterior surface of body of pubis, just lateral to pubic symphysis

Insertion
Middle third of linea aspera, between the medial adductor magnus and brevis insertions and the lateral origin of the vastus medialis</td>
<td>Functions
• Adducts and flexes the thigh
• Laterally rotate the hip joint</td>
</tr>
</table>

Table 4.9. KTH Muscles: characteristics and models (Muscle Atlas, 2008)

<table>
<tr><td colspan="2">Medial thigh Muscles: Adductor Brevis</td><td colspan="2">Pennation Angle: 0 degrees</td></tr>
<tr>
<td> 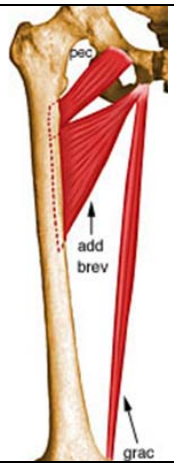
</td>
<td> 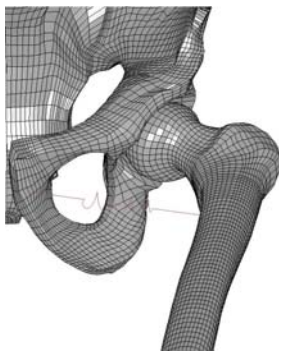 </td>
<td>Origin
Anterior surface of inferior pubic ramus, inferior to origin of adductor longus

Insertion
Pectineal line and superior part of medial lip of linea aspera</td>
<td>Functions
• Adduction and flexion thigh
• Laterally rotate the thigh</td>
</tr>
<tr><td colspan="2">Medial thigh M.: Adductor Magnus</td><td colspan="2">Pennation Angle: 3-5 degrees</td></tr>
<tr>
<td>  </td>
<td> 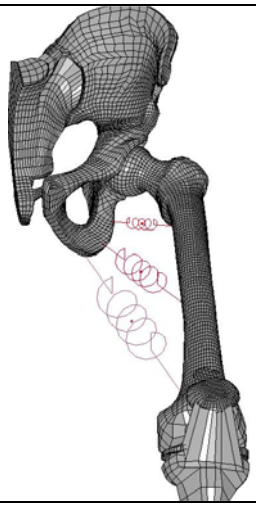 </td>
<td>Origin
Inferior pubic ramus, ischial ramus, and inferolateral area of ischial tuberosity

Insertion
Gluteal tuberosity of femur, medial lip of linea aspera, medial supracondylar ridge, and adductor tubercle</td>
<td>Functions
• Adductor thigh
• Flexor thigh
• Extensor thigh</td>
</tr>
<tr><td colspan="2">Medial thigh M.: Gracilis</td><td colspan="2">Pennation Angle: 3 degrees</td></tr>
<tr>
<td> 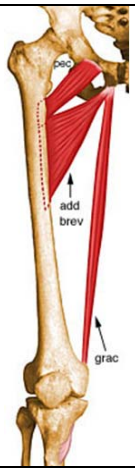
</td>
<td>  </td>
<td>Origin
Inferior margin of pubic symphysis, inferior ramus of pubis, and adjacent ramus of ischium

Insertion
Medium surface of tibial shaft, just posterior to sartorius</td>
<td>Functions
• Flexes knee
• Adducts thigh
• Medially rotates tibia on the femur</td>
</tr>
</table>

Table 4.9. KTH Muscles: characteristics and models (Muscle Atlas, 2008)

<table>
<tr><td colspan="2">Gluteus Muscles: Gluteus Maximus</td><td colspan="2">Pennation Angle: 0-5 degrees</td></tr>
<tr><td> 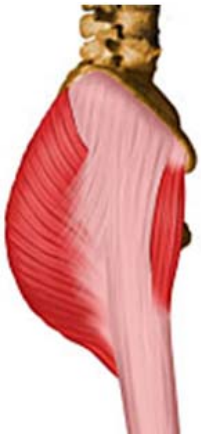 </td><td> 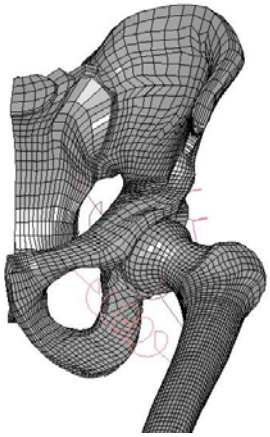 </td><td>Origin
Posterior aspect of dorsal ilium posterior to posterior gluteal line, posterior superior iliac crest, posterior inferior aspect of sacrum and coccyx, and sacrotuberous ligament

Insertion
Primarily in fascia lata at the iliotibial band; also into the gluteal tuberosity on posterior femoral surface</td><td>Functions
• Flexes the knee
• Rotates laterally the tibia</td></tr>
<tr><td colspan="2">Gluteus Muscles: Gluteus Medius</td><td colspan="2">Pennation Angle: 0-19 degrees</td></tr>
<tr><td>  </td><td> 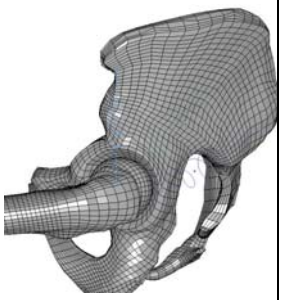 </td><td>Origin
Dorsal ilium inferior to iliac crest

Insertion
Lateral and superior surfaces of greater trochanter</td><td>Functions
• Abductor thigh
• Rotates hip medially
• Rotates hip laterally</td></tr>
<tr><td colspan="2">Gluteus Muscles: Gluteus Minimus</td><td colspan="2">Pennation Angle: 0-10 degrees</td></tr>
<tr><td>  </td><td> 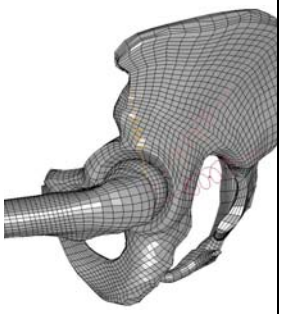 </td><td>Origin
Dorsal ilium between inferior and anterior gluteal lines; also from edge of greater sciatic notch

Insertion
Anterior surface of greater trochanter</td><td>Functions
• Abducts hip joint
• Medially rotates hip joint</td></tr>
</table>

Table 4.9. KTH Muscles: characteristics and models (Muscle Atlas, 2008)

<table>
<tr><td colspan="2">Gluteus Muscles: Piriformis</td><td colspan="2">Pennation Angle: 10 degrees</td></tr>
<tr>
<td> 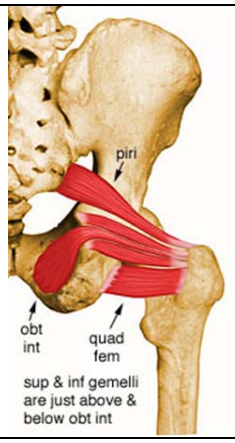
</td>
<td> 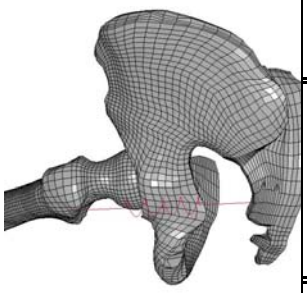 </td>
<td>Origin
Anterior surface of lateral process of sacrum and gluteal surface of ilium at the margin of the greater sciatic notch

Insertion
Superior border of greater trochanter</td>
<td>Functions
• Rotates laterally hip joint
• Abducts the flexed hip</td>
</tr>
<tr><td colspan="2">Gluteus Muscles: Gemelli</td><td colspan="2">Pennation Angle: 0 degrees</td></tr>
<tr>
<td> 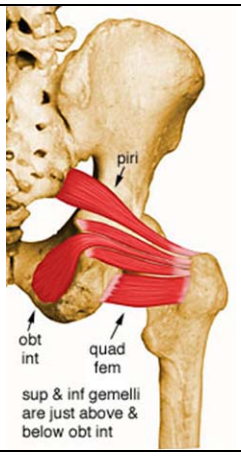
</td>
<td> 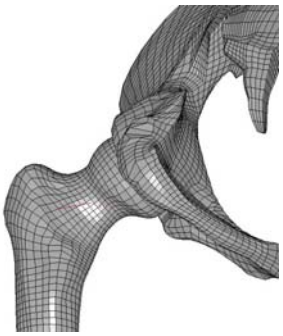 </td>
<td>Origin
Posterior portions of ischial tuberosity and lateral obturator ring

Insertion
Medial surface of greater trochanter of femur, in common with obturator internus</td>
<td>Functions
• Rotates thigh laterally
• Abducts the flexed thigh</td>
</tr>
<tr><td colspan="2">Gluteus Muscles: Quadratus Femoris</td><td colspan="2">Pennation Angle: 0 degrees</td></tr>
<tr>
<td> 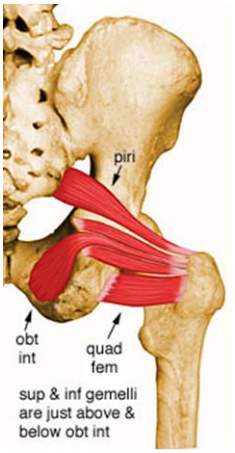
</td>
<td> 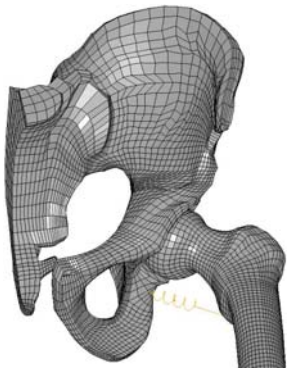 </td>
<td>Origin
Lateral margin of obturator ring above ischial tuberosity

Insertion
Quadrate tubercule and adjacent bone of intertrochanteric crest of proximal posterior femur</td>
<td>Functions
• Rotates hip laterally
• Adducts hip</td>
</tr>
</table>

Table 4.9. KTH Muscles: characteristics and models (Muscle Atlas, 2008)

<table>
<tr><td colspan="2">Posterior thigh M.: Semitendinosus</td><td colspan="2">Pennation Angle: 5 degrees</td></tr>
<tr><td>  </td><td> 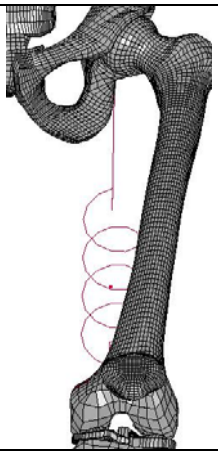 </td><td>Origin
From common tendon with long head of biceps femoris from superior medial quadrant of the posterior portion of the ischial tuberosity

Insertion
Superior aspect of medial portion of tibial shaft</td><td>Functions
• Extends thigh
• Flexes knee
• Rotates tibia medially, with flexed knee</td></tr>
<tr><td colspan="2">Posterior thigh M.: Semimembranosus</td><td colspan="2">Pennation Angle: 15 degrees</td></tr>
<tr><td>  </td><td> 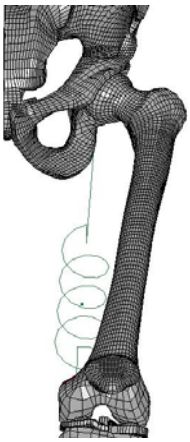 </td><td>Origin
Superior lateral quadrant of the ischial tuberosity

Insertion
Posterior surface of the medial condyle</td><td>Functions
• Extends thigh
• Flexes knee
• Rotates tibia laterally, with flexed knee</td></tr>
<tr><td colspan="2">Posterior thigh M.: Biceps femoris</td><td colspan="2">Pennation Angle: 0 degrees</td></tr>
<tr><td>  </td><td> 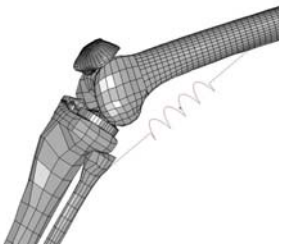 </td><td>Origin
Lateral hip of linea aspera lateral supracondylar ridge of femur, and lateral intermuscular septum of thigh

Insertion
Primarily on fibular head; also on lateral collateral ligament and lateral tibial condyle</td><td>Functions
• Flexes the knee
• Rotates laterally the tibia</td></tr>
</table>

4.4. Finite Element Modeling of the KTH Ligaments

As explained earlier, the LLNL model includes only ligaments in the knee region and an artificial, non-anatomical preloaded ligament in the hip joint. It was necessary to also model the major ligaments of the pelvis region to replicate the correct relative movement between the pelvis and the femur.

In the KTH model, ligaments and the patellar tendon were represented with discrete springs with nonlinear translational and rotational properties. Loading and unloading curves for each of these ligaments were defined.

4.4.1 Material Modeling

Some material models for representing biological soft tissues are already available in LS-DYNA970, including: (LSTC, 2003a)

- Material type S_06 is for discrete springs and dampers. This material provides a general one dimensional nonlinear translational or rotational spring with arbitrary loading and unloading definitions.
- Material type 176 is a solid, quasi-linear, isotropic, viscoelastic material introduced by Fung which represents biological soft tissues. (Bonifasi Lista, 2003)
- A more recent model (material type 91) was developed by Weiss *et al*. and Puso and Weiss. This model sues an isotropic Mooney-Rivlin matrix reinforced by fibres having a strain energy contribution with the qualitative material behaviour of collagen. (LSTC, 2003a) The model has a viscoelastic option which activates a six-term Prony series kernel for the relaxation function.

It was choosen to model ligaments with nonlinear discrete spring elements and LSDYNA material type S04 (i.e., *MAT_SPRING_NONLINEAR_ELASTIC). The springs are given a small initial tension to pre-load the joint. The spring force increases with stretch to a maximum value and then decreases rapidly with any further elongation

until a near zero value is reached. The spring tension then remains at this near-zero value for any additional elongation. This model permits the analyst to recognize that a ligament has "failed" once it has lost the capacity to carry tensile load and provides reasonable post-failure behaviour of the element. If the spring is compressed after the maximum allowable force has been reached, the spring load curve is followed backward and a force is developed again in compression, even if the element is supposed to have yielded or failed. Such a response is non-physical but it is a feature of using a simple nonlinear spring. (Figure 4.6)

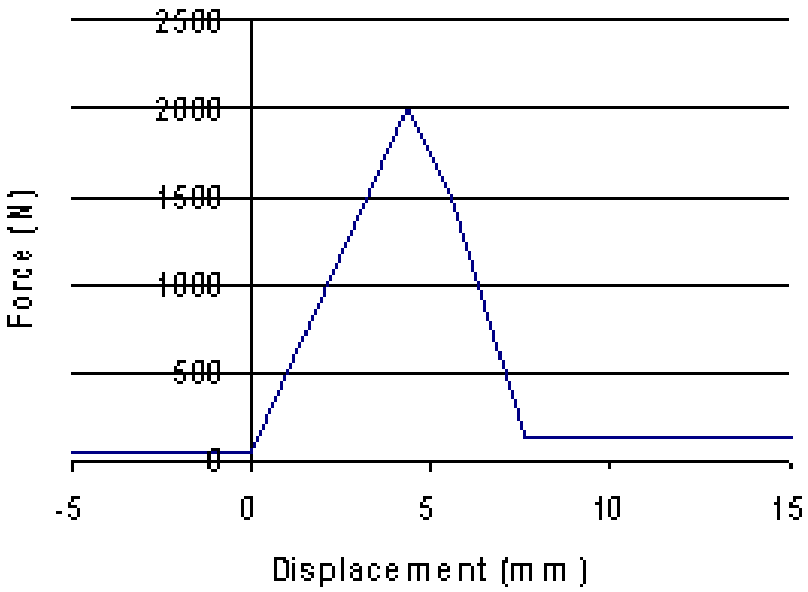

Figure 4.6. Generic force vs. displacement curve used for modeling knee ligaments.

One of the targets of the new model was to include a representation of the hip ligaments that would include failure. A new philosophy in the material conception was used in the improved WPI model. The material model LSDYNA MAT_S06 SPRING GENERAL NON LINEAR was adopted. This material allows an unloading curve to be defined in order to model the behaviour of the ligaments in compression, after yielding or failure occurred.

The springs are again given a small pre-load to keep the joint in place. Tension increases with elongation until a maximum value is obtained after which the element is considered yielded. After this point, if the elongation increases further, the tension starts to decrease. A zero value is then reached and the spring remains at this value for further elongation. Once the force in the element exceeds the yield point, the unloading curve is used for unloading. The unloading curve is set to be equal to a very small value (0.1 N) so that for compressions after ligament failure, no force can possibly be developed in the spring. Ligaments should behave like a cable and they cannot sustain any compression load. As an example, Figure 4.7 represents the force vs. displacement curve used for modelling the mechanical behaviour of the capitis femoris ligament, which connects the pelvis to the femoral head.

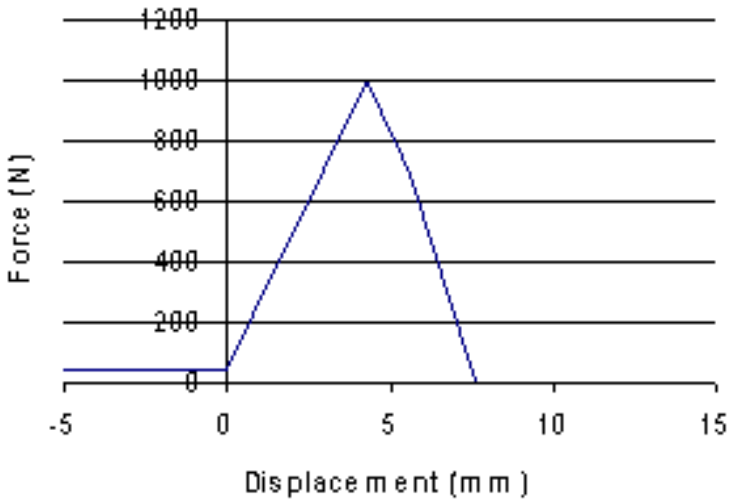

Figure 4.7. Force vs. displacement curve used for modeling capitis ligament.

The initial yield compression force was set to -1.000 N for all of the pelvis ligaments. Table 4.10 shows the initial yield force in tension which was given to each of the pelvis ligaments:

Table 4.10. Initial Yield Force for the different Pelvic Ligaments

Pelvis Ligament	Initial yield force (N)
Capitis femoris	900
Ischiofemoral	2400
Iliofemoral	1900

Since the exact material properties of the hip ligaments were not available due to a lack of data in the existing literature and to the impossibility of a test session on human hip-ligaments, some assumptions were made to obtain properties for the finite element simulations.

The knee ligaments are among the most studied ligaments. A lot of data are available on tensile properties of these ligaments (Decraemer, 1980; Barbenel, 1973). If it is assumed that all ligaments in the human body share similar mechanical properties, the hip ligaments properties can be obtained simply by scaling them based on their geometry. (Lanir, 1980) The anatomy of the hip ligaments was thoroughly investigated through selected literature and the following assumptions were made: (Decraemer, 1980; Barbenel, 1973)

- The thickness of the hip ligaments is approximately equal to the thickness of the MCL (i.e., average thickness $\approx 1.5 \cdot 10^{-3} m$),
- The iliofemural ligament has a surface which is three times greater than the MCL surface area, and
- The ischiofemural ligament has a surface which is 2.5 times greater than the MCL surface area.

The human MCL was assumed to have the following properties:

Max Force = 4,000 N

Width = 0.002 m

Thickness = 0.0015 m

$F_{MCL} = (\sigma)A$

$\sigma = F_{MCL} / A = 4{,}000 \text{ N} / 30 \cdot 10^{-6} \text{ m} = 133 \text{ MPa}$

The properties of the hip ligaments can be obtained using the simple geometric transformation discussed above:

$F_{ilio} = 3 \; F_{MCL} = 12{,}000 \text{ N}$
$F_{ischio} = 2.5 \; F_{MCL} = 10{,}000 \text{ N}$
$F_{pubo} = 1.9 \; F_{MCL} = 7{,}600 \text{ N}$

The iliofemural ligament was modelled by six discrete elements, the ischiofemural by four elements, and the pubofemural by three elements. Each ligament was split in more discrete elements in order to redistribute on more elements the force that the ligament should sustain. The maximum force for each single strand (i.e., element) was the total ligament force divided by the number of strands as follows:

$F_{ilio} / 6 \text{ el} = 2{,}000 \text{ N}$
$F_{ischio} / 4 \text{ el} = 2{,}500 \text{ N}$
$F_{pubo} / 3 \text{ el} = 2{,}530 \text{ N}$

The force-displacement curve for all the KTH ligaments are shown in Table 4.4.

Table 4.11. Material properties for ligaments and patellar tendon used in the KTH model.

Capitis Femoris Ligament	Force vs. Displacement / Capitis Femoris
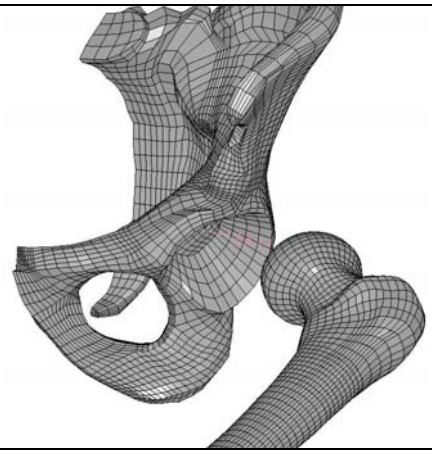	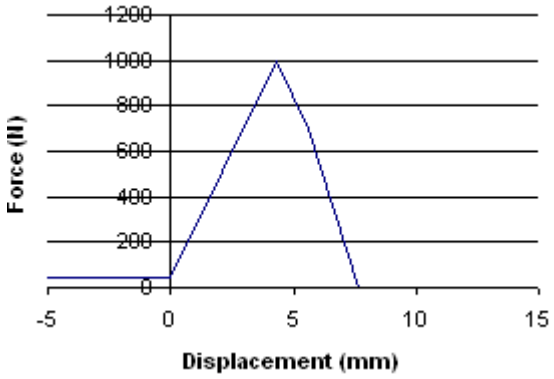
Iliofemoral Ligament	Force vs. Displacement / Iliofemoral
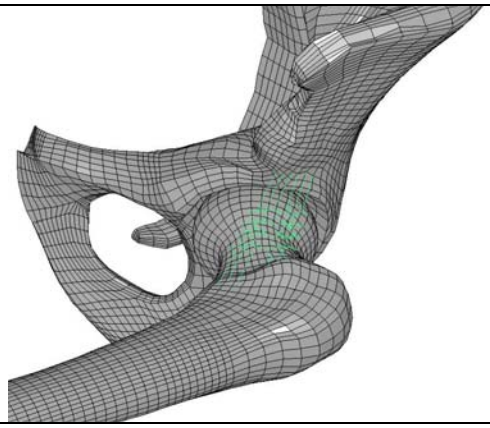	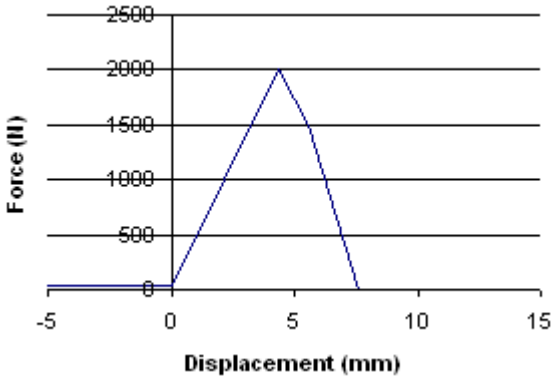
Ischiofemoral Ligament	Force vs. Displacement / Ischiofemoral
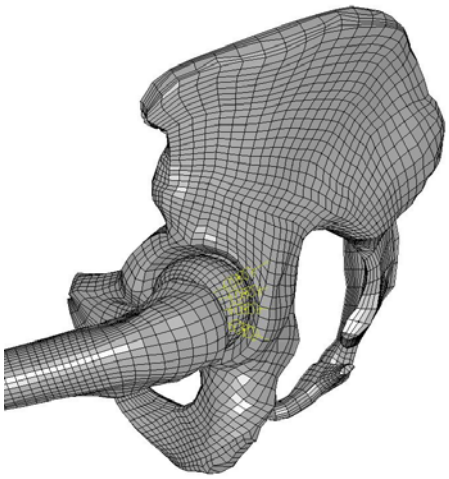	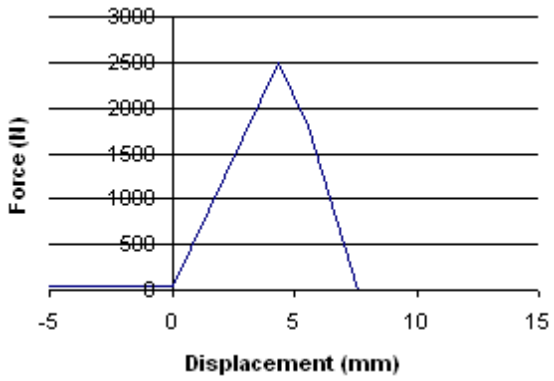

Table 4.11. Material properties for ligaments and patellar tendon used in the KTH model (continued).

Pubofemoral Ligament	Force vs. Displacement / Pubofemoral
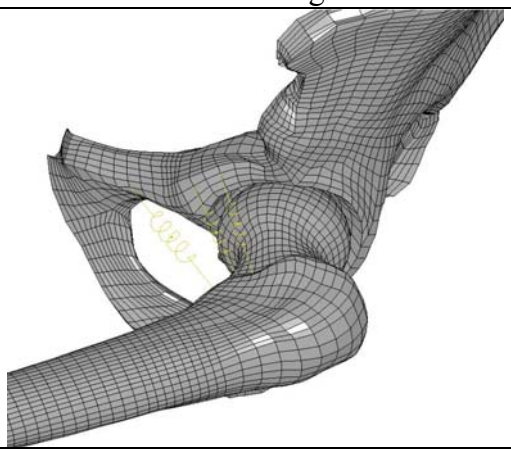	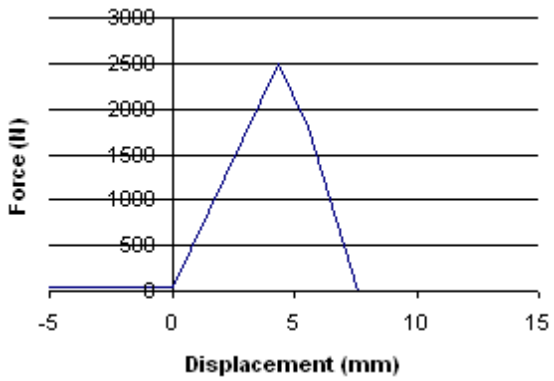
ACL Ligament	Force vs. Displacement / ACL
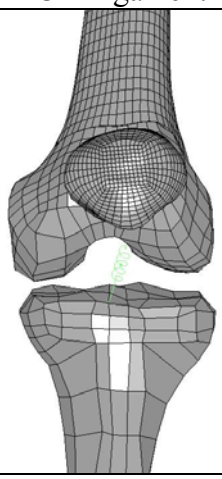	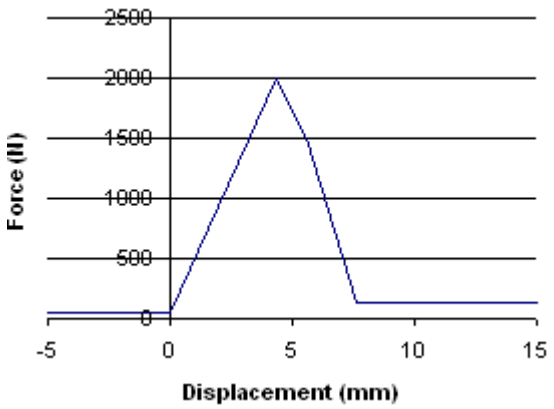
PCL Ligament	Force vs. Displacement / PCL
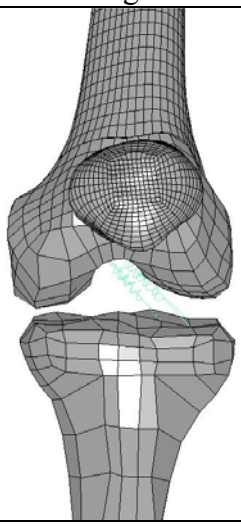	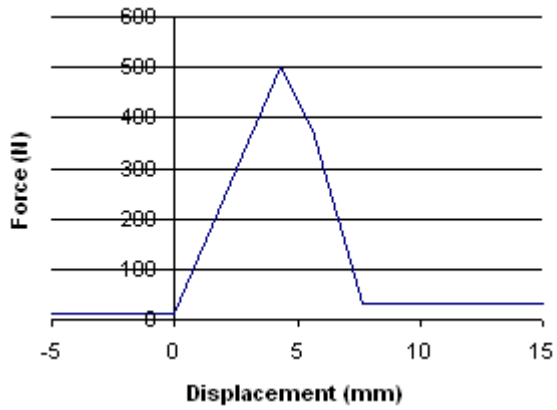

Table 4.11. Material properties for ligaments and patellar tendon used in the KTH model (continued).

<table>
<tr><td>MCL Ligament</td><td>Force vs. Displacement / MCL</td></tr>
<tr><td> 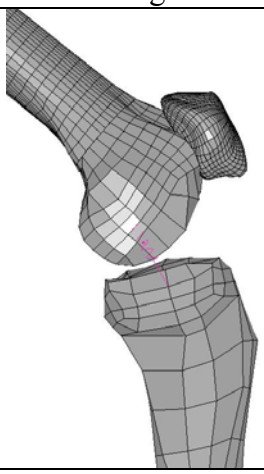 </td><td> 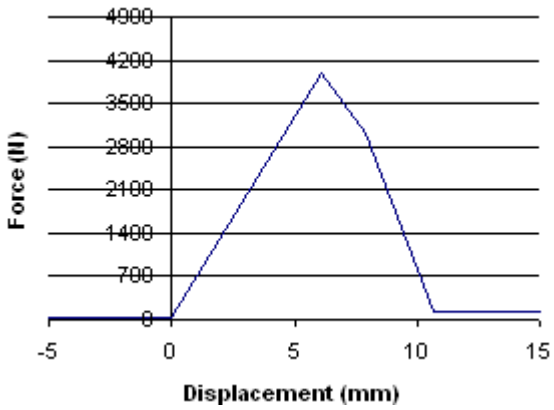
</td></tr>
<tr><td>LCL Ligament</td><td>Force vs. Displacement / LCL</td></tr>
<tr><td> 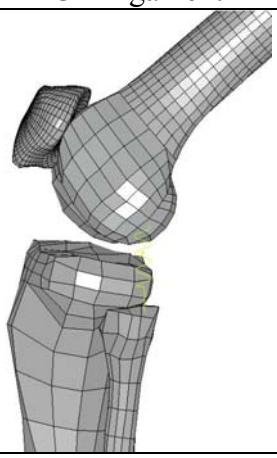 </td><td> 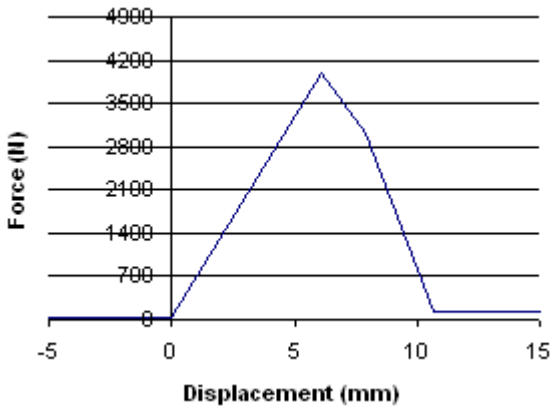
</td></tr>
<tr><td>Patellar Tendon</td><td>Force vs. Displacement / Patellar Tendon</td></tr>
<tr><td> 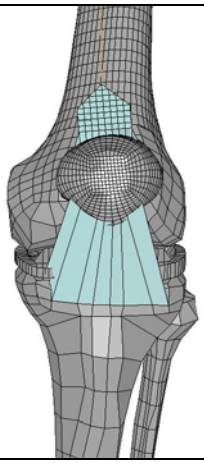 </td><td>

MAT	Elastic (# 1)
Density	1.9E-9 ton/mm^3
Young Mod.	17000 Mpa
Poisson	0.36
Elem. Form. Option	Belytschko-Leviathan
Shell Thickness	0.1 mm - each node

</td></tr>
</table>

4.5. Nodal Mass Calculation and Distribution

In the LLNL model, the contribution of mass from flesh, fat and muscles was not considered. The involvement of this mass, however, becomes relevant when it comes to impact investigations. During a car crash, the human body experiences acceleration/decelerations due to the impact and is also potentially subjected to impacts with different parts of the interior car structure. Inertia is an important effect in all vehicle crash scenarios.

In the specific case of the KTH, during a car crash this part of the body impacts the knee-bolster. Because of the impact, an acceleration is transmitted to the femur or pelvis through the knee. This acceleration is an index of the force that the leg experiences. The real force depends on the mass of the body.

Injury thresholds have been studied and defined for different parts of the body. These thresholds are indicators of force values that can be sustained by that particular part of the body before injury. Therefore, generally the part of the body will be affected by injury once it is subjected to a level of inertial force higher than the defined threshold.

In order to correctly predict fractures occurring at impacts, the right inertial forces acting on the human extremity during crashes must be investigated. With this refined KTH representation, the mass of soft tissue at different parts of lower extremities was evaluated and included as nodal lumped masses in the model.

4.5.1 Geometry and Representation of Soft Tissue Mass

4.5.1.1 Calculation of Body Segment Masses

A method described by Zatsiorskji and Selujanov (1983) allows calculating mass values for each body segment by linearly relating the total mass and the height of a person with use of some parameters according to the following equation (Zatsiorskji, 1983):

$$m_i = B_0 + B_1 m + B_2 v \quad (2.9)$$

where *m* is total mass of a person and *v* is the height of a person. Masses have to be expressed in kilograms and height in centimeters. Parameter B_0 is in kg, B_1 is non-dimensional and B_2 is kg/cm.

In consideration of the fact that the KTH model will be validated by taking into account results from a particular sled test impact of a male cadaver of 100 kg and 178 cm in height, the Zatsiorskji method gave the body segment mass values shown in Table 4.12:

Table 4.12. Body Segment mass values for a 100 kg, of 178 cm tall male. (www.biomech.ftvs.cuni.cz, 2005)

Segment	B_0[kg]	B_1	B_2[kg/cm]	Weight [kg]
Head+neck	1.296	0.0171	0.0143	5.5514
Hand	-0.1165	0.0036	0.00175	0.555
Forearm	0.3185	0.01445	-0.00114	1.56058
Upperarm	0.25	0.03012	-0.0027	2.7814
Leg (Foot)	-0.829	0.0077	0.0073	1.2404
Shank (Fibula and Tibia)	-1.592	0.03616	0.0121	4.1778
Thigh (Femur and Patella)	-2.649	0.1463	0.0137	14.4196
Trunk				45.13568
Upper part of the trunk	8.2144	0.1862	-0.0584	16.4392
Middle part of the trunk	7.181	0.2234	-0.0663	17.7196
Lower part of the trunk	-7.498	0.0976	0.04896	10.97688
Arm total				4.89698
Leg total				19.8378
Total:				100.15664

4.5.1.2 Calculation of Soft Tissue Mass

For a single body segment, the weight of soft tissue (kg) to be added was calculated as difference between the total weight (kg) obtained by Zatsiorskji and Selujanov method and the bone weight (kg) obtained from LsPrePost as follows:

	TOTAL MASS	–	BONE MASS	=	SOFT TISSUE MASS
Foot:	1.24	-	0.5266	=	0.7133
Tib+Fib:	4.17	-	0.6798	=	3.4901
Fem+Pat:	14.41	-	0.3971	=	14.0028

The mass was added by assigning mass to nodes of bones with use of the LSDYNA card *ELEMENT_MASS. The value obtained from the shank segment was partitioned equally between the tibia and the fibula while the mass obtained from the thigh segment was distributed only as nodal masses on the femur.

Since with this method there was not a clear distinction of the pelvis bone from the lower and middle part of the trunk, calculation of the pelvic region mass was performed according to Schneider. According to Schneider, the pelvic region represents the 15% of body weight. Thus, in this case, the whole pelvis would weight 15 kg. In this model, symmetry was used and only half of the pelvis was modeled. As consequence, the pelvis region mass was 7.5 kg.

Half Pelvis: $7.5 - 1.0395 = 6.4604$

Nodal mass values considered for each bone of the KTH model are reported in Table 4.13.

When Zatsiorskji and Selujanov method is used with the values of 175 cm and 77 kg (i.e., 50^{th} percentile male), the segment masses are found to be those shown in Table 4.14.

Table 4.13. Nodal mass values for each bone of the KTH model.

Bone	Mass	N. Nodes	Nodal Mass (Mg)
Pelvis	6.46044	10907	5.92E-07
Femur	14.0028	15060	9.30E-07
Tibia	1.7451	923 (Tib+Fib)	3.78e-6 (Tib+Fib)
Fibula	1.7451		
Foot	0.713384	729	9.79E-07

Table 4.14. Body segment mass values for a 50th percentile male (i.e., 77 kg – 175 cm) (www.biomech.ftvs.cuni.cz, 2005)

Segment	B_0[kg]	B_1	B_2[kg/cm]	Weight [kg]
Head+neck	1.296	0.0171	0.0143	5.1724
Hand	-0.1165	0.0036	0.00175	0.47395
Forearm	0.3185	0.01445	-0.00114	1.22709
Upperarm	0.25	0.03012	-0.0027	2.08594
Leg	-0.829	0.0077	0.0073	1.0706
Shank	-1.592	0.03616	0.0121	3.35822
Thigh	-2.649	0.1463	0.0137	11.0684
Trunk				33.39434
Upper part of the trunk	8.2144	0.1862	-0.0584	12.0982
Middle part of the trunk	7.181	0.2234	-0.0663	12.5151
Lower part of the trunk	-7.498	0.0976	0.04896	8.78104
Arm total				3.78698
Leg total				15.49722
Total:				77.13514

From comparison of mass values between the 50th percentile male and the male cadaver reproduced for validation, it can be noted that it is an acceptable choice to use the mass values of a 100 kg man for a 50th percentile male since the differences are small (Table 4.15):

Table 4.15. Comparison between lower extremity segment masses from a 100 kg and 178 cm man and a 50th percentile male.

	100 kg – 178 cm KTH Cadaver Model	**77 kg - 175 cm** 50th Percentile Male
Lower Extremity Segment		
Foot (Kg)	1.2404	1.0706
Shank (Tibia+Fibula) (kg)	4.1778	3.35822
Thigh (Femur+Patella) (kg)	14.4196	11.0684
Total (kg)	19.8378	15.49722

V. MODEL VALIDATION

The finite element model was used to replicate the results of physical experiments obtained from the NHTSA database. Three different component simulations were first run to test the validity of the bone material and the geometry of a portion of each bone model. These simulations reproduced the same setup of the corresponding NHTSA tests on femoral head, pelvis bone and femoral condyles. In essence, these component-level experiments are useful since they isolate the material behavior from the soft tissue behavior and the overall kinematics of a whole-cadaver test.

A whole-cadaver test performed by University of Michigan Research Institute (UMTRI) and sponsored by NHTSA was used to validate the entire model including the ligament and passive muscle forces.

5.1. Component Validation Simulations

5.1.1 NHTSA Tests – General Setup

Tests of whole cadavers and specific components were performed by University of Michigan Research Institute (UMTRI) and sponsored by NHTSA. (Rupp, 2003b; Rupp, 2003c; Rupp, 2003d) They are available on-line at the NHTSA biomechanical database. (NHTSA, 2005) The goal of the tests was to analyze the response of cadaver KTH bones when impacted at different angles of flexion and adduction. Specific injuries in the KTH region were investigated by isolating particular biological structures. The setup of the testing machines allows the KTH specimen to be loaded with different velocities and orientations. The test setup for a biological component test of the pelvis is shown in Figure 5.1 as an example.

The cannon accelerates a sled and, through a series of shock absorbers, accelerates a ram that impacts the specimen. Symphysis post was added to test fixture to prevent rotation

about the y-axis. The knee and the ram were already in contact at the beginning of the impact. A padded interface between the knee and the ram was added in some cases. In other tests, the ram was not padded and a flat steel surface impacted the bones directly.

Tests were performed the following way: at first, the isolated pelvis was impacted, left and right sides separately. After this, if the femurs were not damaged, femur tolerance tests were performed under loading by molded and flat-plate knee interfaces, right and left sides separately. After these tests, if failure did not occur to the knees, knee tolerance were performed with a padded impact surface, right and left separately.

Force, displacement and acceleration time histories of the ram and forces, accelerations and displacement of a load cell positioned on the specimen were collected. These tests were used to validate the finite element models that will be described in the following sections. Specific comparisons of the physical tests and simulations will be presented in a later section.

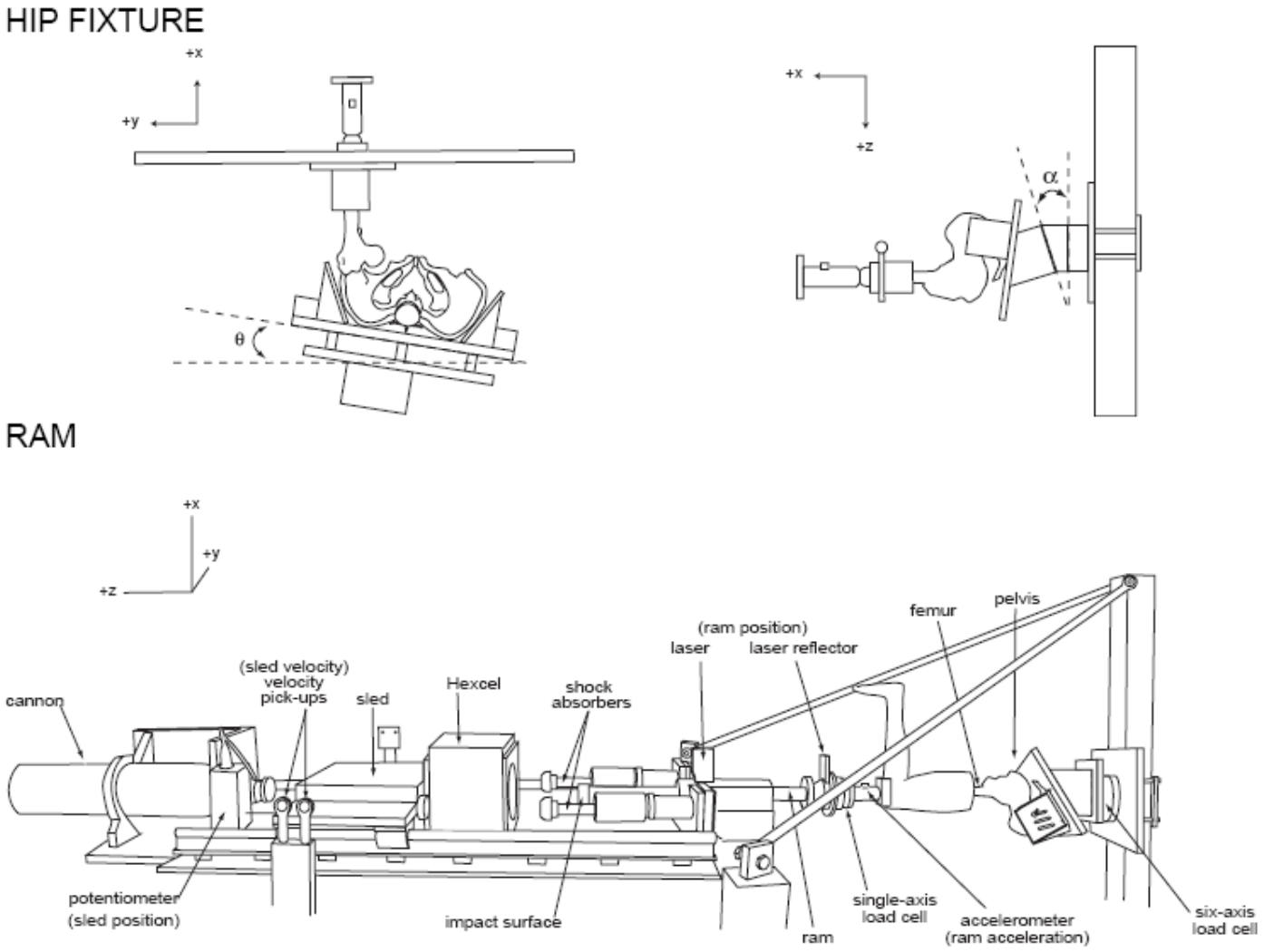

Figure 5.1. Testing machine setup. (Rupp, 2003b)

5.1.2 NHTSA Tests – Cadaver Characteristics

The average age of the cadavers was 69.6 years, the average T-score was -1.22 and the average Z-score 0.7. These scores indicate the amount the cadaver's bone mineral density varies from the mean. Negative scores show lower bone density, while positive scores indicate higher.

- **T-score value**: the T-score value is generally used over age 50 because it better predicts risk of fracture. A T-score of -1.0 is normal. Osteopenia is indicated when the T-score value is between -2.5 and -1.0. With an average T-score equal to -1.22, like in the UMTRI tests, it means that the bone density is 1.22 standard deviations below the mean of a thirty year old individual.

- **Z-score value:** the Z-score is the number of standard deviations a patient's bone mineral content differs from the average value of individuals of their sex, age and ethnicity.

5.1.3 Pelvis Validation

The pelvis tests were used to validate the material properties of the bone material model of the pelvis as well as its failure mechanism especially for acetabular fractures. Since the physical experiments are tests to-failure, the model should be able to correctly replicate the fracture pattern and ultimate load experienced in the physical experiments.

5.1.3.1 NHTSA Pelvis Test Setup

A total of 74 tests were performed by UMTRI involving impacts to the pelvis with different angles of flexion and abduction (0˚ flex/0˚ abd, 0˚ flex/-10˚ abd, 0˚ flex/10˚ abd, 0˚ flex/15˚ abd, 30˚ flex/0˚ abd). (Rupp, 2003c) Forty two tests were performed on pelvis with 0˚ flexion and 0˚ abduction and were used to validate the finite element mesh of the pelvis.

The pelvis was dissected from all flesh as was the femur bone until the middle of the shaft. The load was applied at the knee and the pelvis was restrained with a supporting device. A ram impacted the knee at a certain velocity to simulate an impact with the knee bolster. Figure 5.2 shows the ram displacement corridor and the average values of pressure and sled velocity obtained when considered data from all 42 tests.

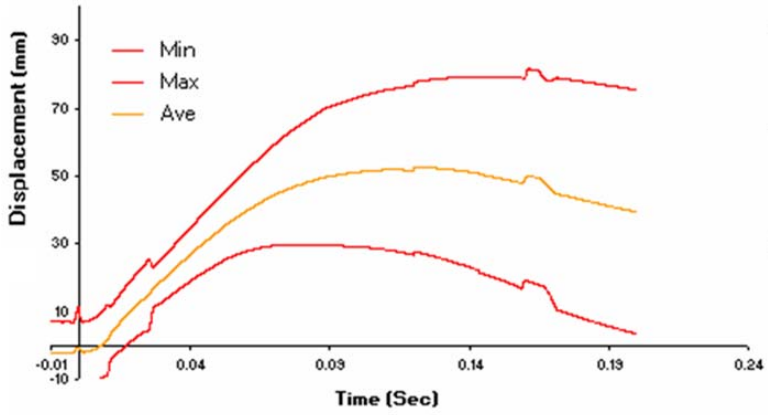

	Pressure (psi)	Sled Velocity (m/sec)	Mass (Kg)
Max	60	1.65	9.81
Min	28	0.97	3.6
Average	34.31	1.2	6.15

Figure 5.2. Ram displacement corridor (left) and pressure, sled velocity and mass values (right) from collection of 42 pelvis tests.

5.1.3.2 NHTSA Pelvis Test Results

The reaction force between the pelvis and the supporting device was recorded: the average peak force for the 42 physical experiments was found to be 4,156 N. A 1.65-N standard deviation wide corridor was established for the purpose of comparison with the FE simulation results. (Figure 5.3) (Ray, 1996)

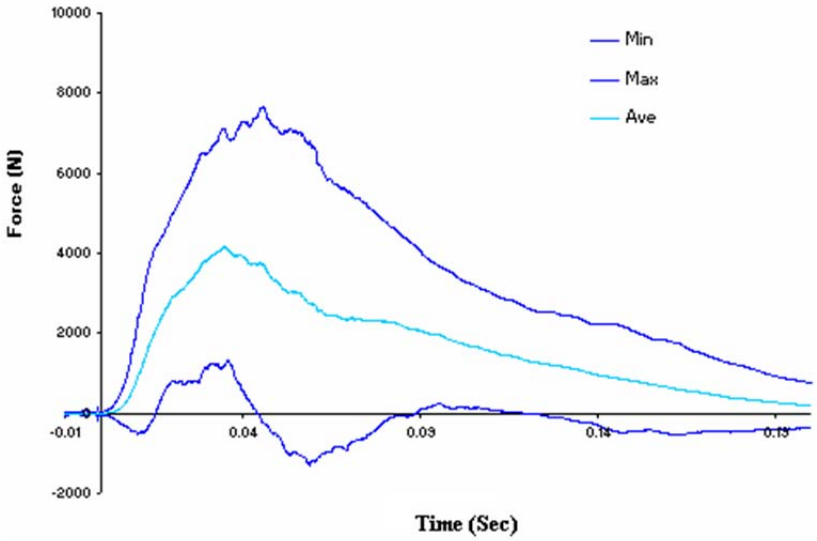

N. Tests: 42	
Invalid Data	7
No Failure	6
Midshaft Femur	2
Supracondylar	2
Femoral Neck	3
Post Wall	14
Ante Wall	2
Post Column	16
Inferior Pubic Ramus	8
Post Rim	4
Ante Rim	1
Post Acetabular Wall	3
Transv. Post Wall	1
Transv. Acetabular	2
I-S Iliac Wing	5
Sup. Labrum Avulsion	1

Figure 5.3. Contact pelvis corridor force (left) and list of fractures resulting (right) from 42 pelvis tests.

Figures 5.4 and 5.5 show the different types of failures observed for the pelvis and the percentages from the 42 tests. The most frequent type of failure documented was a wall column fracture which represented 45.8% of all failures in the test series. Other types of frequent fractures were inferior pubic ramus and acetabulum wall failures.

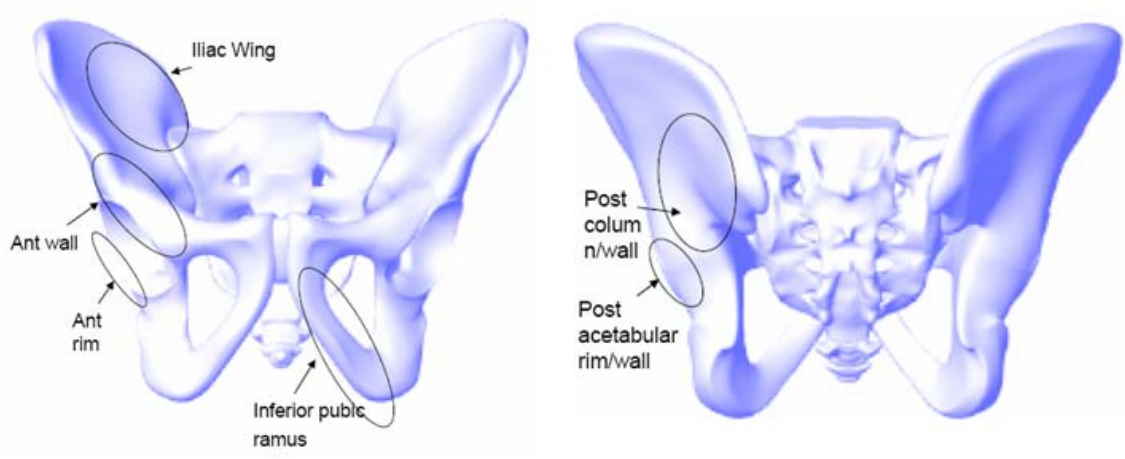

Figure 5.4. Locations of the common pelvis tests fractures in 42 pelvis impacts.

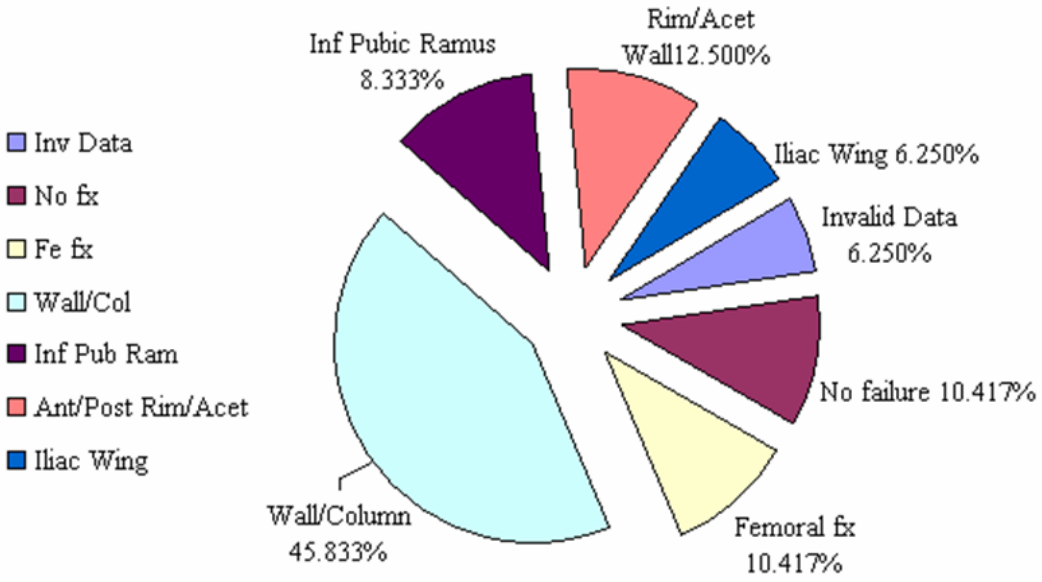

Figure 5.5. Percentage of different types of failures occurred in 42 pelvis tests.

5.1.3.3 Pelvis FE Simulation Setup

A finite element simulation was performed using the same impact and boundary conditions used in the physical tests as shown in the right portion of Figure 5.6.

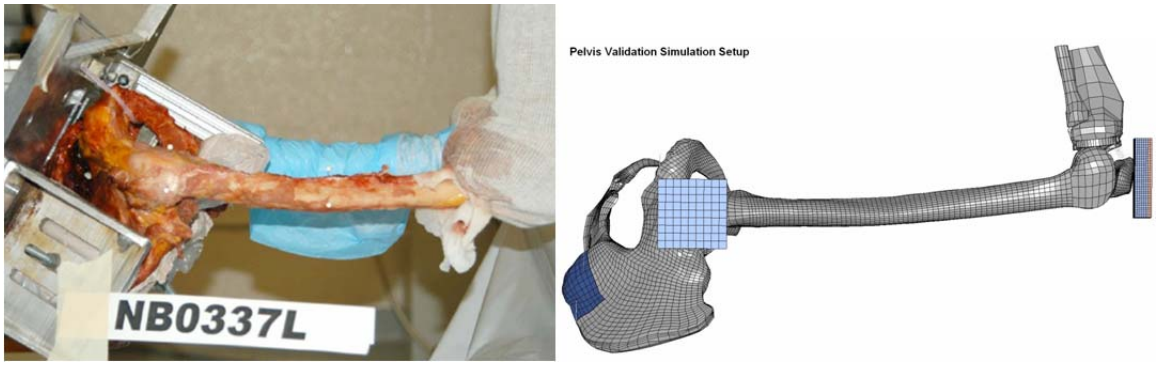

Figure 5.6. Pelvis validation test (left) and simulation (right) setup. (Rupp, 2003b)

The pelvis in the FE simulation was restrained using displacement boundary conditions corresponding to the areas of the pelvis that were clamped in the physical tests. The femur was placed in anatomical position related to the hip and the abduction and flexion angle are zero.

The impactor was represented by a square flat steel plate to which was added a 13 cm-thick blue floatation foam. A picture of the constrained pelvic extremity and of the constraints applied to the femur are shown in Figure 5.7.

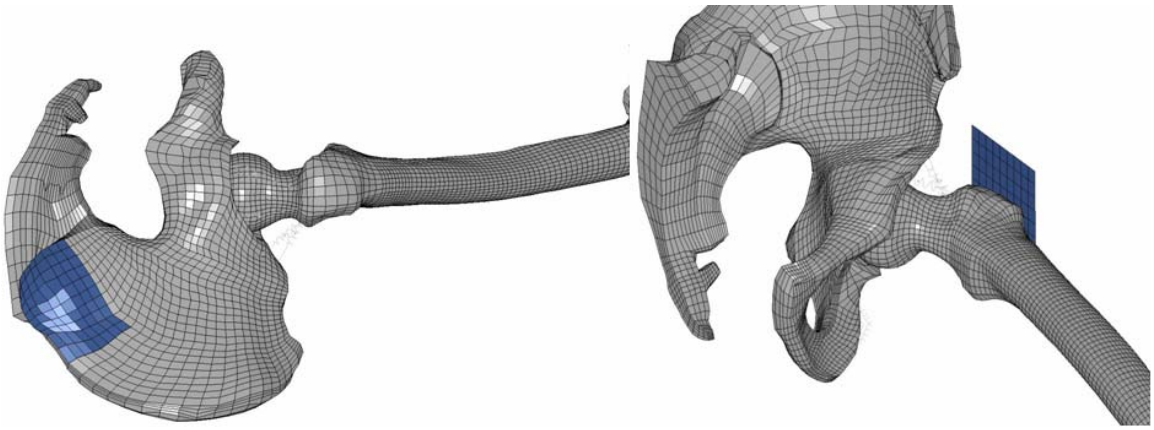

Figure 5.7. Constrained pelvic extremity (left) and constraints applied to the femur (right) from the FE pelvis simulation setup.

A displacement-time history was imposed on the flat steel plate part of the impactor in the FE simulation with the LSDYNA card *BOUNDARY_PRESCRIBED_MOTION_RIGID which allows for a prescribed displacement curve. (Figure 5.8) The time-displacement curve imposed was the maximum ram-displacement values from the corridor shown earlier in Figure 5.3. The model was then restrained from all displacements except the longitudinal direction.

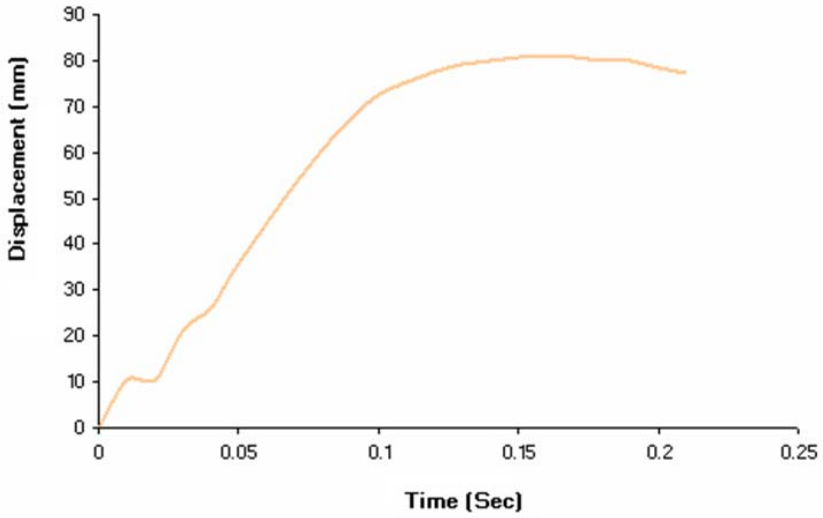

Figure 5.8. Displacement-time curve imposed to the impactor during simulations.

5.1.3.4 Pelvis FE Simulation Results

In the tests, the contact force between the pelvis and the supporting device was recorded. This force was then used to validate the FE model.

In the simulation, the *RCFORC card was inserted and the contact force between the pelvis and the supporting device modeled on the posterior iliac wing of the bone was collected using LsPrePost. It was then filtered with filtered fir100, at 1,000 Hertz.

As shown in Figure 5.9, the force time history of the pelvis reaction force in the FE simulation falls within the physical test corridor although generally right above the minimum test value. The FE results lie within the corridor through the peak load and into the unloading phase. The peak pelvis reaction force in the FE simulation was found to be 1,850 N compared to the average test result of 4,156 N. Based on Figure 5.9, the FE simulation provides an acceptable estimate of the pelvis reaction force compared with the 42 physical experiments since it remains within the one-standard deviation corridor throughout the event.

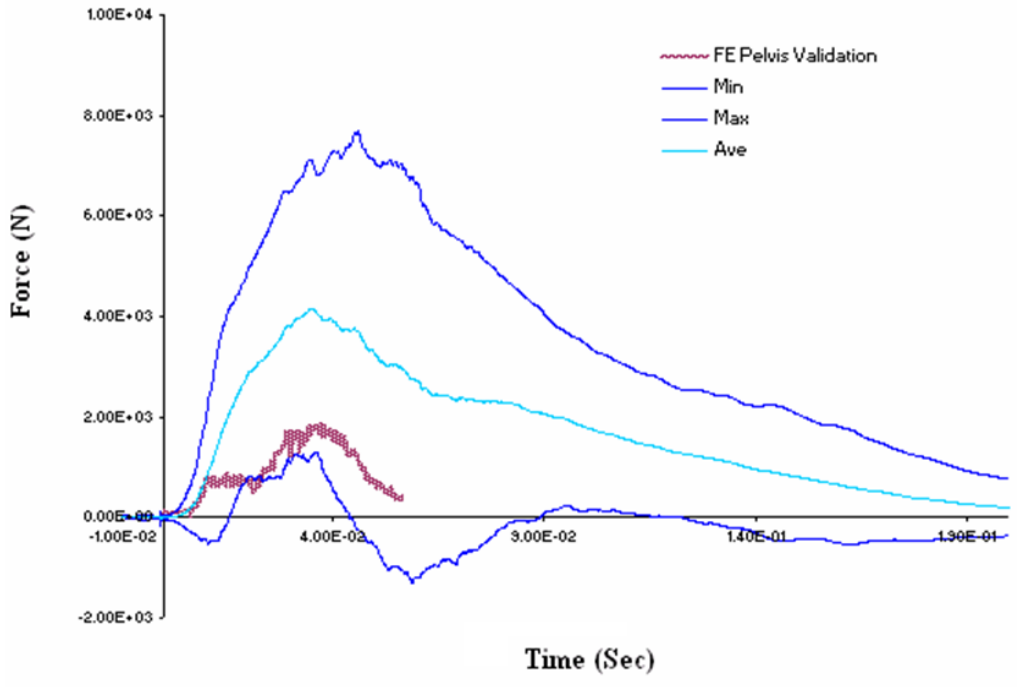

Figure 5.9. Femoral contact axial force behavior in the physical tests (dashed lines) and in the FE model simulation (dotted line).

The model also behaves correctly from a phenomenological point of view since the FE simulation resulted in similar pelvis fractures recorded during tests as shown in Figure 5.10. A fracture of the interior acetabular cup and of the posterior wall-iliac wing occurred in the FE simulation.

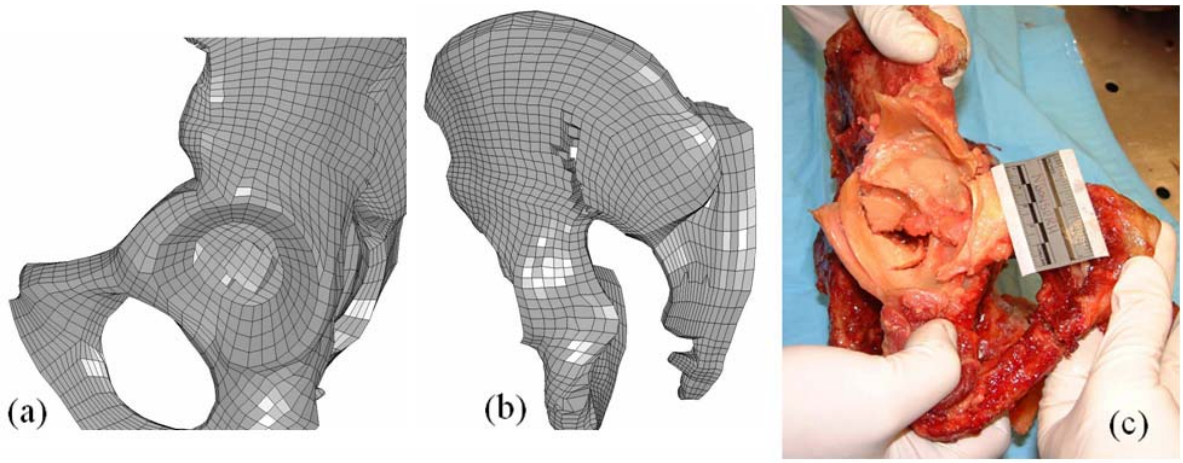

Figure 5.10. Comparison of the pelvis fracture in an FE simulation ((a) and (b)) and a physical test (c) of the pelvis (Rupp, 2003b).

\

With both qualitative and quantitative simulation results well reproducing the tests results, the FE pelvis model was considered validated.

5.1.4 Femoral Head Validation

The femoral head tests were used to validate the material properties of the bone material model of the femur particularly in the area of the femoral head as well as the failure mechanism in the proximal femur. Since the physical experiments are tests to-failure, the model should be able to correctly replicate the fracture pattern and ultimate load experienced in the physical experiments.

5.1.4.1 NHTSA Femoral Head Test Setup

Thirty seven tests were performed by UMTRI and obtained from the NHTSA database. (Rupp, 2003c) Unfortunately, for many of these tests the type of impactor used was not reported and whether the surface was padded or not. Even from the pictures of the reports it was not always possible. For the tests whose impactor geometry and material was known, determine the nature of the impact not used in all of them used the same type. Having a padded rather than a flat, rigid impactor resulted in very different simulation results. It was then decided to consider only 15 of the 37 tests for comparison to the FE model, because there was certainty that these tests used a squared, flat, padded impactor. The thickness of the impactor pad, however, had to be guessed from pictures of the reports.

The femur was placed in an anatomical position with abduction and flexion angles of zero degrees. The lower extremities were detached from the pelvis and the femoral head was mounted in a fixed cup which represented the acetabulum. (Figure 5.14) A ram impacted the knee at a certain velocity to simulate an impact with the knee bolster. Figure 5.11 shows the ram displacement corridor and the average values of pressure and sled velocity obtained from all 15 tests.

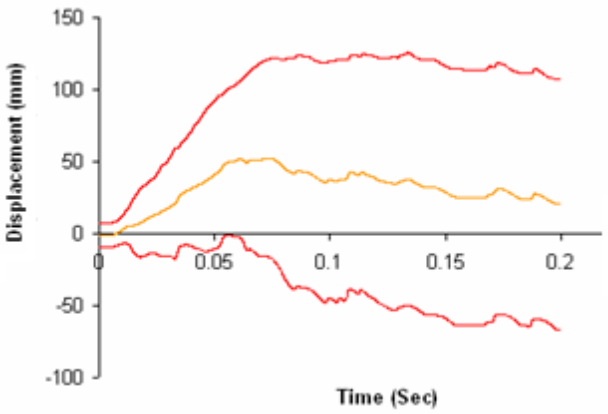

	Pressure (psi)	Sled Velocity (m/sec)
Min	35	1.13
Max	78	1.9
Average	46.14	1.43

Figure 5.11. Ram displacement corridor (left) and pressure and velocity values (right) from collection of 15 femoral head tests.

5.1.4.2 NHTSA Femoral Head Test Results

The reaction force at the fixed cup was then measured during the experiment. Figure 5.12 shows the corridor obtained from the measured cup-femoral head contact force from all 15 tests and a list of femoral fracture modes observed in the experiments.

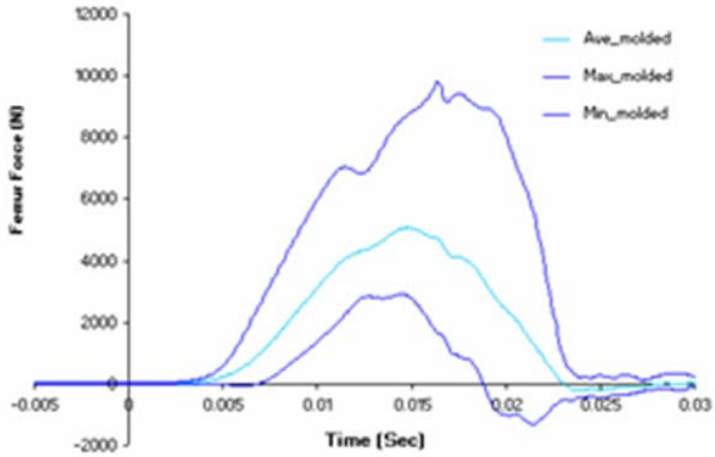

N. Tests: 14	
Femoral Neck	11
Intertrochanteric	2
Condylar	2
Femoral Shaft	2

Figure 5.12. Cup-femoral head contact force corridor and average value (left) and list of fractures results (right) from collection of the 15 femoral head tests.

The average peak acetabular force for the 15 physical tests was observed to be 5,075 N with a maximum value of 9,806 N and a minimum value of 2,897 N as shown in Figure 11. Figure 5.13 shows the percentage of the different types of femoral failure modes from results of the 15 tests. The most frequent type of failure documented was a femur neck fracture which represented the 64% of all failure modes in the 15 tests. Other types of fractures happened in minor percentages to the intertrochanteric region, to the shaft and the femur condyles.

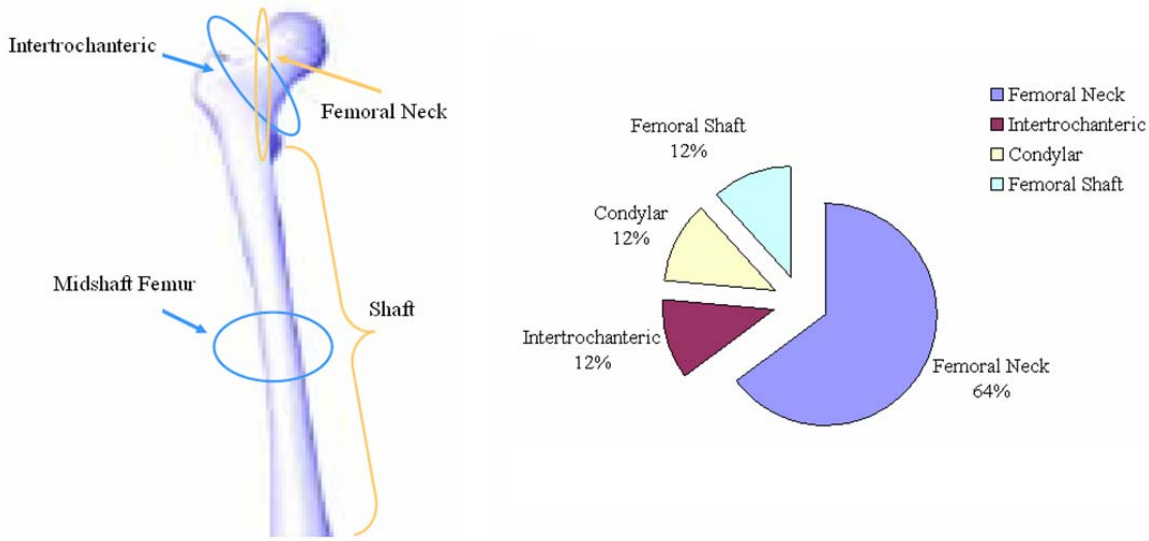

Figure 5.13. Locations of the common head femoral fractures (left) and percentage of these types of failures occurred in the 15 head femoral tests (right).

5.1.4.3 Femoral Head FE Simulation Setup

A finite element simulation was performed using the same impact and boundary conditions used in the physical tests as shown in the right portion of Figure 5.14.

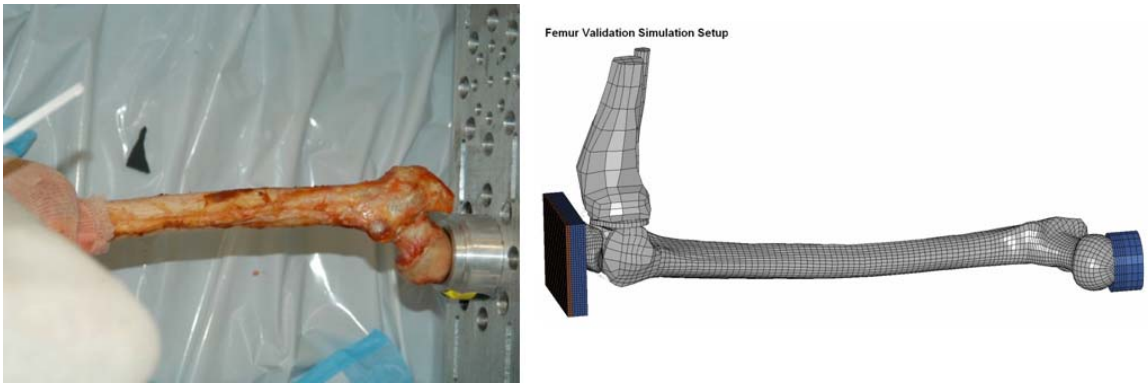

Figure 5.14. Femoral head validation test (left) and simulation (right) setup. (Rupp, 2003c)

The head of the femur was placed in the head device and their interaction was recorded using the LSDYNA card *CONTACT_AUTOMATIC_SURFACE_TO_SURFACE. In the simulation, like in all other simulations used for validation of this research, gravity was not included. The impactor was composed of a square flat steel plate to which was added a 13 cm-thick blue floatation foam. A picture of the head device and the impactor is shown in Figure 5.15.

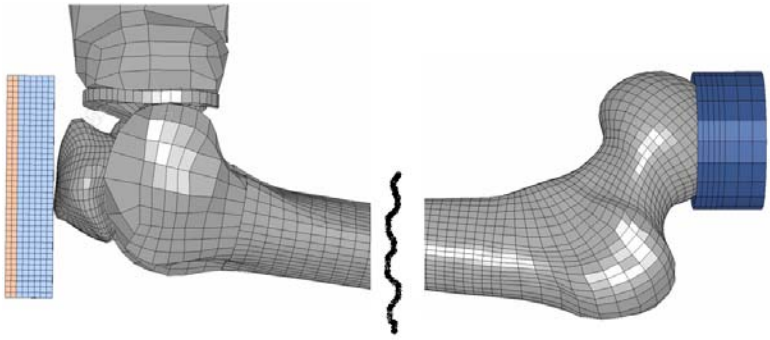

Figure 5.15. Impactor and head device details from the FE femoral head simulation setup.

A displacement-time history was imposed on the flat steel plate part of the impactor in the FE simulation with the LSDYNA card *BOUNDARY_PRESCRIBED_MOTION_RIGID which allows for a prescribed displacement curve. (Figure 5.16) The time-displacement curve imposed was the maximum ram-displacement values from the corridor reported in Figure 5.11. The model was then restrained from all displacements except the longitudinal direction.

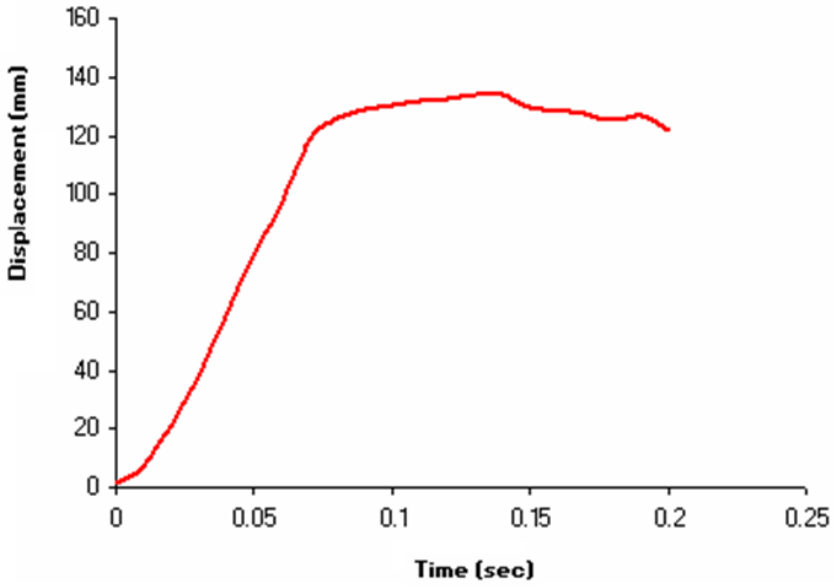

Figure 5.16. Displacement-time curve imposed to the impactor during the femoral head simulations.

5.1.4.4 Femoral Head FE Simulation Results

The contact force between the femoral head and the fixed cup representing the acetabulum was recorded in the physical test and used to validate the FE Model. It was filtered at 1,000 Hz.

In the simulation, the *RCFORC card was inserted and the contact force between the femoral head and the head device parts was examined in LsPrePost. It was then filtered with filter type SAE available in LsPreProst at 1,000 Hz as in the tests.

The peak force in the simulation, also shown in Figure 5.17, was 3,650 N. The simulation provides a result within the range of the tested values. A 1.65-N standard deviation wide corridor was established for the purpose of comparison with the FE simulation results. Figure 5.18 shows a comparison between the FE simulation femur force and the femur forces recorded in the NHTSA femur tests considered in this project. The simulation results are within the test corridor although they are at the lower boundary of the corridor.

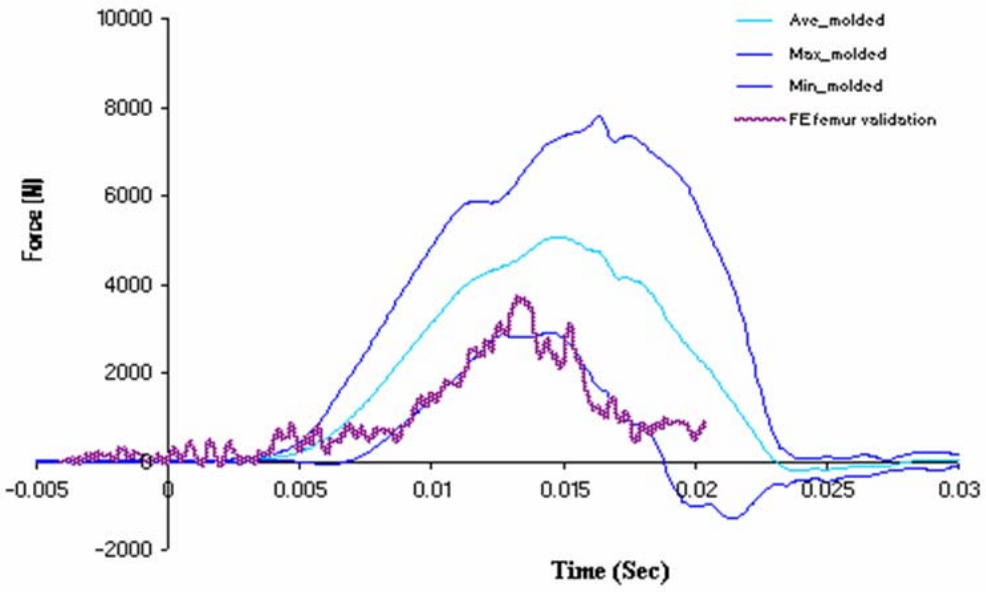

Figure 5.17. Cup-femoral head contact force behavior in the physical tests (dashed lines) and in the FE model simulation (dotted line).

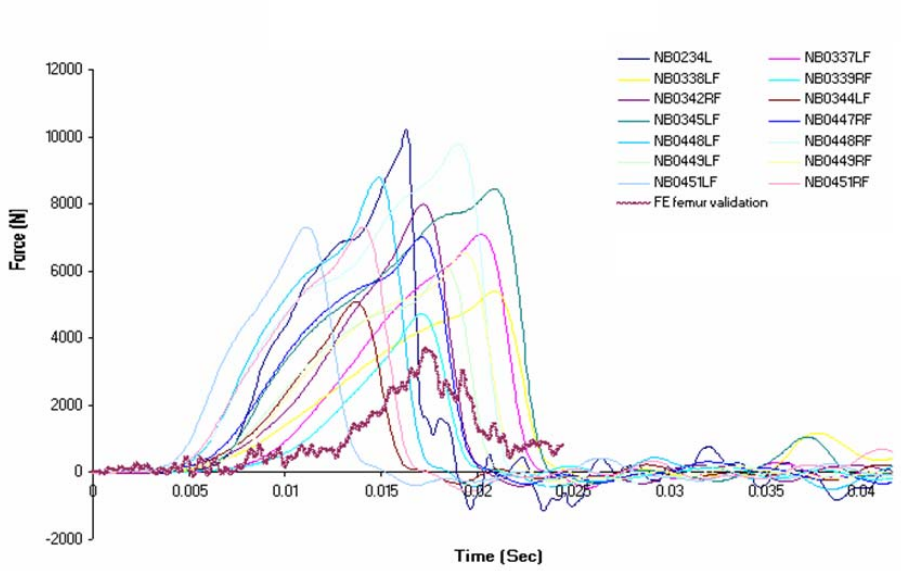

Figure 5.18. Cup-femoral head contact force behavior in the physical tests, and in the FE model simulation (dotted line).

The model also behaves correctly from a phenomenological point of view since the femur in both the test and simulation fractures between the femoral head and the trochanter as shown in Figure 5.19.

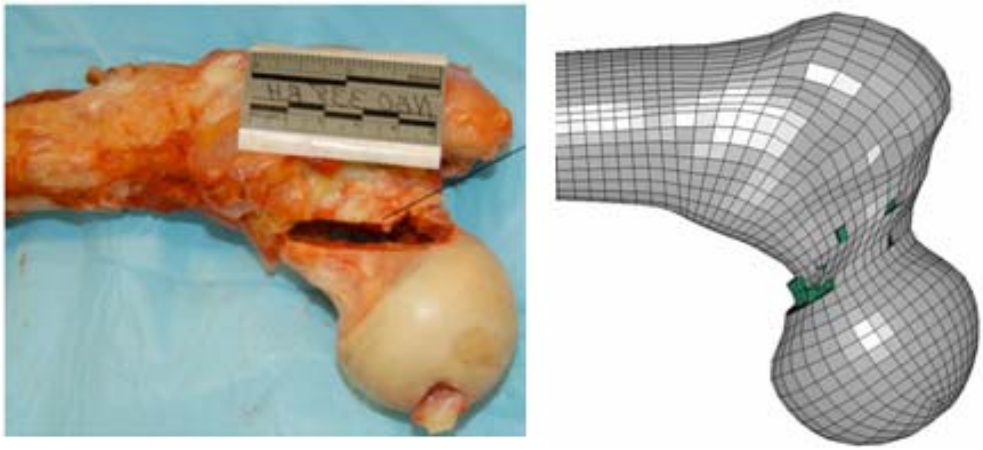

Figure 5.19. Intertrochanteric fracture mode from the Femoral Head Validation Test (Rupp, 2003c)

With both qualitative and quantitative simulation results comparing favorably with the tests results, the FE femoral head model was considered validated.

5.1.5 Femoral Condyles Validation

The femoral condyles tests were used to validate the material properties of the bone material model of the femur particularly in the area of the knee where are the femoral condyles, as well as their failure mechanism. Since the physical experiments are tests to failure, the model should be able to correctly replicate the fracture pattern and ultimate load experienced in the physical experiments.

5.1.5.1 NHTSA Femoral Condyles Test Setup

A total of 14 tests were performed by UMTRI involving impacts to the femoral condyles with different types of interfaces between the knee and the impactor (i.e., flat, lightly padded, flat, flat-rubber-floatation). (Rupp, 2003d) Seven flat, lightly padded tests were used to validate the finite element model of the lower part of the femur. In these tests, the femur was cut at the midshaft and a load cell inserted. It was then positioned with abduction and flexion angles of zero degrees. (Figure 5.23) The load was applied at the condyles and the femur was restrained at the mid-shaft load cell location. A ram impacted the knee at a certain velocity to simulate an impact with the knee bolster. Figure 5.20 shows the ram displacement corridor and the average values of pressure and sled velocity obtained when considered data from all seven tests.

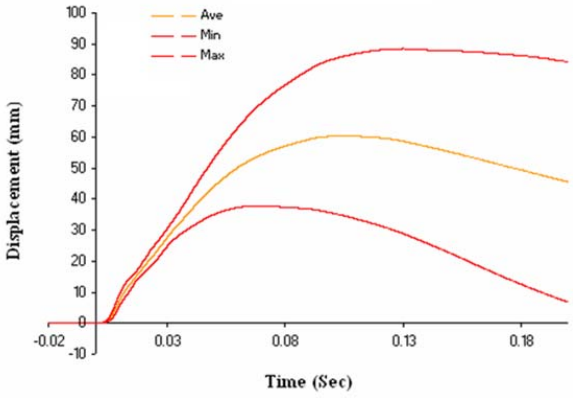

	Pressure (psi)	Sled Velocity (m/sec)	Mass (Kg)
Max	60	1.6	4.3
Min	40	1.28	1.96
Average	49.24	1.47	3.02

Figure 5.20. Ram displacement corridor (left) and pressure, sled velocity and mass values (right) from collection of seven femoral condyle tests.

5.1.5.2 NHTSA Femoral Condyles Test Results

The peak femur forces shown in Figure 5.21 correspond to the appearance of a crack between the condyles which propagates longitudinally up the femur. The average peak forces for the seven physical experiments was found to be 1,0311 N (i.e., the minimum value found was to be 6,272 N while the maximum was 13,129 N).

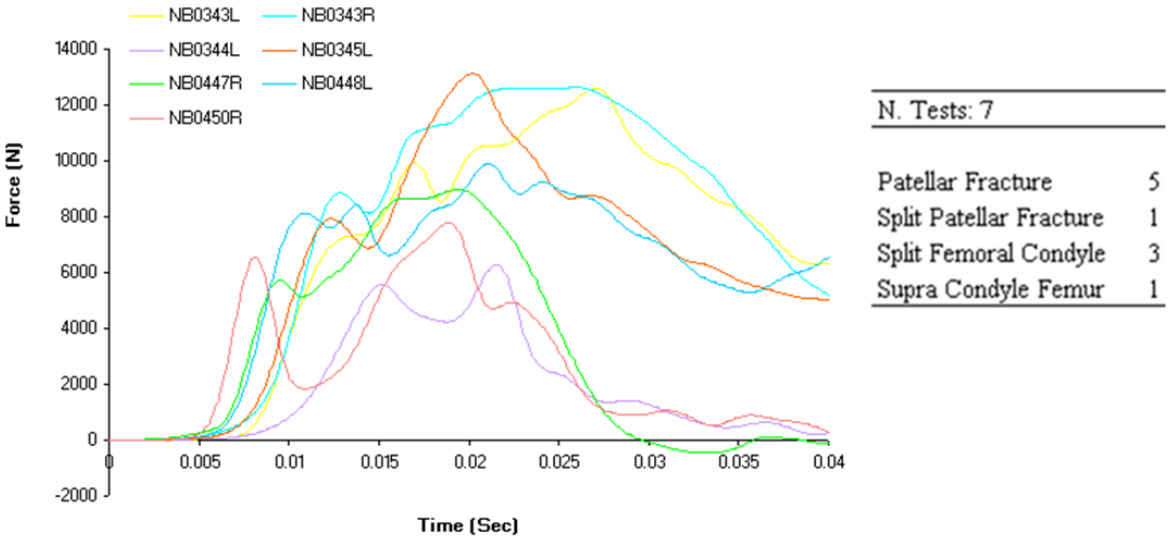

Figure 5.21. Femoral contact axial force (left) and list of fractures results (right) from collection of the seven femoral condyle tests.

Figure 5.22 shows the percentage of the different types of knee failure modes from results of the seven tests. The most frequent type of failure documented was a patellar fracture which represented the 50% of all failure modes during the seven tests. Another type of fracture happened to the supra condyle femur.

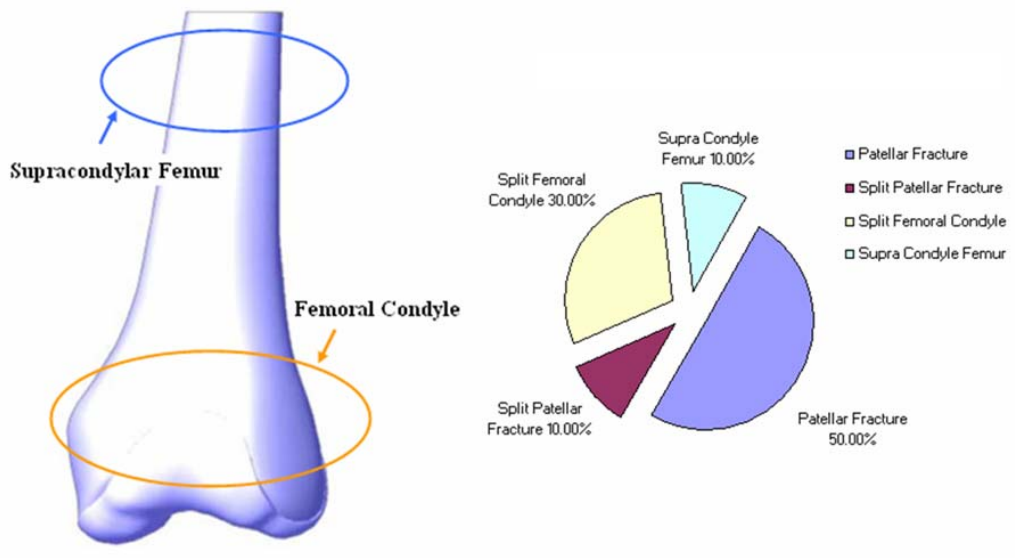

Figure 5.22. Locations of the common femoral condyle tests fractures (left) and percentage of these types of failures occurred in the seven tests (right).

5.1.5.3 NHTSA Femoral Condyles FE Simulation Setup

A finite element simulation was performed using the same impact and boundary conditions used in the physical tests and is shown in the right portion of Figure 5.23.

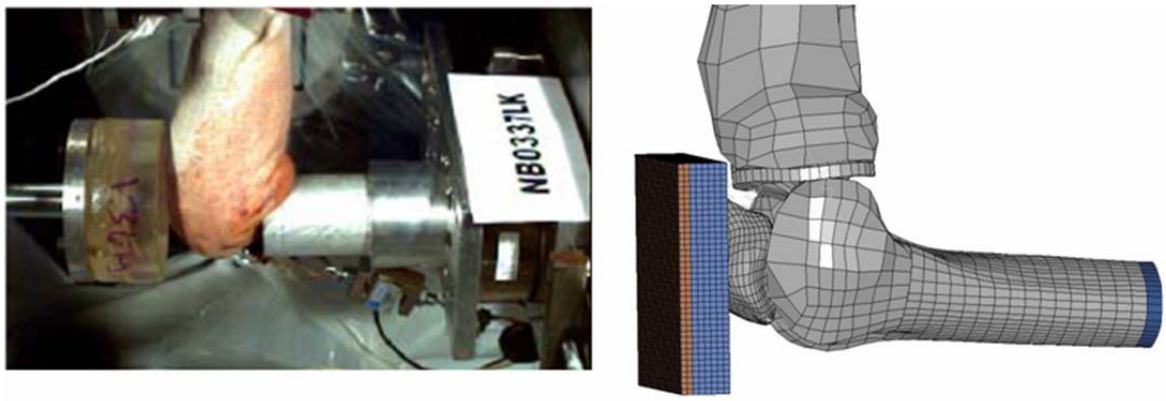

Figure 5.23. Femoral head validation test (left) and simulation (right) setup. (Rupp, 2003d)

The femur was cut at its mid-shaft and was restrained at this extremity in all directions for both translations and rotations. This constrained extremity reproduce the load cell which was implanted in the midshaft femur in real tests. In the simulation, like in all other simulations used for validation of this research, gravity effect were not included. The impactor was composed of a square flat steel plate to which was added a 13 cm-thick blue floatation foam. A picture of the constrained extremity and of the impactor is shown in Figure 5.24.

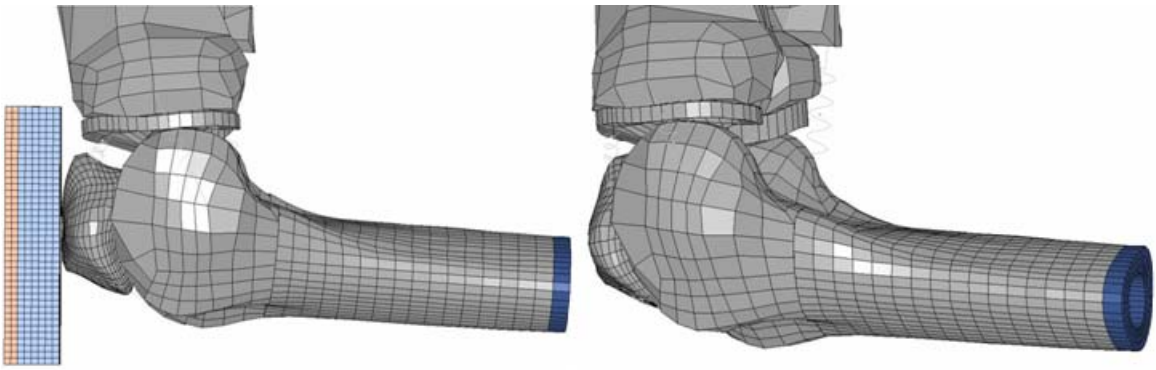

Figure 5.24. Impactor and load cell details from the FE femoral condyle simulation setup.

A displacement-time history was imposed on the flat steel plate part of the impactor in the FE simulation with the LSDYNA card *BOUNDARY_PRESCRIBED_MOTION_RIGID which allows for a prescribed displacement curve. (Figure 5.25) The time-displacement curve imposed was the maximum ram-displacement values from the corridor shown in Figure 5.20. The model was then restrained from all displacements except the longitudinal direction.

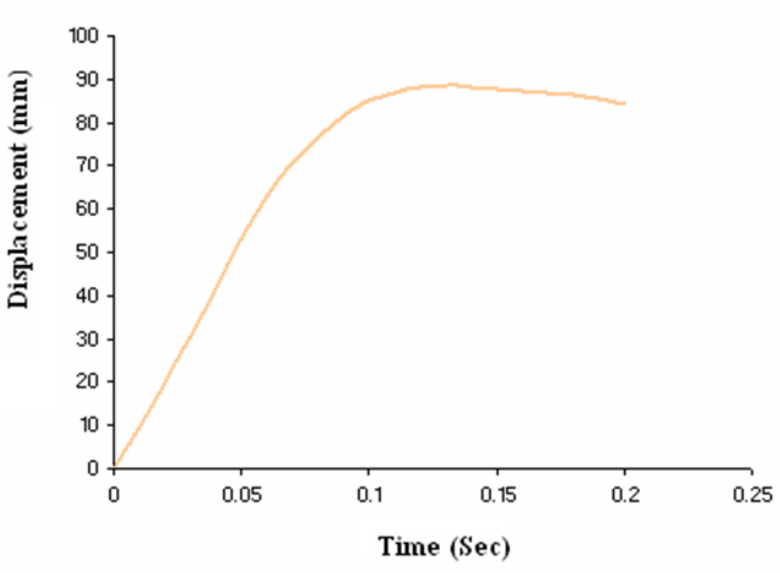

Figure 5.25. Displacement-time curve imposed to the impactor during simulations.

5.1.5.4 NHTSA Femoral Condyles FE Simulation Results

The femoral midshaft force recorded by the load cell implanted in the midshaft of the femur was obtained in the physical tests and used to validate the FE model. In the simulation, the *RCFORC card was inserted and the contact force between the femoral shaft and the constrained femoral extremity parts was recorded and examined using LsPrePost. The force time history was filtered with fir100 filter type available in LsPreProst at 1,000 Hz, as in the tests.

The peak force in the simulation, shown in Figure 5.26, was 8,450 N. The simulation provides a result well within the range of the tested values. A 1.65-N standard deviation wide corridor was established for the purpose of comparison with the FE simulation results.

The model behaves correctly from a phenomenological point of view since the femur in both the test and simulation fractures between the femoral head and the trochanter as shown in Figure 5.27.

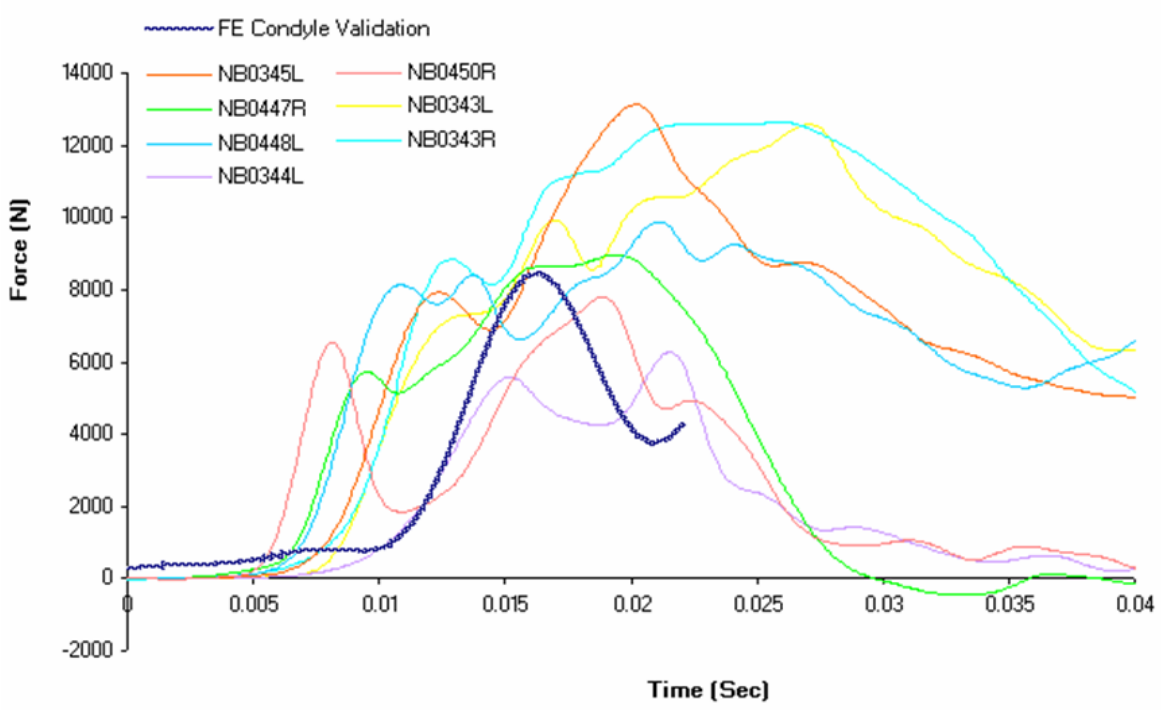

Figure 5.26. Femoral contact axial force behavior in the physical tests (dashed lines) and in the FE model simulation (dotted line) (from condyle2.k)

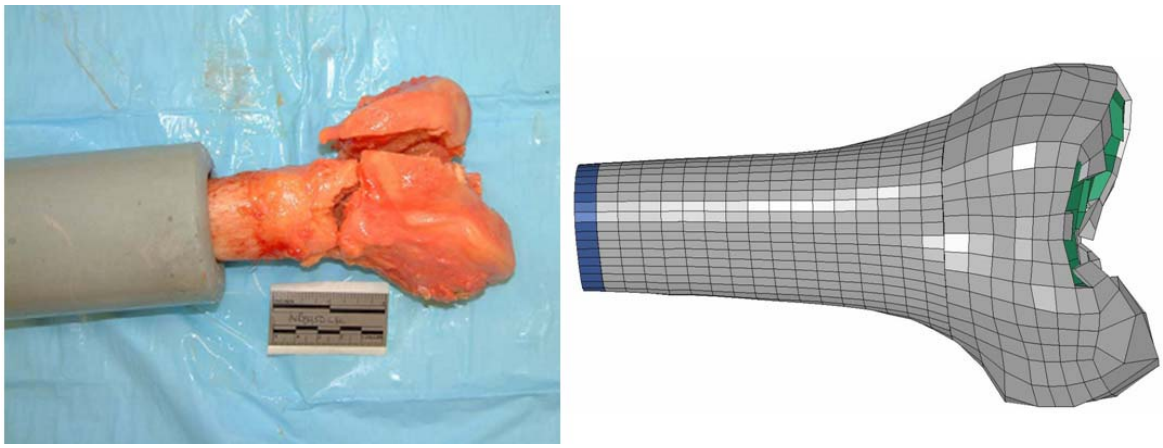

Figure 5.27. Intertrochanteric fracture mode from the femoral head validation test (left) and from the FE simulation (right) (Rupp, 2003cd

With both qualitative and quantitative simulation results comparing favorably with the tests results, the FE femoral condyle model was considered validated.

5.2. Whole Body Validation Simulation

5.2.1 Whole Sled Cadaver Test Setup

A whole cadaver test was performed by UMTRI and obtained from the NHTSA database. (Rupp, 2002) The whole-cadaver test provides a way to validate the FE simulation including all the soft tissue mass, the ligaments and the passive muscle forces as well as the bones. This test involved accelerating a cadaver seated in a driving position on a sled to a prescribed velocity of 50 km/hr into a simulated knee bolster (Figure 5.28).

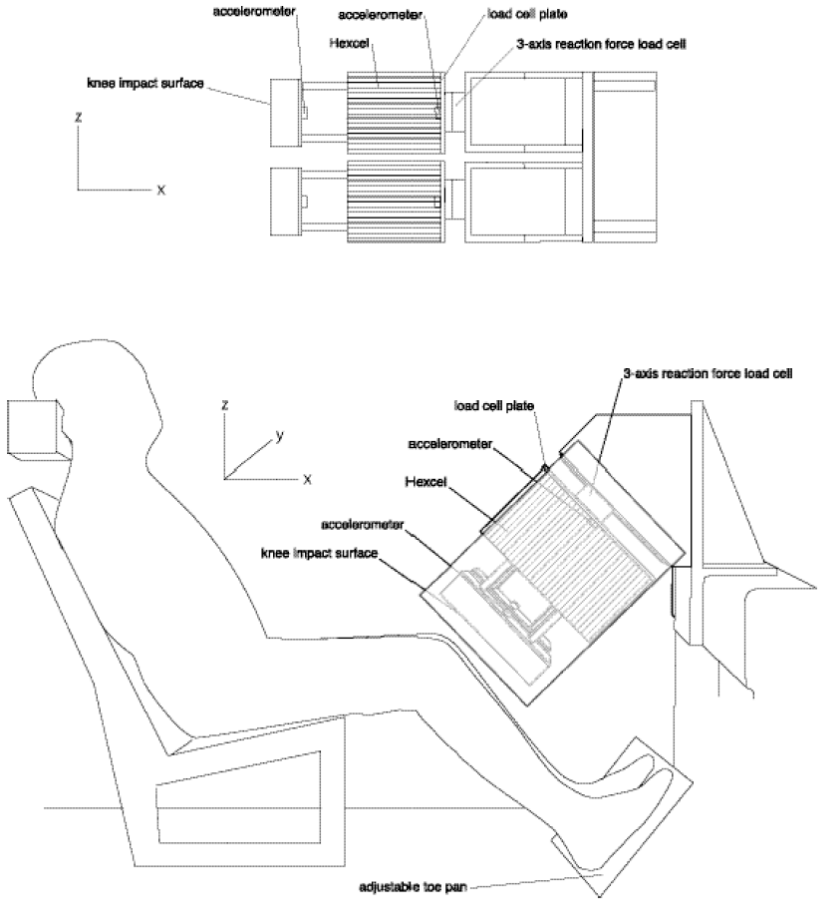

Figure 5.28. Setup of the cadaver sled test performed by UMTRI. (Rupp, 2002)

As the sled is decelerated, the lower extremities slide forward such that the knees strike the knee bolster loading the KTH. The knee bolster was made with a hex cell aluminium panel with an impact surface of floatation foam material. The thickness of the foam was 63.5 mm and the knee to bolster spacing was 38.1 mm (Figure 5.29).

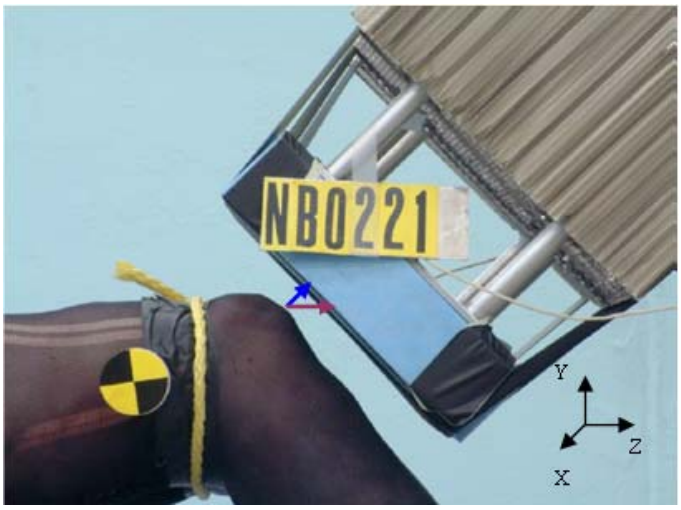

Figure 5.29. Knee bolster made of floatation foam material used in the sled cadaver test. (Rupp, 2002)

A load cell was implanted into the mid-shaft of the femur of the left side to measure the femur force in the experiments but the femur on the right side was uninstrumented (Figure 5.30).

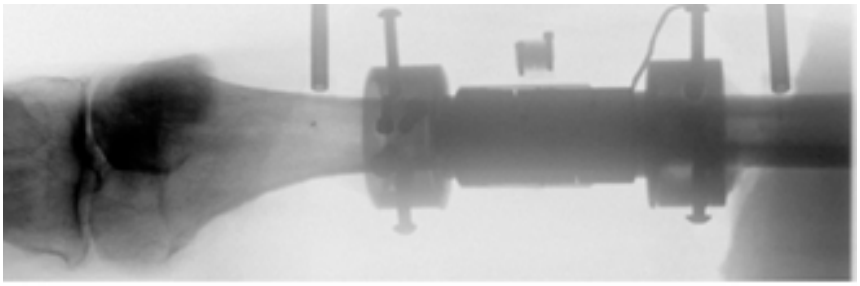

Figure 5.30. Load cell implanted into the mid-shaft of the femur of the left side of the cadaver. (Rupp, 2002)

The reactions on the left and right side of the knee bolster were also measured in the experiment.

In the UMTRI report, the initial pelvis angle was 15 degrees with respect to the femur axis, while the femur had both angles of flexion and abduction of zero degrees. The angle between the femur and tibia was approximately 135 degrees and the feet rested on an adjustable toe pan. The cadaver specimen was a 73 year old male with a mass of 100 kg and a height of 1,780 mm. Test configuration is summarized in Figure 5.31.

Test Configuration

Target force (N)	8000
Flexion angle (α, °)	0
Abduction angle (θ,°)	0
Target Sled velocity	30 mph
Target Average sled g's	18
Bolster material	2.5" blue floatation foam
Torso belt slack	6.0"
Knee-to-bolster spacing	1.5"
Initial Pelvic angle	50
Mass of knee impact plate'	1.12 kg
Mass of load cell mounting plate, Hexcel, and 1/2 load cell mass'	1.94 kg

Figure 5.31. Cadaver sled test configuration. (Rupp, 2002)

5.2.2 Whole Sled Cadaver Test Results

Results obtained from the test are summarized in Figure 5.32.

SUMMARY

Flexion angle at max force (α, °)[1]	~10	
Estimated Abduction angle at max force (θ,°)	-10 (left leg), 0 (right leg)	
Actual sled velocity (mph)	30	
Actual average sled g's	18	
Peak Knee loads (kN)	6.67 (left knee)	8.40 (right)
Peak Femur loads (kN), right leg only	6.65	
Failure mode/location	Left intertrocanteric fracture	
Impact duration (ms)	62.8 (from right femur force LC)	
Rise time (ms)	42.5 (from right femur force LC)	

Figure 5.32. Sled cadaver test results. (Rupp, 2002)

The impact test resulted in an intertrochanteric fracture of the left femur (Figure 5.33). The peak femur load was measured to be 6,650 N in the right leg, since the load cell was implanted only in this leg. Knee loads were found to be 6,670 N for the left knee and 8,400 N for the right one. The asymmetry of the knee bolster forces indicate the impact was not perfectly symmetrical, loading the right side more than the left. Interestingly, the femur with the fracture was on the more lightly loaded side. The maximum flexion angle at maximum impact force was ten degrees, while the estimated adduction angle at maximum impact force was ten degrees for the left leg and zero degree for the right one.

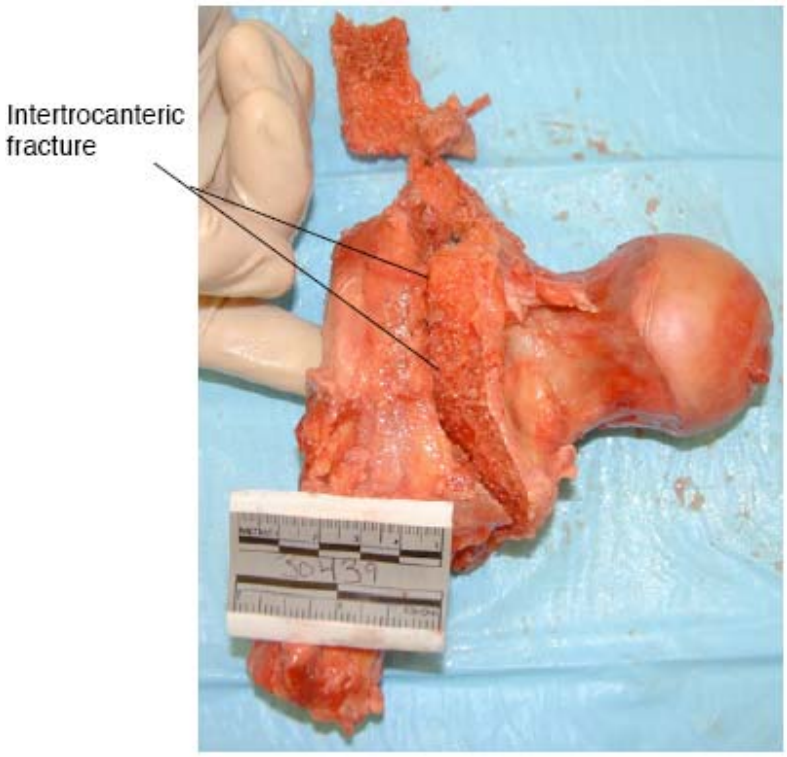

Figure 5.33. Intertrochanteric fracture of the left femur occurred in the sled cadaver test. (Rupp, 2002)

5.2.3 Whole Sled Cadaver FE Simulation Setup

The general setup for the FE simulations is shown in Figure 5.34: lateral and top views of the simulation setup are compared to lateral and top views for cadaver sled test setup. A few important uncertainties about the initial test setup required a parametric study for simulation replication.

Initial test Configuration Lateral View	Initial FE Configuration Lateral View
	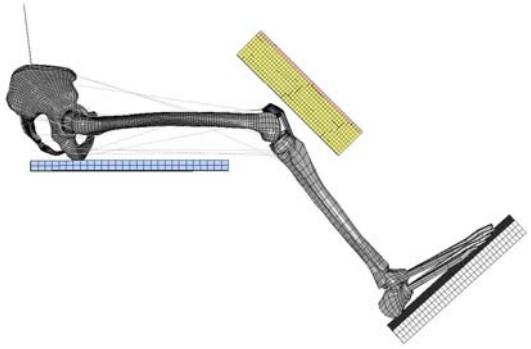
Initial test Configuration Top View	Initial FE Configuration Top View
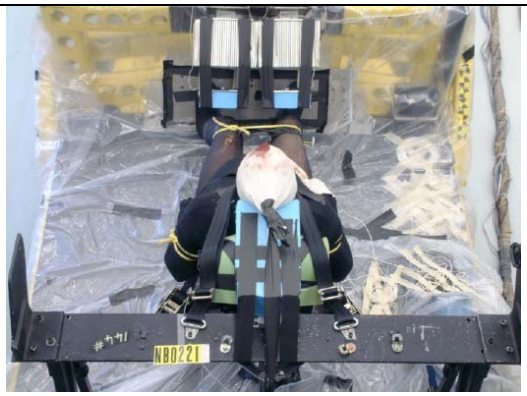	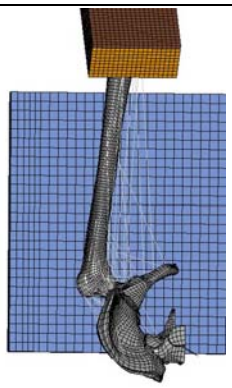

Figure 5.34. Lateral and top views of simulation setup, compared to lateral and top views of sled cadaver test setup.

Due to the uncertainties about the initial position of the cadaver in the sled test, a parametric study was necessary for simulation replication. Simulations were run, where changes were made with respect to values of five different parameters: knee-bolster spacing, femur cross-section location, initial angle for knee extension, initial angle of adduction and initial angle of thigh flexion (Figure 5.35).

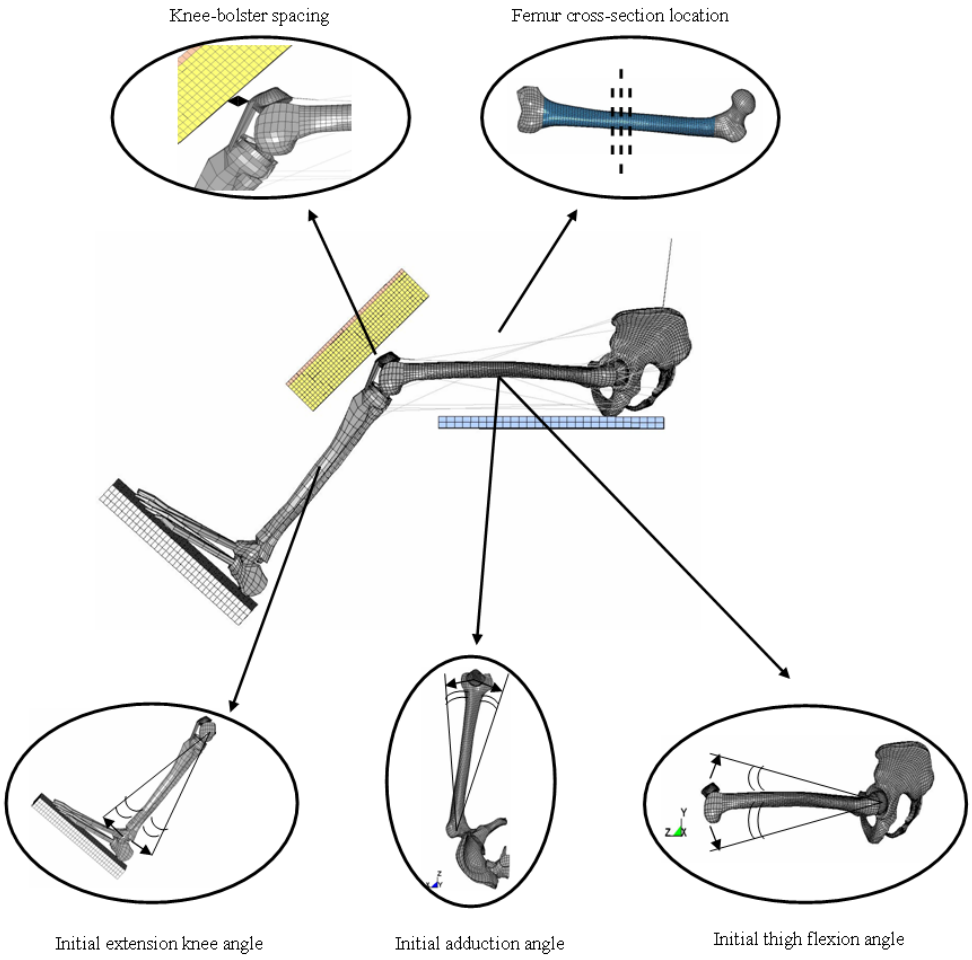

Figure 5.35. Simulation setup for the FE simulations and parameters considered for comparison.

Any eventual bone fractures and the axial force recorded in the mid-shaft femur during each simulation will be considered and compared to those obtained in the cadaver sled test. The dependence of the results on these five initial parameters will be pointed out and analyzed in the following sections.

5.2.3.1 Uncertainty About the Knee-Bolster Spacing

An FE simulation was performed using the test configuration and impact conditions used in the physical experiment. In fact, it was very hard to define the correct initial position of the cadaver. While it was reported that the knee-bolster spacing was 1.5 inches (38mm), it was not specified if this was the distance between the knee and the dashboard on z-axis or if this was the shortest distance between the cadaver and the knee-bolster (Figure 5.36).

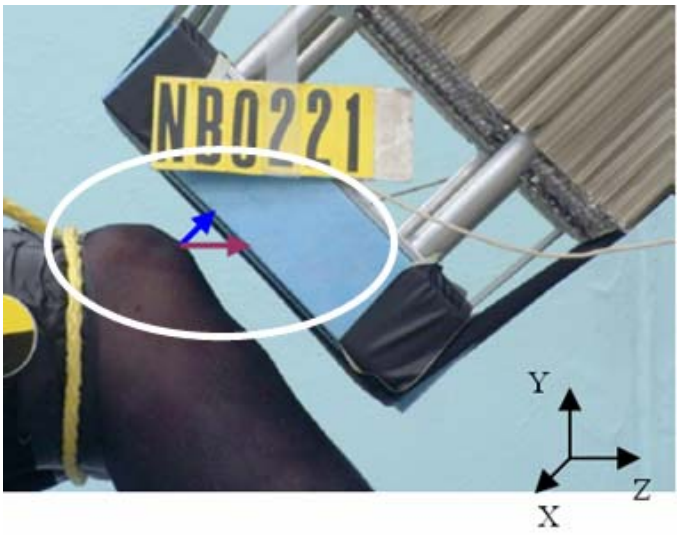

Figure 5.36. Uncertainty about the knee-bolster distance in the sled cadaver test. (Rupp, 2002)

Moreover, carefully examining the cadaver test configuration top view photograph, it can be seen that the knee to bolster spacing is different when considering the distance between the bolster and the left knee or the knee bolster and the right knee (Figure 5.37). Not to forget, in the sled test, the femur load was measured in the right leg only, while the intertrochanteric fracture occurred in the left leg.

Figure 5.37. Top view zoom of the knee to bolster spacing in the cadaver test configuration for both left and right legs. (Rupp, 2002)

Simulations were performed with different knee-bolster spacing values to verify any eventual dependence of the results on this angle value.

5.2.3.2 Uncertainty About the Exact Location of the Load Cell Implanted in the Right Femur

From the x-ray picture showing the load cell implanted in the right femur of the cadaver, the exact location of the force measurement in the mid-shaft had to be determined (Figure 5.38).

In fact, just from the picture itself, it is not possible to exactly locate the position of the load cell in the mid-shaft femur. Axial femur forces will be considered at four different mid-shaft femur cross-sections, close to each other, to be able to understand how sensitive the results are with respect to the exact location. Figure 5.38 shows the location in the FE model where local femoral axial forces started being considered for comparison with the tests results.

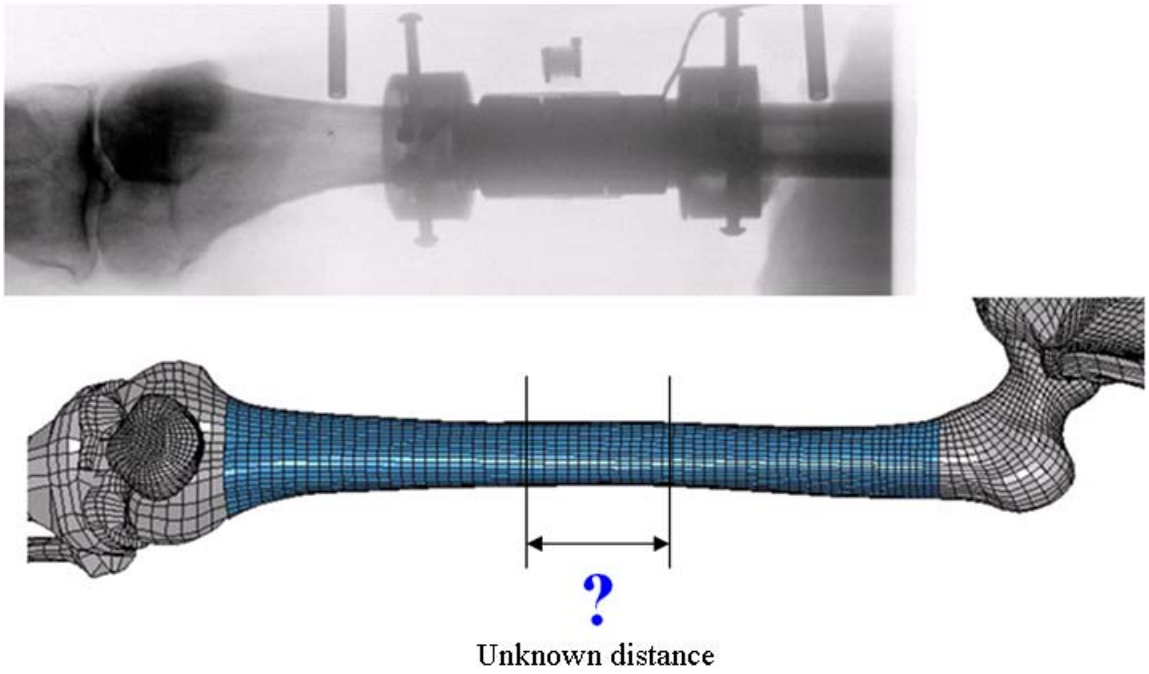

Figure 5.38. Location of the mid-shaft femur considered for record of local femoral axial force.

A database to obtain an output file containing cross section forces was defined with the LSDYNA card *DATABASE_CROSS_SECTION_SET (LSTC, 2007a). This card allows for defining a cross section for resultant forces written to ASCII file SECFORC. When the "set" option is used, a set of all nodes and sets of all types of different elements present in the cross-section must be defined. The node set defines the cross-section while the forces from the elements belonging to the element sets are summed up to form the section forces.

Since the load cell implanted in the cadaver femur gives forces in a local coordinate system, it was necessary to obtain local forces from the cross section in the mid-shaft in the FE model. For this reason, a local coordinate system was defined on the cross section, with the z' axis parallel to the axial direction of the femur (Figure 5.39).

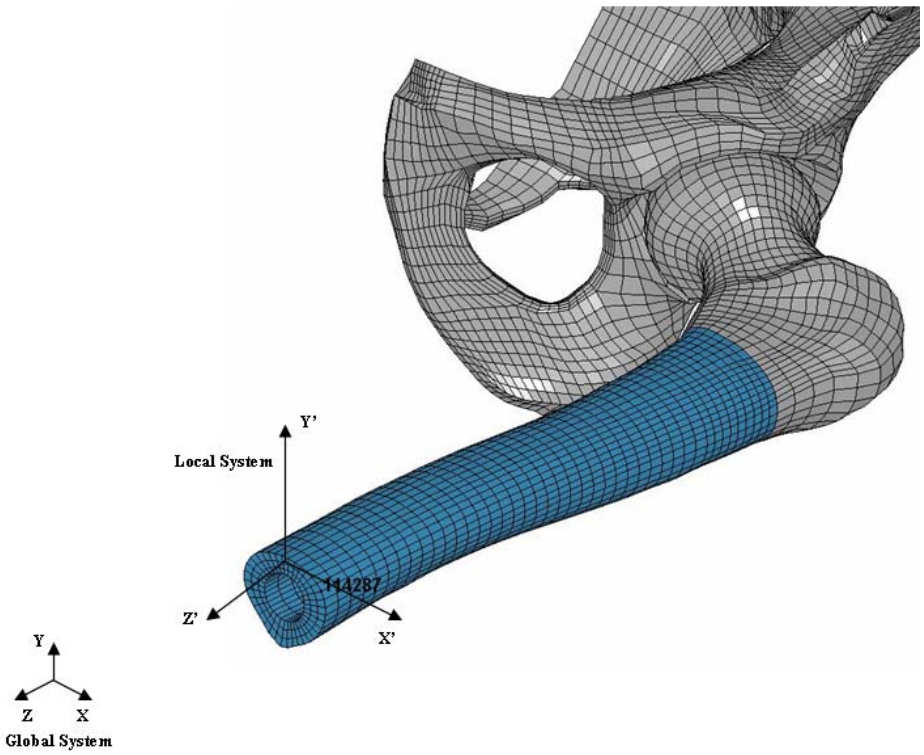

Figure 5.39. Local coordinate system used for local axial forces output from a cross-section of the femur bone.

5.2.3.3 Uncertainty About the Initial Knee Extension Angle

The value for the initial angle of knee extension was not found in the cadaver test sled report. Its value was approximated from test photographs. It is difficult, however, to define exactly the relative angle between the femur and the tibia bones mainly because the cadaver was not dissected and obviously there is flesh around bones. (Figure 5.40) It would have been of more help to have x-ray lateral views of the cadaver leg. Simulations were run with different angles of initial knee extension to verify any dependence of the results on the knee-extension angle.

Figure 5.40. Uncertainty about the initial knee extension angle in the cadaver test. (Rupp, 2002)

5.2.3.4 Uncertainty About the Initial Adduction Angle

The test report defines the initial angle of adduction to be zero degrees but it was not specified how the angle was measured and which was the range of precision for the measurement. Moreover, it was not written if the initial adduction angle was measured for either legs, just one of them, or an average of the two. Two considerations should be made at this point. First of all, looking at the pictures from the test report, it looks like the two legs did not have the same initial adduction angle. The left one seems to be more adducted than the right one. The second consideration which arises is with respect to which axis this initial adduction angle is measured. In its natural position, the femur presents an adduction angle of 12 degrees from the ideal line connecting the femoral head to the knee condyle. (Figure 5.41)

Figure 5.41. Initial adduction angle in cadaver test (left) and anatomical adduction angle for the femur bone in its natural position (right). (Rupp, 2002)

Simulations were performed with different angles of initial adduction to verify any dependence of the results on this angle value.

5.2.3.5 Uncertainty About the Initial Thigh Flexion Angle

The test report defines the initial angle of flexion to be zero degrees but it was not specified how the angle was measured and what was the range of precision for the measurement. Again, with its natural position, the femur bone presents a flexion angle of 7 degrees from the ideal line connected the femoral head to the knee condyle. Simulations were performed with different angles of initial thigh flexion to verify any dependence of the results on this angle value.

5.2.3.6 Knee-Bolster Properties Reproduction

A simple low friction-seat was implemented in the FE model. The real seat material was unknown and the soft tissue which would actually contact the seat was not represented in the FE model. Conventional steel material properties were used to model the toe pan and the plate at the back of the bolster. The steel bolster backup plate was connected to the bolster foam with a tied contact. The floatation foam was modelled with material number 57 (*MAT_LOW_DENSITY_FOAM). Input parameters for the floatation foam were obtained through physical quasi-static tests of the actual foam material used in the tests. Figure 5.42 shows the stress-strain curve of the bolster material and the input parameters used for the characterization of the material in the FE model.

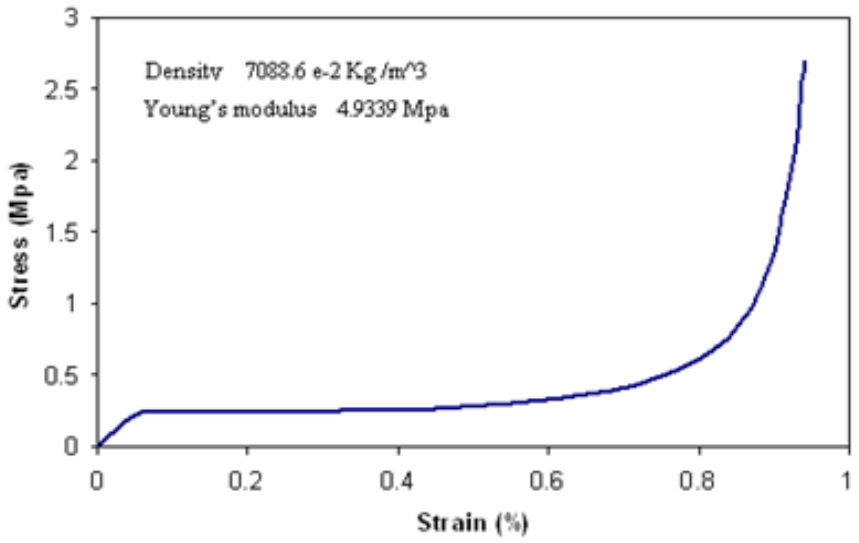

Figure 5.42. Stress-strain curve of the bolster material used in the FE model.

5.2.3.7 Replication of Boundary Conditions

Symmetrical boundary conditions were applied to the midsagital plane of the pelvis to represent this symmetry boundary condition. The foot was positioned such that it was already in contact with the toe pan at the beginning of the simulation as was the case in the test. To reproduce the upper body inertial effects, a nodal mass was positioned at the centre of gravity of the half upper part of the body and connected with shells to the pelvis. The value of the upper body nodal mass was around 25 kg (e.g., the whole upper body was assumed to have a mass of 50 kg).

In the FE simulation, all parts of the KTH and seat had an initial velocity of 13.41 m/s. A deceleration curve obtained from the physical tests was imposed on the sled to replicate exactly the deceleration experienced in the physical experiment. With the exception of the symmetry boundary condition on the pelvis, the FE model of the KTH and upper body mass were unconstrained and free to displace in response to the sled deceleration.

Different simulations were performed to analyze the sensitivity of the model to parameters like the knee-bolster spacing, the initial angle of flexion of the leg and the location of the femur mid-shaft from where requesting the cross-sectional axial forces. Results are presented and commented in the next paragraph.

5.2.4 Whole Cadaver Sled FE Simulation Results

Since a parametric study for the FE simulations was considered with respect to five different variables, results for each investigation will be reported separately in the next sections and, finally, all related in a general comment at the end.

5.2.4.1 Femur Force Sensitivity with Respect to the Knee-Bolster Distance

The knee-bolster spacing in the report was defined to be 38 mm. It was not specified which direction and moreover it was not defined which leg was considered for measurement. Consequently, from the pictures available, the distance between the right leg and the knee bolster along z-axis was scaled. The knee-bolster spacing for the right knee scaled from the photograph was21 mm. Two whole body FE simulations were then run with the same initial conditions but with a dashboard distance from the patella bone of 21 mm and 38 mm, respectively. Initial thigh flexion and adduction angles of zero degrees and knee extension angle of 45 degrees were used. The femur force behaviour was requested at the same location of the mid-shaft femur for both the simulations.

The simulation with the 21-mm dashboard distance resulted in a less stiff response than the 38-mm distance simulation. More important, at the same femur bone cross-section, the 21-mm distance curve had a maximum value of 8,000 N, while the 38-mm spacing gave a peak value of 10,287 N, more than 28 percent higher than the 21-mm spacing simulation (Figure 5.43).

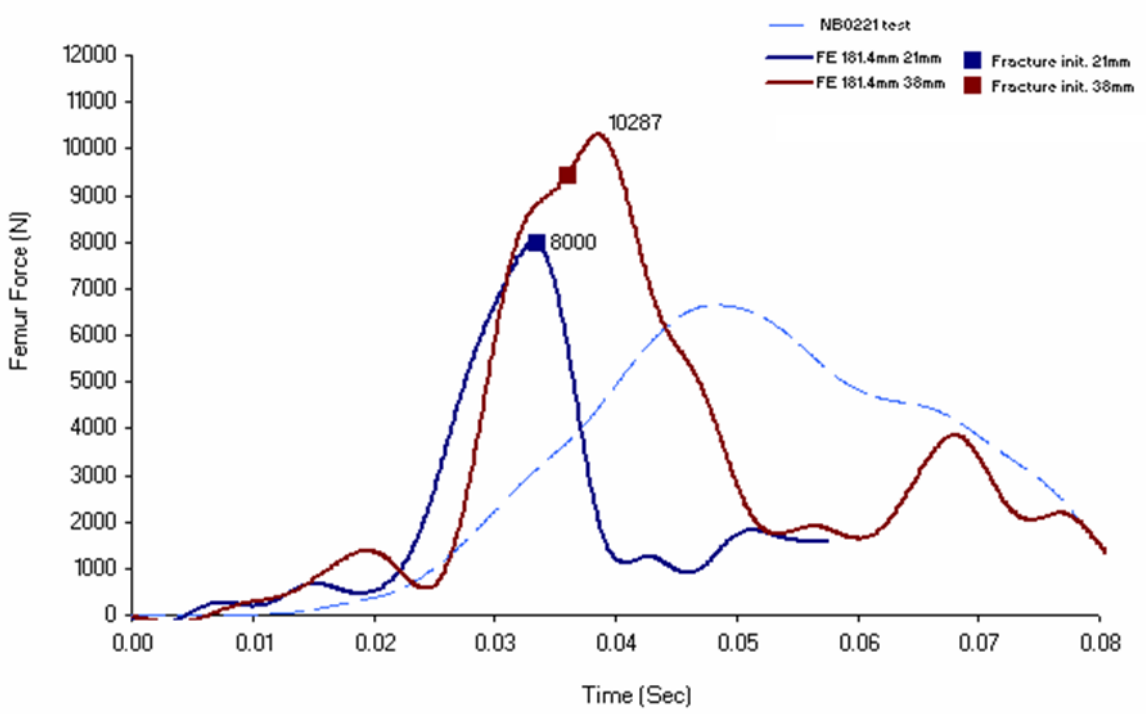

Figure 5.43. Femur force sensitivity with respect to the knee-bolster distance (21 mm and 38 mm).

The femur force from the test was recorded only in the right leg and its peak resulted in a value of 6,650 N. The errors are 20 percent and almost 55 percent for the 21-mm and the 38-mm respectively. This shows how even just a few millimetres difference in the knee-bolster spacing could make a significant difference in the femur force results. A knee-bolster only 17 millimetres closer to the patella bone dropped the error from the test result of 35 percent points.

It is interesting to note the fracture initiation femur force for both simulations: for the 38 mm simulation, it was found that bone fracture started at 9,440 N while for the 21-mm spacing, the failure initiation occurred at 7,970 N.

It is evident that lack of knowledge about the precise distance between the dashboard and cadaver knee can make the precision of the femur force uncertain.

5.2.4.2 Femur Force Sensitivity with Respect to Different Mid-Shaft Femur Cross-Section Locations

To show the sensitivity of the femur axial force results with respect to the exact location of the femur mid-shaft from where the force is registered, different mid-shaft cross-sections, were considered for measuring femur axial forces. Initial thigh flexion angle of zero degrees and knee extension angle of 45 degrees were considered. A simulation with a knee-bolster spacing of 21 mm was run. Ten cross-sections corresponding to the femur load cell location in the test were considered. Locations for these cross-sections were measured from the condyles of the knee. All femur force curves had the same general behaviour, but the peaks were different. The highest peak resulted at the cross-section closest to the knee region (location #1 at a distance of 181.4mm). Moving towards the femoral head, the femur force peak decreased. (Figure 5.44).

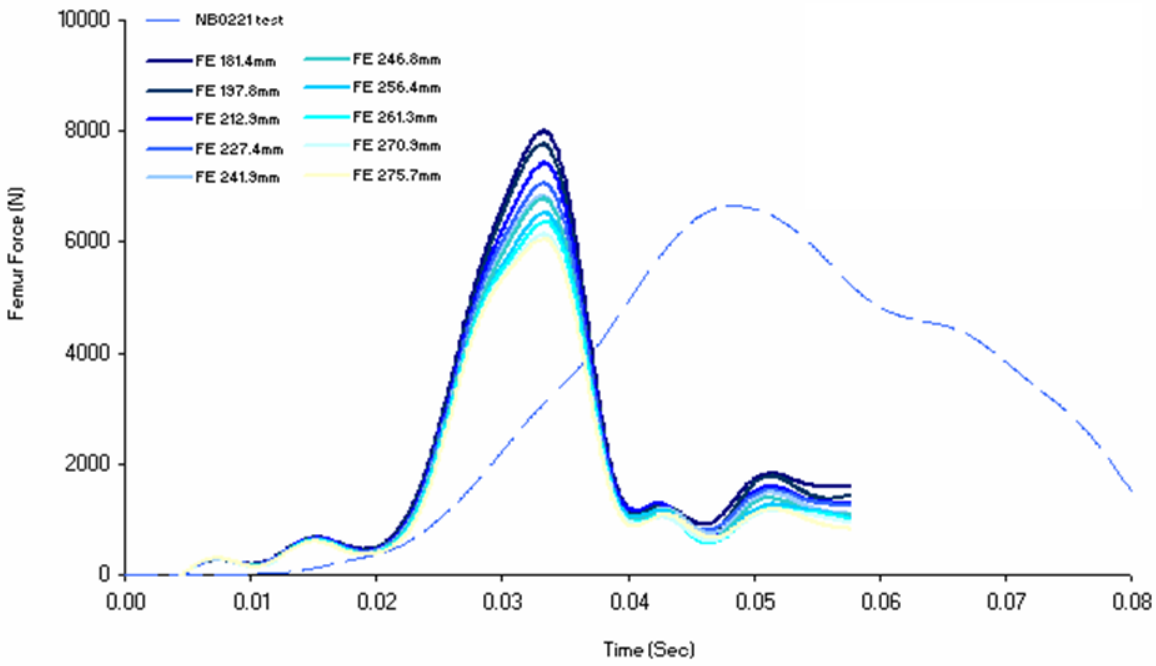

Figure 5.44. Femur force sensitivity with respect to different mid-shaft femur cross-section locations.

The femur force at location #1 was 8,000 N, while the femur force at location #10 was 6,057 N. The difference is of 1,943 N. The cross section which gave the femur force value closest to the test one was that at 256.4 mm from the knee condyle, at location #7. It resulted in a femur force of 6,529 N, corresponding to a two percent error from the value recorded in the load cell in the test. (Figure 5.45)

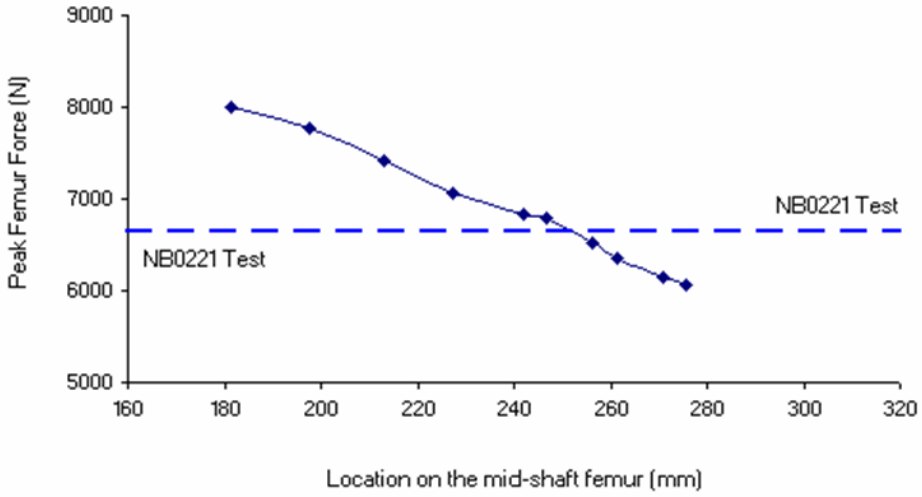

Figure 5.45. Peak femur force obtained at different mid-shaft femur cross-section locations in the FE simulation.

Considering the seventh cross-section instead of the first one for obtaining the femur force value decreased the discrepancy from the test result by 18 percent. (Figure 5.46) Location of the femur cross section where the femur force is recorded certainly influences the force results. Similar results were obtained for simulation with a knee-bolster spacing of 38 mm.

It is evident that knowledge of a more precise location of the load cell implant in the cadaver femur would help a lot in the definition of the right femur cross-section to be used for comparing simulation and test results. From now on, femur forces of next FE simulations will be recorded and compared always at the femur cross-section corresponding to location #7 (Figure 5.47). The behaviour shown in Figure 5.44 also

illustrates that even in a frontal collision crash test, the femur does not experience only axial loads. The change in femur force value with length indicates the femur is also experiencing bending stresses.

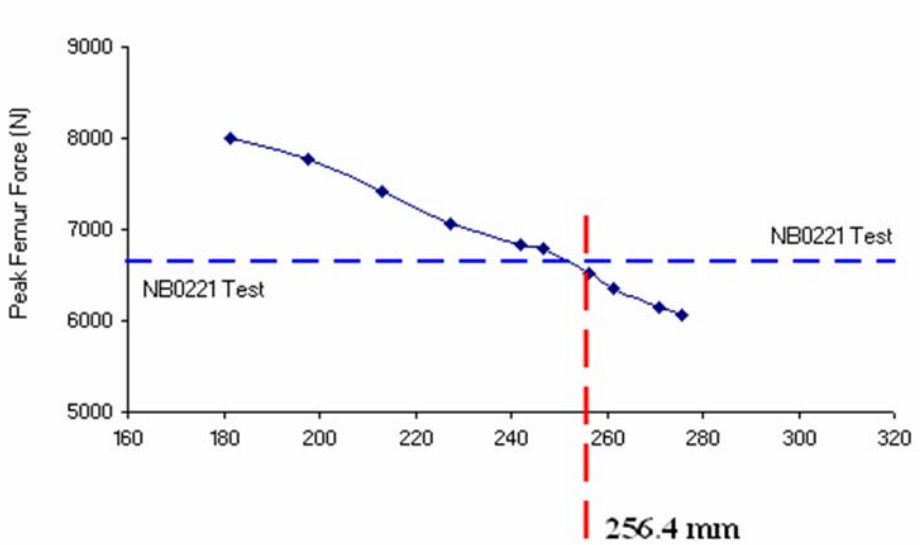

Figure 5.46. Peak femur force obtained at different mid-shaft femur cross-section locations in the FE simulation.

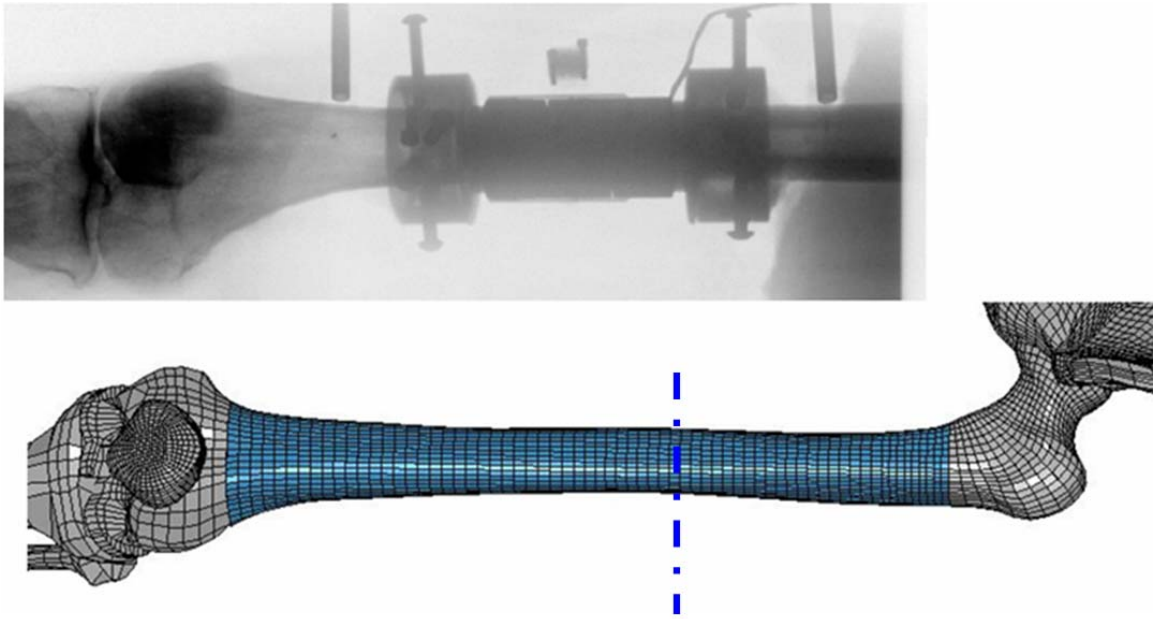

Figure 5.47. Peak femur force obtained at different mid-shaft femur cross-section locations in the FE simulation.

5.2.4.3 Femur Force Sensitivity with Respect to the Initial Knee Extension Angle

To show the sensitivity of the femur axial force results with respect to the initial knee extension angle, parametric FE simulations were run, with different values for the knee extension angle as initial position for the leg. The angle of knee extension was defined equal to zero when the axis of the tibia bone formed an angle of 90 degrees with the 0 degree-oriented thigh flexion axis. Initial knee extension angles of 40, 45, 50 and 55 degrees were used for four different simulations (with tibia bone moving clockwise).

Simulations with a knee-bolster spacing of 21 mm were performed. Initial adduction and thigh flexion angles of zero degrees were considered. The femur force behaviour was requested at the same location of the mid-shaft femur, at 256.4 mm distance from the knee condyle. All femur force curves had similar behaviours, but the peaks were different. (Figure 5.48).

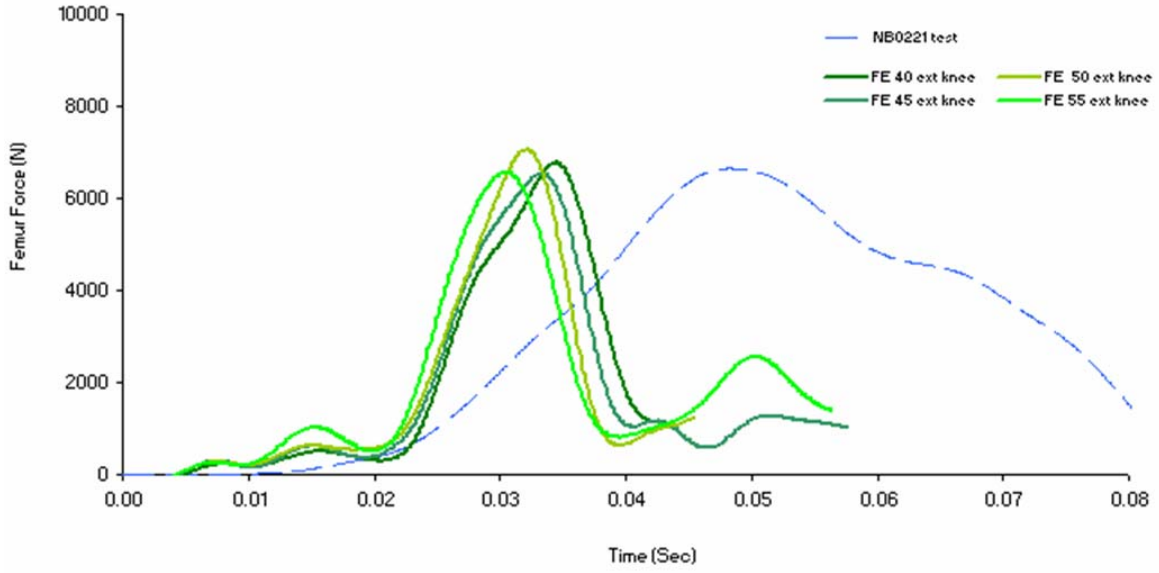

Figure 5.48. Femur force sensitivity with respect to different initial knee extension angles.

The highest femur force recorded was 7,075 N for an initial angle of knee extension of 50 degrees. The lowest value was 6,529 N for a 45 degree initial angle.

More interesting is an evaluation of the sensitivity percentages for each of these four cases: the variation from the test result drops from 6.39 percent for a 50 degree flexion angle to 1.5 percent when considering an initial knee extension of 55 degree (Figure 5.49).

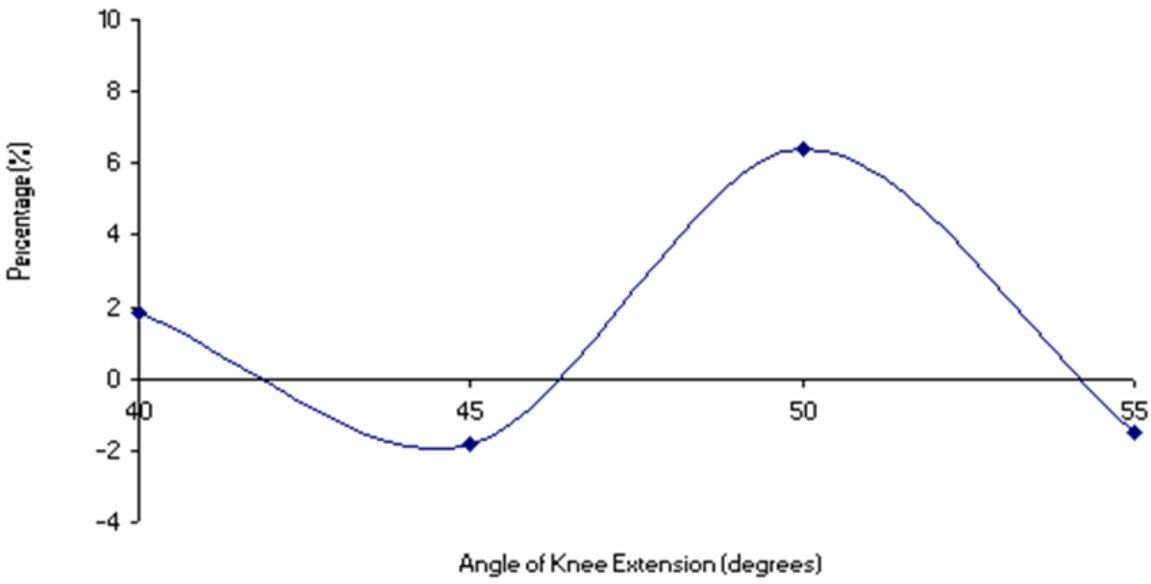

Figure 5.49. Femur force errors with respect to the test value for different initial knee extension angles.

Similar results were obtained for simulation with a knee-bolster spacing of 38 mm. Knowledge of the precise initial cadaver position would help for reproducing the same results with finite element simulations.

Figure 5.50 shows the femur force fracture initiation sensitivity with respect to the initial thigh flexion angle of the femur bone. It is interesting to note that the femur fracture initiation force was found to be 7,040 N for an angle of 50 degree knee extension and dropped to 6,510 N for a 45 degree angle, with a major gap of more than 7 percent among the four cases considered.

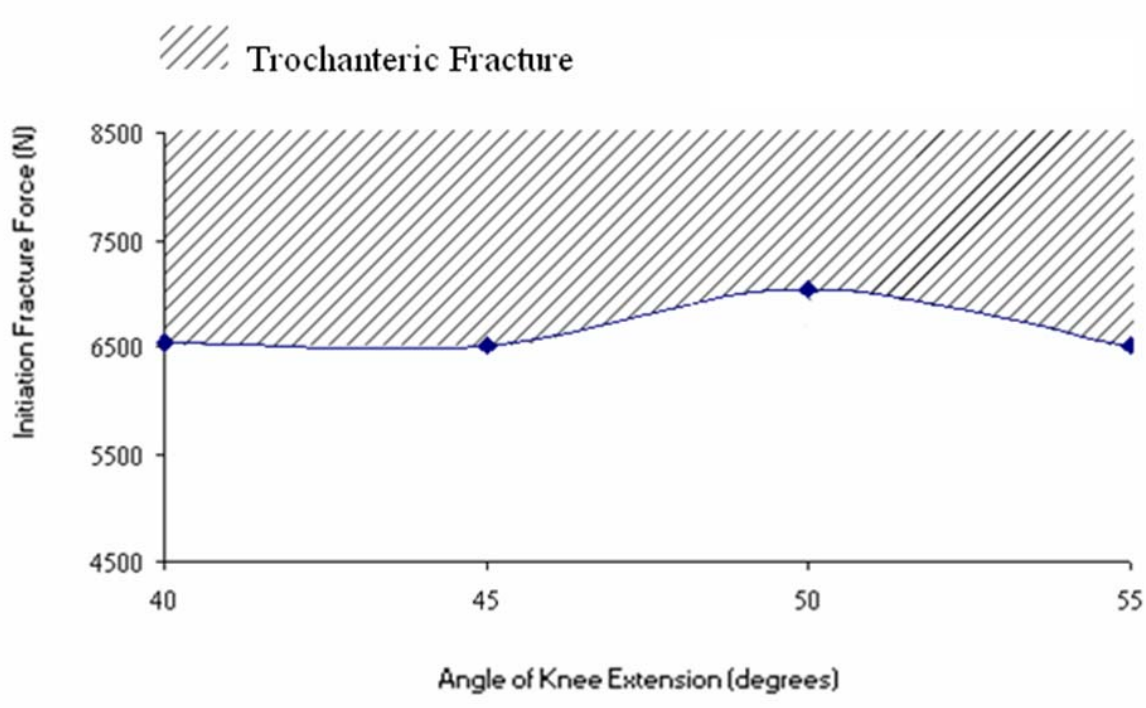

Figure 5.50. Fracture initiation comparison for different angles of knee extension.

A trochanteric fracture of the femur was observed in all these simulation cases. No fractures were observed for the pelvis bone or the condyles (Table 5.1).

Table 5.1. FE femur fracture mechanism for different initial knee extension angles.

40 deg.	45 deg.	50 deg.	55 deg.
Trochanters	Trochanters	Trochanters	Trochanters
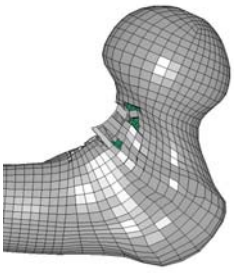	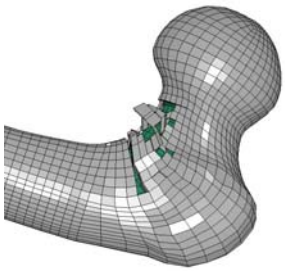	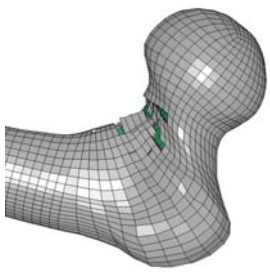	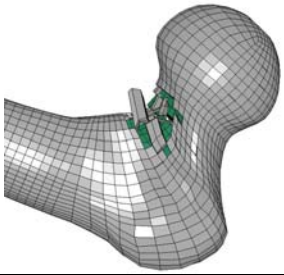

Kuppa et al. presented an injury criteria associated with various lower extremity injuries and reported calculation for the probability of knee-thigh-hip injuries as a function of applied femur force (Kuppa, 2001):

$$p(AIS \cdot 2+) = \frac{1}{1 + e^{5.7949 - 0.5196 \cdot F}} \tag{5.1}$$

$$p(AIS \cdot 3+) = \frac{1}{1 + e^{4.9795 - 0.326 \cdot F}} \tag{5.2}$$

where the variable F represents the femur axial force in kN.

The probabilities of AIS 2+ and AIS 3+ were calculated in using the injury criteria proposed by Kuppa (Table 5.2). For the FE simulations, AIS 2+ and 3+ results were investigated according to the different angles of initial knee extension (Figures 5.51 and 5.52).

Table 5.2. Femur force sensitivity with respect to different initial knee extension angles.

Knee Ext (degrees)	Peak force (N)	AIS2+	AIS3+
40	6.774	0.0932	0.0589
45	6.529	0.0830	0.0546
50	7.075	0.1073	0.0646
55	6.55	0.0838	0.0550

According to this analysis, a femur axial force of 6,774 N for an initial knee extension angle of 40 degrees is associated to a 9.32% probability of AIS 2+ and to a 5.89% probability of AIS 3+ knee-thigh-hip injury.

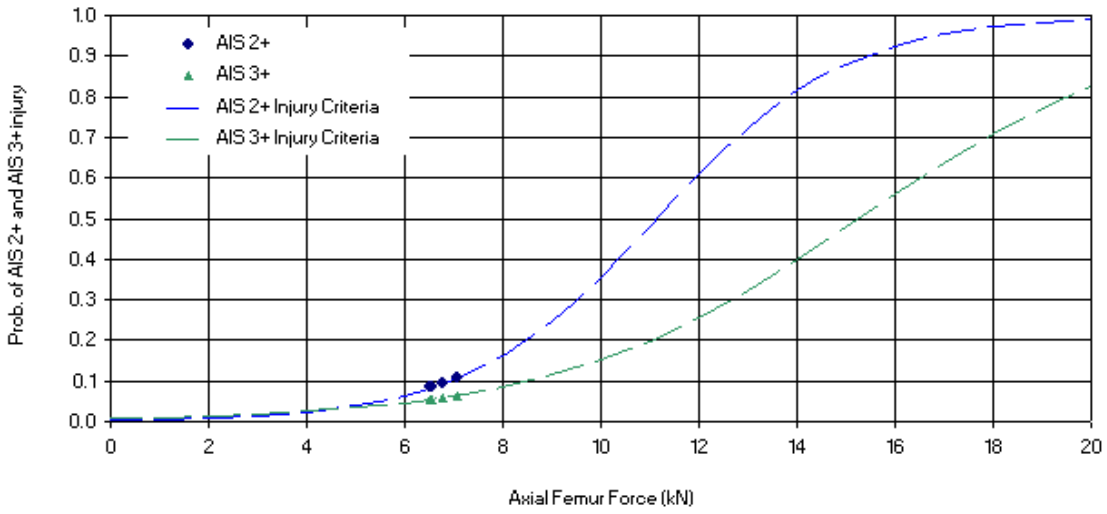

Figure 5.51. Probability of AIS 2+ and AIS 3+ knee-thigh-hip injuries for different angles of knee extension.

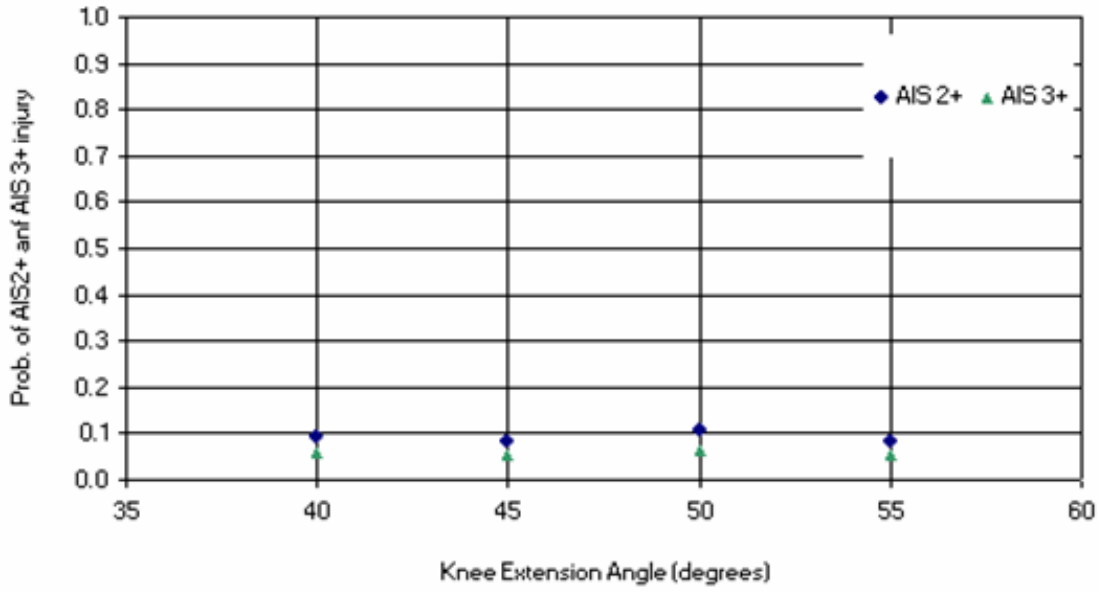

Figure 5.52. Probability of AIS 2+ and AIS 3+ knee-thigh-hip injuries for different angles of knee extension.

5.2.4.4 Femur Force Sensitivity with Respect to the Initial Adduction Angle

To show the sensitivity of the femur axial force results with respect to the initial adduction angle, parametric FE simulations were performed with different values for the initial adduction angle. Initial knee extension angles of -5, -2, 0, +2 and +5 degrees were used for four different simulations with the femur moving clockwise with the plus sign.

Simulations with a knee-bolster spacing of 21 mm were performed. An initial thigh flexion angle of zero degrees and knee extension angle of 45 degrees were considered. The femur force behaviour was collected at the same location of the mid-shaft femur as in the previous simulations (i.e., 256.4 mm distance from the knee condyle). All femur force curves had similar behaviour, but the peaks were different. (Figure 5.53).

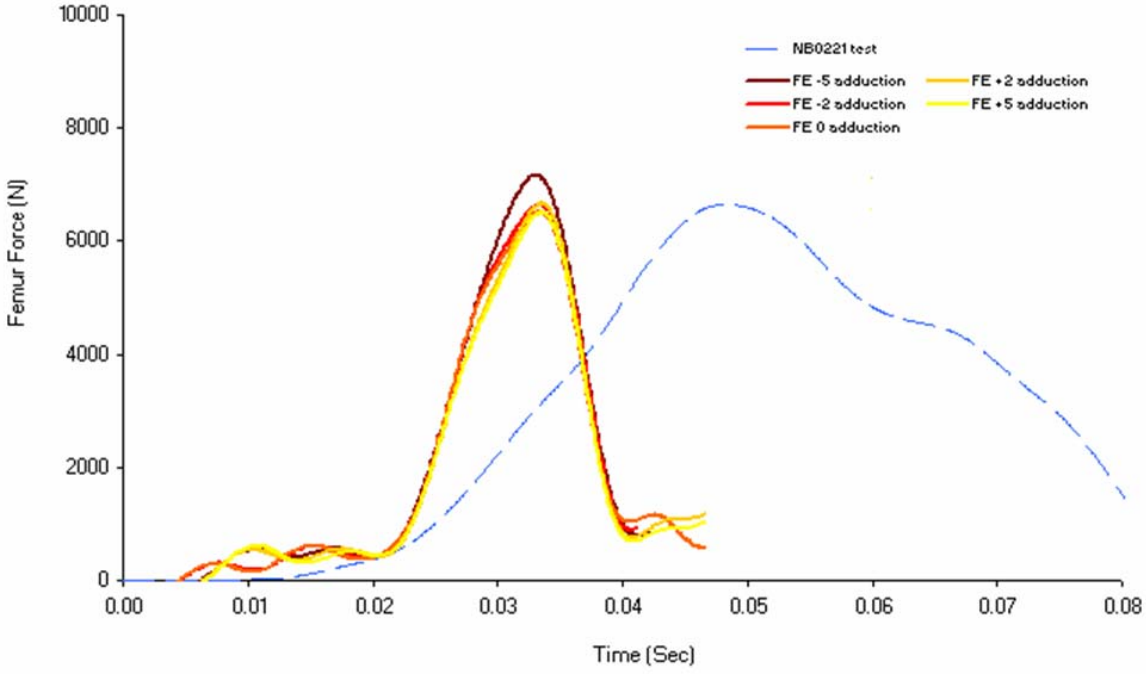

Figure 5.53. Femur force sensitivity with respect to different initial adduction angles.

The highest femur force recorded was 7,162 N for an initial angle of adduction of -5 degrees. The lowest value was 6,514 N for a +5 initial angle. More interesting is an

evaluation of the variance percentages for each of these five cases: the variance from the test result drops from 7.7 percent for a -5 degree adduction angle to 0.12 percent when considering an initial adduction of -2 degrees (Figure 5.54).

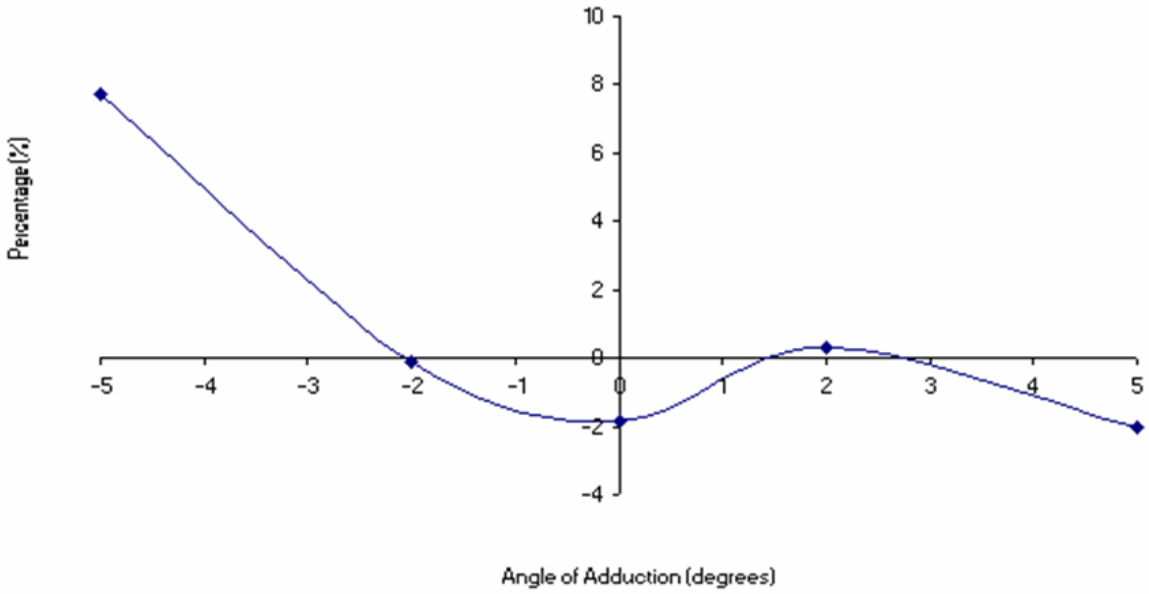

Figure 5.54. Femur force errors with respect to the test value for different initial adduction angles.

Similar results were obtained for simulations with a knee-bolster spacing of 38 mm. Also in this case, knowledge of the precise cadaver position is essential for reproducing the same results with finite element simulations.

Figure 5.55 shows the initiation fracture femur force sensitivity with respect to the initial thigh flexion angle of the femur bone. It is interesting to note that the femur fracture initiation force was 6,560 N for an angle of -2 degrees of adduction and dropped to 5,260 N for a -5 degrees of adduction, with a change of more than 20 percent among the five cases considered.

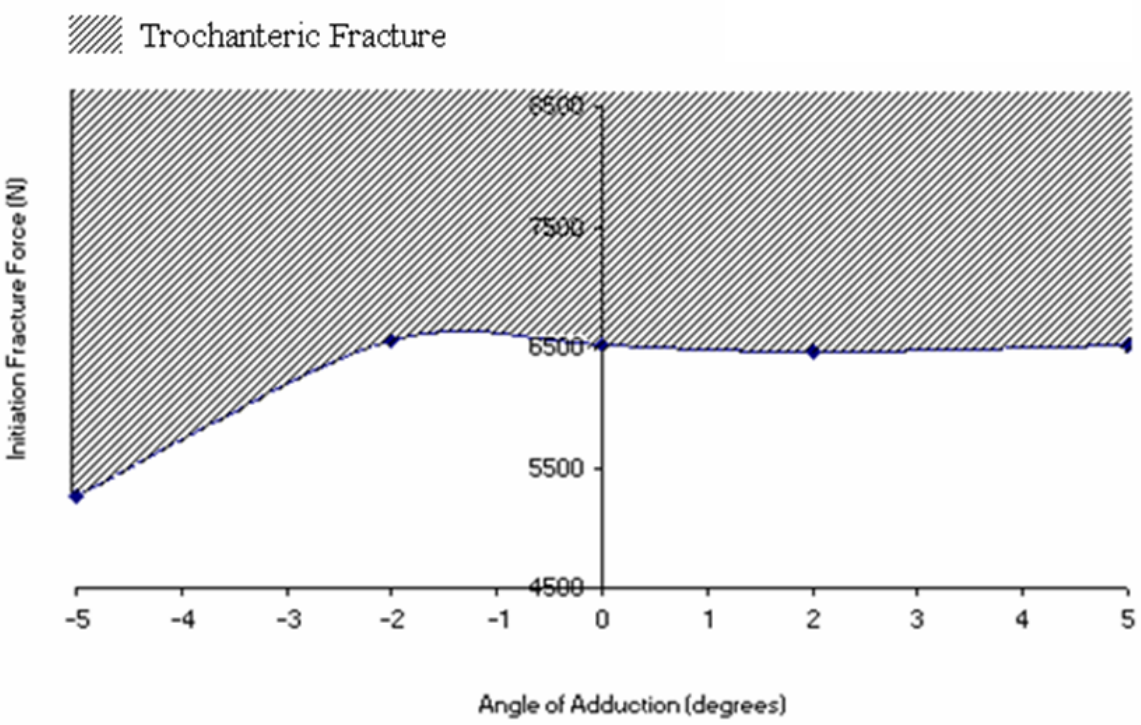

Figure 5.55. Fracture initiation comparison for different angles of adduction.

A trochanteric fracture of the femur was observed in all these cases (Table 5.3). Fractures in the front and in the back of the acetabular cup external walls and an initial failure of the iliac wing were experienced only in the +5 degree adduction case.

Table 5.3. FE femur fracture mechanism for different initial adduction angles.

-5 deg.	**-2 deg.**	**0 deg.**	**+2 deg.**	**+5 deg.**
Trochanters	Trochanters	Trochanters	Trochanters	Trochanters
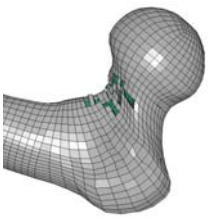	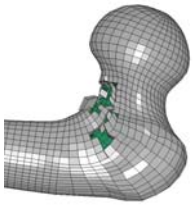	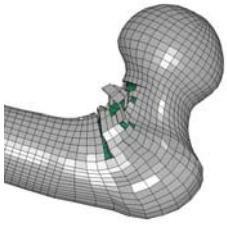	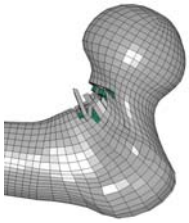	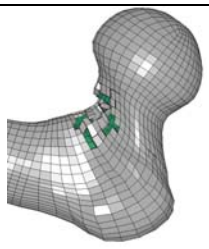

Values of AIS 2+ and AIS 3+ were calculated with the use of this injury criteria proposed by Kuppa (Table 5.4). For the FE simulations, AIS 2+ and 3+ results were investigated according to the different angles of initial adduction (Figures 5-56 and 5-57).

Table 5.4. Femur force sensitivity with respect to different initial knee extension angles.

Adduction (degrees)	Peak force (N)	AIS2+	AIS3+
-5	7.162	0.1117	0.0663
-2	6.642	0.0876	0.0566
0	6.529	0.0830	0.0546
2	6.672	0.0888	0.0571
5	6.514	0.0824	0.0544

According to this analysis, a femur axial force of 7162 N for an initial adduction angle of -5 degrees is associated to a 10.1% probability of AIS 2+ and to a 6.63% probability of AIS 3+ knee-thigh-hip injury.

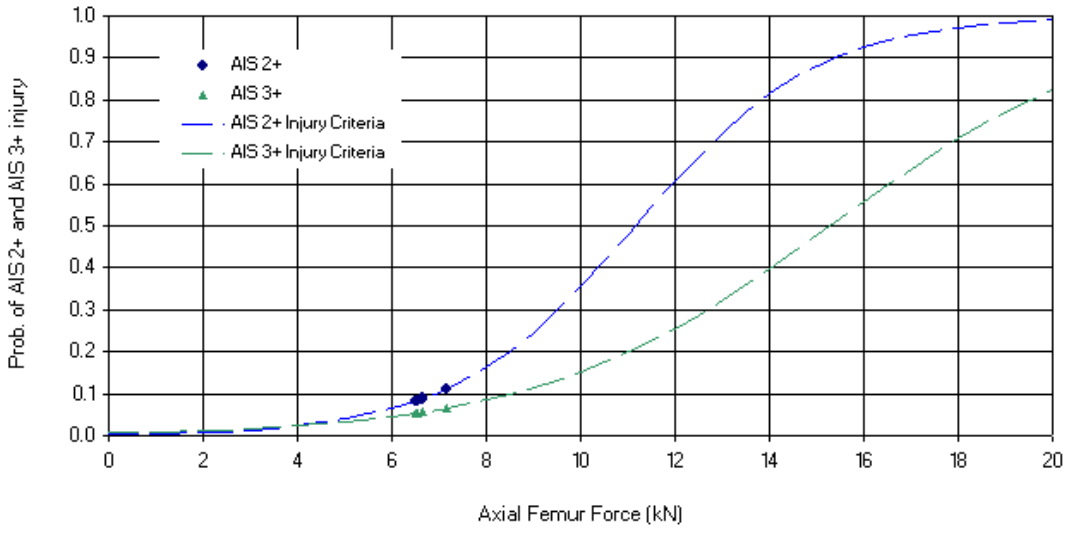

Figure 5.56. Probability of AIS 2+ and AIS 3+ knee-thigh-hip injuries for different angles of adduction.

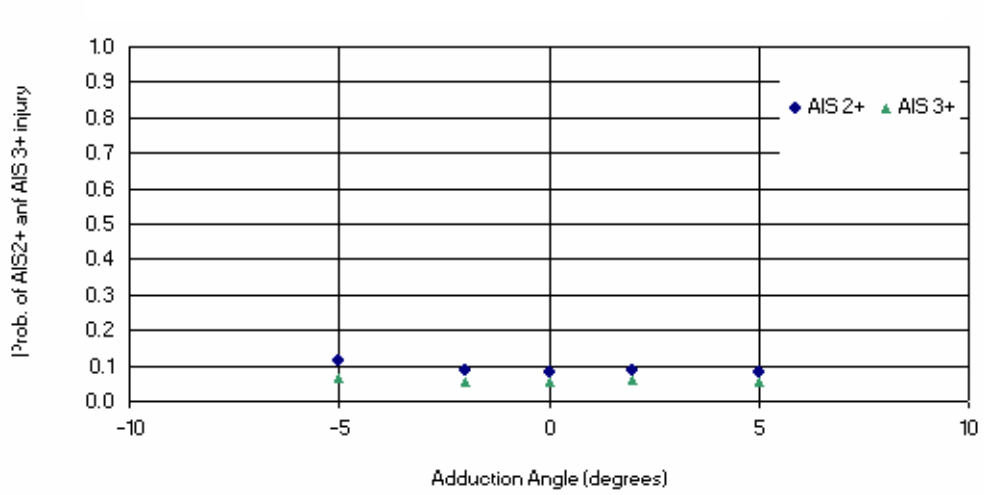

Figure 5.57. Probability of AIS 2+ and AIS 3+ knee-thigh-hip injuries for different angles of adduction.

5.2.4.5 Femur Force Sensitivity with Respect to the Initial Thigh Flexion Angle

To show the sensitivity of the femur axial force results with respect to the initial thigh flexion angle, parametric FE simulations were performed, with different values for the initial thigh flexion angle. The angle of thigh flexion was defined equal to zero when the femur axis was aligned to the z-axis. Initial thigh flexion angles of zero, minus five, minus two, plus two and plus five degrees were used for five different simulations (i.e., the femur moving counter clockwise with the minus sign and clockwise with the plus sign). Simulations with a knee-bolster spacing of 21 mm were performed. Initial adduction angle of zero degrees and initial knee extension angle of 45 degrees were used. The femur force behaviour was collected at the same location of the mid-shaft femur as in the previous simulations (i.e., 256.4 mm distance from the knee condyle). All femur force curves had similar behaviour, but the peaks were different. (Figure 5.58).

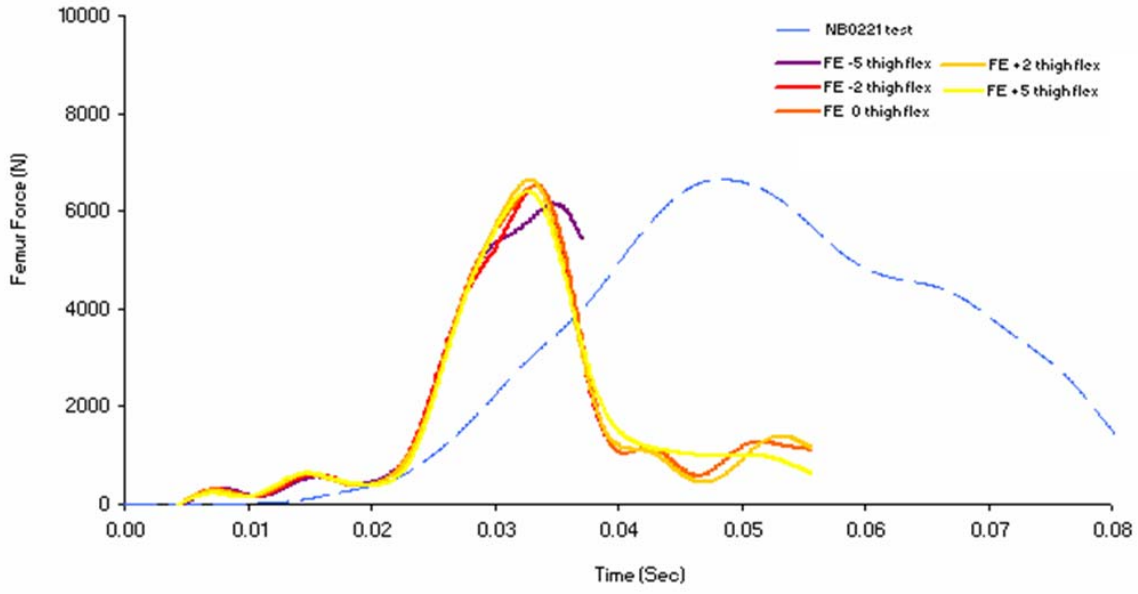

Figure 5.58. Comparison of local femur force for different angles of thigh flexion and a 21-mm distance bolster impact simulation.

The highest femur force recorded was 6,632 N for an initial angle of thigh flexion of +2 degrees. The lowest value was 6,144 N for a -5 initial angle. More interesting is an

evaluation of the variation percentages for each of these five cases: the variation from the test result drops from 7.62 percent for a -5 degrees flexion angle to 0.27 percent when considering an initial thigh flexion of +2 degrees (Figure 5.59).

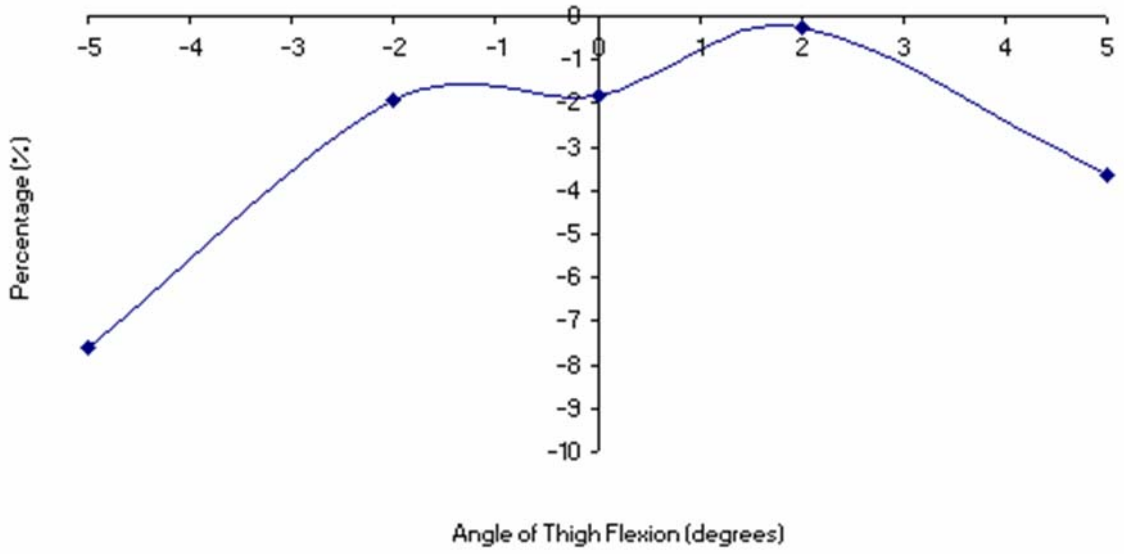

Figure 5.59. Femur force errors with respect to the test value for different initial thigh flexion angles.

Similar results were obtained for simulation with a knee-bolster spacing of 38 mm. Also in this case, knowledge of the precise cadaver position is essential for reproducing the same results with finite element simulations.

Figure 5.60 shows the femur fracture initiation force sensitivity with respect to the initial thigh flexion angle of the femur. The fracture initiation femur force was found to be 6,510 N for an angle of 0 degrees thigh flexion and dropped to 5,660 N for a +2 degrees angle, a change of more than 13 percent among the five cases considered.

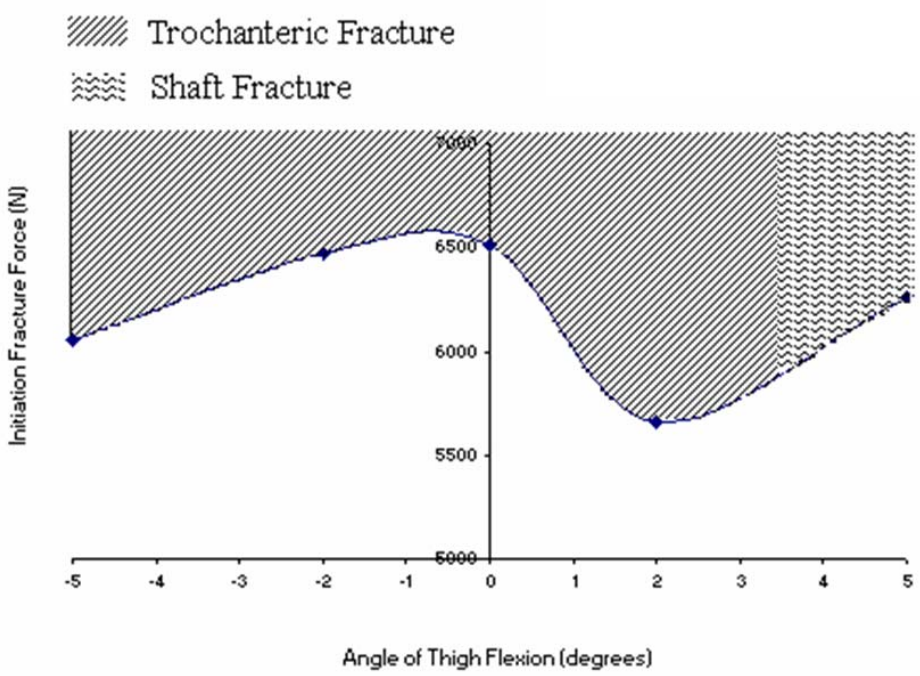

Figure 5.60. Fracture initiation comparison for different angles of thigh flexion.

Trochanteric fractures of the femur occurred in all but two of the five simulations. The femoral head fractured in the -2 degree thigh flexion case and the shaft of the femur fractured in the +5 degree thigh flexion case. No fractures were observed for the pelvis bone or the condyle (Table 5.5).

Table 5.5. FE femur fracture mechanisms for different initial thigh flexion angles.

-5 deg.	**-2 deg.**	**0 deg.**	**+2 deg.**	**+5 deg.**
Trochanters	Femoral Head	Trochanters	Trochanters	Shaft
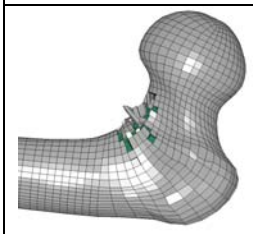	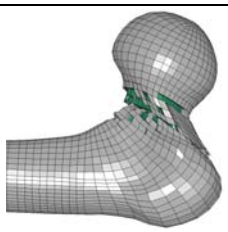	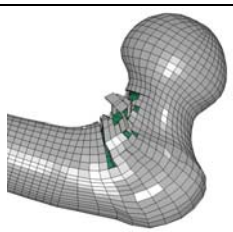	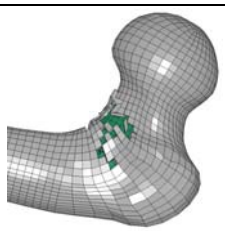	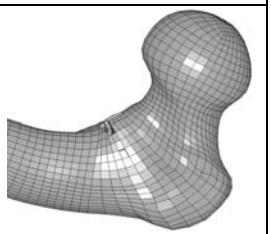

Values of AIS 2+ and AIS 3+ probabilities were calculated using the injury criteria proposed by Kuppa (Table 5.6). For the FE simulations, AIS 2+ and 3+ results were investigated according to the different angles of initial thigh flexion (Figures 5.61 and 5.62).

Table 5.6. Femur force sensitivity with respect to different initial thigh flexion angles.

Flexion (degrees)	Peak force (N)	AIS2+	AIS3+
-5	6.144	0.0690	0.0485
-2	6.521	0.0827	0.0545
0	6.529	0.0830	0.0546
2	6.632	0.0872	0.0564
5	6.406	0.0783	0.0526

According to this analysis, a femur axial force of 6144 N for an initial thigh flexion angle of -5 degrees is associated to a 6.90% probability of AIS 2+ and a 4.85% probability of AIS 3+ knee-thigh-hip injury in the general population.

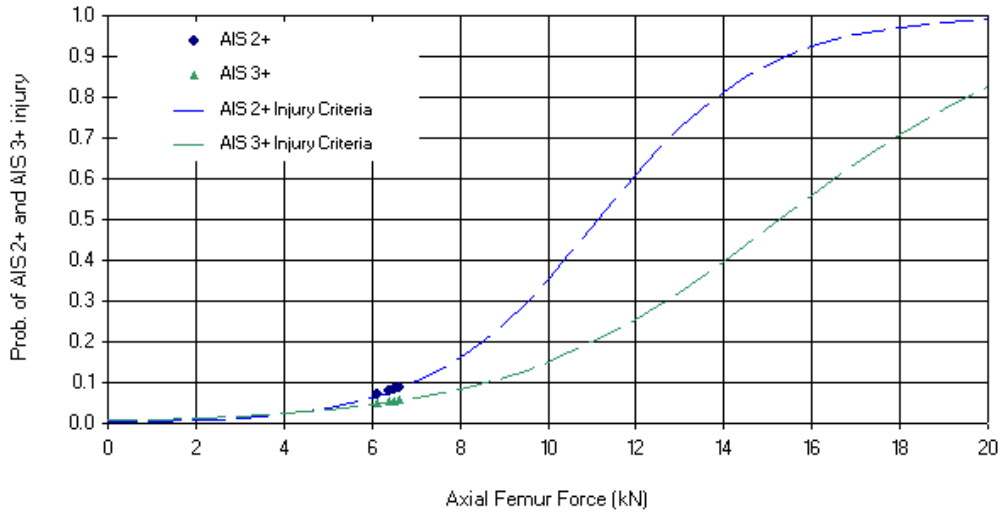

Figure 5.61. Probability of AIS 2+ and AIS 3+ knee-thigh-hip injuries for different angles of thigh flexion.

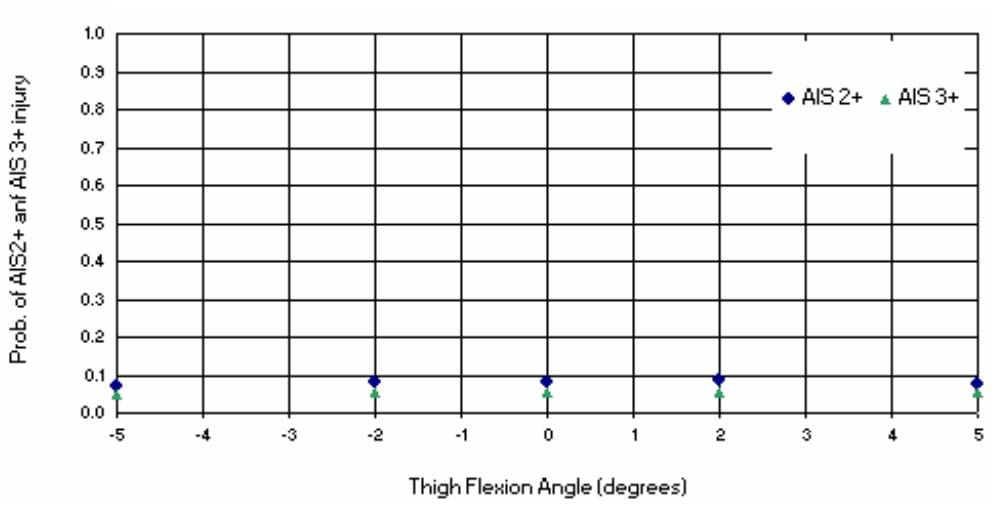

Figure 5.62. Probability of AIS 2+ and AIS 3+ knee-thigh-hip injuries for different angles of thigh flexion.

5.3. Conclusions about Model Validation

Peak forces obtained from the three FE simulations for validations of the bone material (i.e., pelvis, femoral head and femoral condyles validation simulations) always resulted in the corridors obtained from the specimen cadaver tests. Also, the shape of these force time-histories resembled those recorded in the tests. Moreover, in all cases, the main fracture mechanism of bones observed in the tests was replicated by FE simulations. The bone materials and meshes were, therefore, considered validated.

A few considerations, however, must be reported. The FE simulations for the pelvis and the femoral head validation resulted in a contact hip force and in a cup femoral head contact force behavior which are very close to the lower bounds of the pelvis and femoral head tests corridors, respectively. On the other hand, the femoral contact force obtained from the FE simulation for the condyles validation resulted to be closer in value to the highest forces recorded in the cadaveric tests. It is also true that the exact location of the femur load cell used for recording the force in the cadaveric tests was not reported. As consequence, in the FE condyle validation simulation, the position on the femur shaft chosen for obtaining the femur force might have been only an approximation of the real test location. Overall, the FE bone models seem to correctly reproduce the results obtained by the cadaveric test and can be considered validated and ready for use with muscle, ligaments and soft tissue replication for a complete validation.

When analysing the results obtained from the whole-body finite element model simulation, three main considerations have to be taken into account:

- There was a lot of uncertainty about the initial position of the cadaver during the test;
- It was difficult to replicate in the FE model simulations the real boundary conditions of the test;
- In the simulation, the effect of soft tissue on the pre-impact dynamics was missing (being the tissue modelled only as nodal masses, not as three-dimensional entity)

In fact, it was very hard to define the correct initial position of the cadaver: uncertainties about the knee bolster spacing, the exact location for recording the femur force, the initial angles of knee-extension, adduction and thigh flexion resulted in playing a considerable role in defining the peak femur force value. Simulations were run to analyze the sensitivity of the model with respect to these parameters.

As results, the force from the 21-mm dashboard distance had a maximum value of 8,717 N, the 38-mm distance give a maximum value of 9,548 N, 8.7 percent higher than the 21-mm distance one. A knee-bolster of only 17 millimetres closer to the patella bone helped dropping the error from the test result of 13 percent.

In both cases, femur force peaks resulted to be at the cross-section closer to the knee region. Moving towards the femoral head, the femur peak force decreased and dropped the error from the test result.

When fixed the knee bolster spacing and the cross-section for the femur force acquisition, the force results happened to be influenced by the initial angles of knee-extension, thigh flexion and adduction. The error from the test results dropped from 6.39 percent for an initial angle of knee extension of 50 degrees, to 1.5 percent for 55 degrees. Similarly, considering an initial adduction angle of -2 degrees instead of -5 degrees helped lower the error from the test peak force from 7.7 to 0.12 percent. Also, an initial angle of thigh flexion of -5 degrees resulted in an error from the test peak force value of the 7.62 percent: however, changing this initial angle to +2 degrees dropped the error to 0.27 percent.

When looking at these results, it would seem that the initial position and setup which closer reproduce the results observed in the whole-body NHTSA test would consider a knee-bolster distance of 21 mm, a position in the femur bone for recording the force located 256.4 mm from the extremity of the knee condyles; in addition, this configuration should take into account an initial position of the KTH of 55 degree angle for knee-extension, -2 degree angle for adduction, and +2 angle for thigh flexion. However, it is not proved that a combination for all these parameters would perform linearly, that is, it

would be necessary to run simulations with different combinations of these initial angles to compare the final results according to these initial "mixed" positions.
These parametric runs showed that a not correct knowledge or replication of the initial position of the cadaver leg can result in a femur force peak value quite different from the one obtained in the test.

Difficulties in reproducing the correct boundary conditions of the test can also be another reason to explain the difference of force results obtained with simulations and the test. In the simulations, the upper part of the body was considered only as a lumped mass of 25 kg connected to the pelvis bone. This certainly helps considering body inertial effects, but does not allow reproduction of the right dynamics and interaction of the different body parts. Also, the midsagital plane of the pelvis was considered to be a plane of symmetry and boundary conditions were applied to its nodes not to move in the perpendicular direction with respect to the plane. In fact, at the end of the test, the cadaver resulted to fall on the ground, showing that there was not movement symmetry with respect to the pelvis midsagital plane. Moreover, in the test, the cadaver was sustained and somehow maintained in a sitting position with the help of a seat belt and bindings. In the simulation, seat belt was not modeled, leaving the body free to displace in response to the sled deceleration.

In the simulation, the tissue was modelled as nodal masses, without three-dimensional reproduction of it, and this did not allow replicating the effect of soft tissue on the pre-impact dynamics. The soft tissue, basically, contributed only for its weight to the inertial dynamic results, but did not permit to replicate the wrapping and holding of all the flesh, muscles, ligaments and bone, as in real life (Figure 5.63). It is of a certain interest to note that the peak and particularly the behaviour of the femur force obtained by this FE whole body simulation perfectly fits in the corridor obtained by the recorded contact femur forces from the specimen cadaveric tests. This could evaluate the consideration that the femur force behaviour in this FE whole-body simulation is greatly influenced by the non-correct reproduction of the boundary conditions and by the lack of flesh modelling.

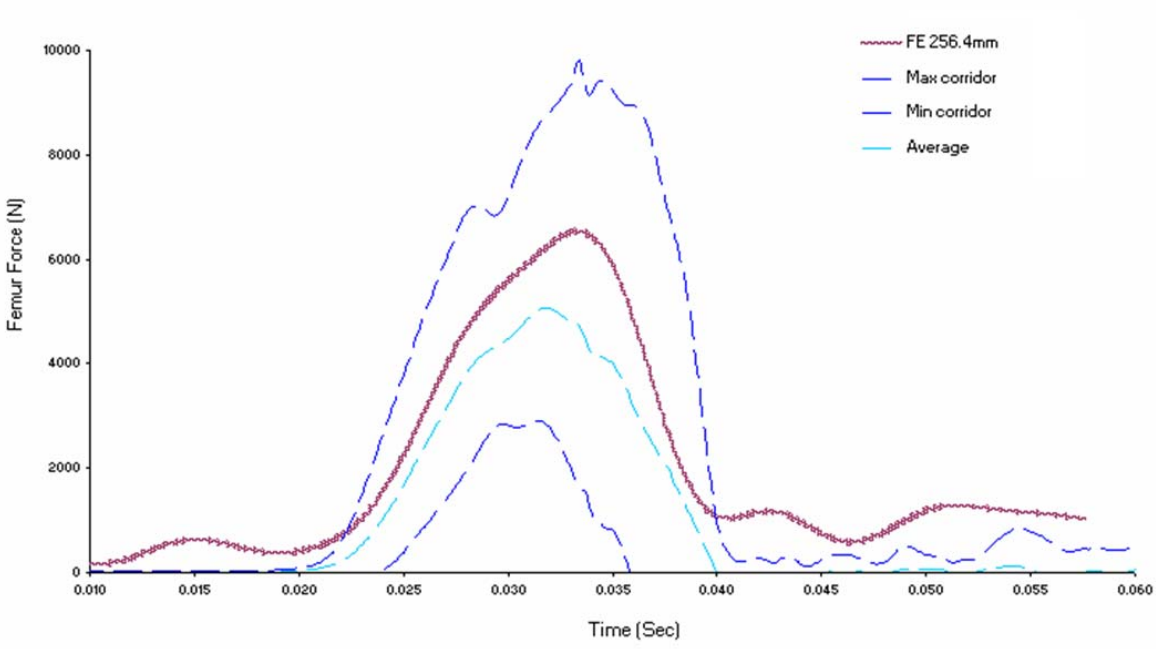

Figure 5.63. Comparison of the whole-body validation femur force vs. corridor for the contact femur force in the femoral head validation.

VI. IMPROVEMENTS TO THE KTH MODEL

Chapter 6 is a review of all improvements which have been made to the KTH model after its validation. A more realistic representation of human ligaments with dynamic failure properties is introduced. Muscle activation is then included as one more feature for further studies. While developing muscle activation properties, the necessity arose for a refined representation of the patellar tendon in order to replicate the correct dynamic of the knee. Also, insertion of revolute joints between tibia, femur and patella bones became necessary as constraints for unrealistic relative movements between these bones.

6.1. Representation of Human Ligaments with Dynamic Failure Properties

In the finite element KTH model developed so far the effect of high strain rates such those experienced in high speed automotive collisions on biomechanical properties of ligaments was not considered. Tough many studies can be found in literature about the effect of strain rate on ligament properties, very few have analyzed high strain rates effects. (Crisco et al., 2002; France et al., 1897; Woo, 1990; Lydon et al., 1995)

Peck investigated the role of strain rates up to $145s^{-1}$ in mechanical failure of porcine bone-collateral ligament-bone complexes. (Peck, 2007) His results were included in the KTH model for a more complete and realistic definition of the FE representation for mechanical properties of ligaments in the KTH model.

6.1.1 NHTSA Tests – Failure Behavior of Ligaments Subjected to High Strain Rates

Peck estimated human ligament properties by performing tests on porcine Medial Collateral Ligaments (MCL) and Lateral Collateral Ligaments (LCL). (Peck, 2007) The porcine knee, when compared to other animals, is the best model for experimental studies to predict human behavior (Xerogeanes et al., 1998) Other studies have found that the properties of rat MCL and LCL were similar, so an assumption is being made that all ligaments share similar constitutive properties. (Peck, 2007) Peck defined the following model for prediction of the failure load for a human ligament (Peck, 2007):

$$P_F = 3.0194 \cdot \varepsilon_{rate} + 1{,}091.5930 \cdot \frac{A_0}{L_0} \tag{6.1}$$

This result revealed there are three reliable predictors of the failure load: the initial cross sectional area, A_0, the initial length L_0, and the applied strain rate ε_{rate}. The regression-based model is composed of two terms: one recalling geometric parameters and describing the quasi-static failure load, while the second one accounts for the strain rate dynamic effect. (Peck, 2007) This relationship can be applied to any ligament knowing its geometrical properties such as its length and initial cross-sectional area. A literature review on human KTH ligaments dimensions was conducted to determine the area and length of all KTH ligaments.

6.1.1.1 Re-definition of Ligaments Physical Properties

Human KTH ligament length and cross-sectional area were searched for in the literature (Hewitt et al., 2002). The values reported in Table 6.1 were chosen for the FE KTH model:

Table 6.1. Ligament length and cross-sectional area values used for KTH model (Hewitt et al., 2002).

	Length (mm)	Area ($mm^{\wedge 2}$)
ACL	30.7	5
PCL	35.4	8
LCL	56	10
MCL	38	11
Ischiofemoral	75	65
Iliofemoral	82	80
Capitis Femoris	15	3

6.1.1.2 Definition of the Material Model used for Modeling in LSDYNA

Material type S04 (*MAT_SPRING_NONLINEAR_ELASTIC) was chosen to model the ligaments. This material provides a nonlinear elastic translational and rotational spring with arbitrary force versus displacement curves. (LSTC, 2003a) Moreover, with this material there is the option of considering strain rate effects through a velocity dependent scale factor. In order to define the curve, reproduced in Figure 6.1, the first part of Peck's model for prediction of the failure load for ligaments was considered. Since, however, there is a scale factor on force on the ordinate axis, the following equation was used:

$$ScaleFactor = \frac{3.0194 \cdot \varepsilon_{rate}}{P_{Static}} \tag{6.2}$$

where P_{Static} is the 2,836 N load at failure for a quasi-static tensile test of a ligament conducted by Peck. (Peck, 2007)

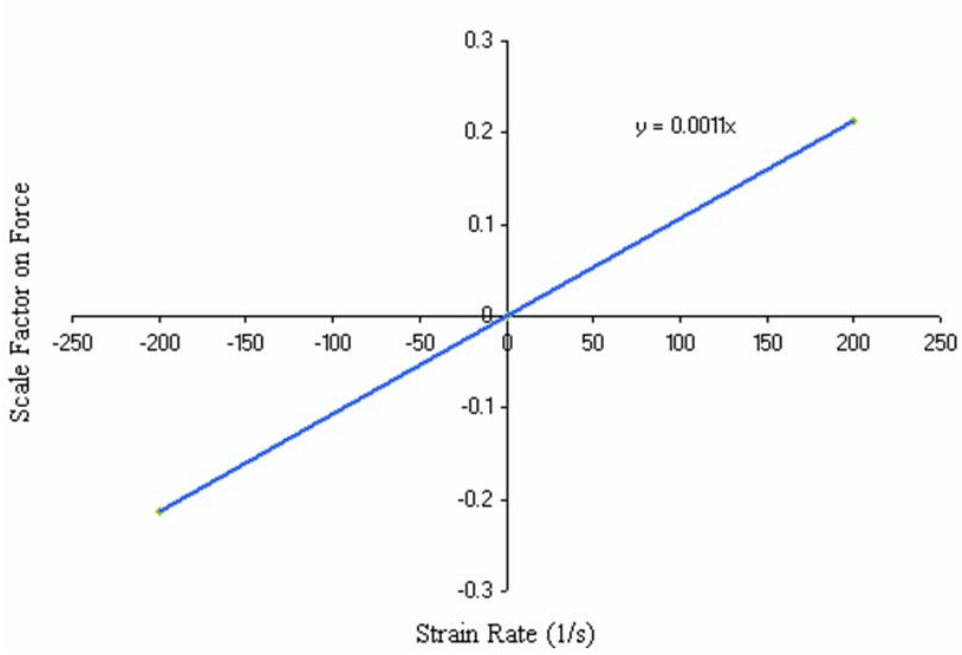

Figure 6.1. Scale factor on force vs. strain rate curve defined to account for strain rate effects.

The failure load vs. displacement curve needed for modeling the mechanical properties of the ligaments in the KTH model was defined as follows. Results of the impact tensile tests performed by Peck of porcine MCL ligaments were used. For each test, the ultimate stress and strain were multiplied, respectively, by the initial cross-sectional area and the length of the considered ligament. These ultimate loads and displacements were then plotted in an Excel graph where a linear regression line was determined passing through the origin. The slope of this regression line was then used to plot the force vs. displacement curve for the ligament considered. The displacement value at which ligament failure would occur was set by setting the curve to zero at the value of displacement. An example of building the curve for the ACL ligament is explained below.

a) Consideration of the ultimate stresses and strains from impact tensile tests from Peck. (Peck, 2007)

Tests #	Failure Strain (%)	Failure Stress (Mpa)
1	31	86
2	52	62
3	27	89
4	21	51
5	31	62
6	17	47
7	30	70
8	37	71
9	36	82

b) Multiplication of the stresses and strain by, respectively, the initial cross-sectional area of the Anterior Cruciate Ligament (ACL). The area of the ACL was defined to be 5 mm$^{\wedge 2}$ and the length was 30.7 mm. (Hewitt et al., 2002)

Tests #	Failure Strain (%)	Failure Stress (Mpa)
1	31	86
2	52	62
3	27	89
4	21	51
5	31	62
6	17	47
7	30	70
8	37	71
9	36	82

L_0 = 30.7 mm

A_0 = 5 mm^2

Failure displacement (mm)	Failure Load (N)
9.517	430
15.964	310
8.289	445
6.447	255
9.517	310
5.219	235
9.21	350
11.359	355
11.052	410

c) These ultimate loads and displacements were plotted in an Excel graph and a linear regression line was calculated passing through the origin.

Tests #	Failure Strain (%)	Failure Stress (Mpa)
1	31	86
2	52	62
3	27	89
4	21	51
5	31	62
6	17	47
7	30	70
8	37	71
9	36	82

ACL

L_0 = 30.7 mm

A_0 = 5 mm^2

Failure displacement (mm)	Failure Load (N)
9.517	430
15.964	310
8.289	445
6.447	255
9.517	310
5.219	235
9.21	350
11.359	355
11.052	410

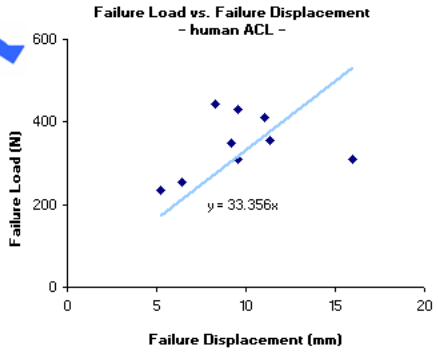

d) The slope of this regression line was used to define the force-displacement curve for the ligament considered where the displacement value at which ligament failure would occur was also imposed.

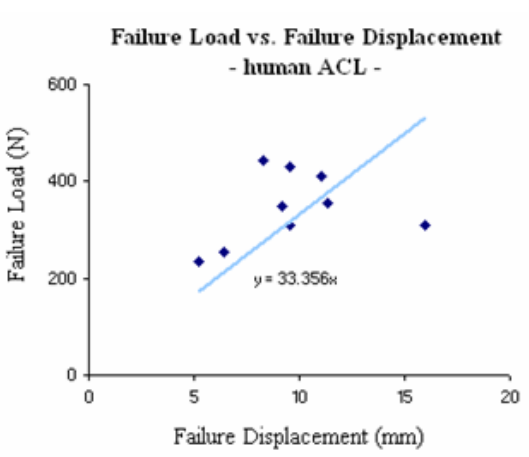

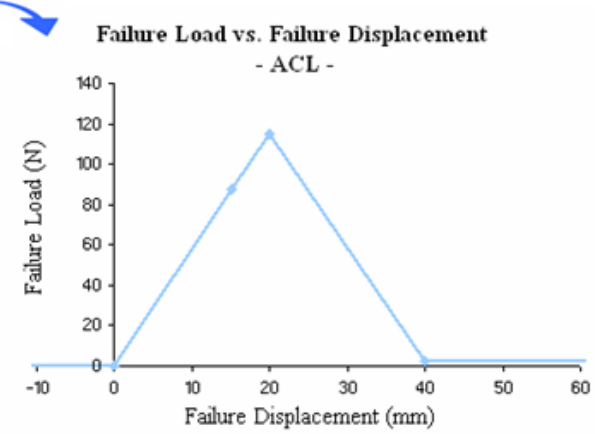

6.1.2 Validation of the Model with Dynamic Failure Properties

It was necessary to validate the new model of ligaments for use in the KTH model. To validate it, experiments conducted by Viano were considered and reproduced in finite element simulations. (Viano, 1978) The model was considered validated only if it was showing the same results obtained previously by Viano tests.

6.1.2.1 Viano Dynamic Tolerance Tests Setup

In 1978, Viano conducted dynamic tolerance tests of the Posterior Cruciate Ligament (PCL) on isolated cadaveric tissues. (Viano, 1978) Mid-tibial and mid-femoral shafts were dissected, cleansed and placed in cylindrical sleeves which were attached to an actuator of a servo-controlled machine. The patella bone was removed as was the tissue covering the knee joint. Keeping the mid-femoral shaft fixed, a dynamic posterior displacement was then applied to the mid-tibial shaft at a constant loading rate of 1.8 m/sec. The tibia was translated across the fixed femur for 50 mm. Five specimens were tested. In the tests, three general modes of joint failure were observed: a mid-ligament rupture of the PCL, avulsion fracture of the PCL from its attachment at the tibial plateau and tibial shaft fracture near the cylindrical potting sleeve of the test fixture.

6.1.2.2 Viano Dynamic Tolerance Tests Results

Viano found out that a partial ligament failure occurred at a relative tibial-femoral displacement of 14.4 mm and a joint load of 2.02 kN. An ultimate collapse occurred at a relative displacement of 22.6 mm between the femur and the tibia and at a load of 2.48 kN.

6.1.2.3 Finite Element Model Dynamic Tolerance Tests Setup

The same test setup was reproduced in a finite element model. Mid-femoral and mid-tibial shafts were considered. Patella bone and muscles were not included in the model to conform to the physical tests. Anterior, Lateral, Median and Posterior Cruciate Ligaments (ACL, LCL, MCL, PCL) were modeled as discrete elements with material type S04 (*MAT_SPRING_NONLINEAR_ELASTIC) including the load-displacement curve

and scale factor on force-displacement curves explained in the previous paragraphs. The mid-femoral shaft was constrained in its movements in all directions and rotations. The mid-tibial shaft was constrained to to move only along direction of the applied velocity. A constant velocity of 1800 mm/sec (1.8 m/sec) was applied to the bottom of the mid-tibial shaft axial direction of the femur. Figure 6.2 shows a frontal view of the finite element model and setup.

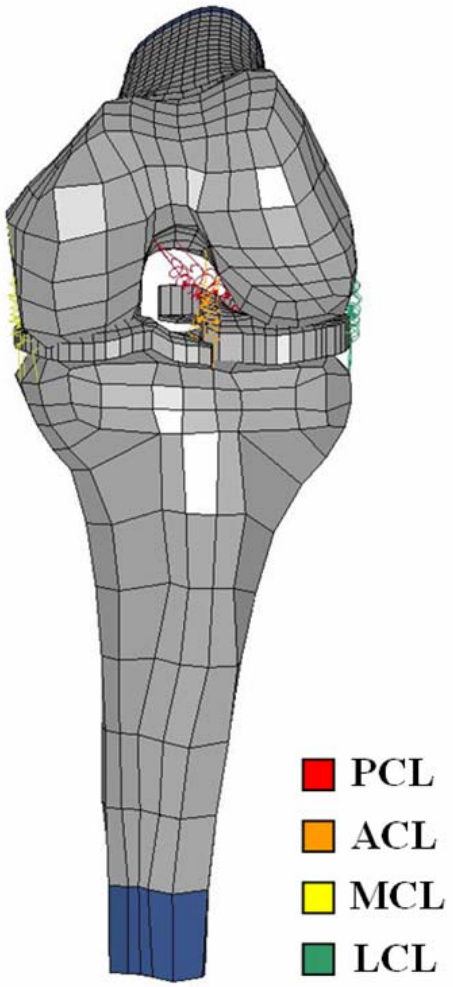

Figure 6.2. Frontal view of the finite element model and setup for ligaments validation.

6.1.2.4 Finite Element Model Dynamic Tolerance Tests Results

Results from the FE simulations showed that an initial failure of the PCL occurs at a relative tibial-femoral displacement of 14.24 mm. At this point, two of the four discrete elements used to model the Posterior Ligament fail at their attachment to the Condyle indicating an avulsion failure. Since two of the four discrete elements for representing the PCL failed, this was interpreted as a partial ligament failure. An ultimate collapse of the PCL (i.e., all four discrete elements detach) occurs at a relative tibial-femoral displacement of 22.94 mm (Figures 6.3 and 6.4). Comparison of the simulation and comparison and Viano experimental results are shown in Tables 6.2 and 6.3.

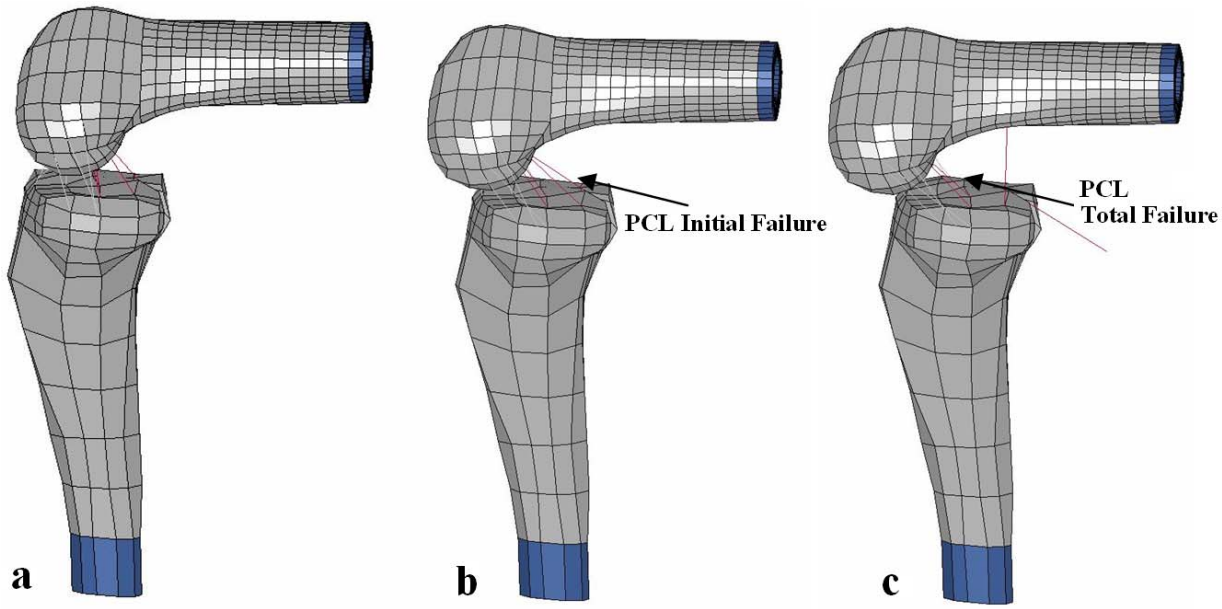

Figure 6.3. Initial and ultimate rupture of the PCL during simulations.

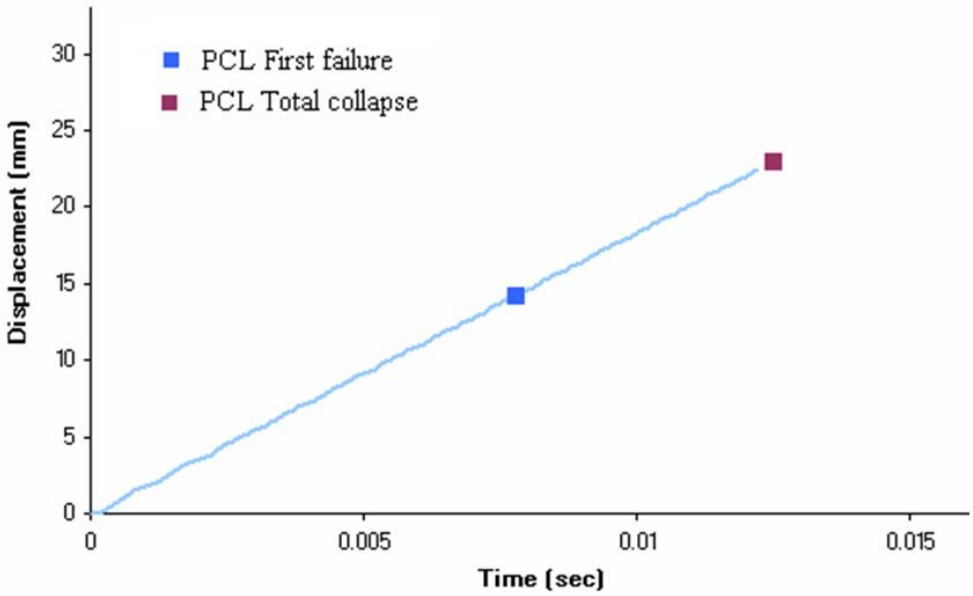

Figure 6.4. Relative displacement of Tibia with respect to the fixed Femur and moments of first failure and total collapse.

Table 6.2. Displacement of tibia relative to fixed femur: comparison between test and simulation.

	Displacement of Tibia relative to Fixed Femur	
	FE (mm)	Viano (mm)
PCL First failure	14.24	14.4
PCL Total collapse	22.94	22.6

Table 6.3. Force at first failure: comparison between test and simulation.

	Force at First Failure	
	FE (kN)	Viano (kN)
First failure	2.97	2.02

Simulation results are very similar to the test results obtained by Viano. Mertz et al. recommended an injury threshold level of 15 mm for relative translation between the femur and the tibia at the knee joint for a 50^{th} percentile male to minimize rupture of the posterior cruciate ligament based on the data from Viano. (Mertz, 1989) The simulation results, therefore, fit nicely with both the test data from Viano and the injury criteria recommended by Mertz. Moreover, according to Anderson, the maximum strain a ligament can tolerate before failure is between nine and 18 percent. (Anderson, 2002) In our case, the two discrete elements failed at a strain of about 14.5 and 15.5 percent respectively, exactly within the expected range. As conclusion, the PCL ligament model can be considered validated. Assuming that all ligaments can be considered to have the same material properties, this model can be applied for representing the other ligaments of the knee and of the pelvic region although material properties are conformed to the different geometries and dimensions of the other ligaments.

A list with the new anatomical relocation of the KTH ligaments, the new number of discrete elements and the new load-displacement curves used for their representations is reported in Table 6.4. The curve was applied to each discrete element used for the representation of the ligament.

In almost all cases, ligaments were split into several discrete elements in order to avoid mesh destabilization problems. Moreover, with multiple discrete elements we can replicate the real geometry of the insertion site.

Table 6.4. Material Properties for Ligaments used in the new KTH Model.

Iliofemoral Ligament	Force vs. Displacement / Iliofemoral
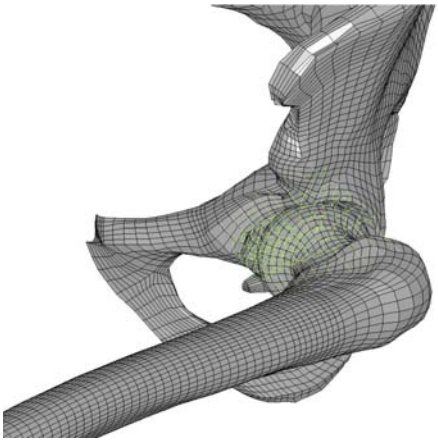	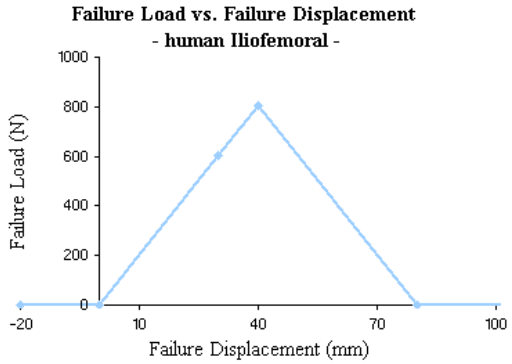
Ischiofemoral Ligament	Force vs. Displacement / Ischiofemoral
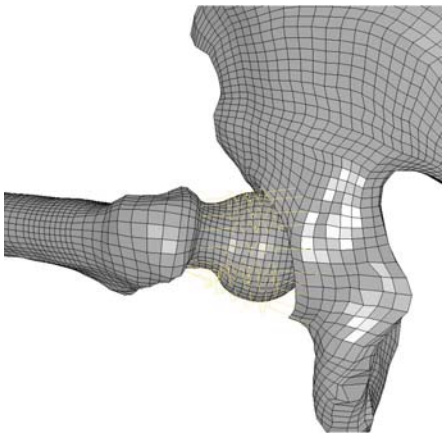	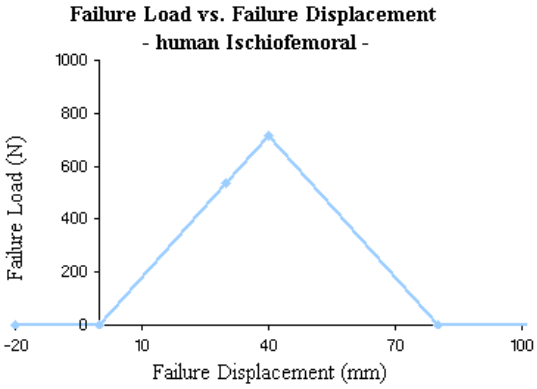
ACL Ligament	Force vs. Displacement / ACL
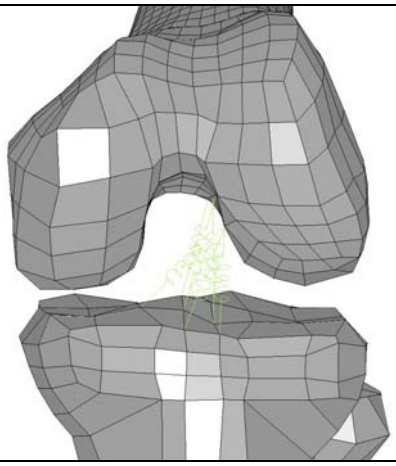	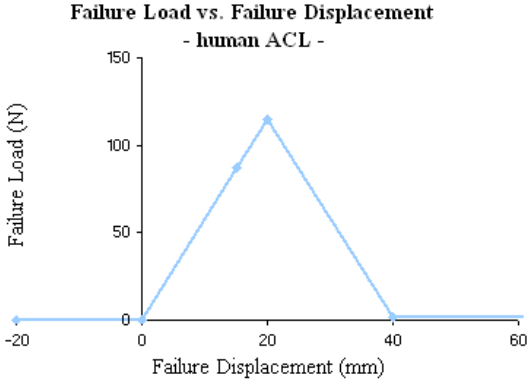

Table 6.4. Properties for Ligaments in the new KTH Model (continued).

PCL Ligament	Force vs. Displacement / PCL
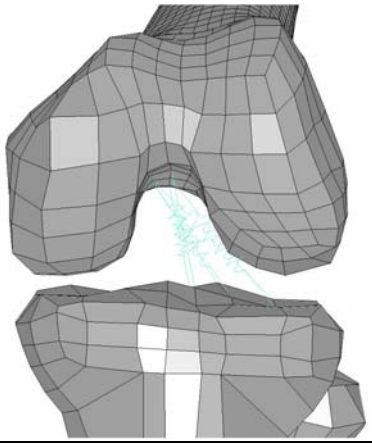	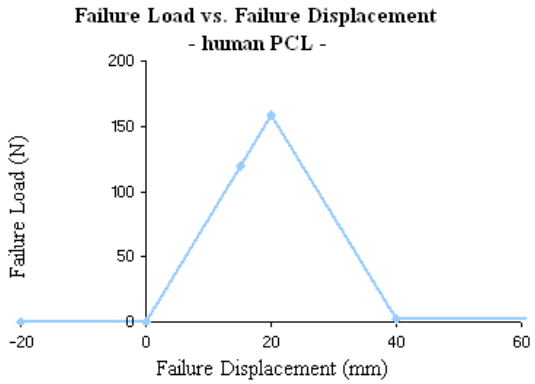
MCL Ligament	Force vs. Displacement / MCL
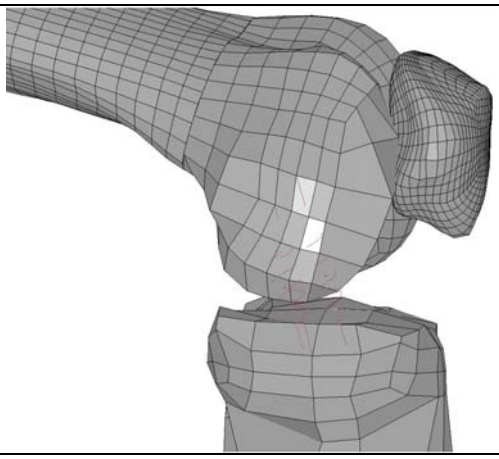	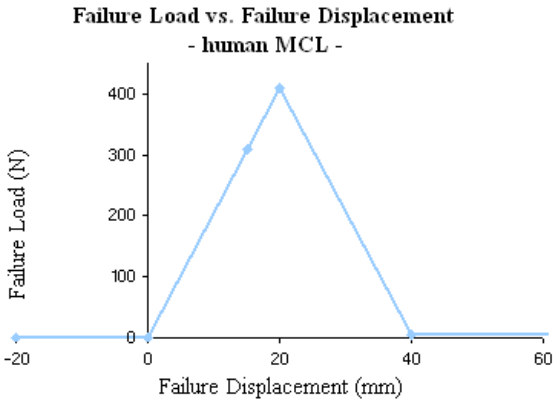
LCL Ligament	Force vs. Displacement / LCL
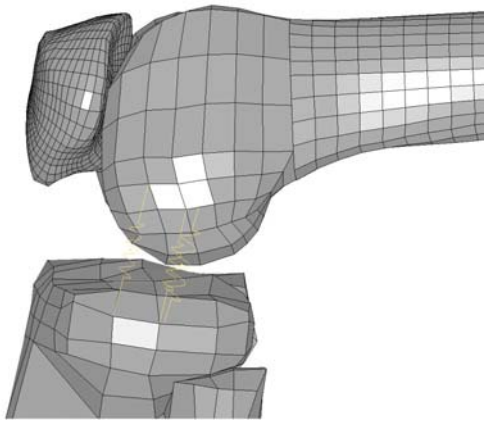	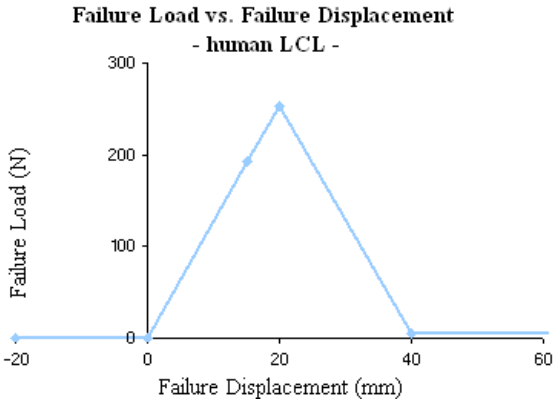

6.2. Improvements to the Knee Region

The original WPI version of the KTH model was able to properly reproduce adduction and abduction movements. The results of knee-extension simulations, however, exhibited numerical problems due to negative volume in solid elements of the patella. In fact, during the first phase of the simulation, when the patella was pulled by the patellar tendon, the bone seemed to get "stuck" against the femur causing the numerical problems.

For this reason, two important changes have been made in the way the patellar tendon is modeled in order to obtain a correct bio-fidelic dynamic response. The first change was about the type of material model and geometry for the patellar tendon. The second change was an introduction of revolute joints between tibia, patella and femur to constrain the relative movements of these bones for avoiding unrealistic actions.

*6.2.1 Physical representation of the patellar tendon using *MAT_SEATBELT*

Originally the patellar tendon was modeled as shell elements that passed over the patella. The muscles are attached to the femur end of the shell element patellar tendon and the upper part of the tibia. This arrangement allowed the patella too much freedom of movement and allowed the patella to "lock" the knee joint at times. A method had to be found to constrain the patella and patellar tendon to a more realistic approach.

The patellar tendon was modeled with spring *MAT_SEATBELT. Three lines of springs were chosen to increase the stability of the movement and avoid unphysical rotation of the patella bone during movements such as extension of the knee (Figure 6.5). The patellar tendon originates at the rectus femoris muscle and is inserted in three different aligned nodes in the tibia. The spring element size was set to 6 mm. The offset between seatbelts and contact elements was selected as one mm.

Each spring is forced to pass through a slipring. The sliprings are positioned on nodes of the patella to permit the patellar tendon to slide on the bone during movements as it happens anatomically. (Figure 6.6)

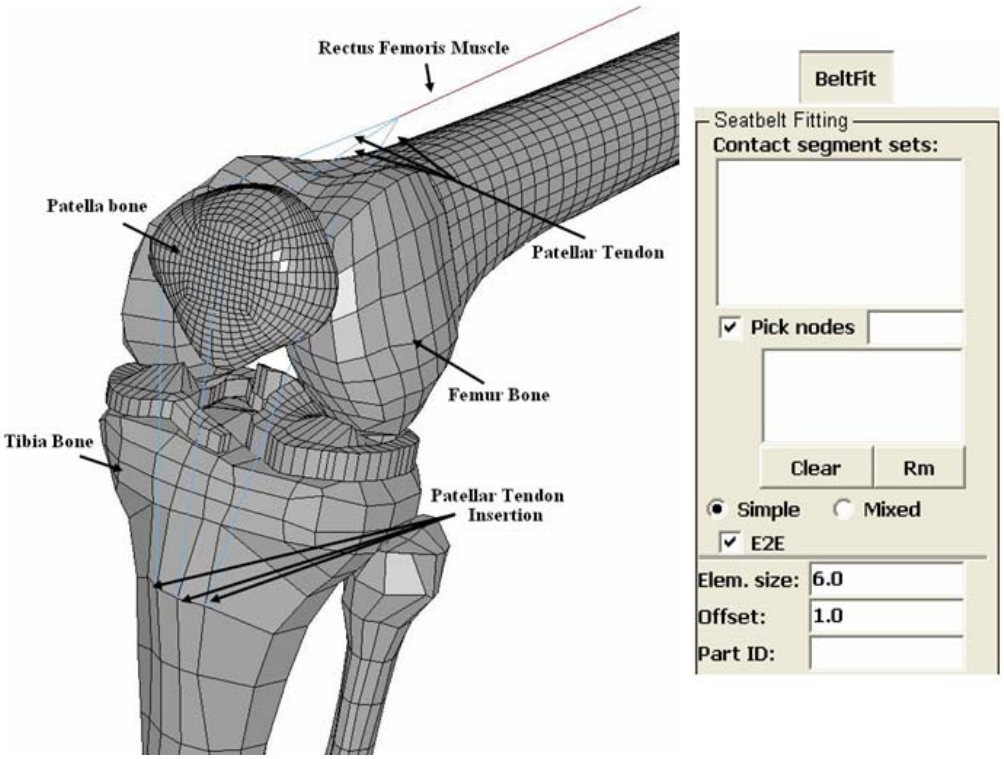

Figure 6.5. Patellar tendon modeled with spring seatbelt material proposed in LSDYNA (left) and LSDYNA "BeltFit" Command Inputs (right). (LSTC, 2007b)

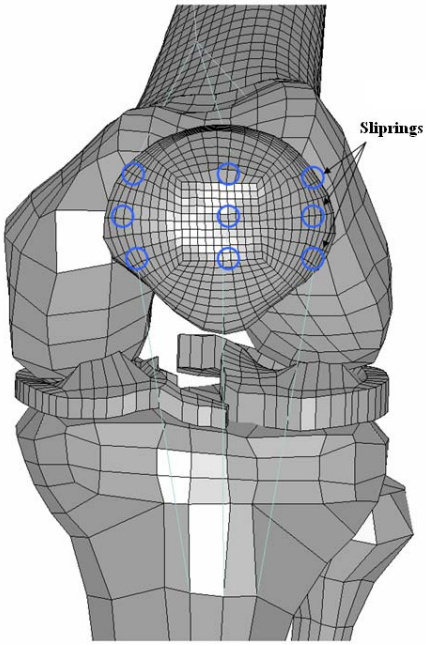

Figure 6.6. Position of sliprings for the three spring-lines on the patella bone.

The mass per unit length of the springs was defined to be 1.90e-06 ton/mm^2. A minimum length of 0.05 mm is considered as input for controlling the shortest length allowed in any element and determining when an element passes through sliprings or is absorbed into the retractors. Normally, according to the LSDYNA manual, one tenth of a typical initial element length is usually a good choice. (LSTC, 2007a)

A load curve (i.e., force vs. engineering strain) for loading is also inserted (Figure 6.7). To define the curve, the same method used to draw the curves for ligaments was followed. An area of 163 mm^2 and an initial length of 156 mm for the patellar tendon was considered for definition of the failure load and strain values.

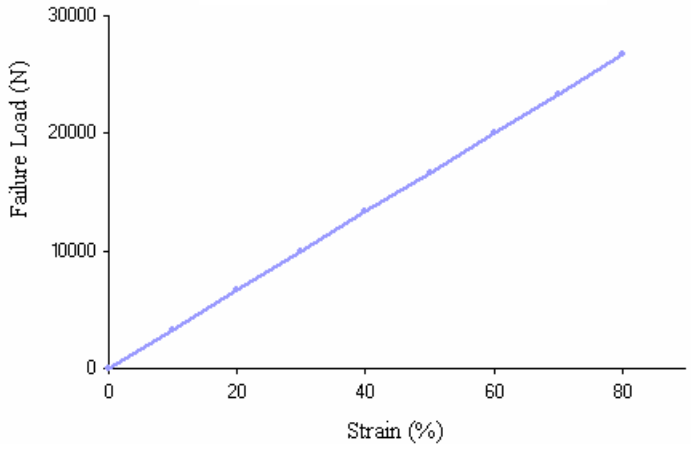

Figure 6.7. Failure load vs. engineering strain curve for patellar tendon mechanical properties definition.

6.2.2 Introduction of Joints Revolute as Dynamic Constraints

In the human knee, soft tissue constrains movements of the knee joint. In the original WPI version of the KTH model, soft tissue was not modeled. As consequence, the need of adding something to the FE model arose, in order to constrain rotations of the joint.

Revolute joints were inserted in the model to constrain movements between tibia and femur and between patella and femur. The *CONTRAINED_JOINT_REVOLUTE is a feature which can be added only between rigid nodes. It creates a revolution axis passing through these nodes and defines the allowable relative rotations between the parts in question. The revolute joint feature connects two nodes of two different but coincident parts.

The tibia and the femur are not rigid parts so the first step was to change some elements belonging to these materials into rigid ones.

A second problem was that no node of the femur could be coincident to any node of the tibia for anatomical obviously reasons. The problem was solved by using the card *CONSTRAINED_EXTRA_NODES_NODE. With this card, extra nodes for rigid bodies may be placed anywhere, even outside the body, and they are assumed to be part of the rigid body. (LSTC, 2007a) This command is frequently used for placing nodes where joints are then attached between rigid bodies.

In the model, two nodes were created and defined as extra nodes for the tibia. The same was done for the femur. The two extra nodes of the femur were placed at the exact same location where the extra nodes of the tibia were previously placed (in Figure 6.8 they appear slightly distant, only to show their both presence). The revolute joint was then defined as an axis passing through the extra nodes which became the axis of revolution between the tibia and the femur. Now, the tibia and the femur could be constrained to rotate around that axis. Rotation of these bones with respect any other axis was not possible as happens anatomically.

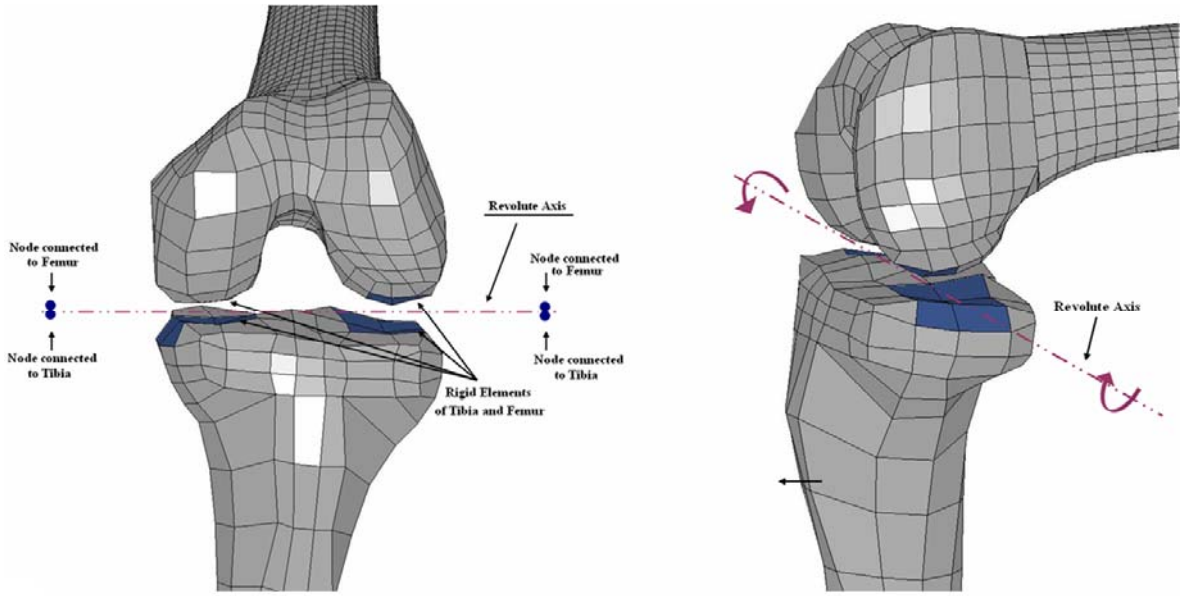

Figure 6.8. Definition of the revolute joint between the tibia and the femur bones.

The same procedure was followed for the definition of a revolute joint between the patella and the femur (Figure 6.9).

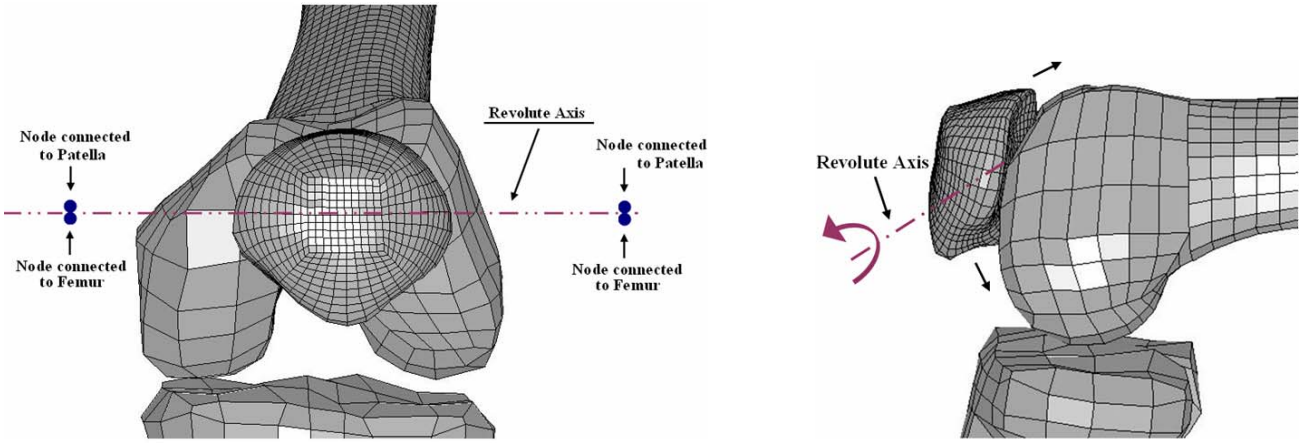

Figure 6.9. Definition of the revolute joint between the patella and the femur bones.

Establishing the revolute joints and adding the new slipring model at the patellar tendon resulted in anatomically correct motions of the knee joints.

6.3. Active Muscle Properties Inclusion

The next step for improving the KTH model was to include activation of muscles. When validating the model, simulations of a cadaver sled tests were performed as discussed in Chapter 5. In that case, there was no need to consider active properties of muscles since the cadaver could not respond actively. Consequently, the FE model was just taking into account the passive properties of the muscles.

Now, the role of active muscle forces on KTH fracture mechanisms during frontal car crash could be explored. In this section, the representation for both active and passive muscle properties was inserted into the KTH model. A simplified example of the active model will be presented before proceeding with more complex lower limb movements.

6.3.1 Modeling the Active Properties of a Muscle in LSDYNA

As it was already explained previously in Chapter 4, muscles were modeled using the *MAT_SPRING_MUSCLE material type in LSDYNA. With this card, one can choose to consider only the passive properties or to include also active muscle force (Figure 6.10).

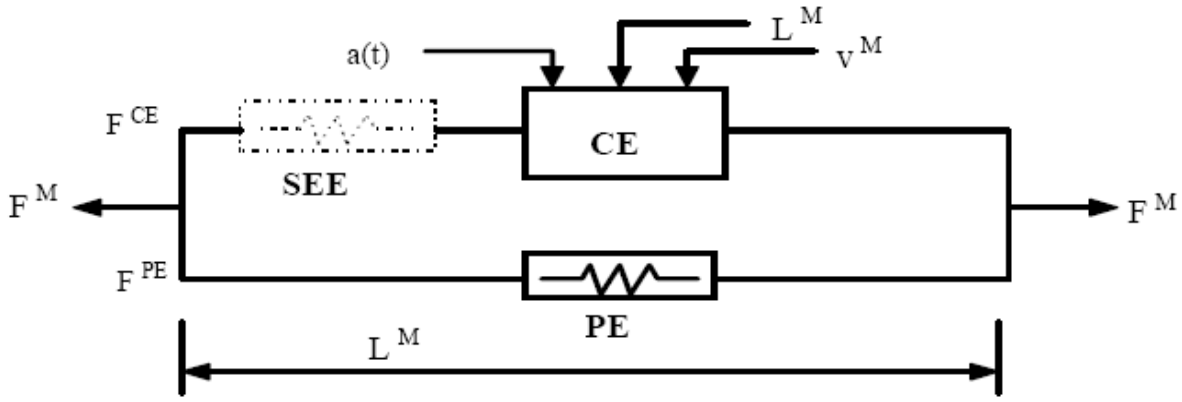

Figure 6.10. Discrete model for muscle contraction dynamics based on a Hill's-type representation available in the *MAT_SPRING_MUSCLE card in LSDYNA. (LSTC, 2007a)

The ultimate total force produced by the muscle including active and passive muscle forces is the sum of the passive and the active forces:

$$F^M = F^{PE} + F^{CE} \tag{6.3}$$

The active force generated by the muscle (F^{CE}) is directly proportional to the activation level a(t) of the muscle up to its peak isometric force, F_{MAX} where the tension-length, $f_{TL}(t)$, and the tension-velocity, $f_{TV}(t)$, functions are provided as curves:

$$F^{CE} = a(t) * F_{MAX} * f_{TL}(L) * f_{TV}(V) \tag{6.4}$$

The activation level curve was chosen to be a linear function of time (Figure 6.11). In fact, when inserting a constant activation level curve of any value between 0.6 and 1.0, the simulations experienced numerical problems. They were due to the high level of stresses which the muscle was imposing to the bone solid elements at its insertion in a very short time. With this linear activation curve, the numerical problems were avoided.

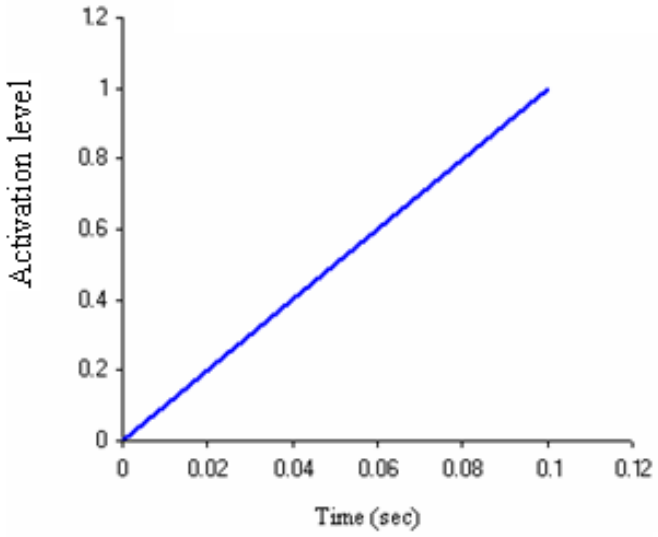

Figure 6.11. Activation level curve as function of time defined for muscles.

The functions describing the behavior of the active tension with respect to the length function and to the velocity function are reported in Figure 6.12 (Olivetti, 2005). Updated muscle insertion sites and main input values are reported in Table 6.5.

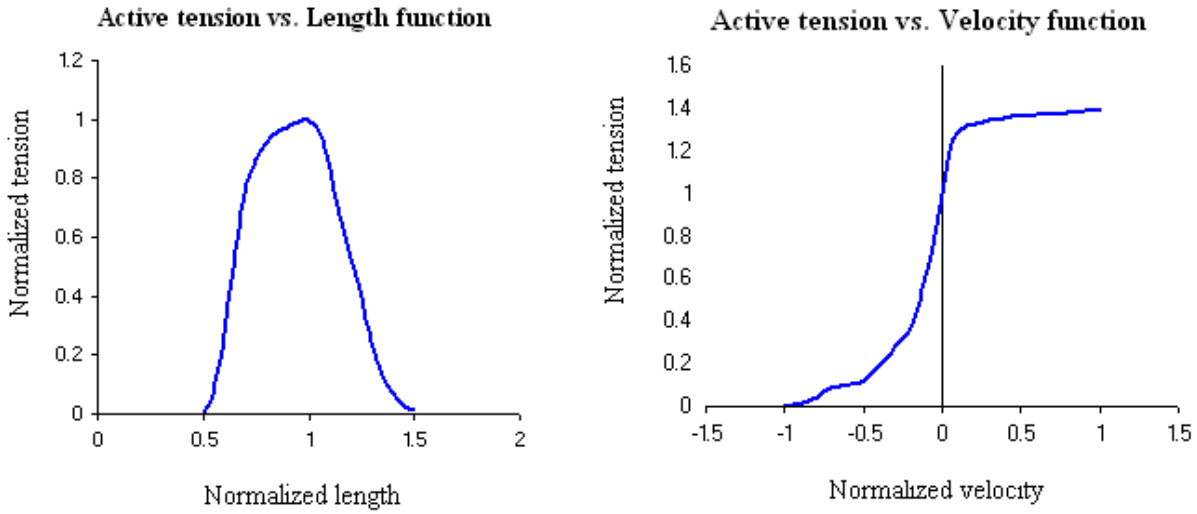

Figure 6.12. Active tension vs. length and active tension vs. velocity functions used for definition of the discrete model for muscle contraction dynamics based on a Hill's-type representation.

Table 6.5. KTH Muscles: characteristics and models (Muscle Atlas, 2008)

Anterior thigh Muscles: **Pectineus**		
	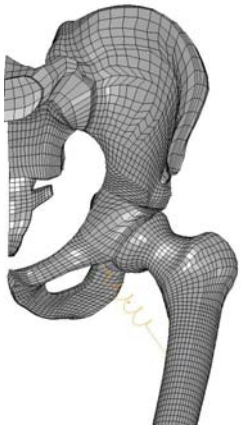	Peak isometric force F_max = 177 N Maximum CE shortening velocity V_max = 582 mm/sec
Anterior thigh Muscles: **Iliacus**		
	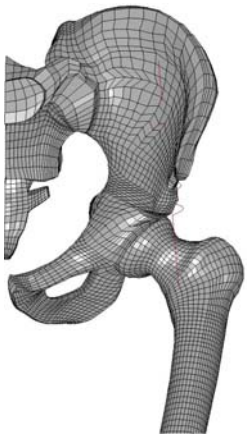	Peak isometric force F_max = 788 N Maximum CE shortening velocity V_max = 1144 mm/sec
Anterior thigh Muscles: **Tensor Fascia Latae**		
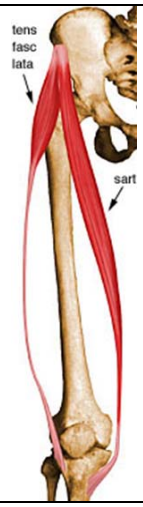		Peak isometric force F_max = 155 N Maximum CE shortening velocity V_max = 588 mm/sec

Table 6.5. KTH Muscles: characteristics and models (continued) (Muscle Atlas, 2008)

Anterior thigh Muscles: **Sartorius**		
	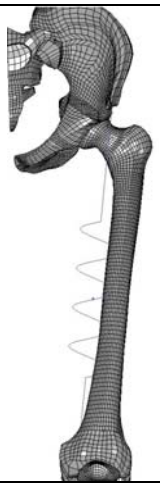	Peak isometric force F_max = 104 N Maximum CE shortening velocity V_max = 2283 mm/sec
Anterior thigh Muscles: **Rectus Femoris**		
	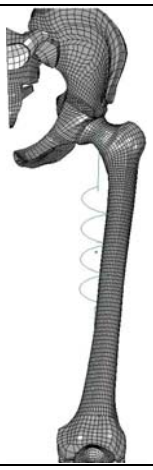	Peak isometric force F_max = 974 N Maximum CE shortening velocity V_max = 1555 mm/sec
Anterior thigh Muscles: **Vastus Intermedius**		
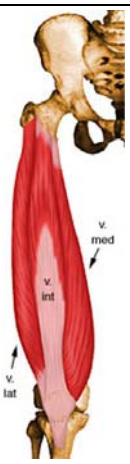	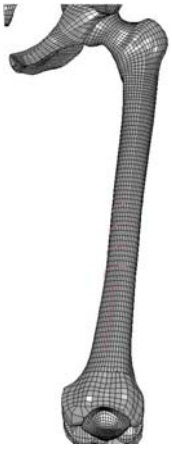	Peak isometric force F_max = 2125 N Maximum CE shortening velocity V_max = 1232 mm/sec

Table 6.5. KTH Muscles: characteristics and models (continued) (Muscle Atlas, 2008)

<table>
<tr><td colspan="3">Anterior thigh Muscles: Adductor Longus</td></tr>
<tr><td>  </td><td> 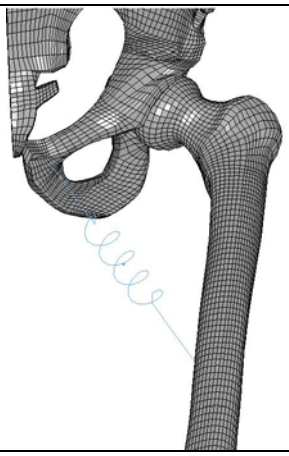 </td><td>Peak isometric force
F_max = 418 N

Maximum CE shortening velocity
V_max = 675 mm/sec</td></tr>
<tr><td colspan="3">Anterior thigh Muscles: Adductor Brevis</td></tr>
<tr><td> 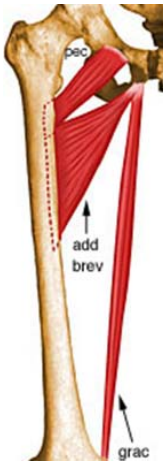
</td><td> 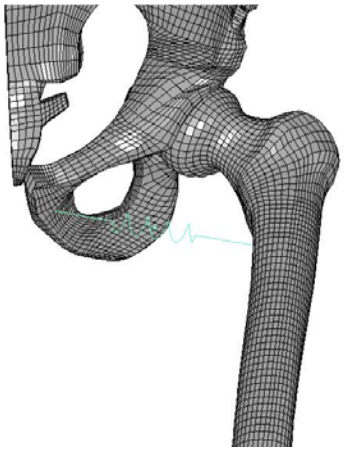 </td><td>Peak isometric force
F_max = 286 N

Maximum CE shortening velocity
V_max = 533 mm/sec</td></tr>
<tr><td colspan="3">Anterior thigh Muscles: Adductor Magnus</td></tr>
<tr><td>  </td><td> 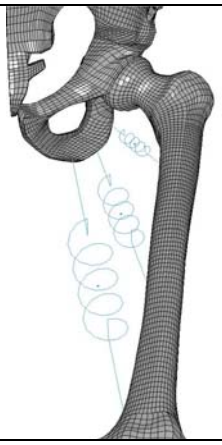 </td><td>Peak isometric force
F_max = 312 N

Maximum CE shortening velocity
V_max = 733 mm/sec</td></tr>
</table>

Table 6.5. KTH Muscles: characteristics and models (continued) (Muscle Atlas, 2008)

Anterior thigh Muscles: **Gracilis**		
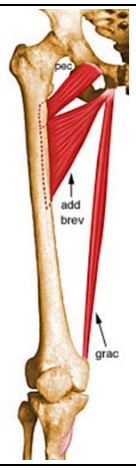	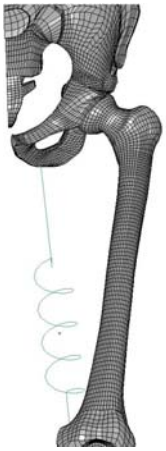	Peak isometric force F_max = 108 N Maximum CE shortening velocity V_max = 1147 mm/sec
Anterior thigh Muscles: **Gluteus Maximus**		
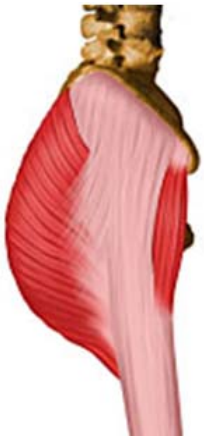	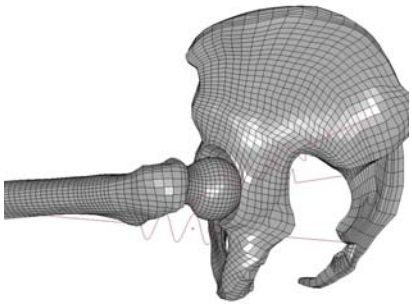	Peak isometric force F_max = 546 N Maximum CE shortening velocity V_max = 682 mm/sec
Anterior thigh Muscles: **Gluteus Medius**		
	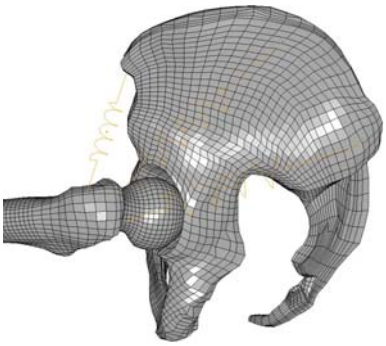	Peak isometric force F_max = 382 N Maximum CE shortening velocity V_max = 572 mm/sec

Table 6.5. KTH Muscles: characteristics and models (continued) (Muscle Atlas, 2008)

<table>
<tr><td colspan="3">Anterior thigh Muscles: Gluteus Minimus</td></tr>
<tr><td>  </td><td> 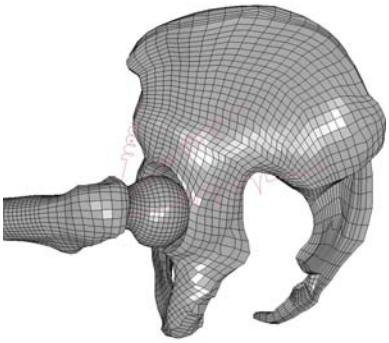 </td><td>Peak isometric force
F_max = 190 N

Maximum CE shortening velocity
V_max = 352 mm/sec</td></tr>
<tr><td colspan="3">Anterior thigh Muscles: Piriformis</td></tr>
<tr><td> 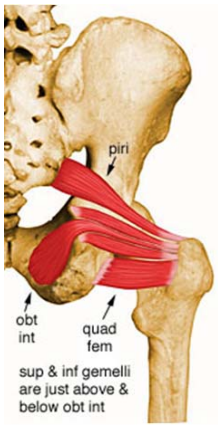
</td><td> 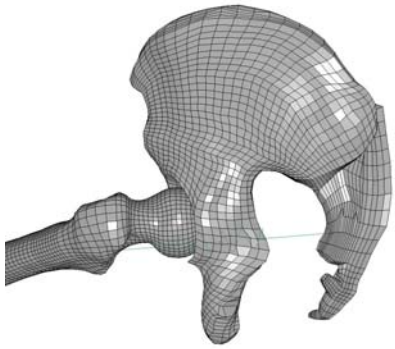 </td><td>Peak isometric force
F_max = 296 N

Maximum CE shortening velocity
V_max = 374 mm/sec</td></tr>
<tr><td colspan="3">Anterior thigh Muscles: Biceps Femoris</td></tr>
<tr><td>  </td><td>  </td><td>Peak isometric force
F_max = 502 N

Maximum CE shortening velocity
V_max = 779 mm/sec</td></tr>
</table>

Table 6.5. KTH Muscles: characteristics and models (continued) (Muscle Atlas, 2008)

<table>
<tr><td colspan="3">Anterior thigh Muscles: Quadratus Femoris</td></tr>
<tr><td> 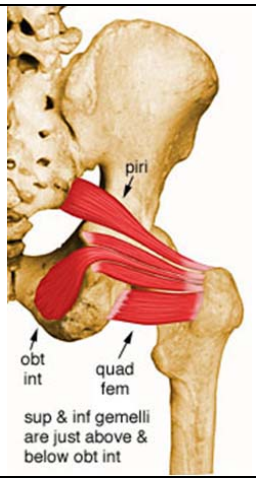
</td><td> 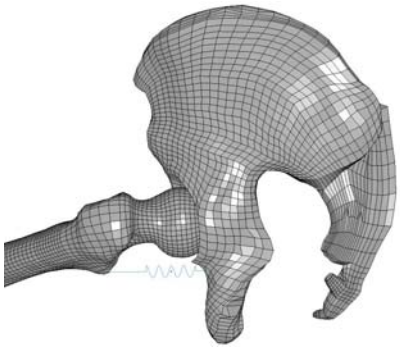 </td><td>Peak isometric force
F_max = 254 N

Maximum CE shortening velocity
V_max = 418 mm/sec</td></tr>
<tr><td colspan="3">Anterior thigh Muscles: Semitendinosus</td></tr>
<tr><td>  </td><td> 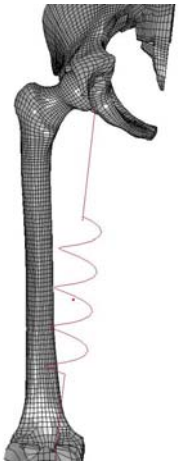 </td><td>Peak isometric force
F_max = 1312 N

Maximum CE shortening velocity
V_max = 1319 mm/sec</td></tr>
<tr><td colspan="3">Anterior thigh Muscles: Semimembranosus</td></tr>
<tr><td>  </td><td> 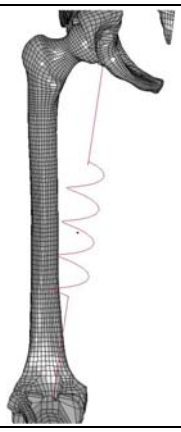 </td><td>Peak isometric force
F_max = 1312 N

Maximum CE shortening velocity
V_max = 879 mm/sec</td></tr>
</table>

Table 6.5. KTH Muscles: characteristics and models (continued) (Muscle Atlas, 2008)

<table>
<tr><td colspan="3">Anterior thigh Muscles: Gemelli Superior</td></tr>
<tr><td> 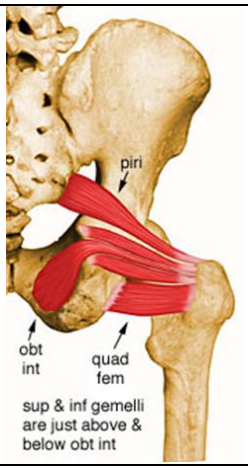
</td><td> 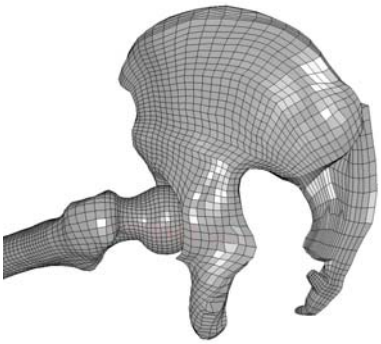 </td><td>Peak isometric force
F_max = 109 N

Maximum CE shortening velocity
V_max = 242 mm/sec</td></tr>
<tr><td colspan="3">Anterior thigh Muscles: Gemelli Inferior</td></tr>
<tr><td> 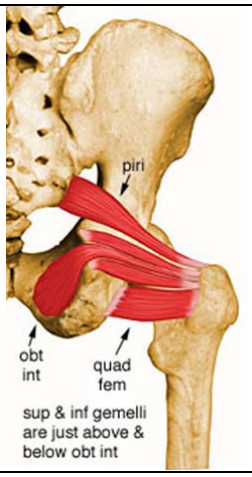
</td><td> 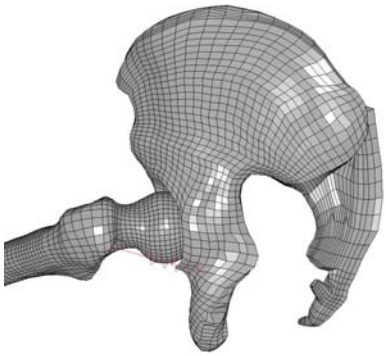 </td><td>Peak isometric force
F_max = 109 N

Maximum CE shortening velocity
V_max = 242 mm/sec</td></tr>
<tr><td colspan="3">Tibial Muscles: Tibialis Anterior</td></tr>
<tr><td>  </td><td>  </td><td>Peak isometric force
F_max = 1375 N

Maximum CE shortening velocity
V_max = 650 mm/sec</td></tr>
</table>

Table 6.5. KTH Muscles: characteristics and models (continued) (Muscle Atlas, 2008)

Tibial Muscles: **Soleus**		
	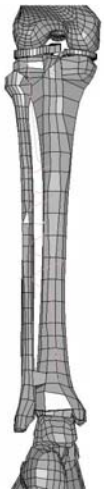	Peak isometric force F_max = 3549 N Maximum CE shortening velocity V_max = 700 mm/sec
Tibial Muscles: **Gastrocnemius**		
		Peak isometric force F_max = 2225 N Maximum CE shortening velocity V_max = 770 mm/sec

As it was shown in Table 6.5, the gemelli muscles, which were first modeled as one muscle, were now divided into the gemelli superior and inferior. Plus, the major muscles of the lower part of the leg were inserted into the model to obtain a better anatomical reproduction of the movements. The new muscles inserted are the tibialis anterior, the soleus and the gastrocnemius.

6.3.2 Example Joint Movement with Active Muscle Forces

A simple example illustrating the use of the activation of muscles was performed. It could be considered as a verification of the active muscle modeling technique before application to the more complex KTH model. Figure 6.13 shows the setup of the simplified model: the femur bone was cut at its mid-shaft and constrained to be fixed at this extremity.

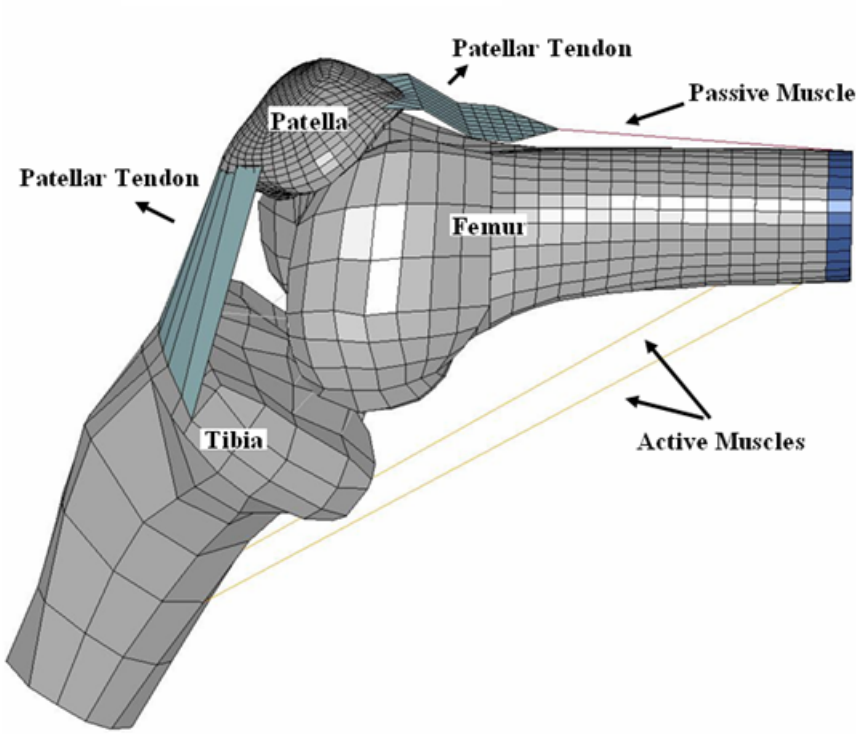

Figure 6.13. Example for muscle activation: setup.

The tibia was cut at its mid-shaft too for simplicity. The patellar tendon, on one side, is attached to one muscle at its origin and is inserted in the patella bone. On the other side, the patellar tendon is connecting the patella with the tibia bone. The muscle from which the patellar tendon originates, was modeled only with passive properties. Two more

muscles were inserted in the model with active properties connecting the fixed extremity of the femur with the tibia.

Results of the simulation are shown in Figures 6.14, 6.15 and 6.16. The active muscles pull the tibia bone as they are supposed to do, while the passive muscle is not working actively. Knee flexion is correctly observed with this example. As it was expected, the active muscles shorten while the passive muscles lengthen (Figure 6.15).

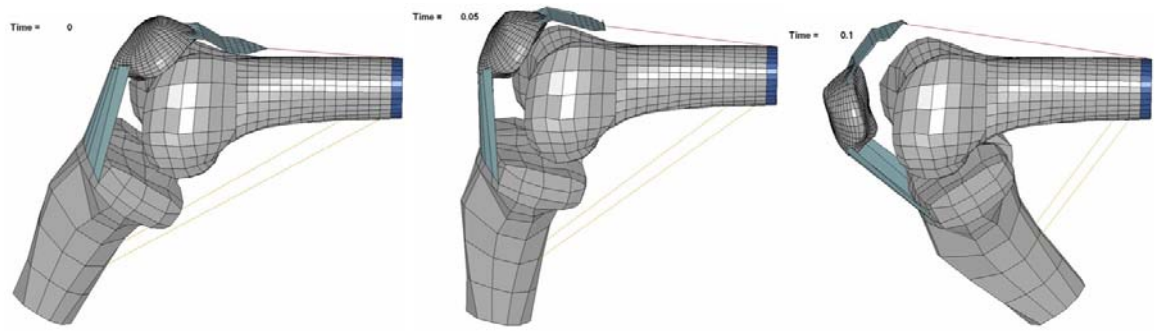

Figure 6.14. Simulation of muscle activation with the patellar tendon modeled with shell elements.

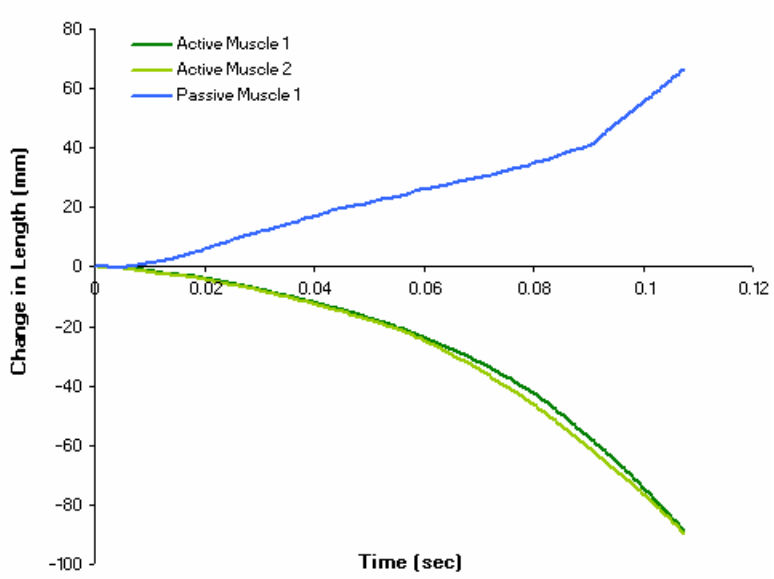

Figure 6.15. Change in length for passive and active muscles from the model.

Figure 6.16 shows the active forces generated by the two active muscles. In this particular example, they do not generate the exact same forces expected, because their origins and insertion sites were not defined symmetrically. The example showed, however, that the active muscles could be used in LSDYNA to generate physically correct joint motion.

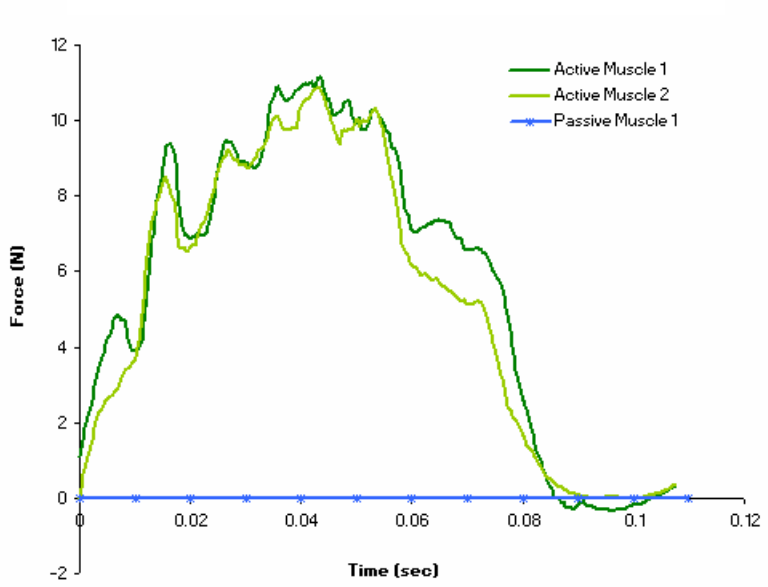

Figure 6.16. Time history of passive and active muscles in a knee flexion.

The only problem encountered during this example was the behavior of the patella which did behave correctly. The patella moves in the right direction but does not slide on the femur bone as it should. It does not seem to be a problem with the patella bone itself but rather the dynamic of the patellar tendon. These non realistic behaviors were overcome by introduction of the patellar tendon modeled with seatbelt material, as already explained in the previous paragraphs.

6.3.3 Including Active Muscle Properties in the KTH model

After ensuring that active muscle properties functioned as expected, activation was applied to selected muscles of the KTH complex in order to perform certain defined movements (i.e., knee flexion, thigh flexion, adduction and abduction). The methodology for defining the activation value for each active muscle during movement is explained in this section. Next, examples are reported with details. Five principal leg movements were considered and reproduced in this part of the research: adduction for 15 degrees, abduction for 15 degrees, thigh flexion of 15 degrees, knee extension and knee flexion of 30 degrees each. Note that thigh extension was not taken into account because of the expectation of not using it to investigate frontal impacts to the KTH at various positions.

6.3.3.1 Methodology

The methodology used integrate of active muscles and their level of activation into the KTH model is described below:

- **Definition of the active muscles**. The first step was to define which muscles are involved for particular movement. A simple way to define the active muscles is to look at the change in length of each muscle from the neutral position to the new configuration. A muscle works when it contracts so those muscles that shorten to reach the new configuration are the active muscles which in fact perform the movement. LsPrePost was used to obtain lengths of each muscle at the initial configuration of zero degrees abduction and thigh flexion (Table 6.6). The command "measure" allows for distances between two nodes (i.e., the nodes of the muscle-spring) to be measured. The KTH model was then moved "manually" with LsPrePost to a new configuration and the lengths of muscles were measured again and compared to the initial ones. For muscles which shortened, active properties were activated in the LSDYNA material model card. For muscles that did not shorten, only passive properties were taken into account.

- **Consideration of the level of activation for each active muscle**. Once the activated muscles were identified, it was necessary to understand the activation level for each of them. In fact, not all muscles involved in a certain movement are participating in the action with the same level of activation. At this point, a simple difference between the new and the initial length for each muscle was calculated and valued as percentage of the muscle initial length.

- **Normalization of the muscles level of activation**. The muscle which reported the highest change in length was assigned the value 1.0 for activation level. All other muscles activation levels were calculated normalizing their own value of percentage of initial length by the higher found. This way, all other activated muscles were assigned values of activation between 0 and 1.0.

- **Definition of the activation level linear curve**. An activation level curve was inserted for the active muscles. A linear curve was chosen and it was defined as shown in Figure 6.17:

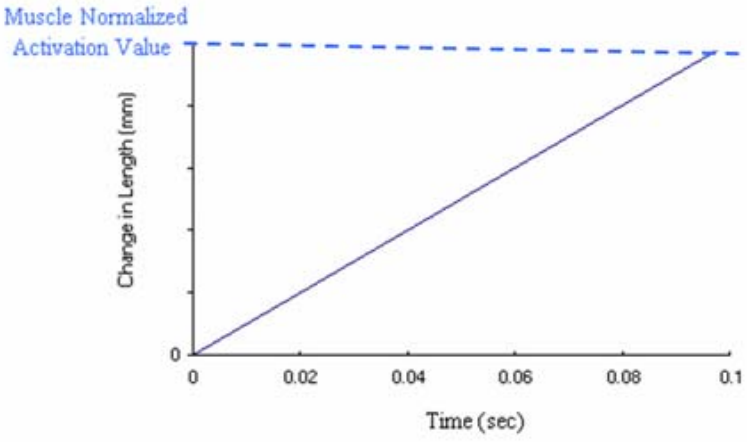

Figure 6.17. Typical activation level curve considered for active muscles.

For a particular movement, the level of activation was defined for each KTH muscles involved in the particular movement by activating the correspondent muscles.
Von Mises stresses were recorded at each step of the simulation.

Table 6.6. Initial length of the KTH muscles with a configuration of zero degrees of thigh flexion and zero degrees of adduction.

Muscle Name	Initial length (mm)	Muscle Name	Initial length (mm)
Pectineus	119.457	Gluteus ME ant	107.426
Iliacus	159.675	Gluteus ME mid	178.822
Tensor FL	468.015	Gluteus ME pos	194.225
Sartorius	468.443	Gluteus MI an	74.4803
Rectus Fem.	392.348	Gluteus MI mi	120.244
Vastus Int.	236.581	Gluteus MI po	149.863
Adductor L	190.729	Piriformis	146.684
Adductor B	106.805	Gemelli	87.19
Adductor M su	109.552	Quadratus	83.899
Adductor M mi	234.13	Semitendinosus	453.602
Adductor M in	351.422	Semimembranosus	405.79
Gracilis	408.189	Biceps Femoris	213.009
Gluteus MA su	177.453	Tibialis Anterior	310.361
Gluteus MA mi	224.126	Soleus	318.204
Gluteus MA in	225.396	Gastrocnemius	432.604

6.3.3.2 15 Degree Abduction

A simulation of an abduction movement of 15 degrees was reproduced. In order to obtain the new configuration of 15 degrees abduction, LsPrePost was used. All bones, with exception of the pelvis, were selected and rotated with respect to node 117006 of the femoral head bone, the center of rotation. The KTH bones were rotated around the "y" axis counterclockwise 15 degrees (Figure 6.18)

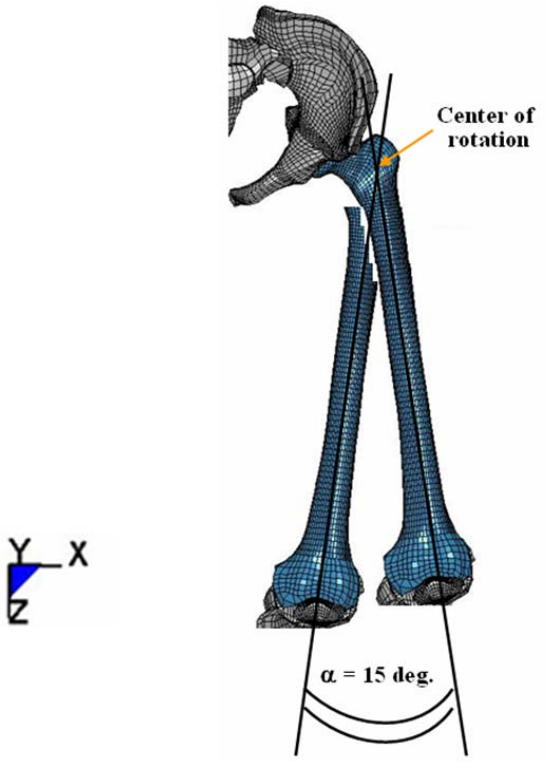

Figure 6.18. Counterclockwise rotation of the model to obtain 15 degrees of abduction.

The methodology explained in the previous pages was followed and lengths of each KTH model muscles were collected at their initial and final position. The difference between the final and initial lengths were computed and reported as a percentage of the initial muscle length. The weight value "a" was then calculated for each active muscle

(Table 6.7). From these data, active muscles during abduction movement were recognized (Figure 6.19).

Table 6.7. Differences in length for all muscles of the KTH after rotation of an angle of 15 degrees in abduction and corresponding activation factor "a" for active muscles.

Part #	Muscle Name	Initial length (mm)	Final length (mm)	DL	|DL|	Percentage of initial length	Weight "a"
100	Pectineus	119.457	132.211	12.754			
101	Iliacus	159.675	154.278	**-5.397**	5.397	3.4	**0.449**
102	Tensor FL	468.015	460.124	**-7.891**	7.891	1.7	**0.224**
103	Sartorius	468.443	461.974	**-6.469**	6.469	1.4	**0.183**
104	Rectus Fem.	392.348	387.73	**-4.618**	4.618	1.2	**0.156**
106	Vastus Int.	236.581	236.581	0			
108	Adductor L	190.729	215.487	24.758			
109	Adductor B	106.805	127.305	20.5			
110	Adductor M su	109.552	112.762	3.21			
111	Adductor M mi	234.13	241.173	7.043			
112	Adductor M in	351.422	363.89	12.468			
113	Gracilis	408.189	424.866	16.677			
114	Gluteus MA su	177.453	172.505	**-4.948**	4.948	2.8	**0.370**
115	Gluteus MA mi	224.126	224.669	0.543			
116	Gluteus MA in	225.396	230.462	5.066			
117	Gluteus ME ant	107.426	107.707	0.281			
118	Gluteus ME mid	178.822	168.525	**-10.297**	10.297	5.8	**0.764**
119	Gluteus ME pos	194.225	186.378	**-7.847**	7.847	4.0	**0.536**
120	Gluteus MI an	74.4803	74.8561	0.3758			
121	Gluteus MI mi	120.244	111.183	**-9.061**	9.061	7.5	**1.000**
122	Gluteus MI po	149.863	140.93	**-8.933**	8.933	6.0	**0.791**
123	Piriformis	146.684	142.643	**-4.041**	4.041	2.8	**0.366**
124	Gemelli	87.19	84.395	**-2.795**	2.795	3.2	**0.425**
125	Quadratus	83.899	87.6184	3.7194			
126	Semitendinosus	453.602	458.444	4.842			
127	Semimembranosus	405.79	422.662	16.872			
128	Biceps Femoris	213.009	213.009	0			
130	Tibialis Anterior	310.361	310.361	0			
131	Soleus	318.204	318.204	0			
132	Gastrocnemius	432.604	432.604	0			

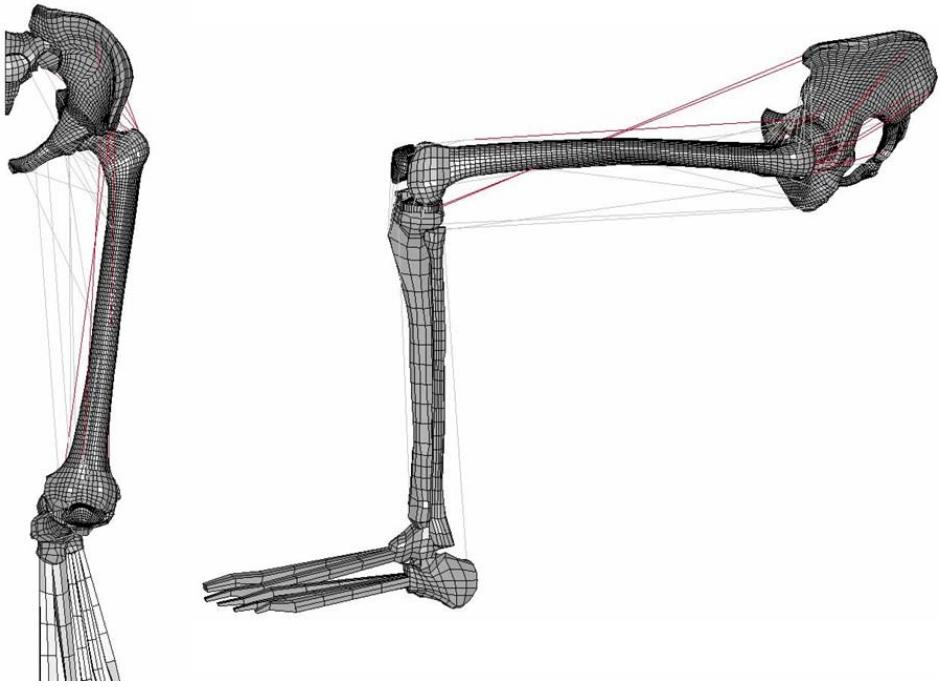

Figure 6.19. Activated muscles for abduction movement: top view (left) and external lateral view (right).

Activation for muscles was included using the LSDYNA *MAT_SPRING_MUSCLE material model card and activation level curves were inserted for each active muscle. The pelvis bone was constrained for all rotations and translations. The femur bone was constrained not to move along "z" axis. Previous simulations showed that, during abduction and adduction movements, thigh flexion was performed, though activation was applied exclusively to those muscles supposed to work on abduction/adduction only. The explanation for this probably has to do with the complex dynamics of muscles which can have different purposes that are not reproduced completely with this simple model. For the purposes of this research, however, it was enough to constrain the "z" translation movement of the femur in order to obtain pure abduction/adduction movements. When using the activation curve, a major problem occurred. Even setting the activation level to zero, after the desired position had been obtained, did not bring the motion to a stop. When activated, the muscle kept working until the end of the simulation, moving the bones far beyond the angle of abduction it was

set to reach. In order to stop the simulation at the right moment, the angle of abduction was requested in LsPrePost, with use of the "Measur – Angle 4node" card. (LSTC, 2007b) This card allows for the measurement of an angle between two pairs of defined nodes. In this case, two fictitious mass nodes were defined in the original model to be parallel to other two nodes located on the axe of the femur. At this point, the angle between this fictitious pair of nodes and the axial-located one was controlled.

In this way, the desired abduction movement was reproduced (Figure 6.20).

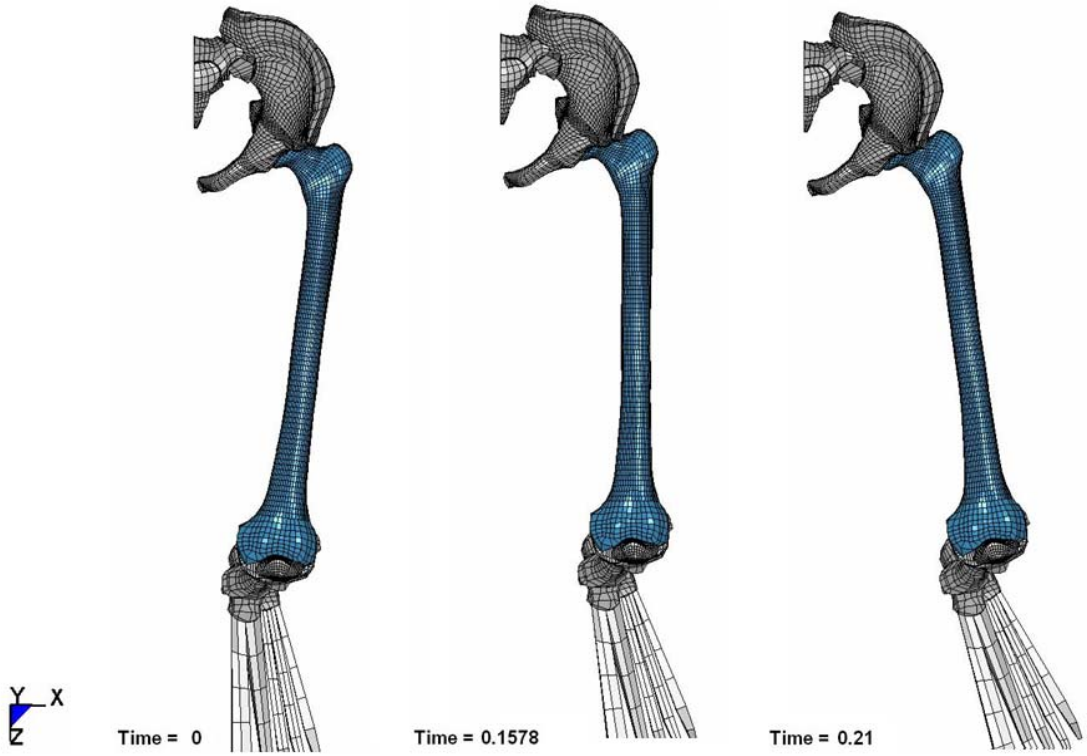

Figure 6.20. Moments of the lower limb abduction movement simulation at time 0 sec, 0.1578 sec and 0.21 sec.

Figures 6.21 and 6.22 shows the change in length and the force generated by the active muscles during the 15 degree abduction movement.

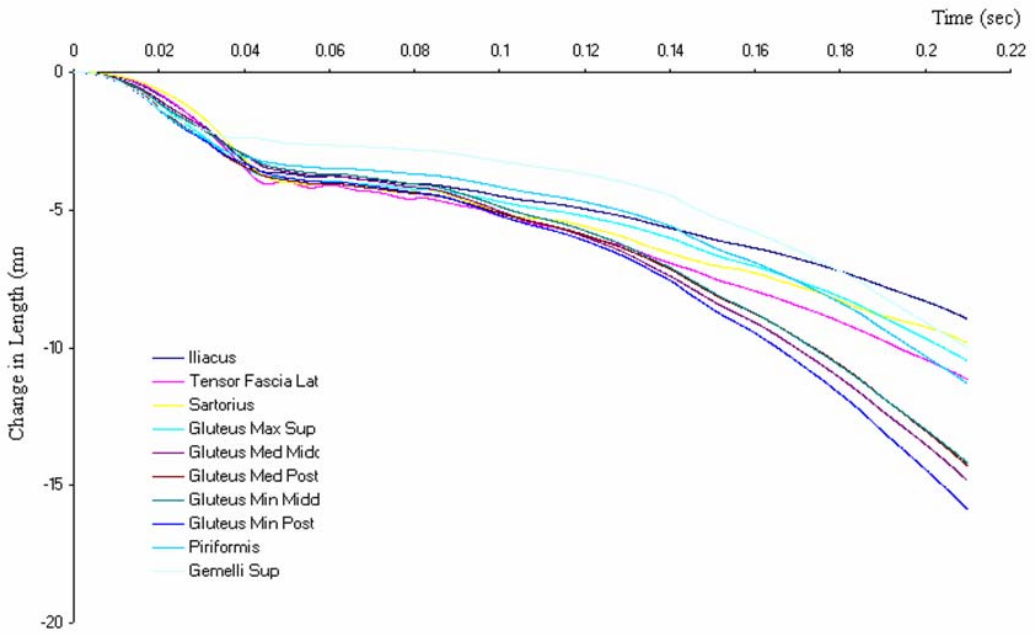

Figure 6.21. Change in length for active muscles during abduction movement.

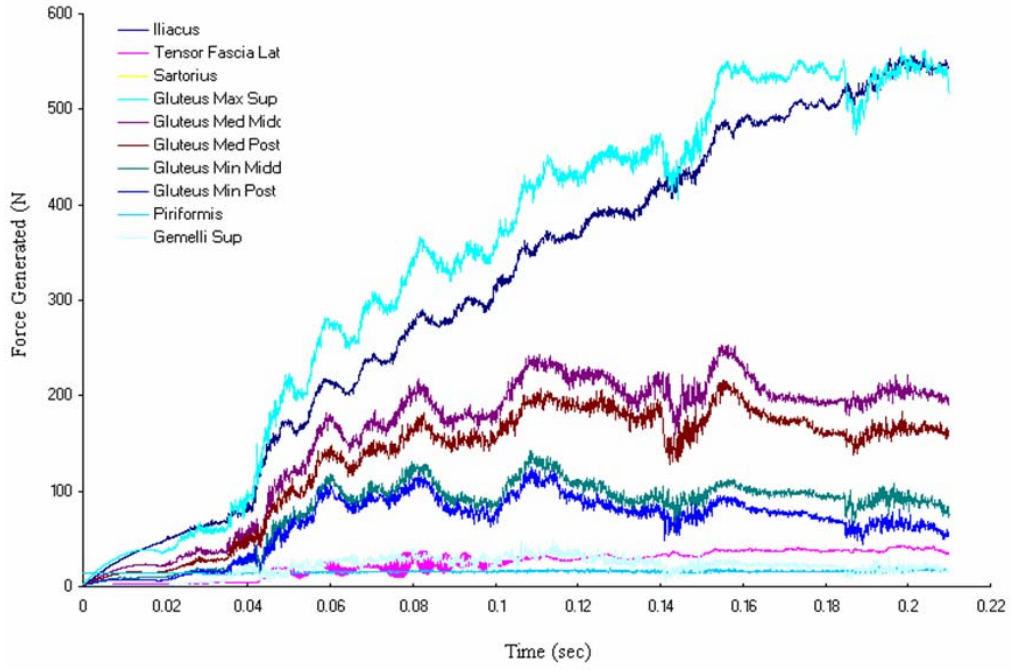

Figure 6.22. Force generated by active muscles during abduction movement.

The command “Fcomp” in LsPrePost allows the visualization of stresses in the model elements. Moreover, by checking the “static” command, a constant min/max range is computed using all time states values (LSTC, 2007b)). (Figure 6.23) Von Mises stresses of the bones were investigated during the movement with LsPrePost (Figures 6.24 and 6.25).

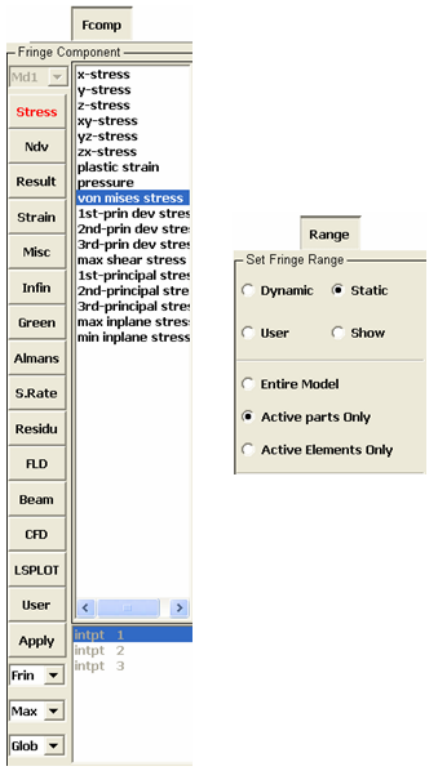

Figure 6.23. “Fcomp” command (left) and “range” command (right) in LsPrePost. (LSTC, 2007b)

Figure 6.25 shows that during the 15 degree abduction movement, higher stresses are recorded at the internal part of the femoral head and at the external conjunction of the femur shaft with the femoral lower trochanter region. These will probably be the candidate zones for bone fractures when impacting the KTH complex in this position. Figure 6.26 shows a linear interpolation of the Von Mises stresses values reached in some indicative elements of these bone areas.

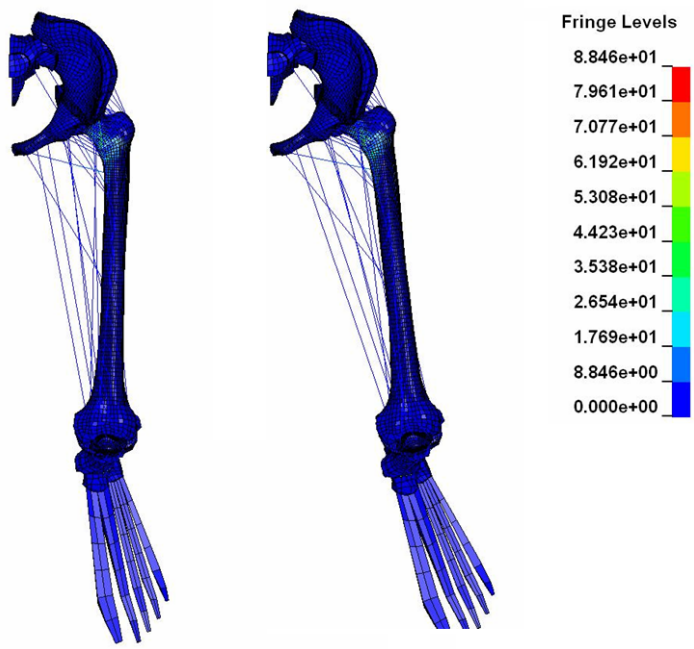

Figure 6.24. Von Mises stresses during abduction movement.

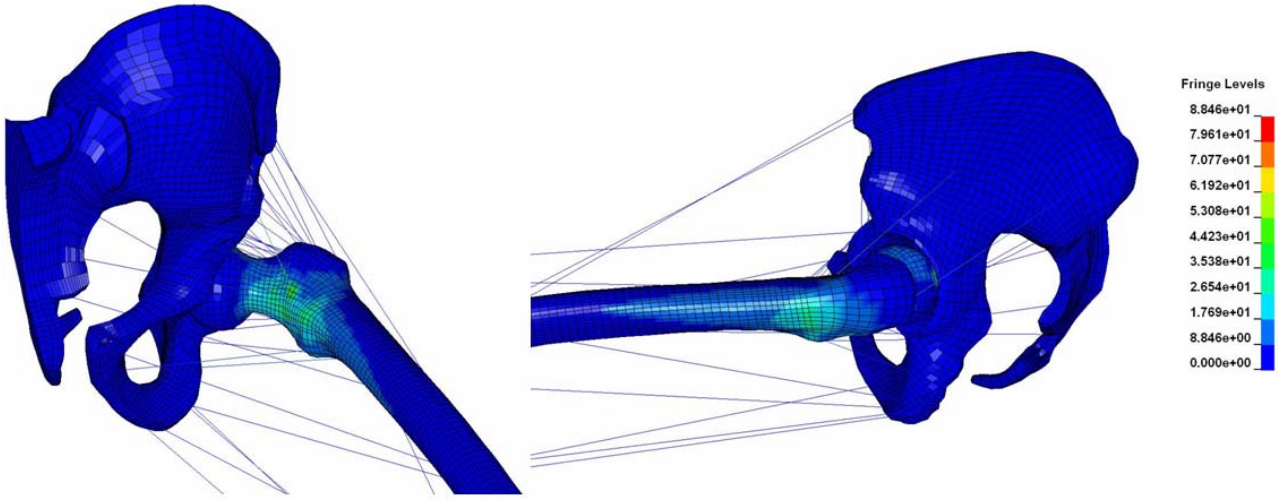

Figure 6.25. Von Mises stresses at the femoral head during abduction movement.

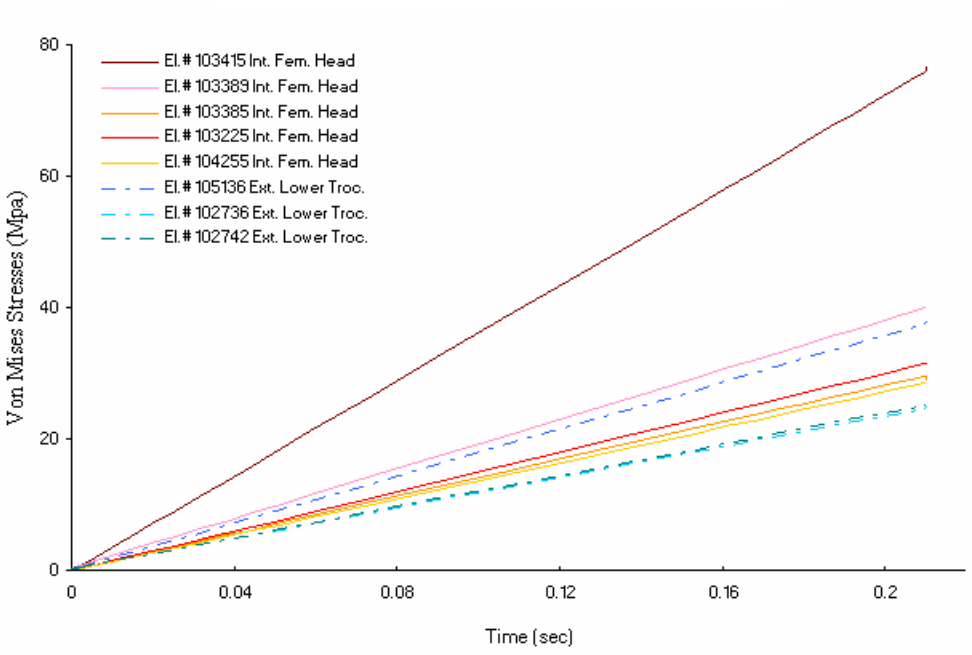

Figure 6.26. Von Mises stresses during the 15 degree abduction movement in the internal femoral head and at the external lower trochanter region.

6.3.3.3 15 Degree Adduction

A simulation of an adduction movement of 15 degrees was reproduced. In order to obtain the new configuration of 15 degrees adduction, LsPrePost was used. All bones, with exception of the pelvis were selected and rotated with respect to node 117006 of the femoral head bone, the center of rotation. The KTH bones were rotated around the "y" axis clockwise of 15 degrees (Figure 6.27)

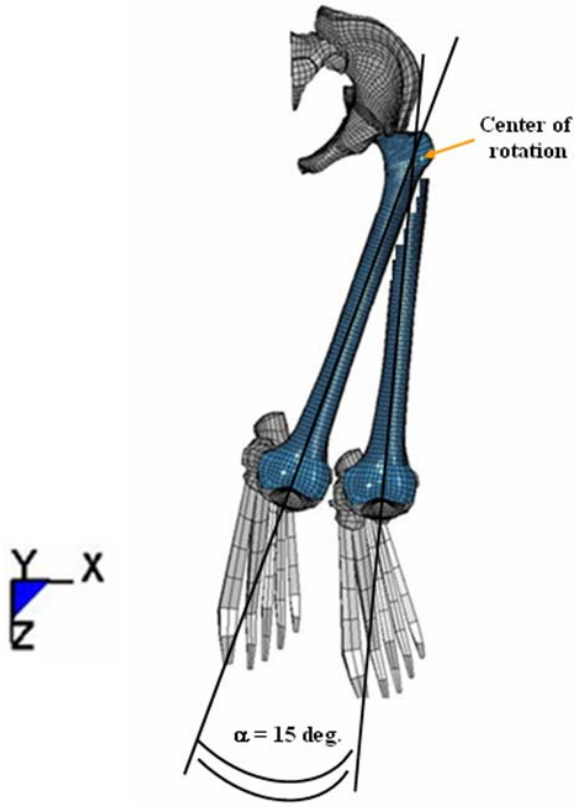

Figure 6.27. Clockwise rotation of the model to obtain 15 degrees of adduction.

The methodology explained in the previous pages was followed and lengths of each of the KTH muscles were collected at their initial and final positions. The difference between the final and initial lengths were computed and reported as a percentage of the initial muscle length. The weight value "a" was then calculated for each active muscle

(Table 6.8). From these data, active muscles during adduction movement were recognized (Figure 6.28).

Table 6.8. Differences in length for all muscles of the KTH after rotation of an angle of 15 degrees in adduction and corresponding activation factor "a" for active muscles.

Part #	Muscle Name	Initial length (mm)	Final length (mm)	DL	|DL|	Percentage of initial length	Weight "a"
100	Pectineus	119.457	109	**-10.457**	10.457	8.8	**0.497**
101	Iliacus	159.675	164	4.325			
102	Tensor FL	468.015	476	7.985			
103	Sartorius	468.443	476	7.557			
104	Rectus Fem.	392.348	397	4.652			
106	Vastus Int.	236.581	236.581	0			
108	Adductor L	190.729	170	**-20.729**	20.729	10.9	**0.617**
109	Adductor B	106.805	88	**-18.805**	18.805	17.6	**1.000**
110	Adductor M su	109.552	106	**-3.552**	3.552	3.2	**0.184**
111	Adductor M mi	234.13	228	**-6.13**	6.13	2.6	**0.149**
112	Adductor M in	351.422	341	**-10.422**	10.422	3.0	**0.168**
113	Gracilis	408.189	394	**-14.189**	14.189	3.5	**0.197**
114	Gluteus MA su	177.453	182	4.547			
115	Gluteus MA mi	224.126	220	**-4.126**	4.126	1.8	**0.105**
116	Gluteus MA in	225.396	217	**-8.396**	8.396	3.7	**0.212**
117	Gluteus ME ant	107.426	110	2.574			
118	Gluteus ME mid	178.822	189	10.178			
119	Gluteus ME pos	194.225	202	7.775			
120	Gluteus MI an	74.4803	130	55.5197			
121	Gluteus MI mi	120.244	130	9.756			
122	Gluteus MI po	149.863	160	10.137			
123	Piriformis	146.684	152	5.316			
124	Gemelli Superior	87.19	92	4.81			
125	Quadratus	83.899	79	**-4.899**	4.899	5.8	**0.332**
126	Semitendinosus	453.602	449	**-4.602**	4.602	1.0	**0.058**
127	Semimembranosus	396	391	**-5**	5	1.3	**0.072**
128	Biceps Femoris	213.009	213	**-0.009**	0.009	0.0	**0.000**
130	Tibialis Anterior	310.361	310.361	0			
131	Soleus	318.204	318.204	0			
132	Gastrocnemius	432.604	432.604	0			
2124	Gemelli Inferior	86.8	88.8	2			

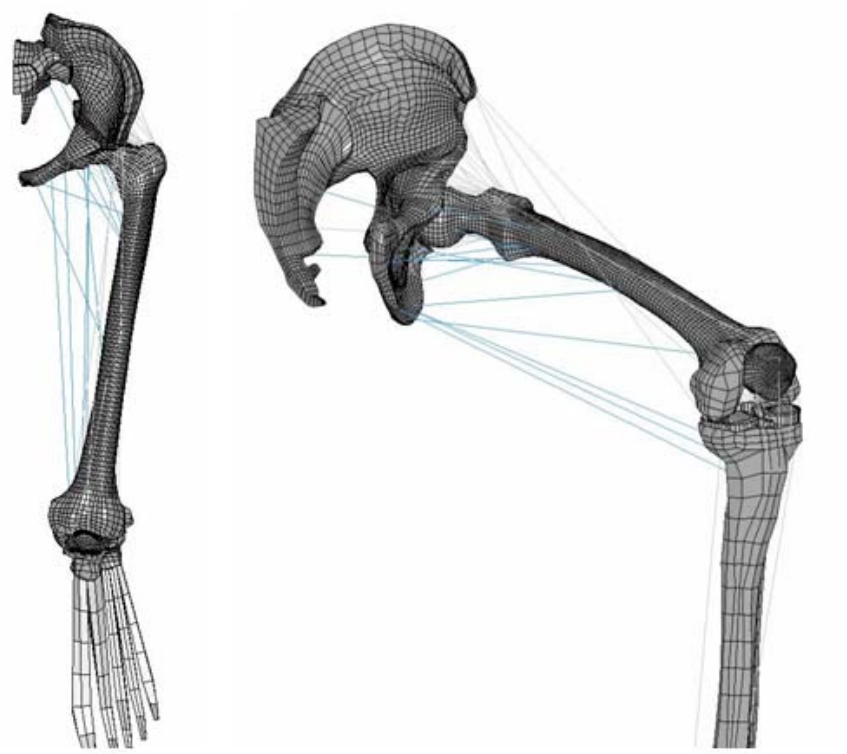

Figure 6.28. Activated muscles for adduction movement: top view (left) and internal lateral view (right).

Activation for the muscles was accomplished using the LSDYNA *MAT_SPRING_MUSCLE material model card and appropriate activation level curves were inserted for each active muscle. The pelvis was constrained for all rotations and translations. The femur was constrained to not move along "z" axis as previously explained for the "abduction" movement. The card "measur – angle 4node" from LsPrePost was used to reaching the correct angle of adduction.

In this way the desired adduction movement was reproduced (Figure 6.29).

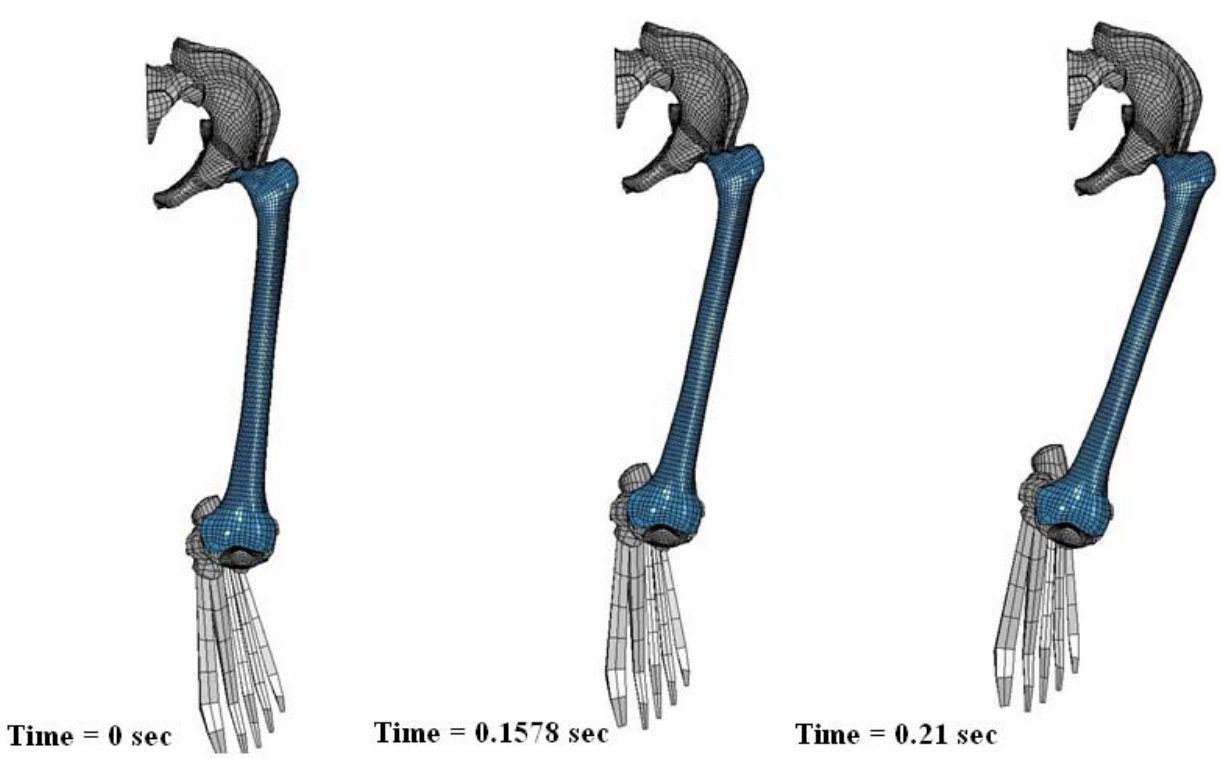

Figure 6.29. Movements of the lower limb for 15 degree adduction movement at time 0 sec, 0.1578 sec and 0.21 sec.

Figures 6.30 and 6.31 show the change in length and the force generated by active muscles during adduction movement. Figures 6.32 and 6.33 show the Von Mises stresses recorded during adduction movement by the KTH bones.

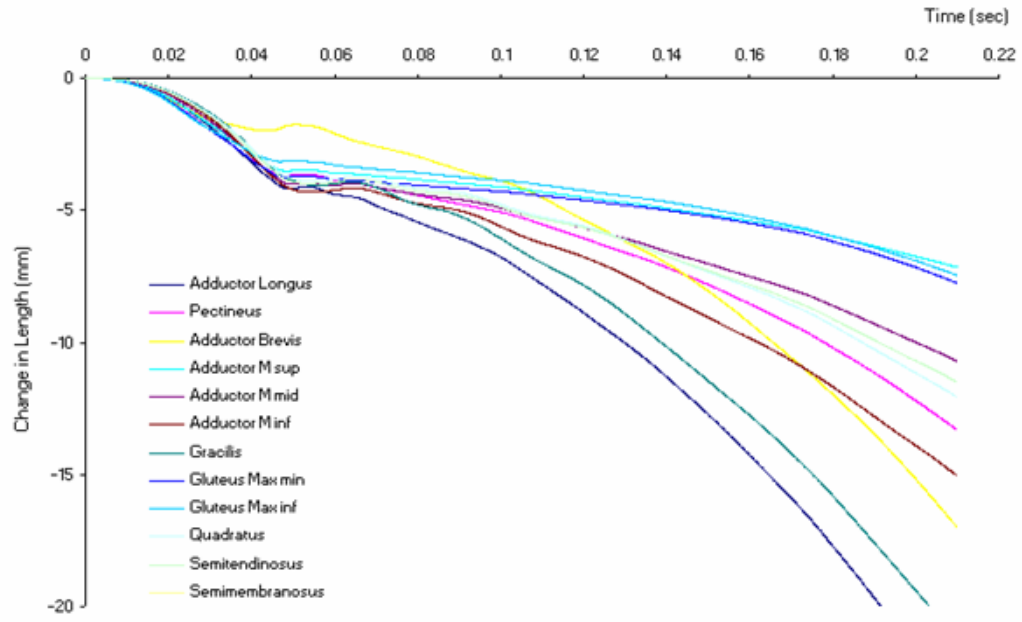

Figure 6.30. Change in length for active muscles during adduction movement.

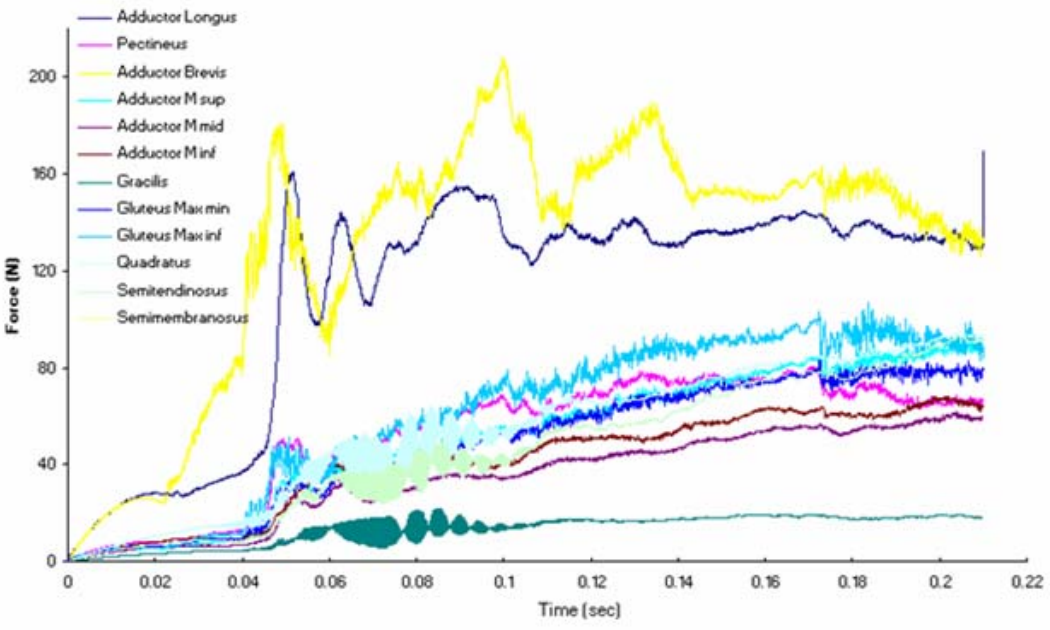

Figure 6.31. Force generated by active muscles during adduction movement.

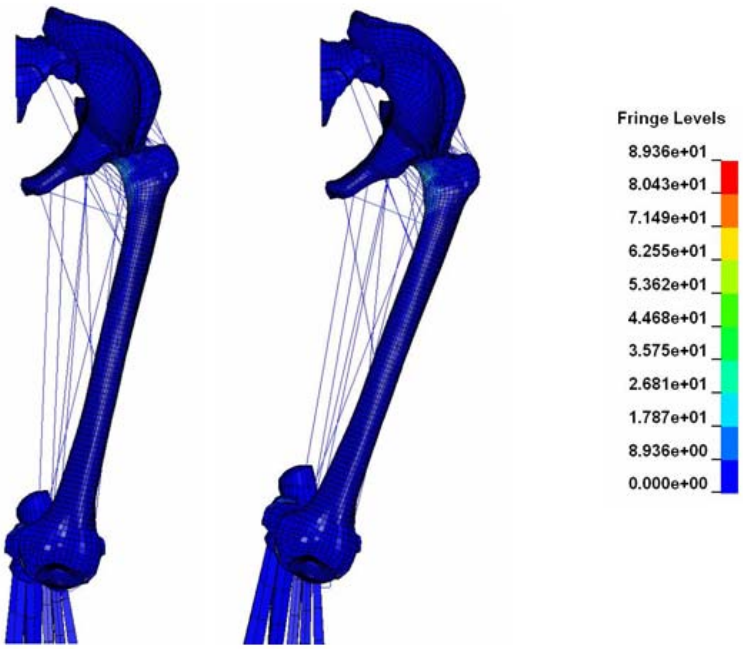

Figure 6.32. Von Mises stresses during adduction movement.

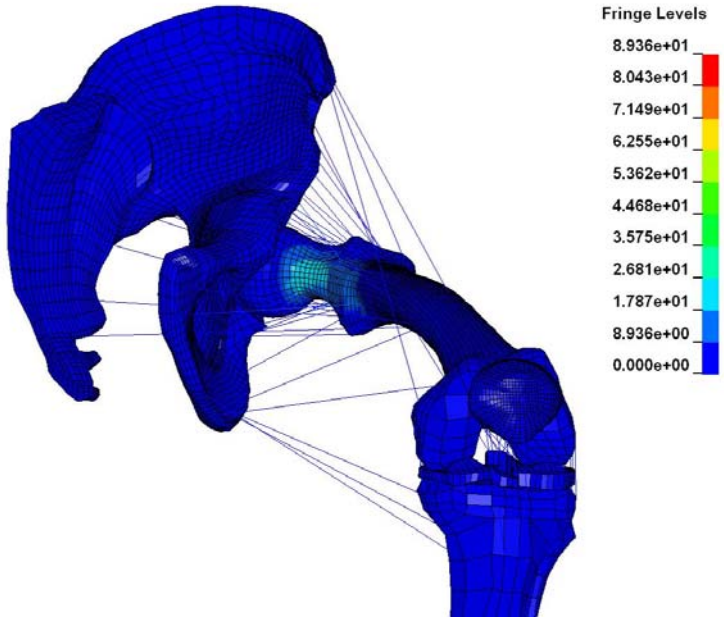

Figure 6.33. Von Mises stresses at the femoral head during adduction movement.

During the movement of adduction, higher stresses are recorded at the internal part of the femoral head and at the internal beginning of the femoral shaft. These will probably be the candidate zones for bone fractures when impacting the KTH complex in this position. Figure 6.34 shows a linear interpolation of the Von Mises stresses values reached in some indicative elements of these bone areas.

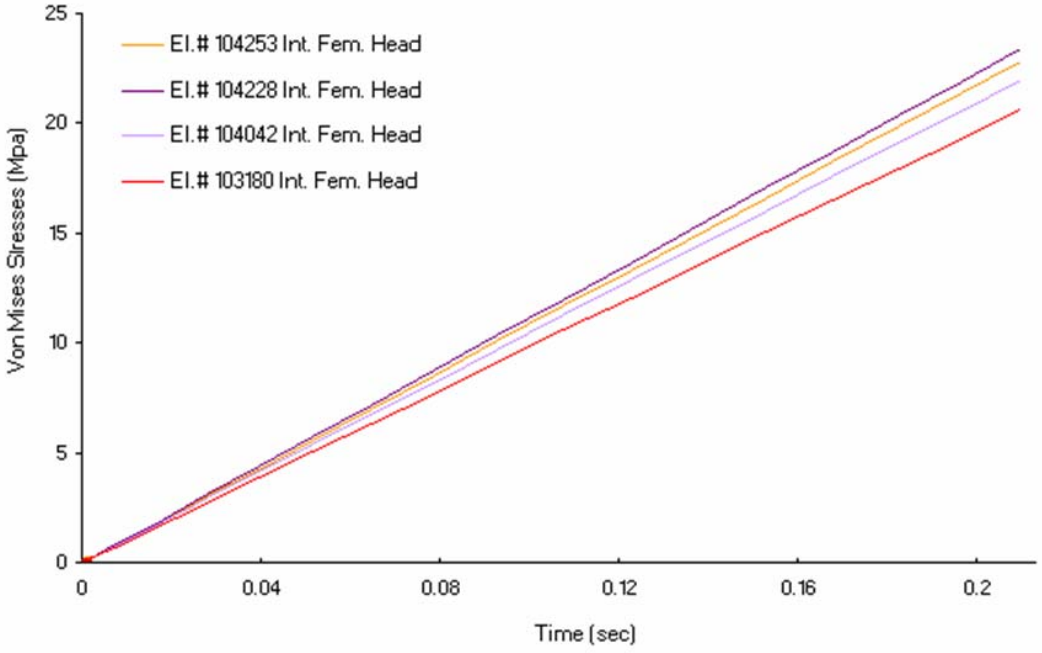

Figure 6.34. Von Mises stresses during adduction movement, recorded at the internal femoral head and at the upper internal femoral shaft regions.

6.3.3.4 15 Degree Thigh Flexion

A simulation of a thigh flexion movement of 15 degrees was reproduced. In order to obtain the new configuration of 15 degrees adduction, LsPrePost was used. All bones, with the exception of the pelvis were selected and rotated negatively around the "x" axis, counterclockwise 15 degrees with respect to node 117006 of the femoral head bone, the center of rotation about the x axis (Figure 6.35).

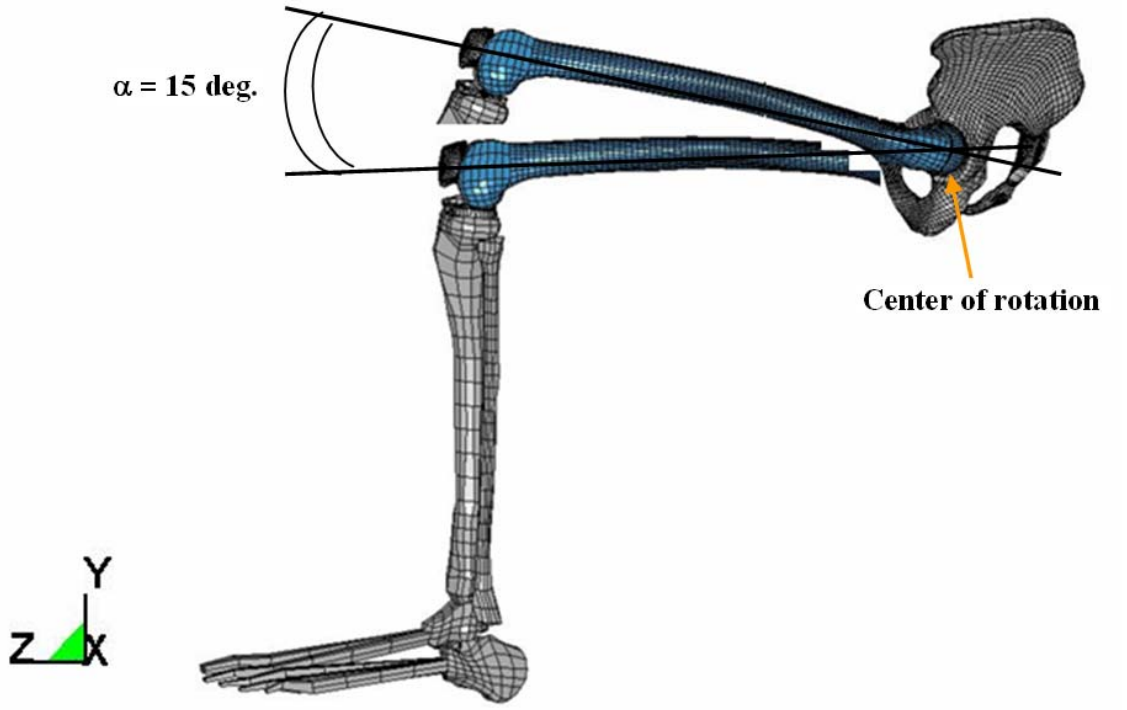

Figure 6.35. Clockwise rotation of the model to obtain 15 degrees of thigh flexion angle.

The lengths of each of the KTH muscles were collected at their initial and final positions. The difference of final and initial lengths were computed and reported also as a percentage of initial muscle length. The weight value "a" was then calculated for each active muscle (Table 6.9).

From these data, active muscles during thigh flexion movement were recognized (Figure 6.36).

Table 6.9. Differences in length for all muscles of the KTH model after 15 degree rotation of thigh flexion and corresponding activation factor "a" for active muscles.

Part #	Muscle Name	Initial length (mm)	Final length (mm)	DL	|DL|	Percentage of initial length	Weight "a"
100	Pectineus	119.457	115	**-4.457**	4.457	3.7	**0.671**
101	Iliacus	159.675	151	**-8.675**	8.675	5.4	**0.977**
102	Tensor FL	468.015	442	**-26.015**	26.015	5.6	**1.000**
103	Sartorius	468.443	442	**-26.443**	26.443	5.6	**1.016**
104	Rectus Fem.	392.348	384	**-8.348**	8.348	2.1	**0.383**
106	Vastus Int.	236.581	236.581	0			
108	Adductor L	190.729	192	1.271			
109	Adductor B	106.805	109	2.195			
110	Adductor M su	109.552	121	11.448			
111	Adductor M mi	234.13	251	16.87			
112	Adductor M in	351.422	371	19.578			
113	Gracilis	408.189	424	15.811			
114	Gluteus MA su	177.453	178	0.547			
115	Gluteus MA mi	224.126	223	**-1.126**	1.126	0.5	**0.090**
116	Gluteus MA in	225.396	231	5.604			
117	Gluteus ME ant	107.426	102	**-5.426**	5.426	5.1	**0.909**
118	Gluteus ME mid	178.822	177	**-1.822**	1.822	1.0	**0.183**
119	Gluteus ME pos	194.225	196	1.775			
120	Gluteus MI an	74.4803	73	**-1.4803**	1.4803	2.0	**0.358**
121	Gluteus MI mi	120.244	120	**-0.244**	0.244	0.2	**0.037**
122	Gluteus MI po	149.863	152	2.137			
123	Piriformis	146.684	151	4.316			
124	Gemelli Superior	87.19	89	1.81			
125	Quadratus	83.899	90	6.101			
126	Semitendinosus	453.602	473	19.398			
127	Semimembranosus	396	437	41			
128	Biceps Femoris	213	213	0			
130	Tibialis Anterior	310.361	310.361	0			
131	Soleus	318.204	318.204	0			
132	Gastrocnemius	432.604	432.604	0			
2124	Gemelli Inferior	86.8	90.5	3.7			

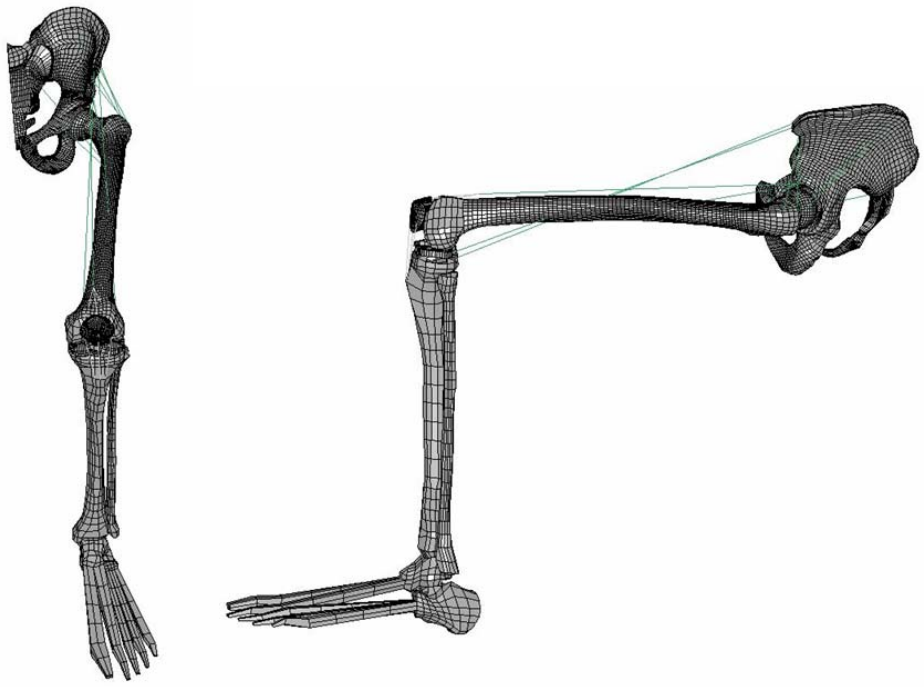

Figure 6.36. Activated muscles for thigh flexion movement: frontal view (left) and external lateral view (right).

At this point, activation for muscles was considered in the LSDYNA *MAT_SPRING_MUSCLE material model Card and adequate activation level curves were inserted for each active muscle. The pelvis bone was constrained in all rotations and translations. The patella bone was constrained not to move along "x" axis. Previous simulations showed that, during flexion movements, the patella was having some unrealistic small translation along "x" axis, though activation was applied exclusively to those muscles supposed to work on flexion only. For the purposes of this research, it was enough to constrain in "x" translation the movement of the patella in order to obtain pure flexion movement. Card "Measur – Angle 4node" from LsPrePost was used for reaching the right angle of thigh flexion.

In this way the desired thigh flexion movement was reproduced (Figure 6.37).

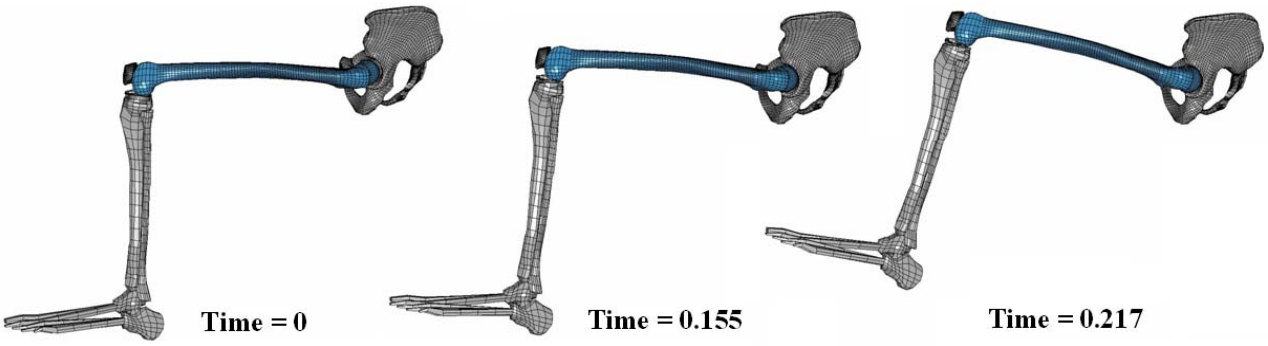

Figure 6.37. Movements of 15 degree thigh flexion at time 0 sec, 0.155 sec and 0.217 sec.

Figures 6.38 and 6.39 show the change in length and the force generated by active muscles during flexion movement.

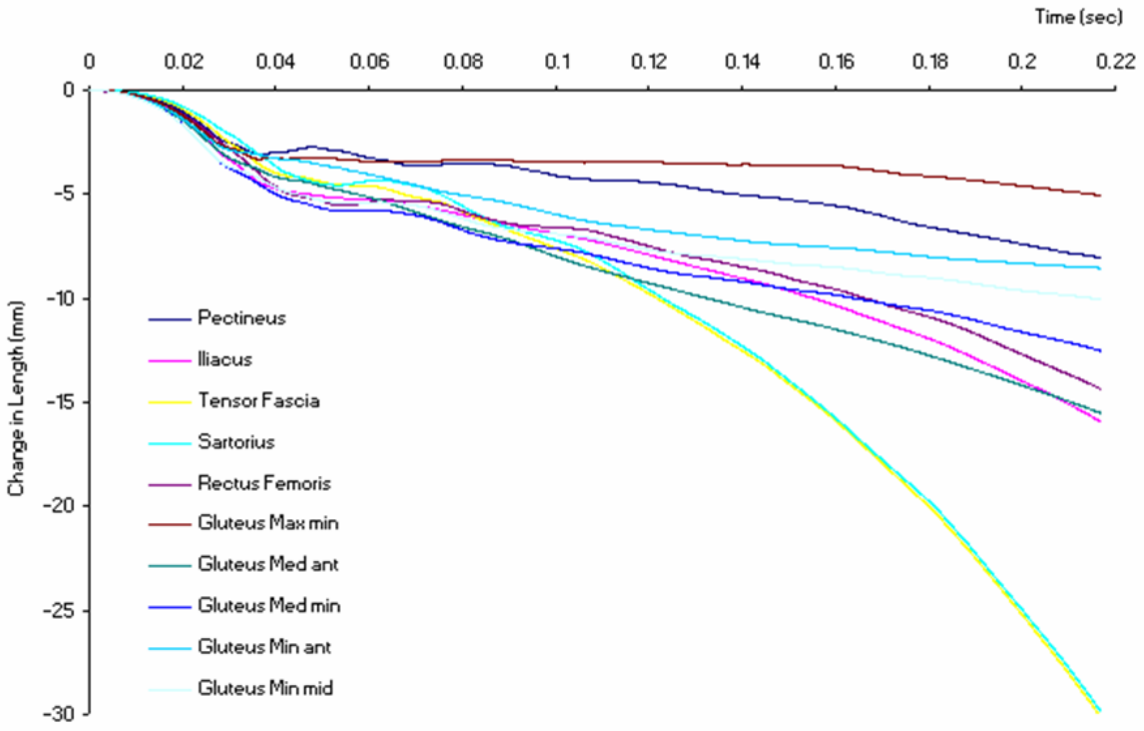

Figure 6.38. Change in length for active muscles during thigh flexion movement.

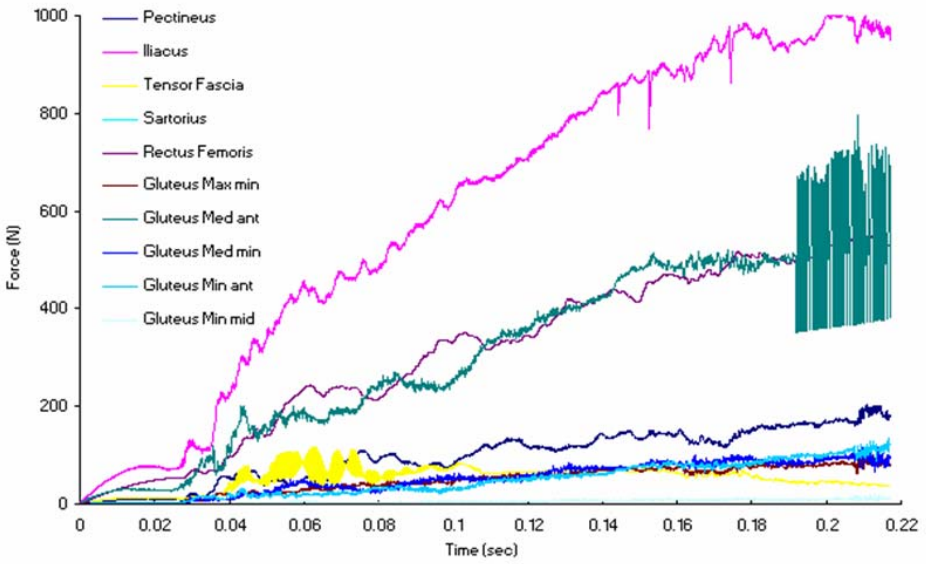

Figure 6.39. Force generated by active muscles during thigh flexion movement.

Figure 6.40 shows the Von Mises stresses of the KTH bones recorded during the 15 degree flexion movement.

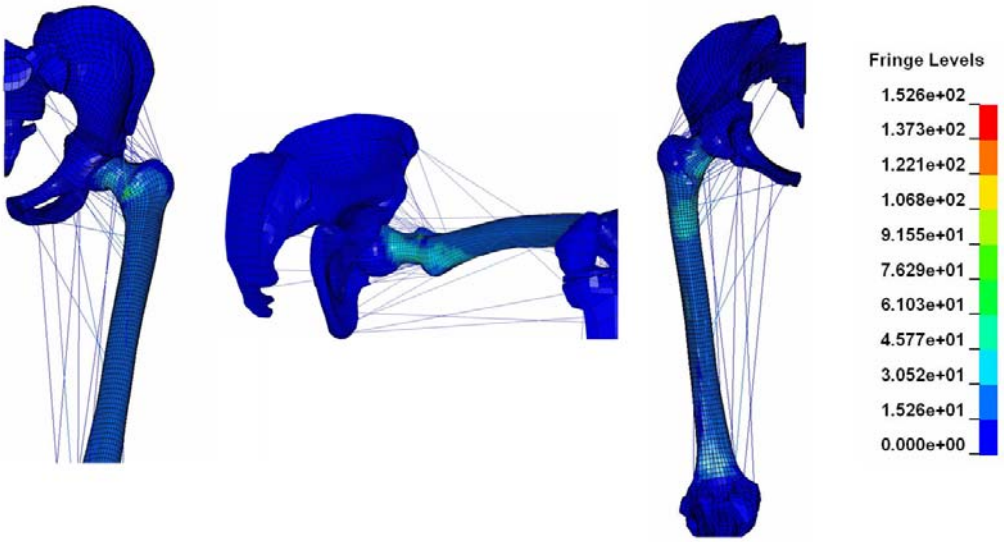

Figure 6.40. Von Mises stresses during 15 degree thigh flexion movement: top view (left), internal view (center) and bottom view (right).

During the 15 degree thigh flexion movement, higher stresses were recorded at the internal part of the femoral head and at the lower trochanter and at the upper posterior femoral shaft. These will probably be the candidate zones for bone fractures when impacting the KTH in this position. Figure 6.41 shows a linear interpolation of the Von Mises stresses values reached in some indicative elements of these bone areas.

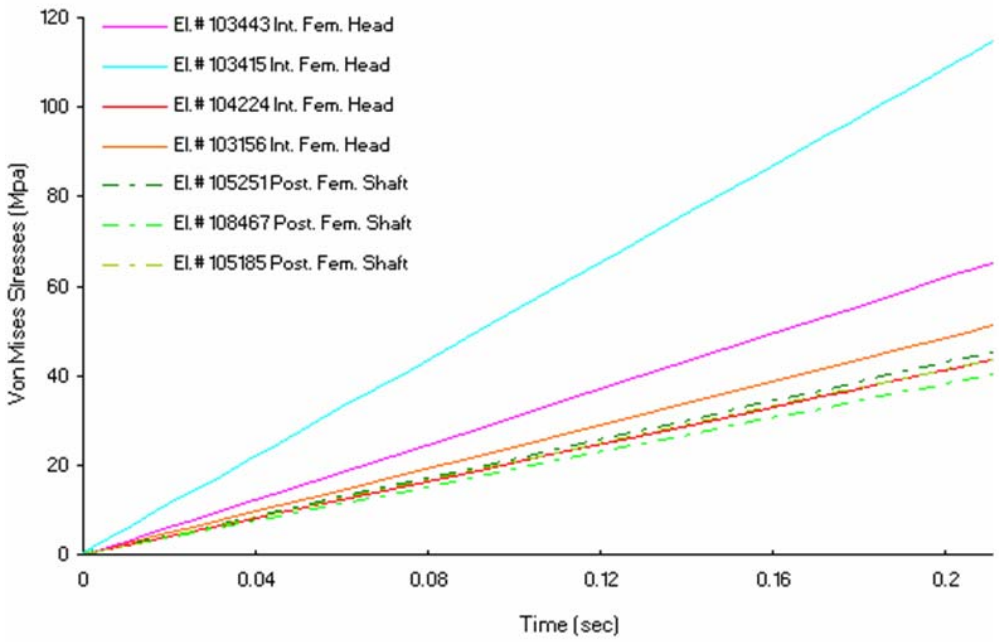

Figure 6.41. . Von Mises stresses during 15 degree thigh flexion movement recorded at the internal femoral head, the lower trochanter and the upper posterior femoral shaft regions.

6.3.3.5 30 Degree Knee Extension

A simulation of knee extension movement of 30 degrees was reproduced. In order to obtain the new configuration of 30 degree knee extension, LsPrePost was used. Tibia, fibula, foot bones and menisci were selected and rotated negatively around the x axis, clockwise 30 degrees with respect to node 101010 of the knee femoral condyles, the center of rotation about the axis (Figure 6.42).

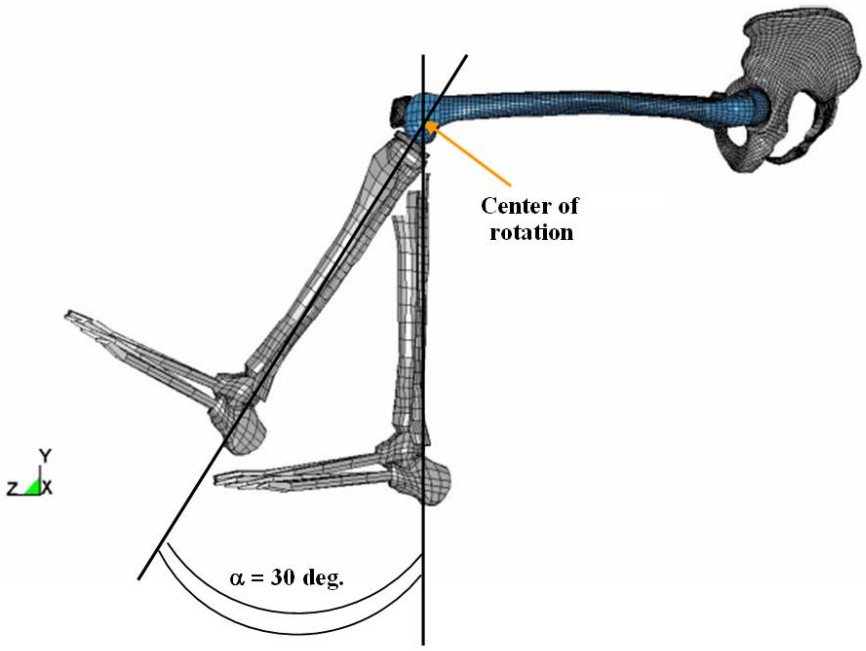

Figure 6.42. Clockwise rotation of the model to obtain 15 degrees of knee extension.

The lengths of each of the KTH muscles were collected at their initial and final positions. The difference of final and initial lengths were computed and reported as a percentage of the initial muscle length. The weight value "a" was then calculated for each active muscle (Table 6.10).

From these data, active muscles during knee extension movement were recognized (Figure 6.43).

Table 6.10. Differences in length for all muscles of the KTH after 30 degree knee extension rotation and corresponding activation factor "a" for active muscles.

Part #	Muscle Name	Initial length (mm)	Final length (mm)	DL	|DL|	Percentage of initial lengtl	Weight "a"
100	Pectineus	119.457	119.457	0			
101	Iliacus	159.675	159.675	0			
102	Tensor FL	468.015	476.505	8.49			
103	Sartorius	468.443	484.321	15.878			
104	Rectus Fem.	392.348	387.848	**-4.5**	4.5	1.1	0.603
106	Vastus Int.	236.581	232.081	**-4.5**	4.5	1.9	1.000
108	Adductor L	190.729	190.729	0			
109	Adductor B	106.805	106.805	0			
110	Adductor M su	109.552	109.552	0			
111	Adductor M mi	234.13	234.13	0			
112	Adductor M in	351.422	351.422	0			
113	Gracilis	408.189	437.482	29.293			
114	Gluteus MA su	177.453	177.453	0			
115	Gluteus MA mi	224.126	224.126	0			
116	Gluteus MA in	225.396	225.396	0			
117	Gluteus ME ant	107.426	107.426	0			
118	Gluteus ME mid	178.822	178.822	0			
119	Gluteus ME pos	194.225	194.225	0			
120	Gluteus MI an	74.4803	74.4803	0			
121	Gluteus MI mi	120.244	120.244	0			
122	Gluteus MI po	149.863	149.863	0			
123	Piriformis	146.684	146.684	0			
124	Gemelli	87.19	87.1947	0.0047			
125	Quadratus	83.899	83.899	0			
126	Semitendinosus	453.602	479.353	25.751			
127	Semimembranosus	396	435.899	39.899			
128	Biceps Femoris	213	218.958	5.958			
130	Tibialis Anterior	310.361	310.361	0			
131	Soleus	318.204	318.204	0			
132	Gastrocnemius	432.604	432.604	0			
2124	Gemelli Inferior	86.8	86.8892	0.0892			

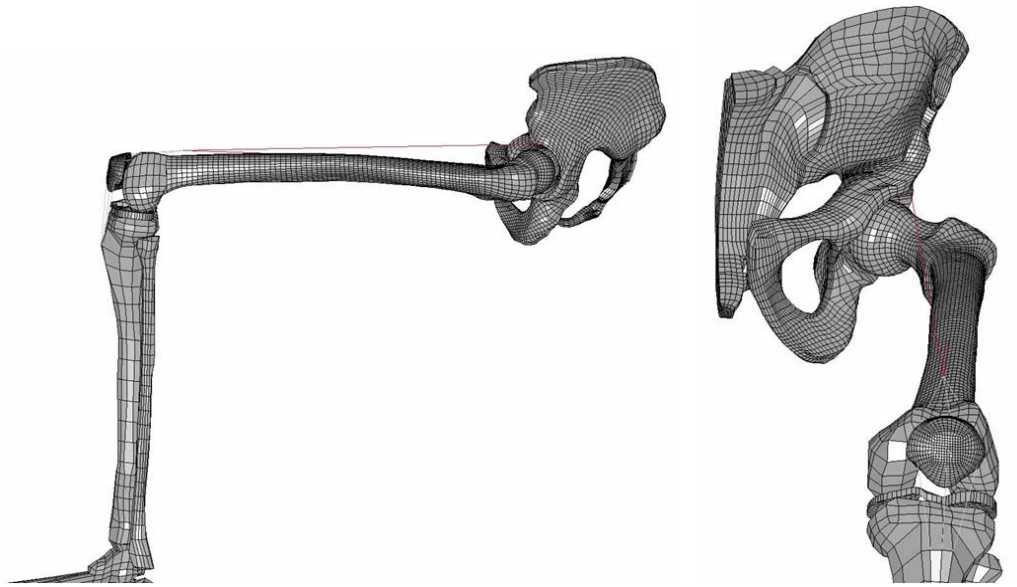

Figure 6.43. Activated muscles for knee extension movement: lateral view (left) and frontal view (right).

Activation for muscles was accomplished using the LSDYNA *MAT_SPRING_MUSCLE material model card and appropriate activation level curves were inserted for each active muscle. The pelvis bone was constrained for all rotations and translations. The card "measur – angle 4node" from LsPrePost was used to set the correct final angle of knee extension.

In this way the desired knee extension movement was reproduced (Figure 6.44).

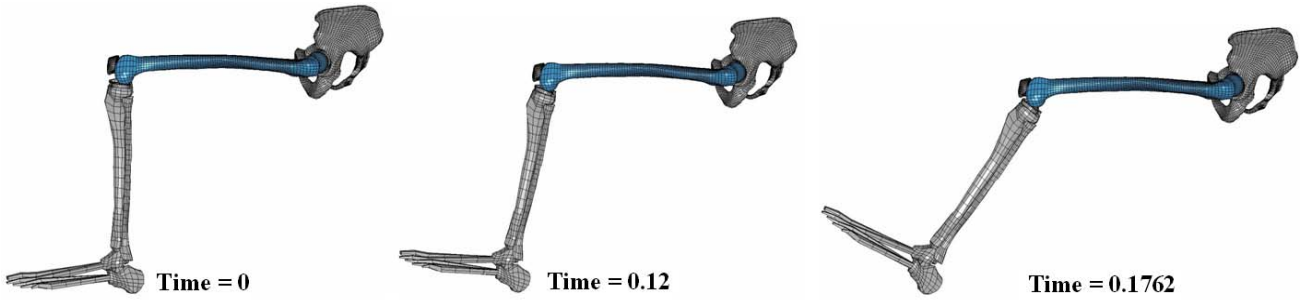

Figure 6.44. Moments of the knee extension movement simulation at time 0 sec, 0.12 sec and 0.1762 sec.

Figures 6.45 and 6.46 show the change in length and force generated by active muscles during the 30-degree knee extension movement.

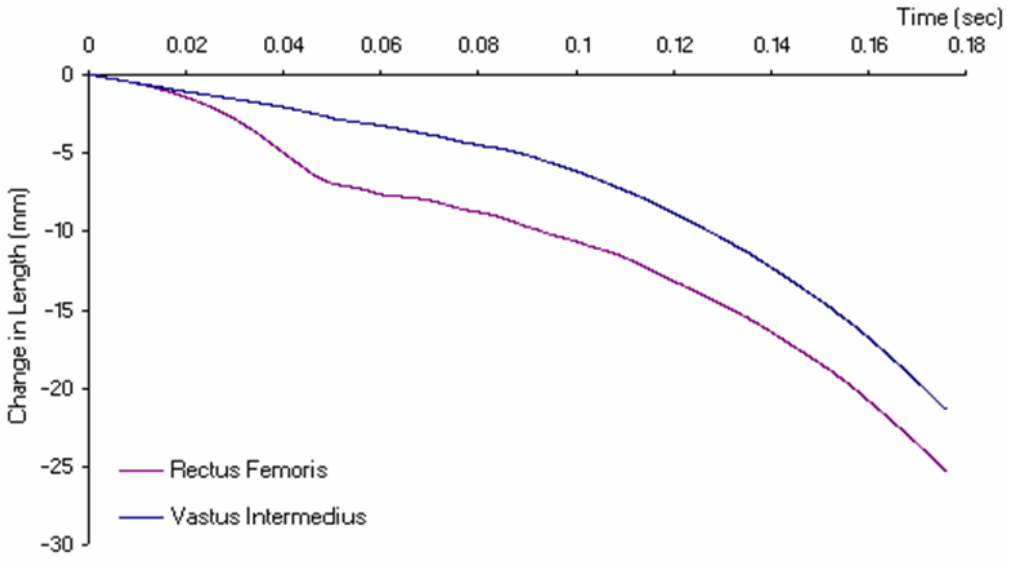

Figure 6.45. Change in length for active muscles during knee extension movement.

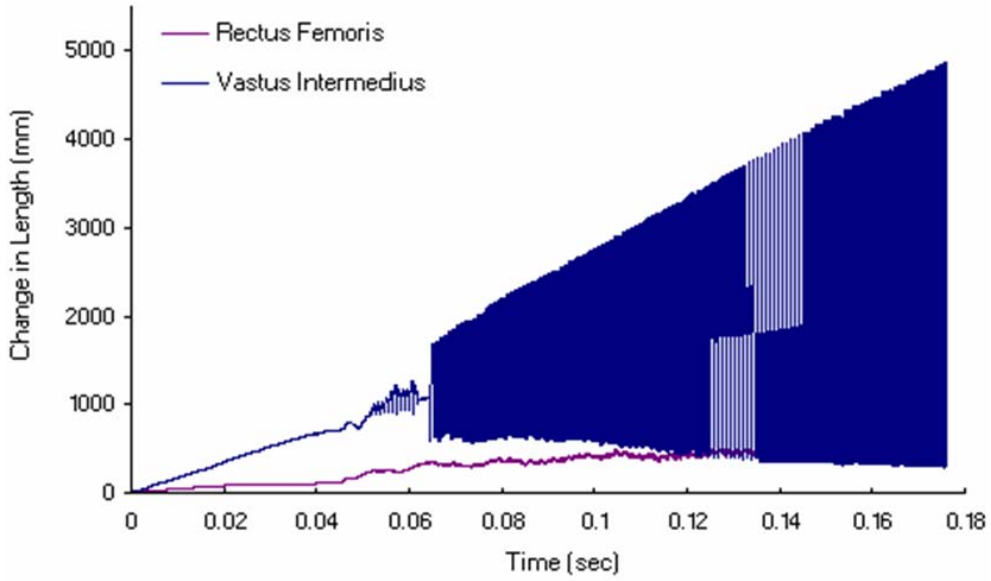

Figure 6.46. Force generated by active muscles during knee extension movement.

Figure 6.47 shows the Von Mises stresses recorded during knee extension movement by the KTH bones.

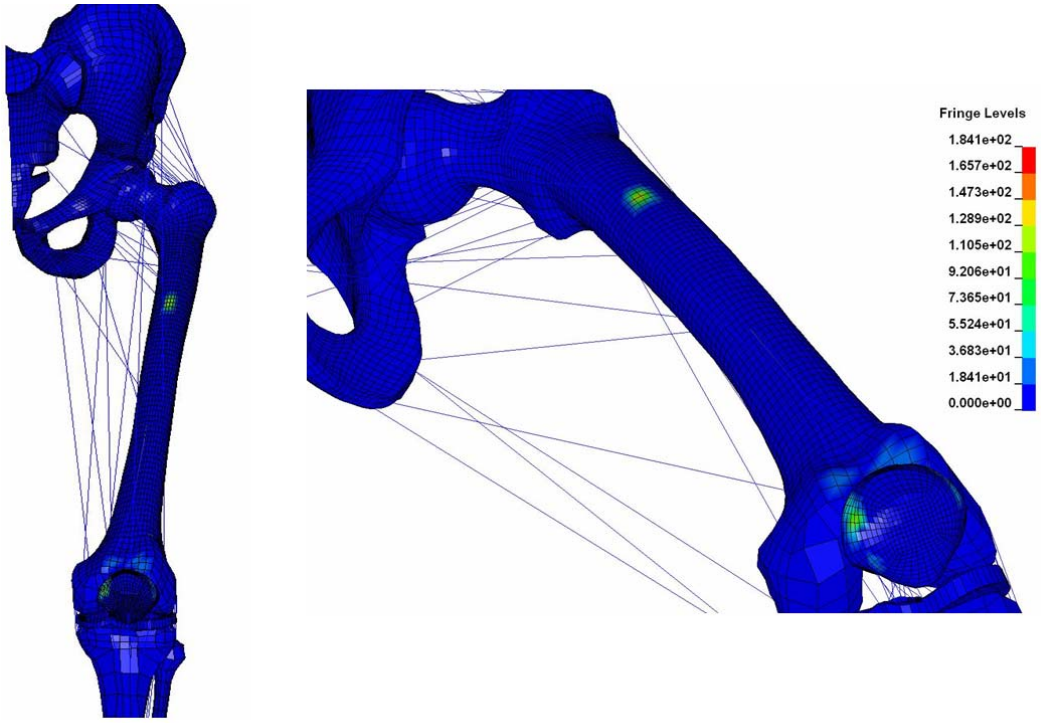

Figure 6.47. Von Mises stresses during knee extension movement at top view (left) and internal view (right).

During the movement of thigh flexion, higher stresses are recorded at the femoral shaft, where the Vastus intermedius muscle inserts, and at the patella bone, where the Patellar tendon inserts. These will probably be the candidate zones for bone fractures when impacting the KTH complex in this position. Figure 6.48 shows a linear interpolation of the Von Mises stresses values reached in some indicative elements of these bones

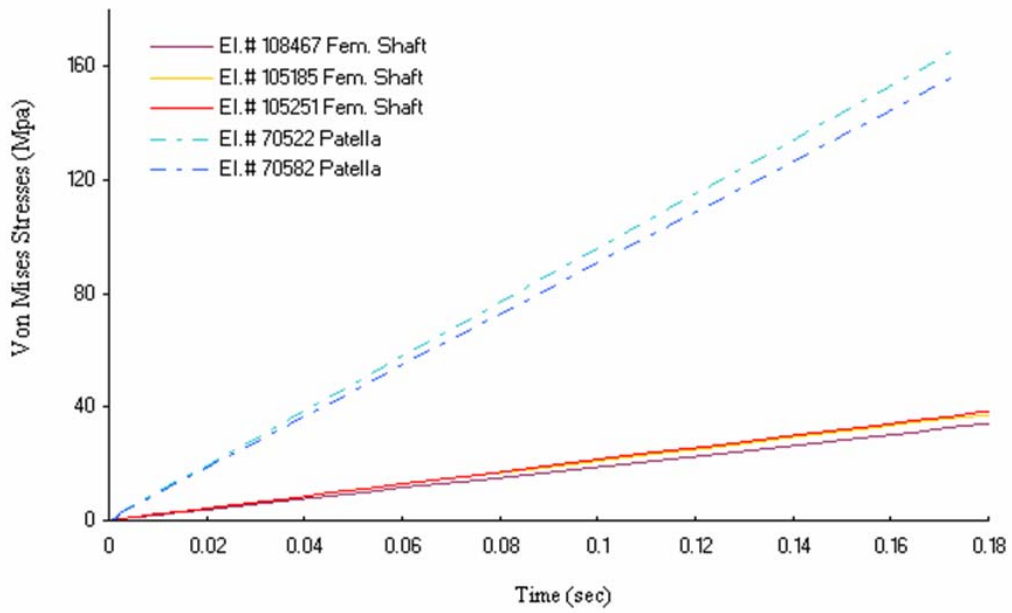

Figure 6.48. Von Mises stresses during knee extension movement, recorded at the femoral shaft and at the patella bone.

6.3.3.6 10 Degree Knee Flexion

A simulation of knee flexion movement of 10 degrees was reproduced. In order to obtain the new configuration of 10 degrees knee flexion, LsPrePost was used. Tibia, fibula, foot bones and menisci were selected and rotated positively around the x axis, counterclockwise 10 degrees with respect to node 101010 of the knee femoral condyles, the center of rotation about the axis (Figure 6.49).

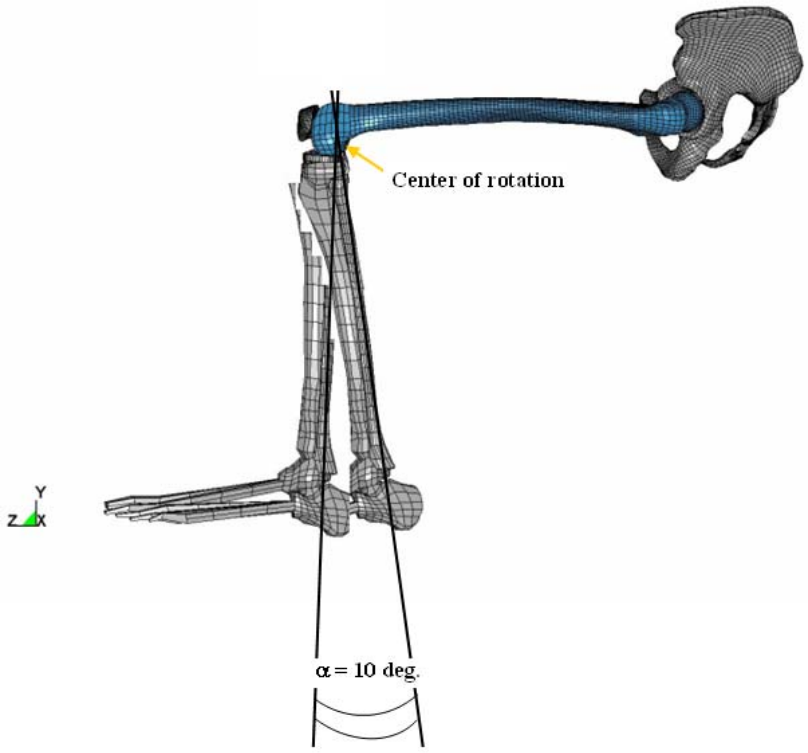

Figure 6.49. Counterclockwise rotation of the model to obtain 10 degrees of knee flexion.

The lengths of each of the KTH muscles were collected at their initial and final positions. The difference of final and initial lengths were computed and reported as a percentage of the initial muscle length. The weight value "a" was then calculated for each active muscle (Table 6.11).

From these data, active muscles during knee extension movement were recognized (Figure 6.50).

Table 6.11. Differences in length for all muscles of the KTH after 10 degree knee extension rotation and corresponding activation factor "a" for active muscles.

Part #	Muscle Name	Initial length (mm)	Final length (mm)	DL	|DL|	Percentage of initial lengtl	Weight "a"
100	Pectineus	119.457	119.457	0			
101	Iliacus	159.675	159.675	0			
102	Tensor FL	468.015	449.515	**-18.5**	18.5	4.0	**0.465**
103	Sartorius	468.443	444.687	**-23.756**	23.756	5.1	**0.597**
104	Rectus Fem.	392.348	418.324	25.976			
106	Vastus Int.	236.581	263	26.419			
108	Adductor L	190.729	190.729	0			
109	Adductor B	106.805	106.805	0			
110	Adductor M su	109.552	109.552	0			
111	Adductor M mi	234.13	234.13	0			
112	Adductor M in	351.422	351.422	0			
113	Gracilis	408.189	373.504	**-34.685**	34.685	8.5	**1.000**
114	Gluteus MA su	177.453	177.453	0			
115	Gluteus MA mi	224.126	224.126	0			
116	Gluteus MA in	225.396	225.396	0			
117	Gluteus ME ant	107.426	107.426	0			
118	Gluteus ME mid	178.822	178.822	0			
119	Gluteus ME pos	194.225	194.225	0			
120	Gluteus MI an	74.4803	74.4803	0			
121	Gluteus MI mi	120.244	120.244	0			
122	Gluteus MI po	149.863	149.863	0			
123	Piriformis	146.684	146.684	0			
124	Gemelli	87.19	87.1947	0.0047			
125	Quadratus	83.899	83.899	0			
126	Semitendinosus	453.602	419.783	**-33.819**	33.819	7.5	**0.877**
127	Semimembranosus	396	397.489	1.489			
128	Biceps Femoris	213	207.115	**-5.885**	5.885	2.8	**0.325**
130	Tibialis Anterior	310.361	310.361	0			
131	Soleus	318.204	318.204	0			
132	Gastrocnemius	432.604	432.604	0			
2124	Gemelli Inferior	86.8	86.8892	0.0892			

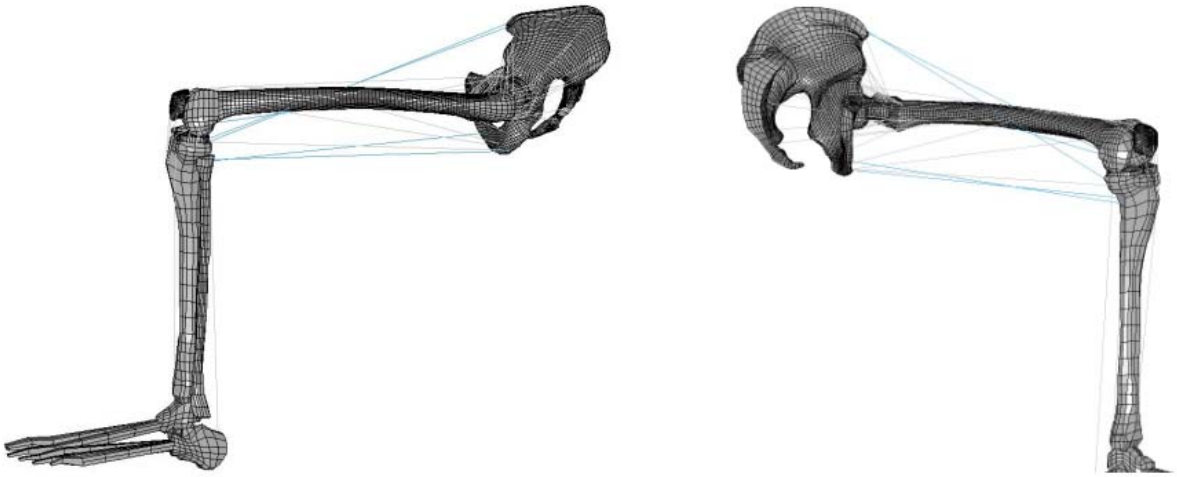

Figure 6.50. Activated muscles for knee flexion movement: frontal view (left) and external lateral view (right).

Activation for muscles was accomplished using the LSDYNA *MAT_SPRING_MUSCLE material model card and appropriate activation level curves were inserted for each active muscle. The pelvis bone was constrained for all rotations and translations. The card "measur – angle 4node" from LsPrePost was used to set the correct final angle of knee flexion.

In this way the desired knee flexion movement was reproduced (Figure 6.51).

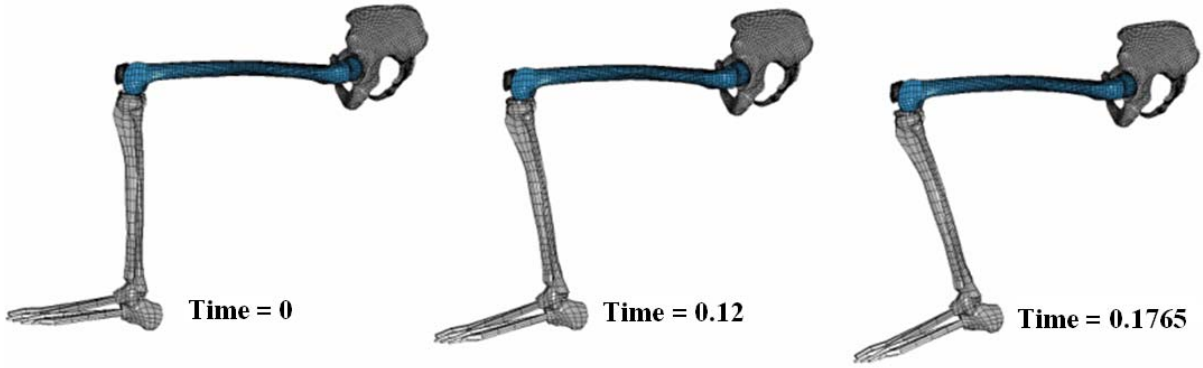

Figure 6.51. Moments of the knee flexion movement simulation at time 0 sec, 0.12 sec and 0.1765 sec.

Figures 6.52 and 6.53 show the change in length and force generated by active muscles during the 10 degree knee extension movement.

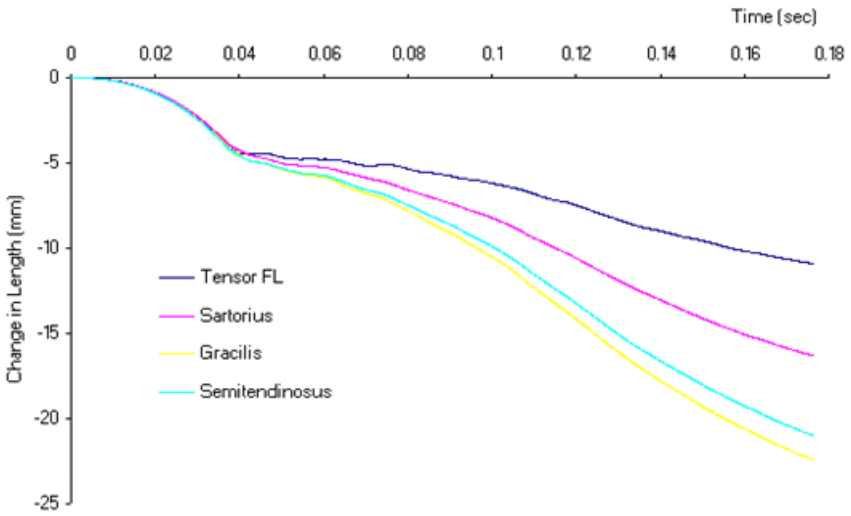

Figure 6.52. Change in length for active muscles during knee flexion movement.

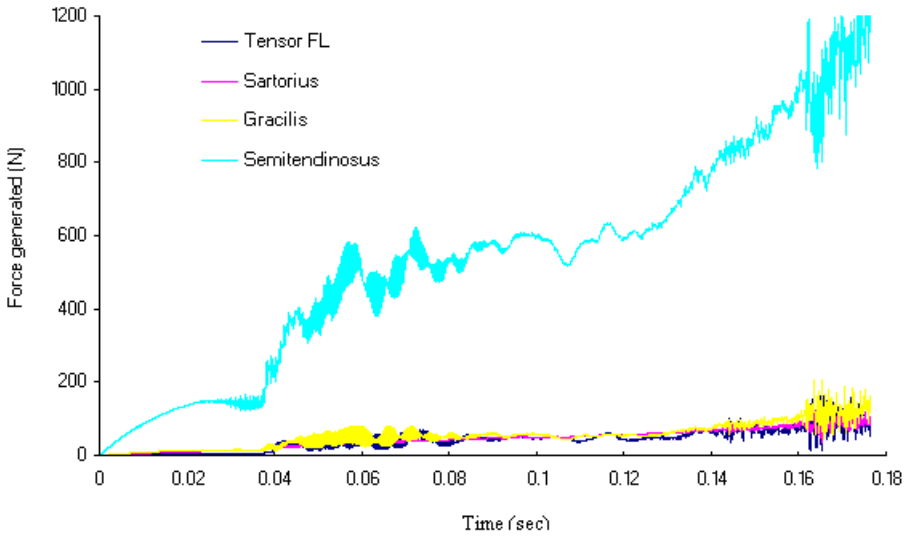

Figure 6.53. Force generated by active muscles during knee flexion movement.

Figure 6.54 shows the Von Mises stresses recorded during knee flexion movement by the KTH bones.

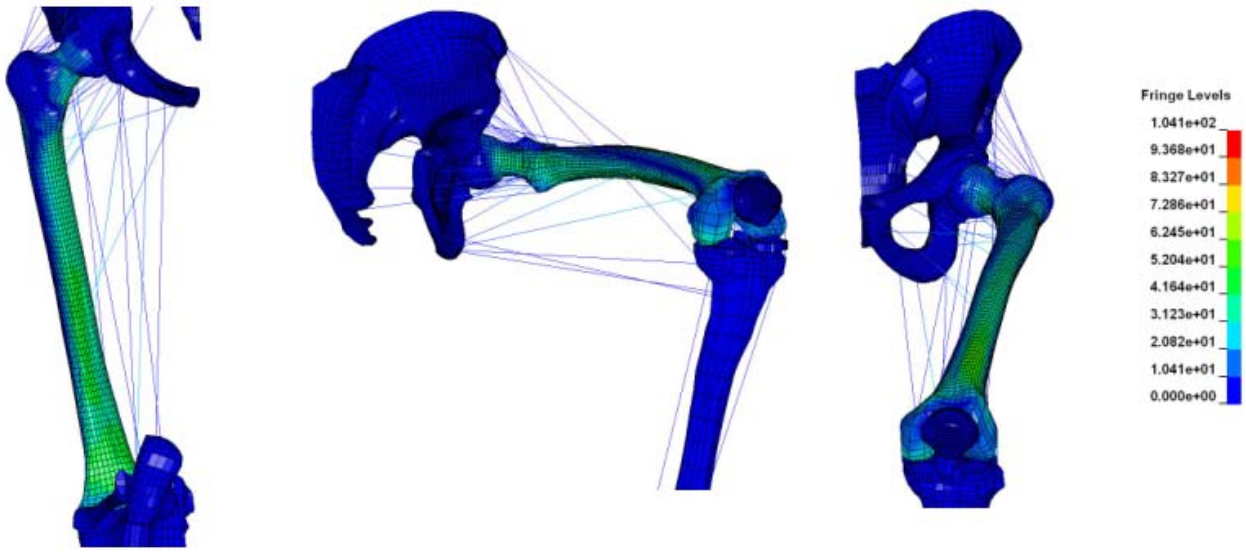

Figure 6.54. Von Mises stresses during knee flexion movement: bottom view (left), internal view (center) and frontal view (right).

During the movement of thigh flexion, higher stresses are recorded along all femoral shaft. These will probably be the candidate zones for bone fractures when impacting the KTH complex in this position. Figure 6.55 shows a linear interpolation of the Von Mises stresses values reached in some indicative elements of these bones

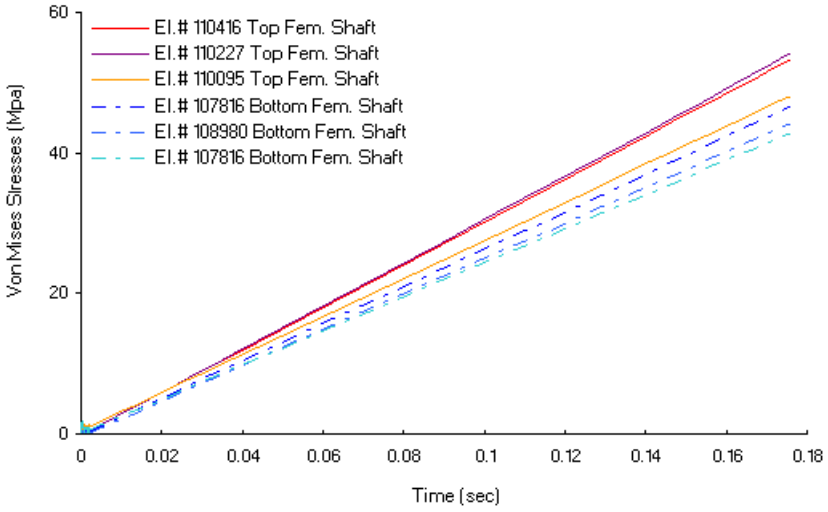

Figure 6.55. Von Mises stresses during knee flexion movement, recorded at the top and bottom of the femoral shaft.

Note that thigh extension movement was not considered because of constraint of car interior: the leg can not perform a considerable angle of thigh extension because of the presence of the seat, which can not obviously be penetrated.

All these results will be used next, when performing frontal impacts to the lower limb at various positions. Values of bone stresses, recorded at different leg positions during simulations of lower limb movements, will be next imported as initial pre-load conditions for the KTH complex already at a certain pose.

VII. IMPACT SIMULATIONS

In this section, simulations of a dashboard impacting the lower limb previously moved to certain positions are described. Results of simulated fracture mechanisms for the KTH are investigated and compared to injuries observed in real-world frontal car-crashes.

7.1 General Simulations Setup

The setup of the impacts and the material models were chosen to be mainly the same of the whole-body validation simulations described in Chapter 6. A few differences, however, were applied:

- The pedal was not inserted into the model;
- The nodal mass reproducing the upper part of the body was not included;
- The nominal position of the lower limb was positioned at zero degrees of adduction and thigh flexion;
- A 90-degree angle was considered as the initial position of the tibia with respect to the femur.

Simulations were performed of impacts of a knee-bolster against a lower limb which was previously moved to a certain position. Initial adduction angles of -30, -15, -10, -5, +5, +10 and +15 degrees and initial thigh flexion angles of +15 and +30 degrees from the nominal position were considered.
"Pure" position impacts were performed with the lower extremity at a certain degree of adduction or thigh flexion. "Mixed" position impacts were run where the lower extremities were in moved both adduction and thigh flexion. The initial distance between the knee and the dashboard was always to be 21 mm.

Since the lower extremity was already configured in the pre-impact position at the beginning of the simulation, only passive properties of the muscles were inserted in the

model. The role of muscle activation, however, needed for moving the leg from the nominal position into the pre-impact one was taken into account. An active muscle contracts and, as consequence, the areas of the bones where it originates and inserts are subjected to higher stresses coming from the muscle contraction. In order to replicate the correct bone stresses due to muscle contraction, a first simulation was run with insertion of muscle activation for obtaining a particular KTH position At the end of this simulation, when the lower limb reached the desired configuration, the stress state for each bone was recorded. This stress was then inserted in the second simulation, the impact-one, as a pre-stressed condition for solid and shell elements. This way the effects of muscle activation for change in movements prior to impact were replicated. When considering a combination of angles of thigh flexion and adduction for the position of the lower limb prior to impact, a linear combination of single activation muscle effects for each movement was evaluated. Matlab routines were programmed in order to calculate the initial solid and shell stresses for all elements of the FE model bones and to have them in the right format for insertion in the appropriate LSDYNA cards. (Appendix A)

7.2 Impact of the Lower Limb at the Neutral Position

7.2.1 Neutral Impact Position Setup

The setup and the initial configuration for the impact simulation of the lower limb at the neutral position of zero-degrees adduction and thigh flexion angles are shown in Figure 7.1. In this case, no bone pre-stresses were considered since the neutral position was considered the stress-free reference position from which to apply muscle activation in order to reach other positions.

Initial Configuration Lateral View	Initial Configuration Top View
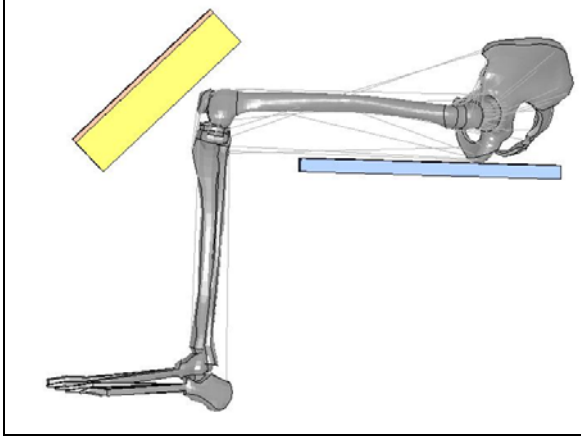	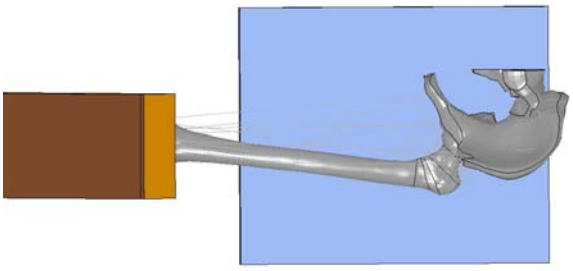

Figure 7.1. Initial configuration for neutral position impact simulation: lateral (left) and top view (right).

7.2.2 Neutral Impact Position Results

The final configuration for the impact simulation of the lower limb at the neutral position is shown in Figure 7.2. The resulting peak femur force observed was 5,328 N.

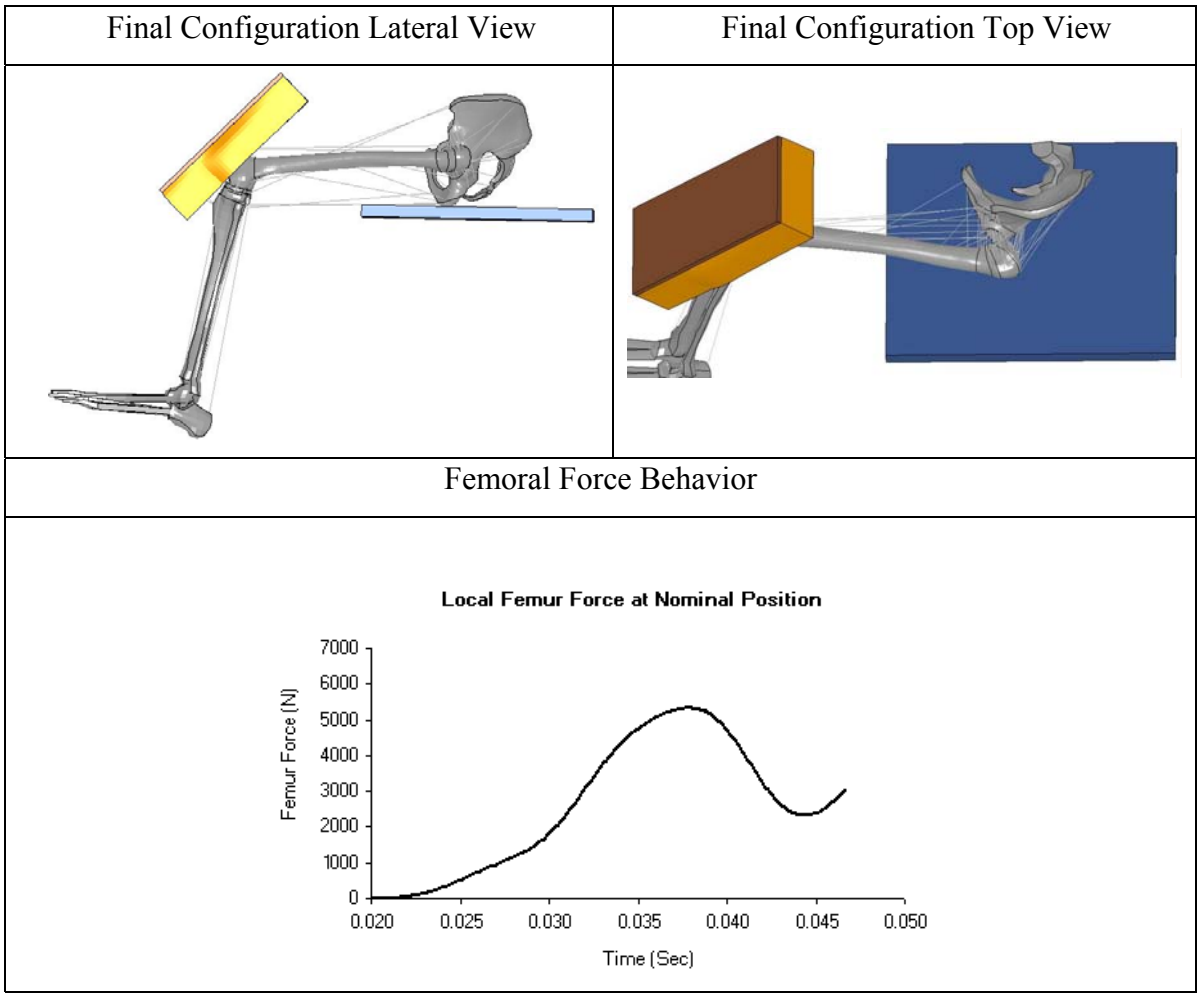

Figure 7.2. Final configuration for the neutral position impact simulation: final configuration lateral view (top left) and top view (top right), and femoral force behavior (bottom).

The fracture mechanism for the KTH obtained for the impact simulation of the lower limb at neutral position is shown in Figure 7.3.

Pelvis	Femur
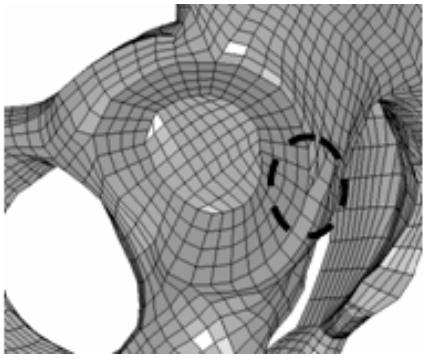	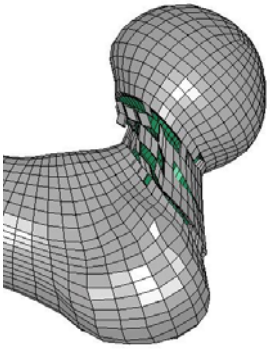

Figure 7.3. Bone fracture results for the neutral position impact simulation: small acetabular fracture (left) and femoral neck-trochanteric failure (right).

A small acetabular cup fracture was observed starting at 4,510 N and a neck-trochanteric failure initiated at 5,300 N. The femoral neck failed because elements reached the ultimate longitudinal compressive strength. An example of a longitudinal compressive ultimate strength fringe plot for the femoral neck region is shown in Figure 7.4.

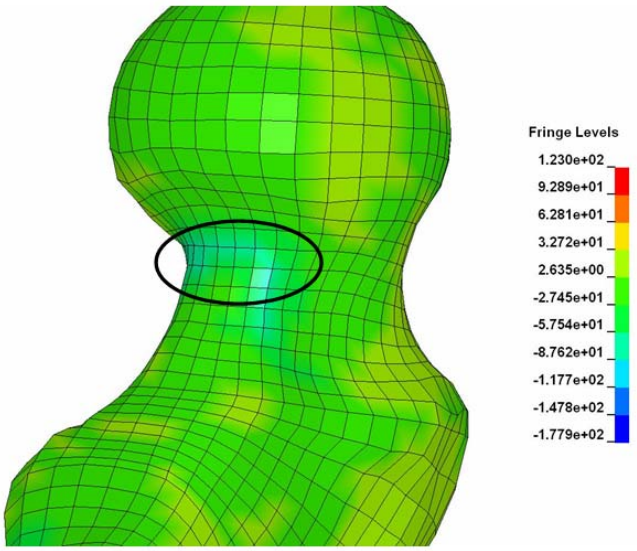

Figure 7.4. Transverse shear ultimate strength fringe plot for the proximal femoral

7.3 Impact of the Lower Limb moved of a Single Angle from the Neutral Position

7.3.1. Impact of the Lower Limb at -30 Degrees Adduction

7.3.1.1 Impact of the Lower Limb at -30 Degrees Adduction: Setup

The setup and the initial configuration for the impact simulation of the lower limb at 30 degrees of abduction are shown in Figure 7.5.

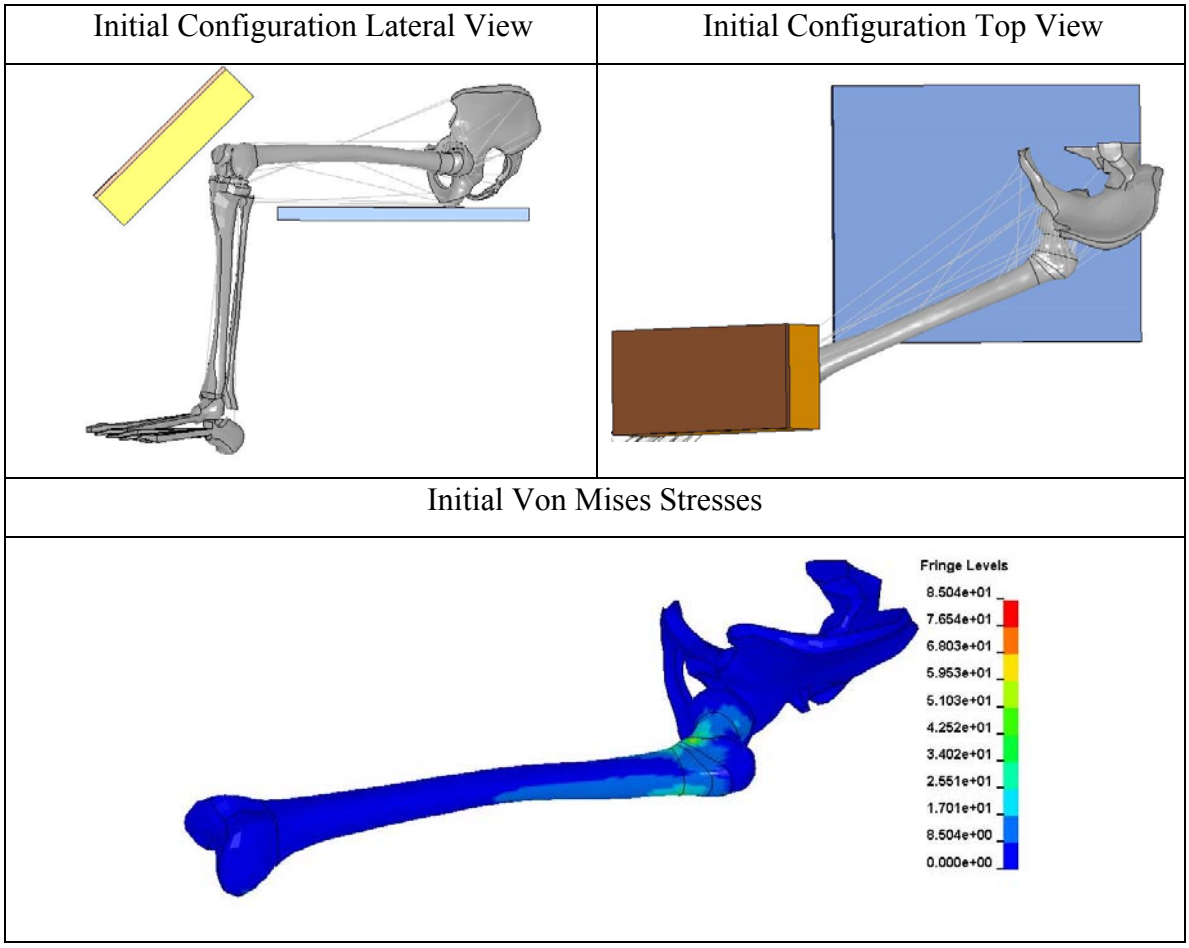

Figure 7.5. Initial configuration for the 30-degrees abduction impact simulation: lateral (top left) and top view (top right), and initial Von Mises stresses (bottom).

7.3.1.2 Impact of the Lower Limb at -30 Degrees Adduction: Results

The final configuration for the impact simulation of the lower limb at 30 degrees of abduction is shown in Figure 7.6. The resulting peak femur force was observed to be 3074 N.

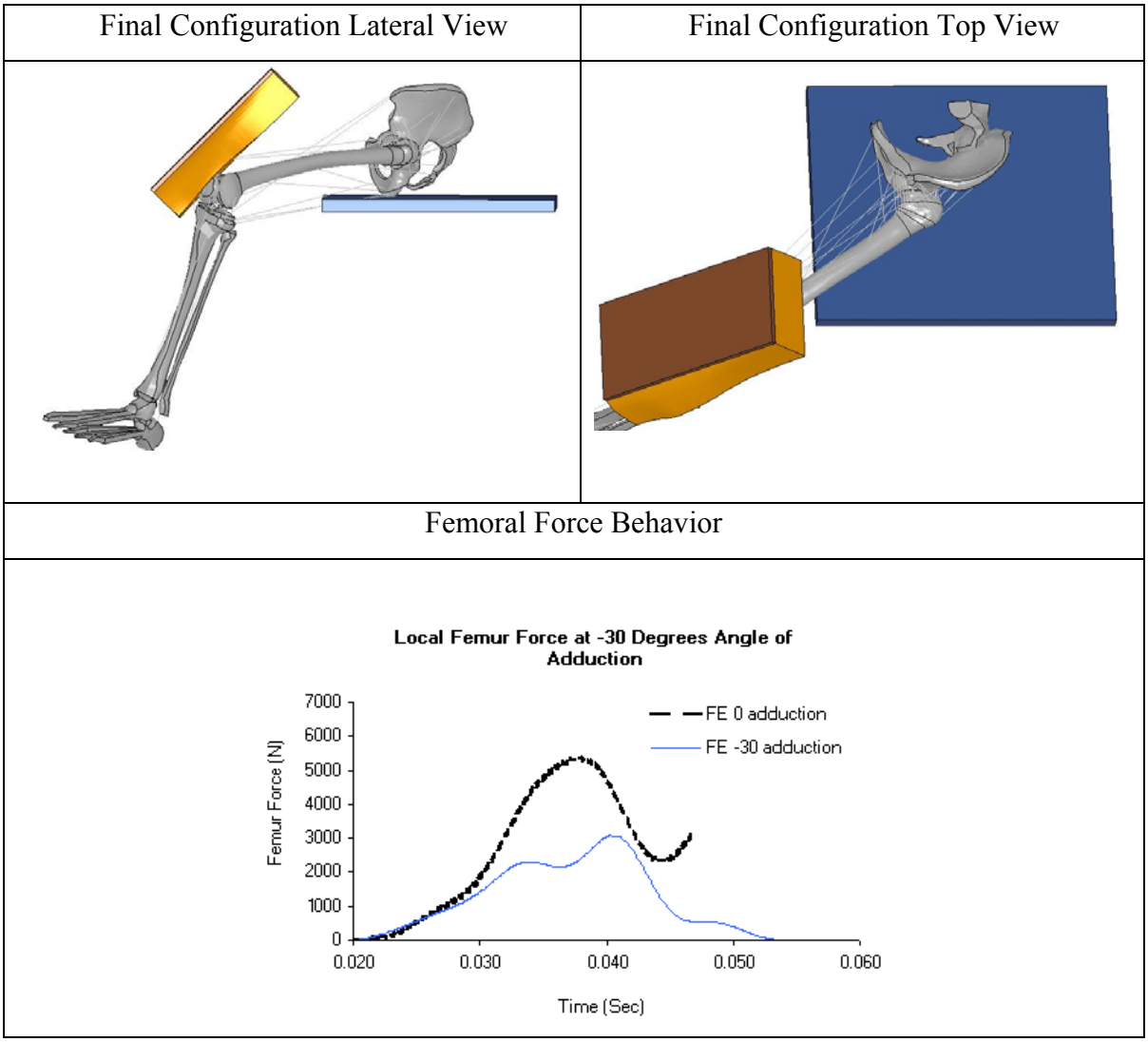

Figure 7.6. Final configuration for 30-degrees leg abduction impact simulation: final configuration lateral view (top left) and top view (top right), and femoral force behavior (bottom).

The fracture mechanism for the KTH in the simulation of a 30-degree abduction is shown in Figure 7.7.

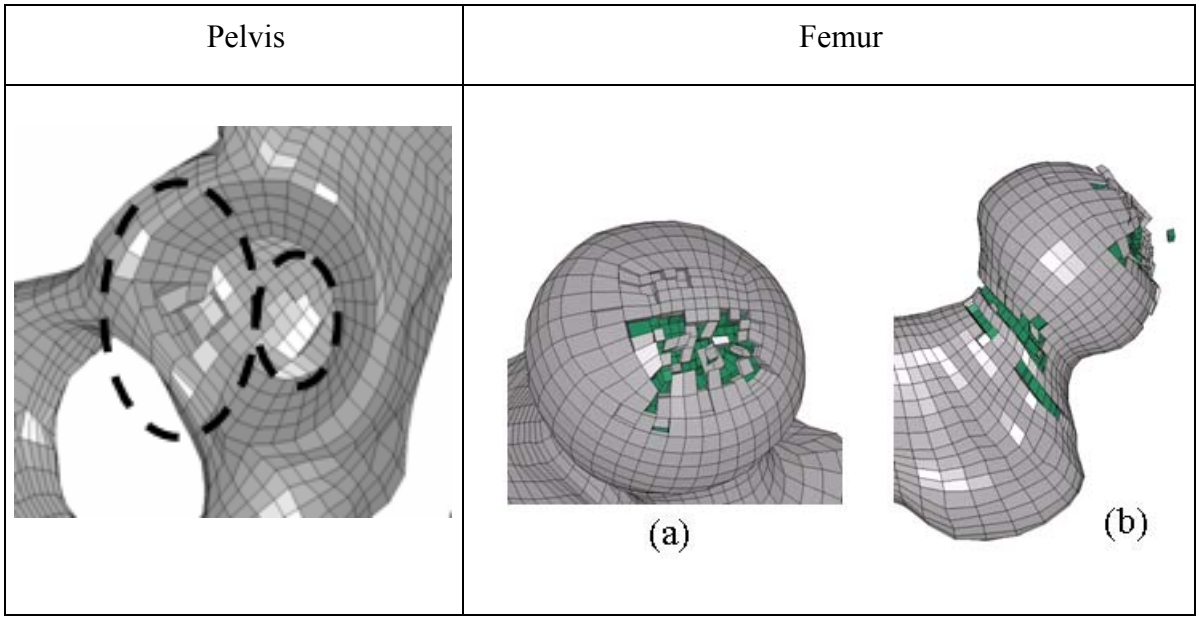

Figure 7.7. Bone fracture results for 30-degree abduction impact simulation: acetabular cup fracture (left), top femur head (right (a)) and femur neck-trochanter (right(b)) failures.

A femur head rupture was observed starting at 2380 N. Also, after the femur force reached its peak, the KTH experienced a failure to the femur neck-trochanter at 2730 N and an internal acetabular cup fracture starting at 2940 N. The femoral neck failed because elements reached the ultimate transverse compressive strength while the top of the femur head fractured when elements reached the transverse shear ultimate strength.

7.3.2. Impact of the Lower Limb at -15 Degrees Adduction

7.3.2.1 Impact of the Lower Limb at -15 Degrees Adduction: Setup

The setup and the initial configuration for the impact simulation of the lower limb at 15 degrees of abduction are shown in Figure 7.8.

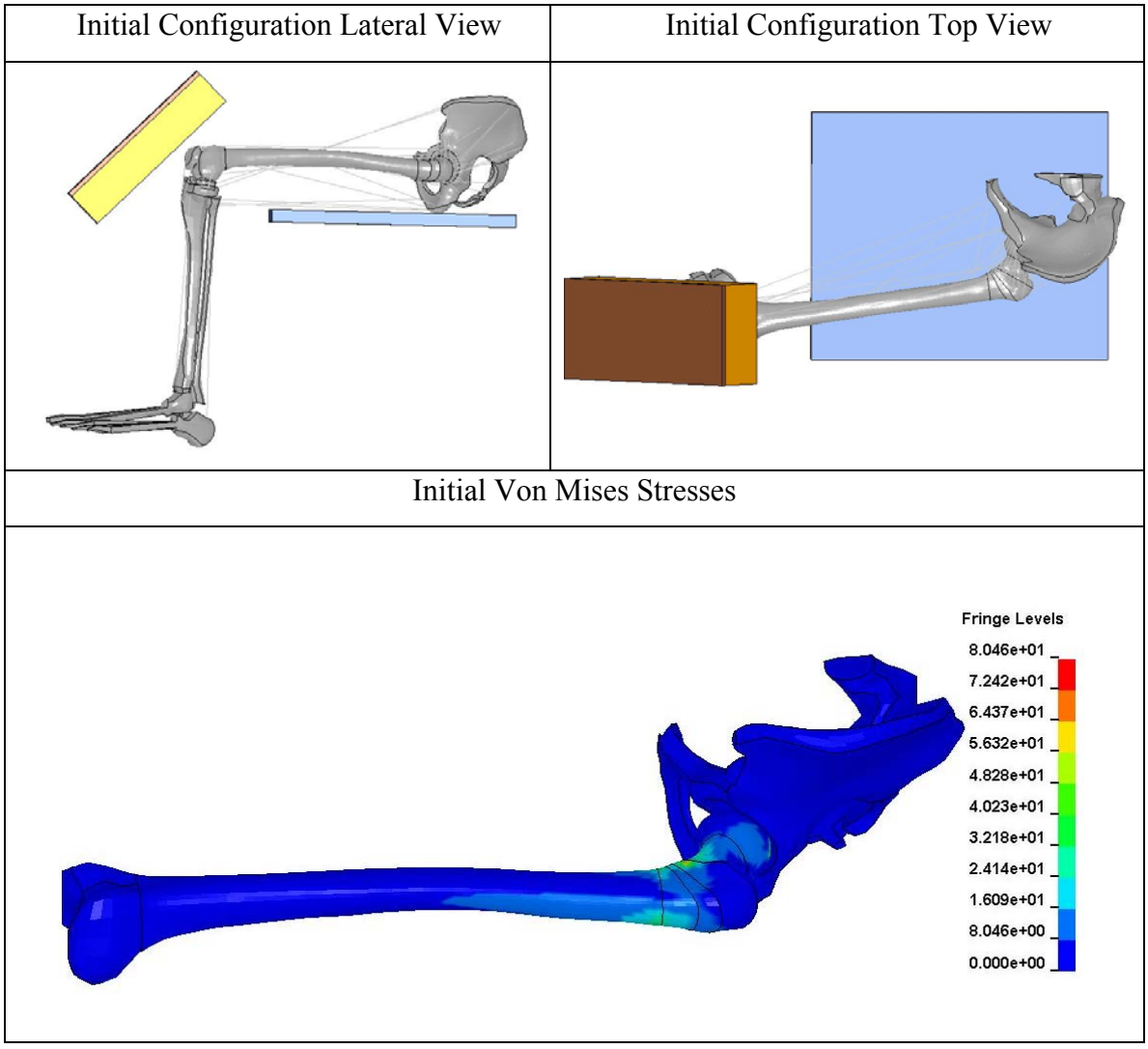

Figure 7.8. Initial configuration for the 15-degrees abduction impact simulation: lateral (top left) and top view (top right), and initial Von Mises stresses (bottom).

7.3.2.2 Impact of the Lower Limb at -15 Degrees Adduction: Results

The final configuration for the impact simulation of the lower limb at 15 degrees of abduction is shown in Figure 7.9. The resulting peak femur force was observed to be 5,722 N.

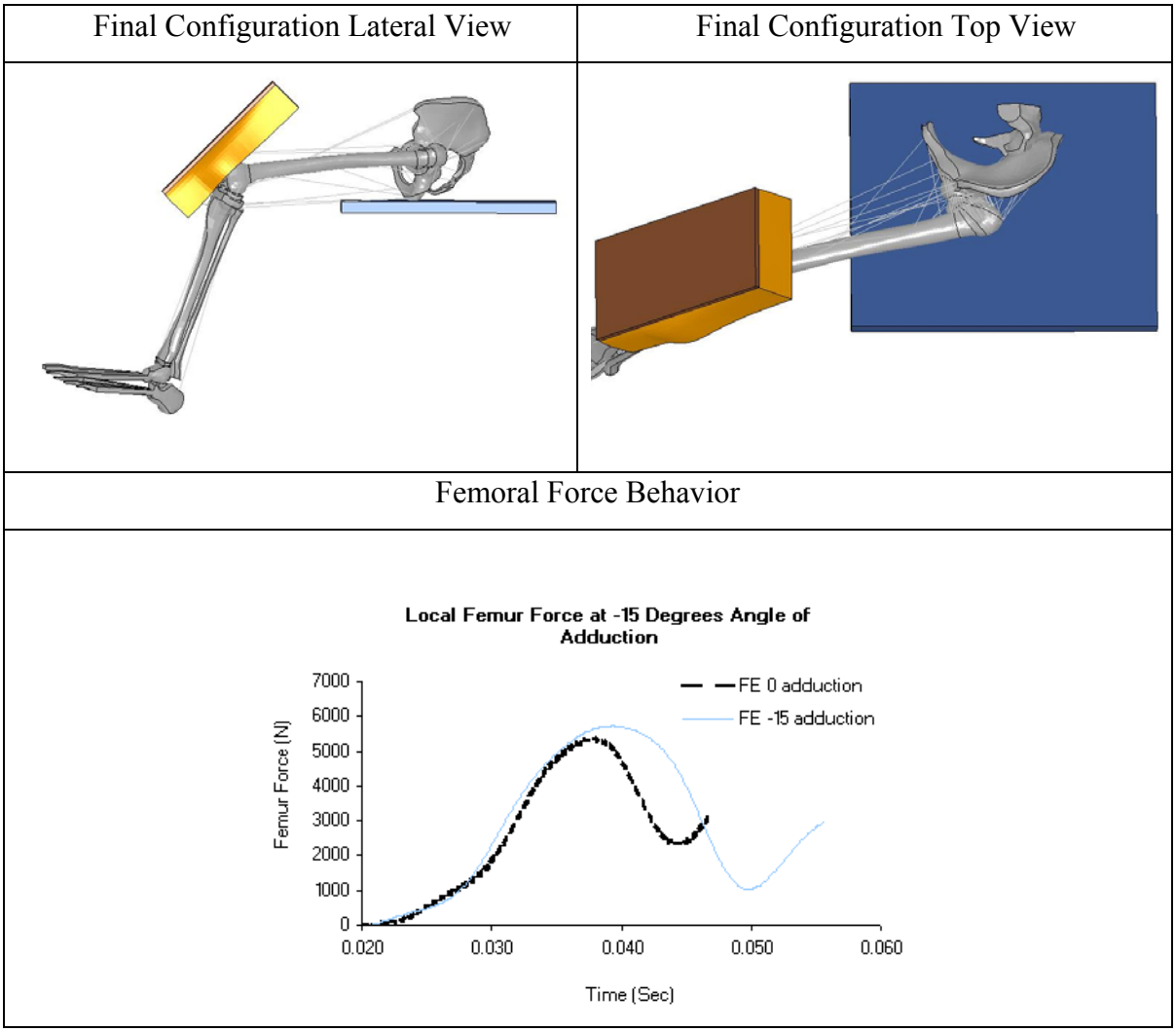

Figure 7.9. Final configuration for 15-degree leg abduction impact simulation: final configuration lateral view (top left) and top view (top right), and femoral force behavior (bottom).

The fracture mechanism for the KTH in the simulation of a 30-degree abduction is shown in Figure 7.10.

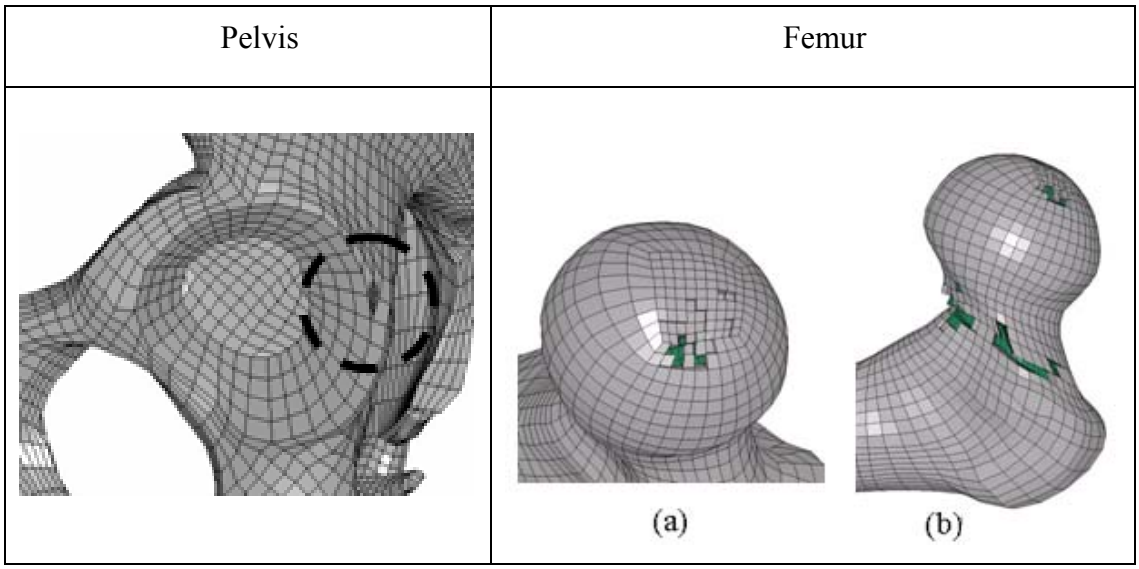

Figure 7.10. Bone fracture results for 15-degree abduction impact simulation: back acetabular cup fracture (left), top femur head (right (a)) and femur neck-trochanter (right(b)) failures.

A small acetabular cup fracture and a top-head femur rupture were observed starting at 2,890 N and at 5,690 N respectively. After the femur force reached its peak, the KTH model experienced also a femoral neck-trochanteric failure starting at 5,650 N. The femoral neck failed because elements reached the ultimate longitudinal compressive strength while the top of the femur head fractured when elements reached the transverse shear ultimate strength.

7.3.3. Impact of the Lower Limb at -10 Degrees Adduction

7.3.3.1 Impact of the Lower Limb at -10 Degrees Adduction: Setup

The setup and the initial configuration for the impact simulation of the lower limb at 10 degrees of abduction are shown in Figure 7.11.

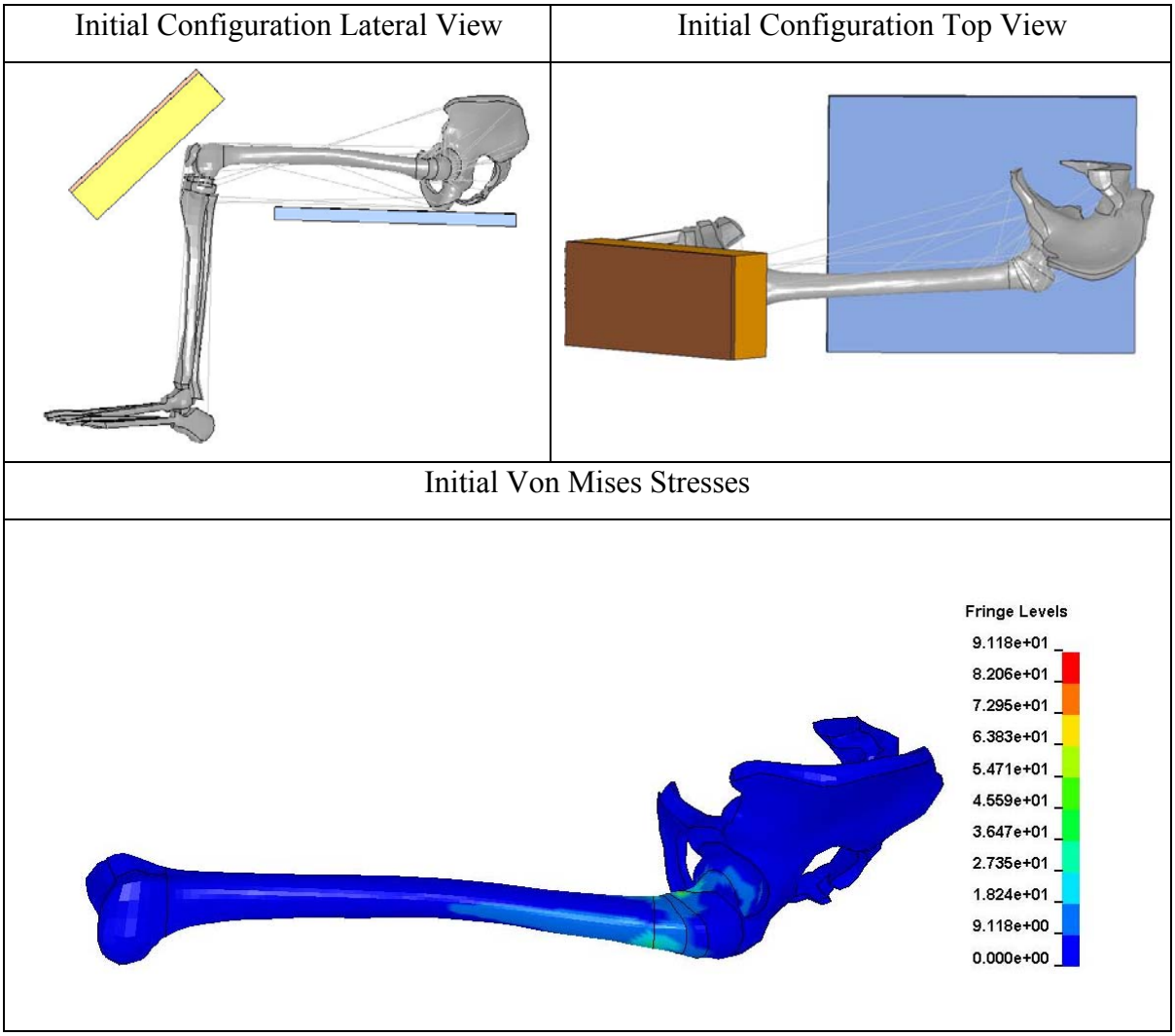

Figure 7.11. Initial configuration for the 10-degree abduction impact simulation: lateral (top left) and top view (top right), and initial Von Mises stresses (bottom).

7.3.3.2 Impact of the Lower Limb at -10 Degrees Adduction: Results

The final configuration for the impact simulation of the lower limb at 10 degrees of abduction is shown in Figure 7.12. The resulting peak femur force was observed to be 5,282 N.

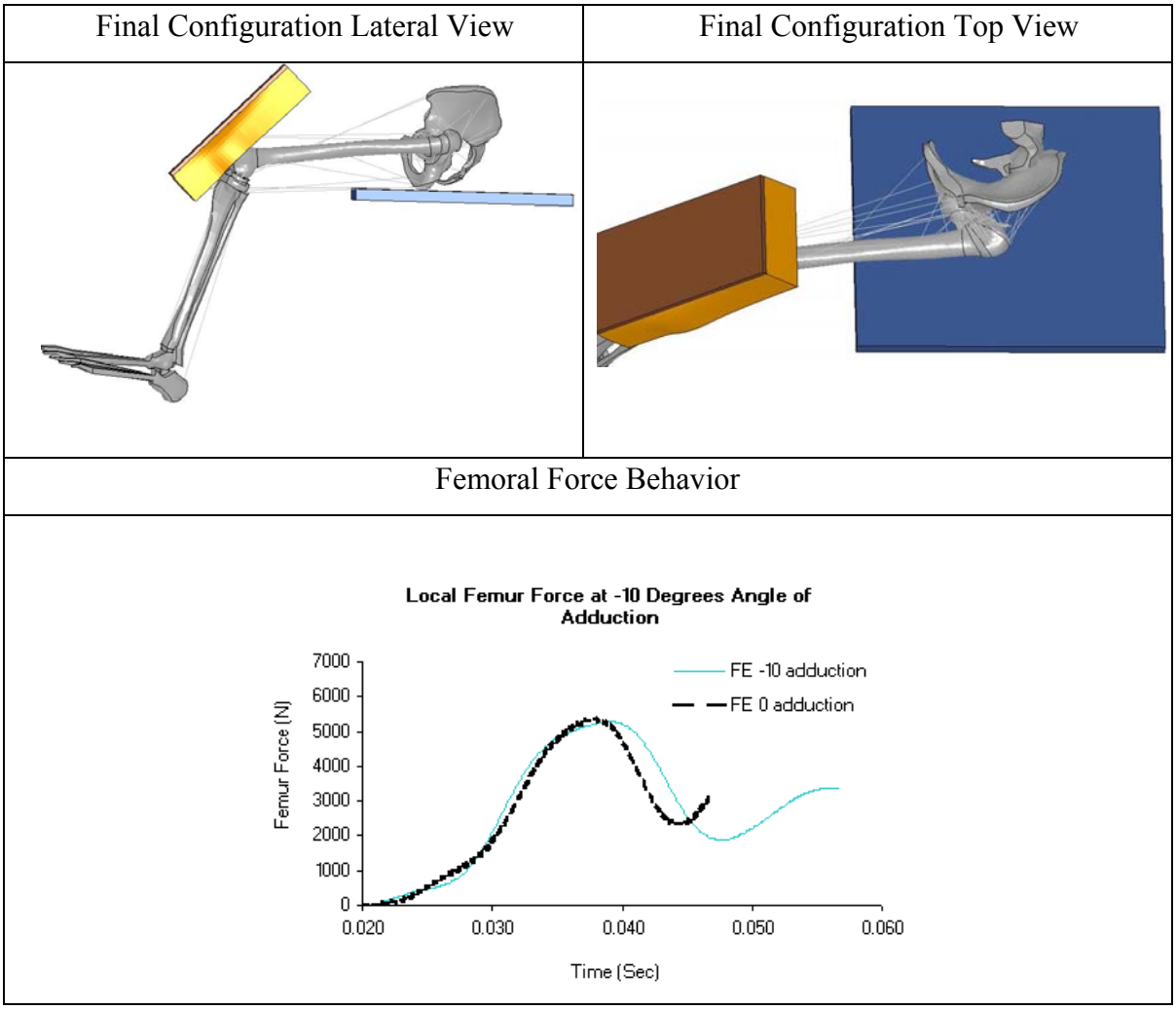

Figure 7.12. Final configuration for 10-degrees leg abduction impact simulation: final configuration lateral view (top left) and top view (top right), and femoral force behavior (bottom).

The fracture mechanism for the KTH in the simulation of a 10-degree abduction is shown in Figure 7.13.

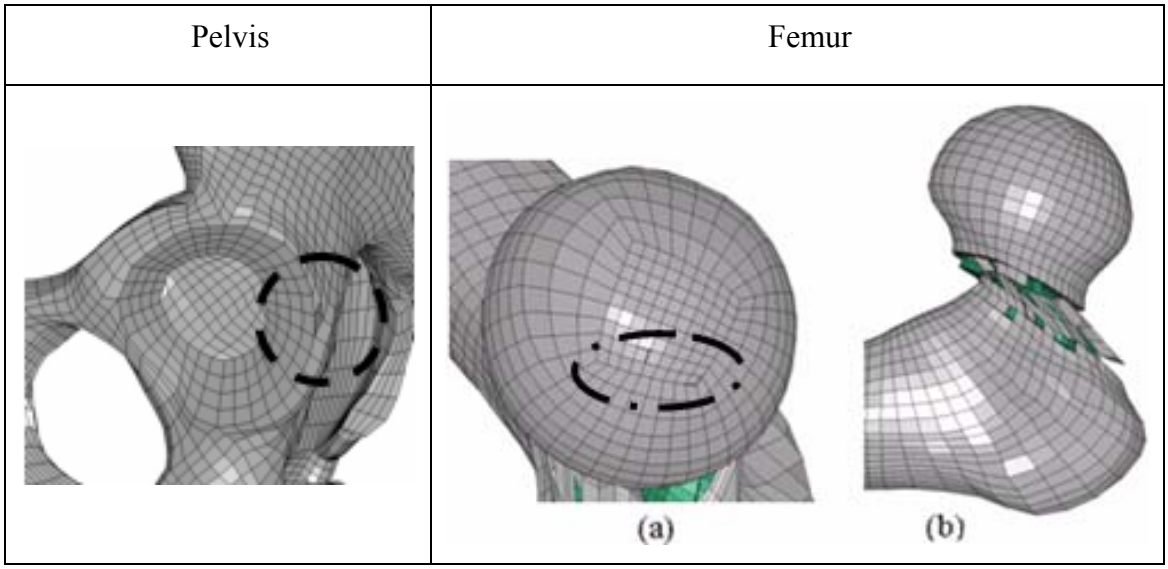

Figure 7.13. Bone fracture results for 10-degree abduction impact simulation: back acetabular cup fracture (left), small top femur head (right (a)) and femur neck-trochanter (right (b)) failures.

A small acetabular cup fracture and a failure to the femur neck-trochanter were observed starting at 4,990 N and at 2,380 N respectively. Also, after the femur force reached its peak, the KTH experienced a very small top-head femur rupture starting at 4,260 N. The femoral neck failed because elements reached the ultimate normal compressive strength, while the top of the femur ball fractured when elements reached the transverse shear ultimate strength.

7.3.4. Impact of the Lower Limb at -5 Degrees Adduction

7.3.4.1 Impact of the Lower Limb at -5 Degrees Adduction: Setup

The setup and the initial configuration for the impact simulation of the lower limb at 5 degrees of abduction are shown in Figure 7.14.

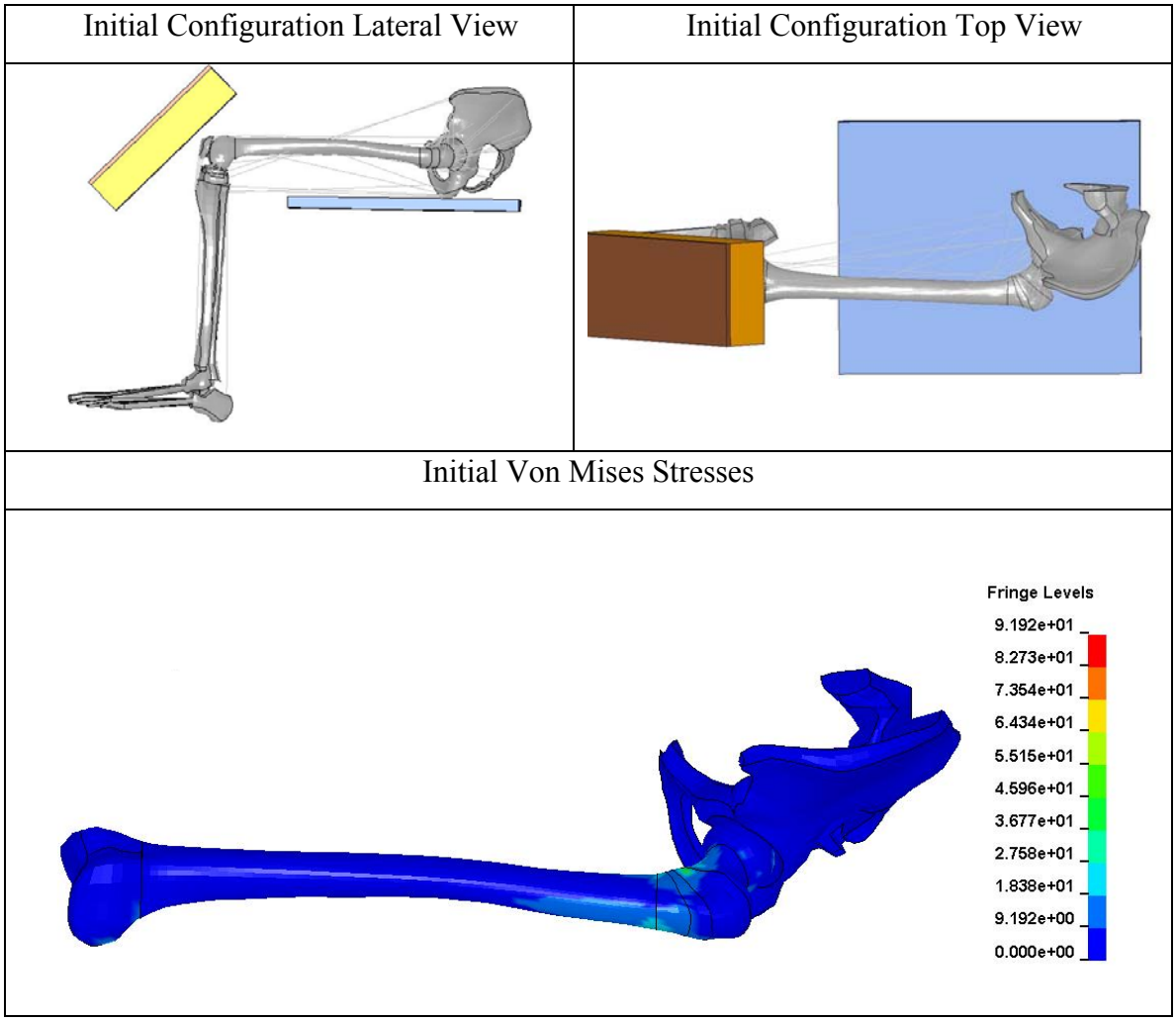

Figure 7.14. Initial configuration for the 5-degree abduction impact simulation: lateral (top left) and top view (top right), and initial Von Mises stresses (bottom).

7.3.4.2 Impact of the Lower Limb at -5 Degrees Adduction: Results

The final configuration for the impact simulation of the lower limb at 5 degrees of abduction is shown in Figure 7.15. The resulting peak femur force was observed to be 5,913 N.

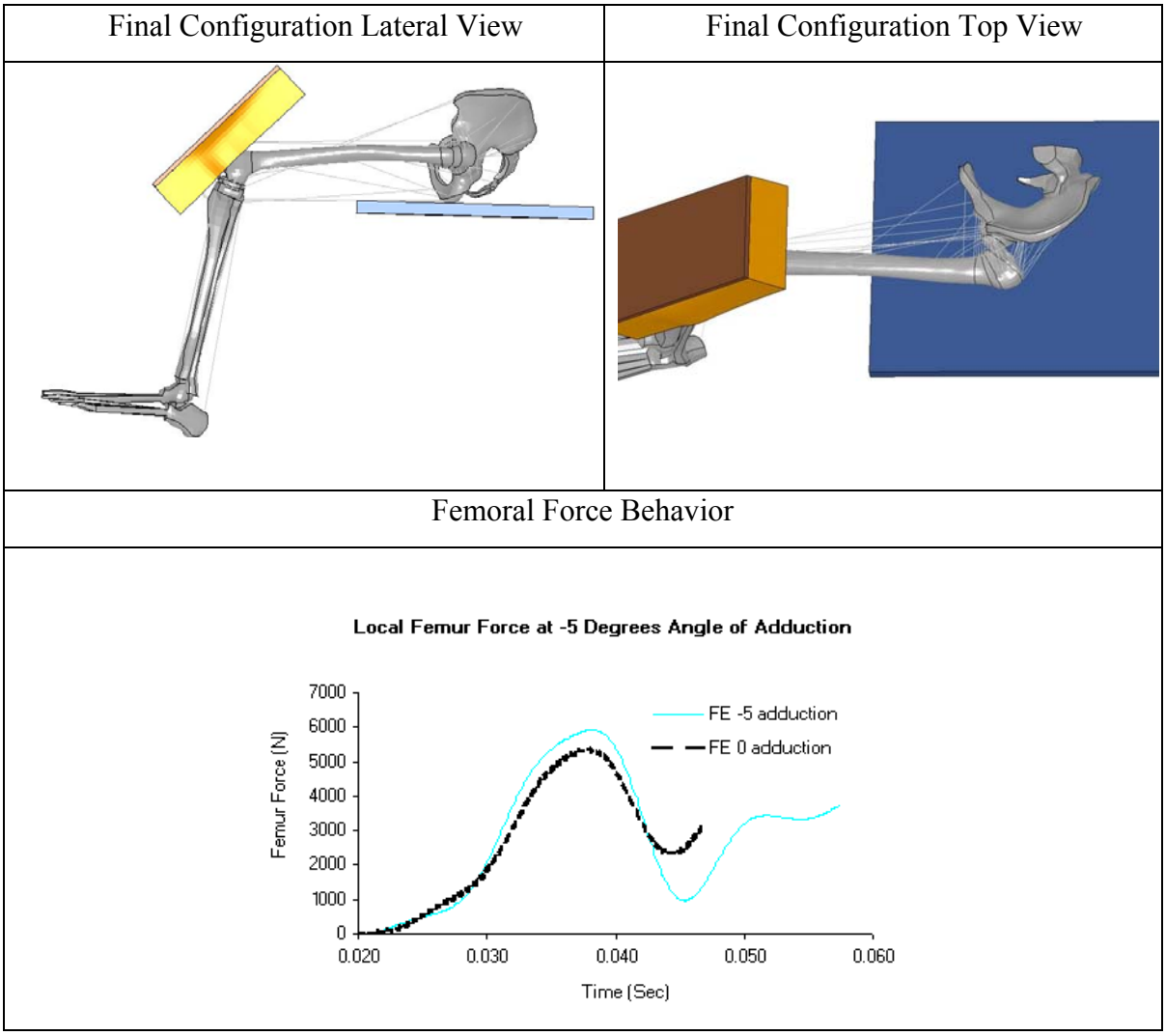

Figure 7.15. Final configuration for 5-degrees leg abduction impact simulation: final configuration lateral view (top left) and top view (top right), and femoral force behavior (bottom).

The fracture mechanism for the KTH in the simulation of a 30-degree abduction is shown in Figure 7.16.

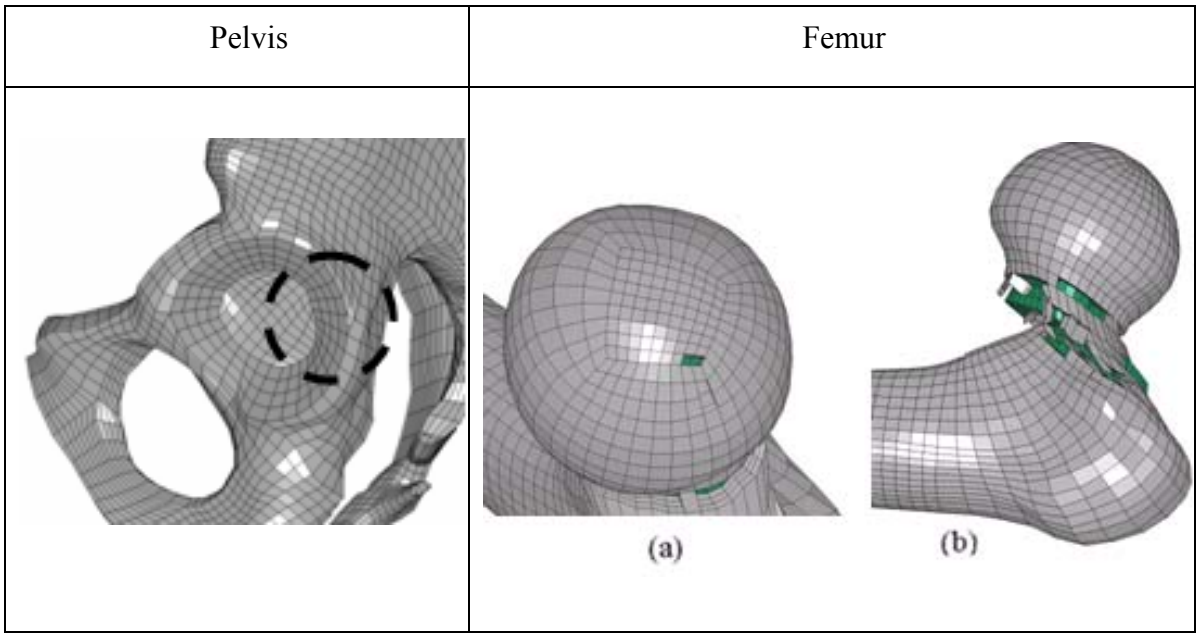

Figure 7.16. Bone fracture results for 5-degree abduction impact simulation: back acetabular cup fracture (left), top femur head (right (a)) and femur neck-trochanter (right (b)) failures.

A small acetabular cup fracture, a top-head femur rupture and a failure to the femur neck-trochanter were observed starting at 3,620 N, 4,380 N and at 5,700 N respectively.
The femoral neck failed because elements reached the ultimate longitudinal and the normal compressive strengths, while the top of the femur ball fractured when elements reached the transverse shear ultimate strength.

7.3.5. Impact of the Lower Limb at 5 Degrees Adduction

7.3.5.1 Impact of the Lower Limb at 5 Degrees Adduction: Setup

The setup and the initial configuration for the impact simulation of the lower limb at 5 degrees of adduction are shown in Figure 7.17.

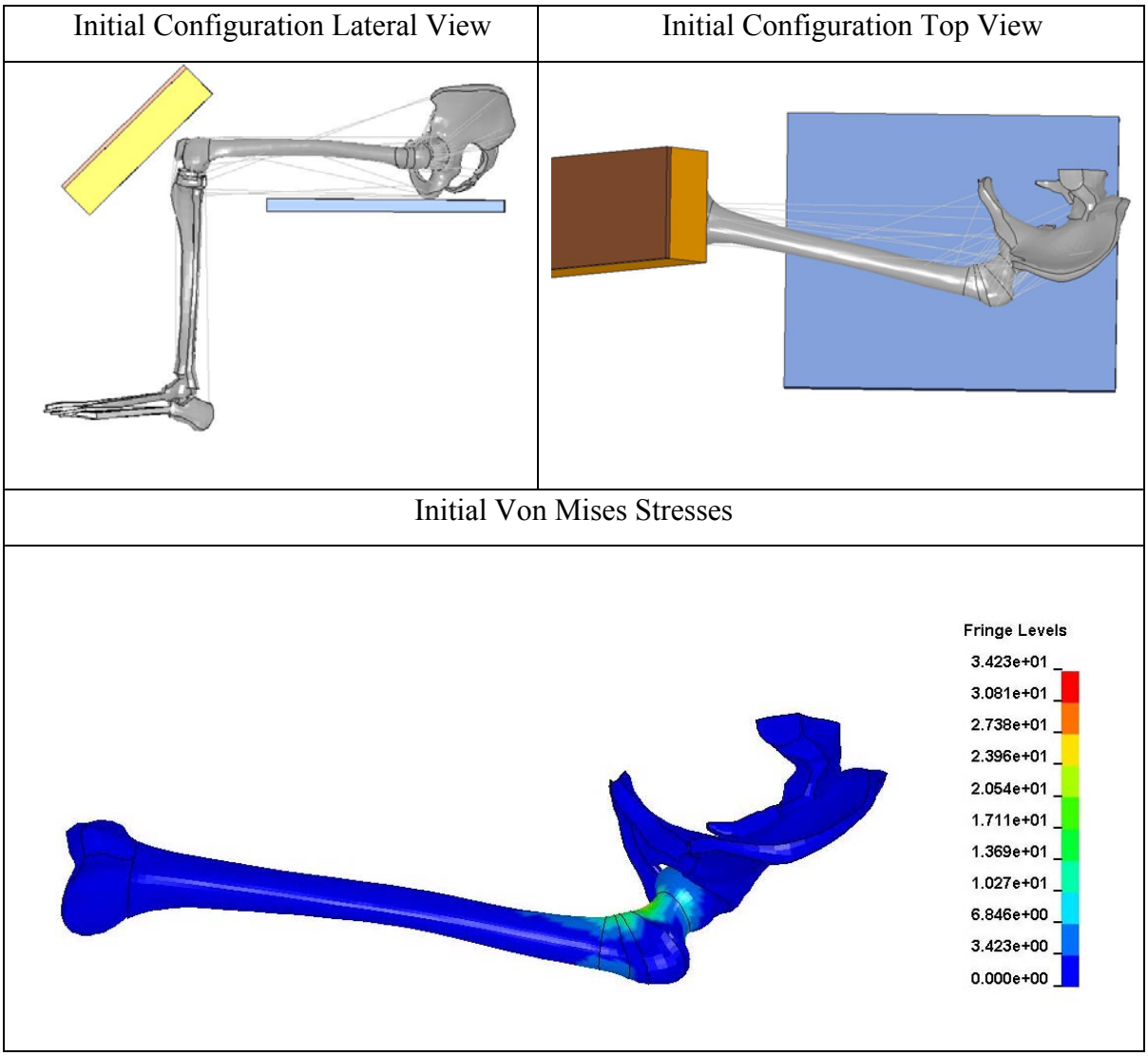

Figure 7.17. Initial configuration for the 5-degree adduction impact simulation: lateral (top left) and top view (top right), and initial Von Mises stresses (bottom).

7.3.5.2 Impact of the Lower Limb at 5 Degrees Adduction: Results

The final configuration for the impact simulation of the lower limb at 5 degrees of adduction is shown in Figure 7.18. The resulting peak femur force was observed to be 4,609 N.

Final Configuration Lateral View	Final Configuration Top View
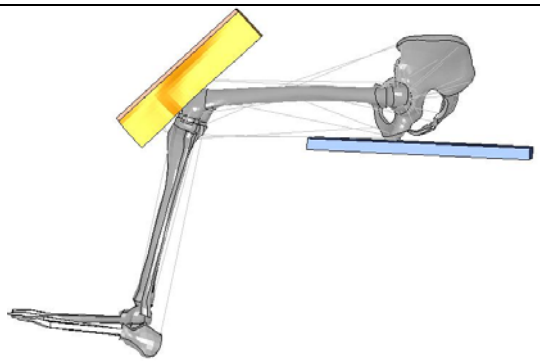	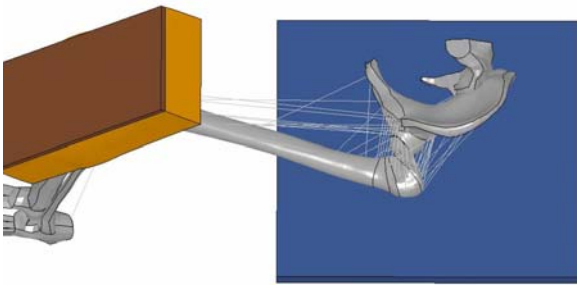
Femoral Force Behavior	
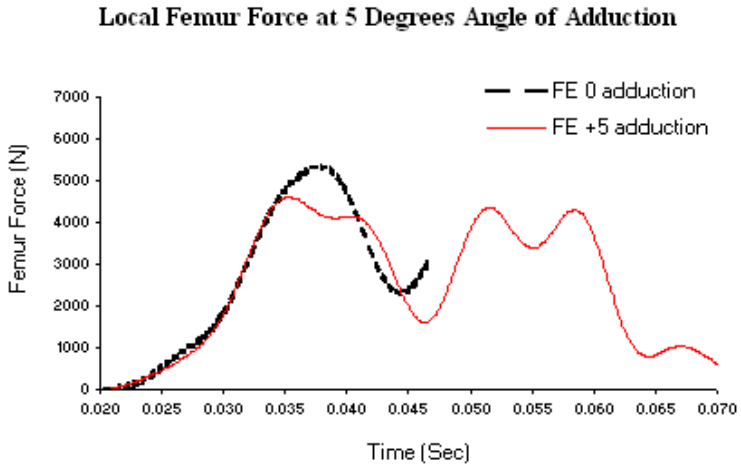	

Figure 7.18. Final configuration for 5-degree adduction impact simulation: final configuration lateral view (top left) and top view (top right), and femoral force behavior (bottom).

The fracture mechanism for the KTH in the simulation of a 5-degree adduction is reported in Figure 7.19.

Pelvis	Femur
—	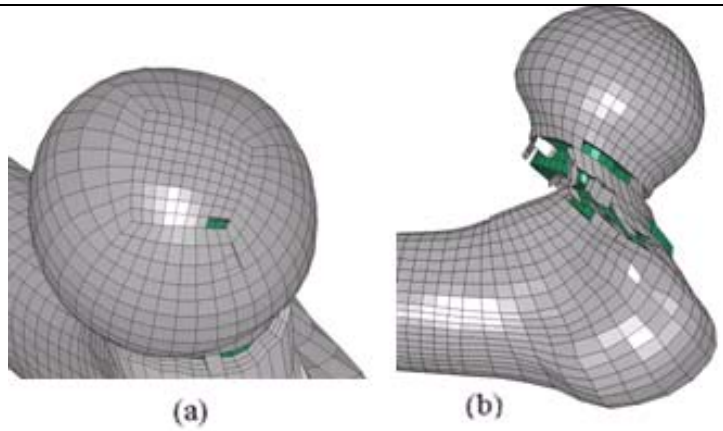

Figure 7.19. Bone fracture results for 5-degree adduction impact simulation: no fractures were observed for the pelvis bone, while both top femur head (right (a)) and femur neck-trochanter (right (b)) resulted in failures.

It was not observed failure to the pelvis bone. A top-head femur rupture was observed starting at 3,440 N. Also, after the femur force reached its peak, a failure to the femur neck-trochanter initiated at 4,540 N.

The femoral neck failed because elements reached the ultimate longitudinal compressive strength, while the top of the femur ball fractured when elements reached the transverse shear ultimate strength. Example of a transverse shear ultimate strength fringe plot for the top ball femoral region is reported in Figure 7.20.

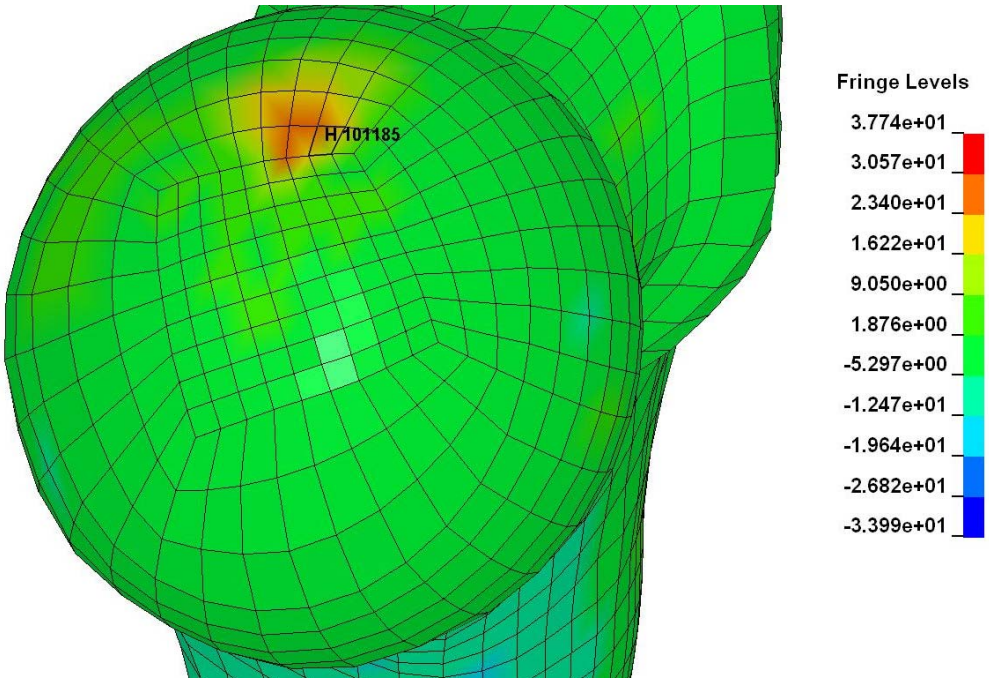

Figure 7.20. Transverse shear ultimate strength fringe plot for the top ball femoral region.

7.3.6. Impact of the Lower Limb at 10 Degrees Adduction

7.3.6.1 Impact of the Lower Limb at 10 Degrees Adduction: Setup

The setup and the initial configuration for the impact simulation of the lower limb at 10 degrees of adduction are shown in Figure 7.21.

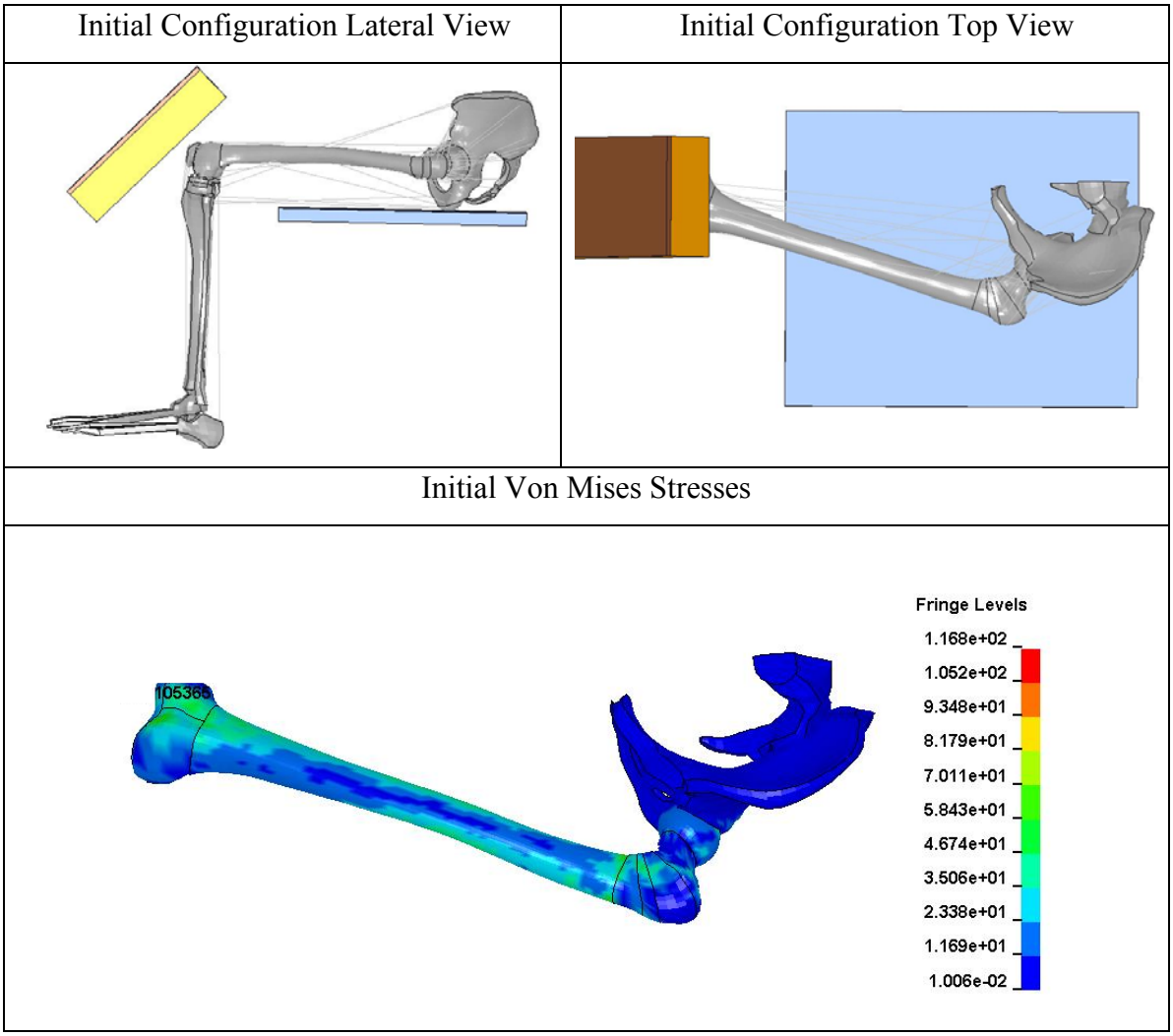

Figure 7.21. Initial configuration for 10-degree adduction impact simulation: lateral (top left) and top view (top right), and initial Von Mises stresses (bottom).

7.3.6.2 Impact of the Lower Limb at 10 Degrees Adduction: Results

The final configuration for the impact simulation of the lower limb at 10 degrees of adduction is shown in Figure 7.22. The peak femur force was observed to be 3,971 N.

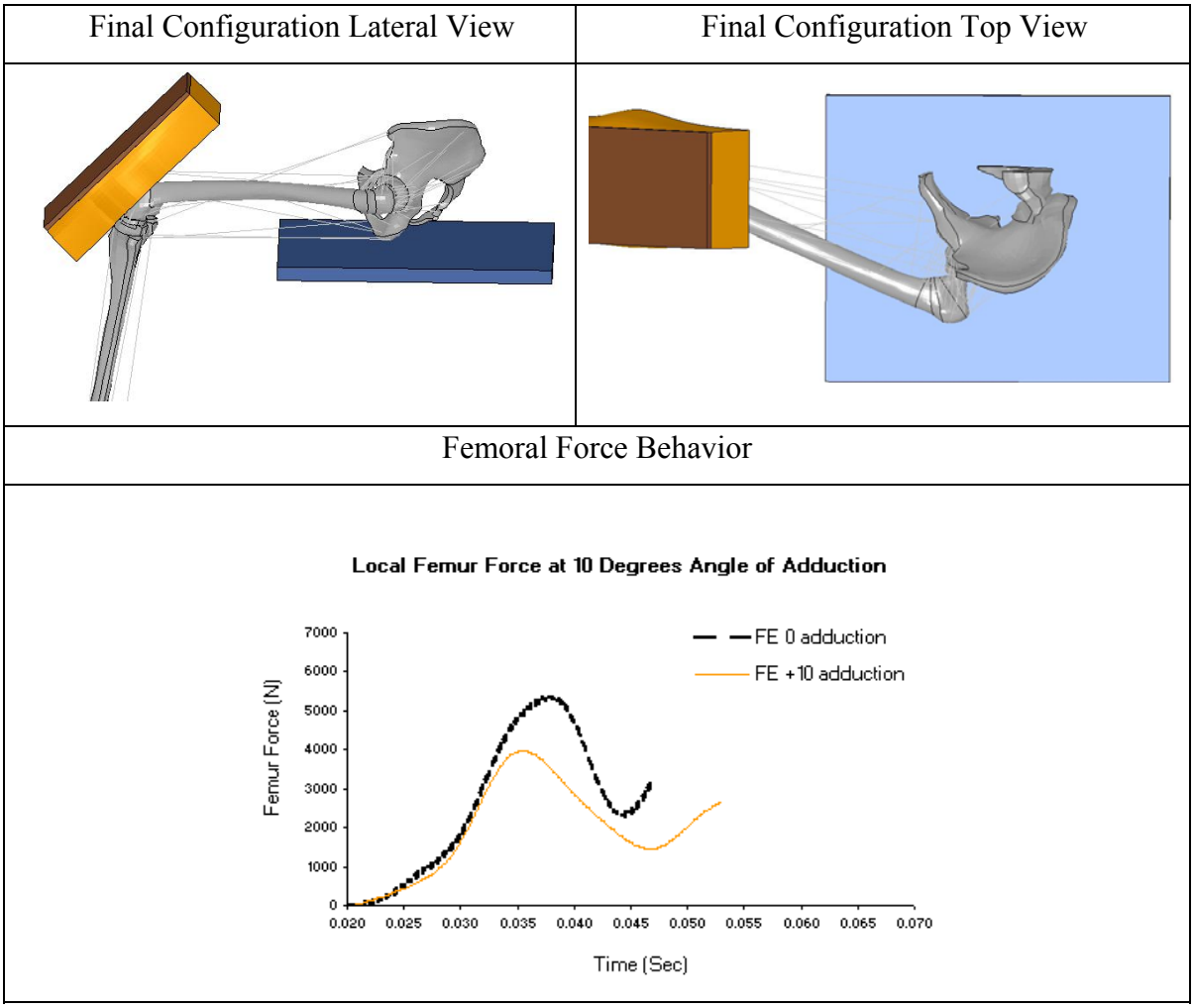

Figure 7.22. Final configuration for 10-degree adduction impact simulation: final configuration lateral view (top left) and top view (top right), and femoral force behavior (bottom).

The fracture mechanism for the KTH in the simulation of a 10-degree adduction is shown in Figure 7.23.

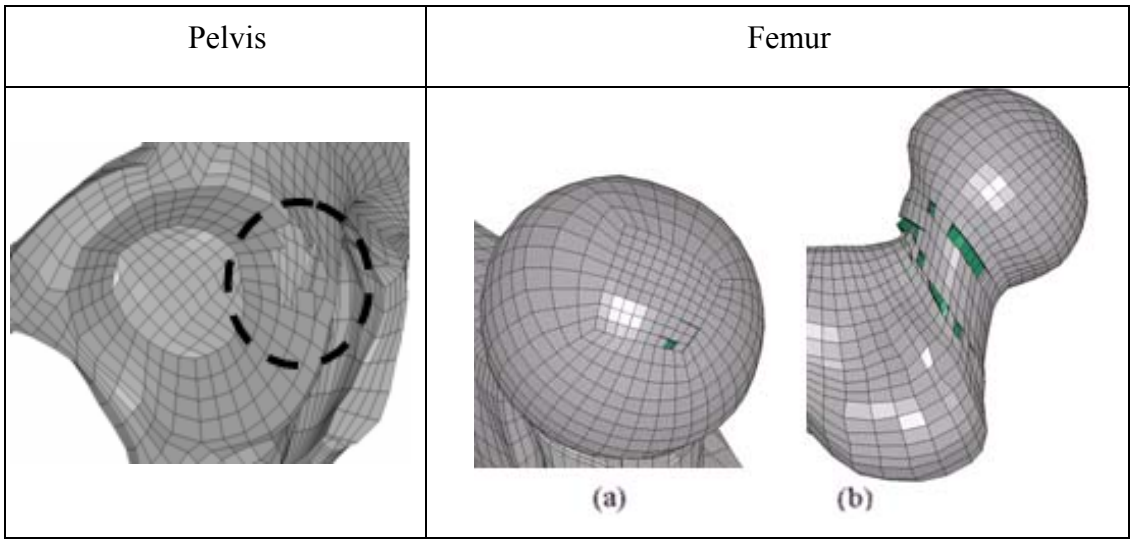

Figure 7.23. Bone fracture results for 10-degree adduction impact simulation: back acetabular cup fracture (left), top femur head (right (a)) and femur neck-trochanter (right (b)) failures.

A consistent acetabular cup fracture and a top-head femur rupture were observed at 3,010 N starting. Also, after the femur force reached its peak, a failure to the femur neck-trochanter was experienced starting at 3,520 N.

The femoral neck failed because elements reached the ultimate longitudinal compressive strength, while the top of the femur ball fractured when elements reached the transverse shear ultimate strength.

7.3.7. Impact of the Lower Limb at 15 Degrees Adduction

7.3.7.1 Impact of the Lower Limb at 15 Degrees Adduction: Setup

The setup and the initial configuration for the impact simulation of the lower limb at 15 degrees of adduction are shown in Figure 7.24.

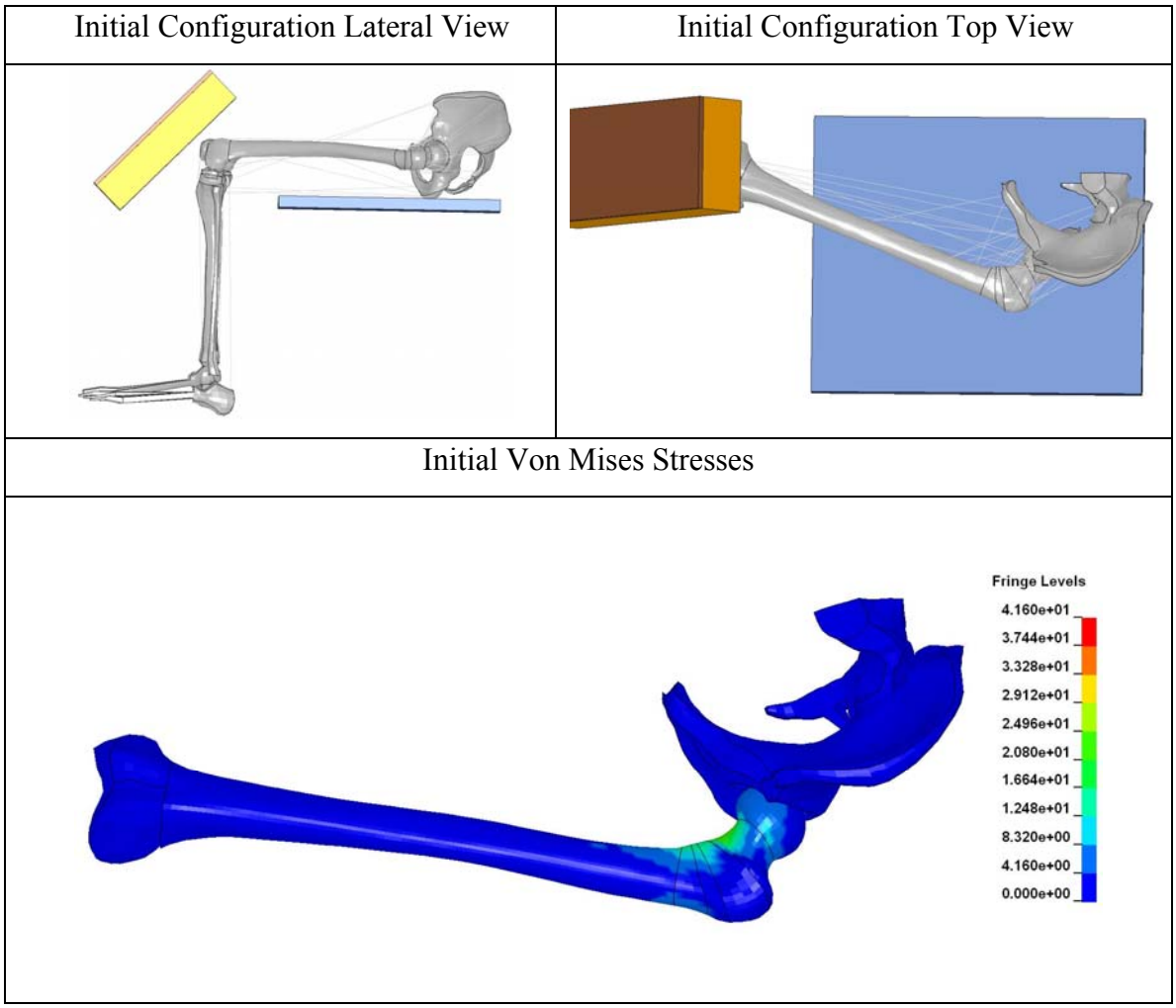

Figure 7.24. Initial configuration for the 15-degree adduction impact simulation: lateral (top left) and top view (top right), and initial Von Mises stresses (bottom).

7.3.7.2 Impact of the Lower Limb at 15 Degrees Adduction: Results

The final configuration for the impact simulation of the lower limb at 15 degrees of adduction is shown in Figure 7.25. The resulting peak femur force was observed to be 3,492 N.

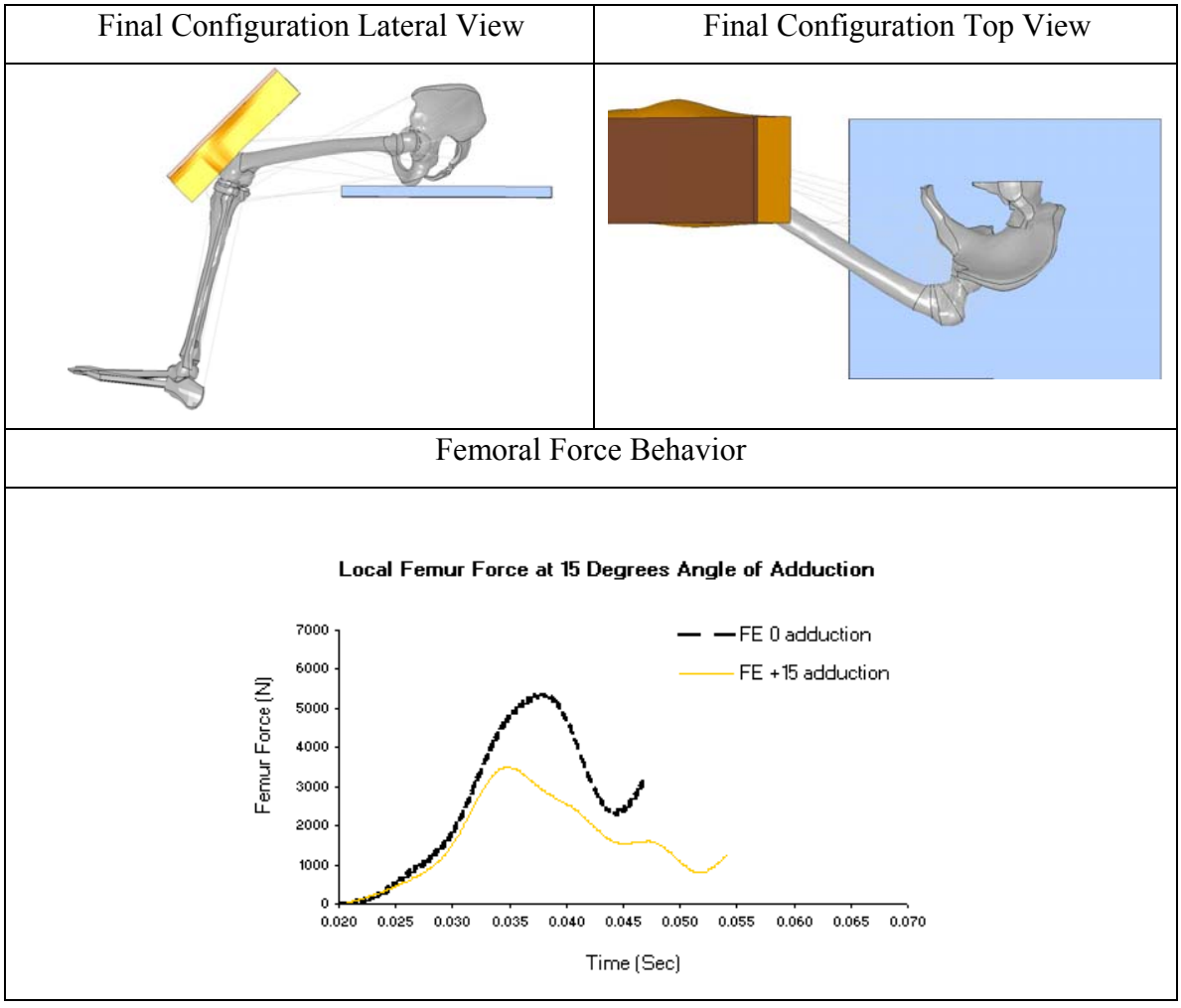

Figure 7.25. Final configuration for the 15-degree adduction impact simulation: final configuration lateral view (top left) and top view (top right), and femoral force behavior (bottom).

The fracture mechanism for the KTH in the simulation of a 15-degree adduction is shown in Figure 7.26.

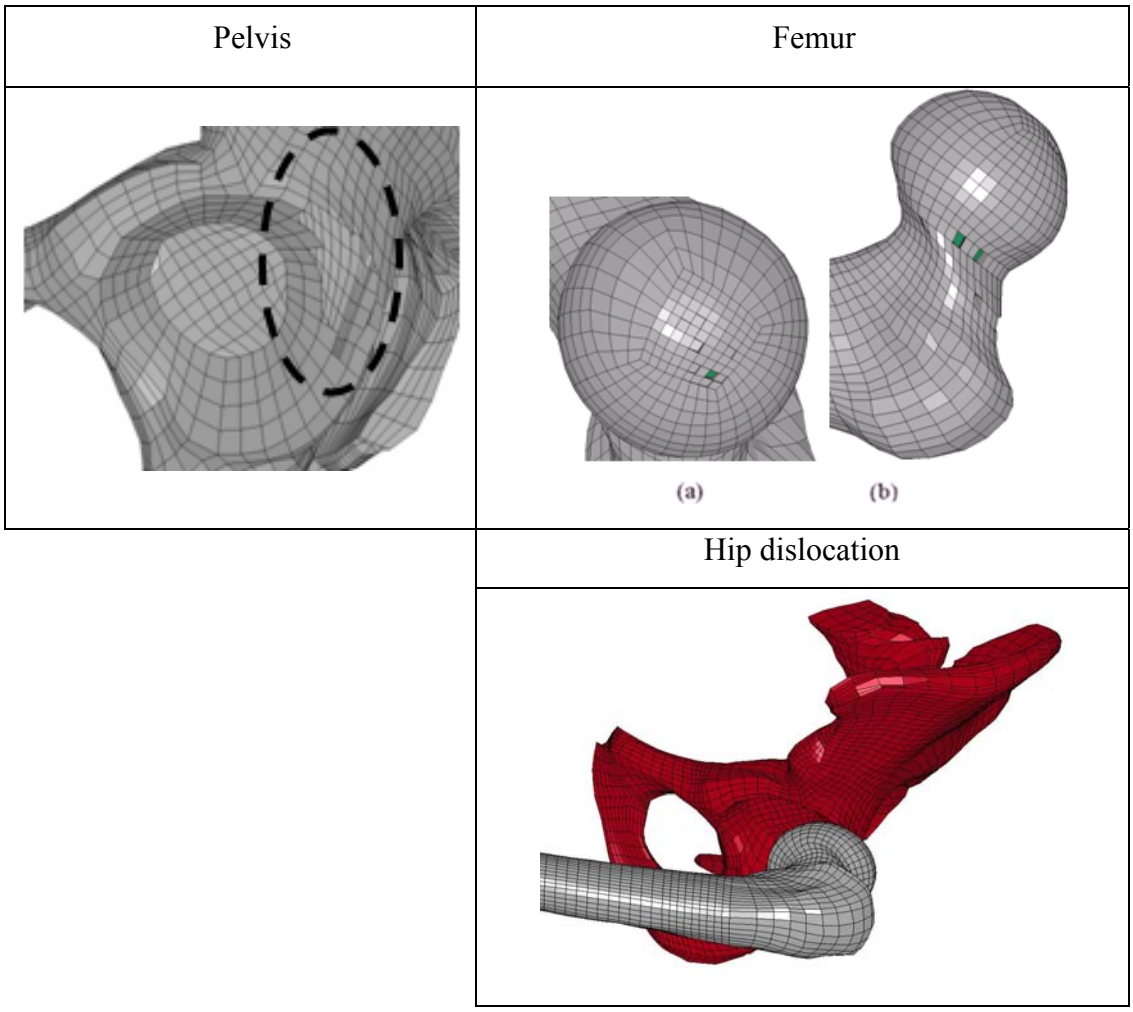

Figure 7.26. Bone fracture results for the15-degree adduction impact simulation: back acetabular cup fracture (top left), top femur head (top right (a)) and femur neck (top right (b)) failures, hip dislocation (bottom).

A consistent acetabular cup fracture and a hip joint dislocation were observed starting at 3,460 N. After the dislocation occurred, fractures to the top-head femur and to the femoral

neck were observed, initiating at 3,030 N and at 1,540 N respectively. Failure to the femoral neck occurred after the femur force reached its peak.

The femoral neck failed because elements reached the ultimate transverse shear strength, while the top of the femur ball fractured when elements reached the transverse compressive ultimate strength. Examples of a transverse shear ultimate strength fringe plot for the femoral neck region and of a transverse compressive ultimate strength fringe plot for the top ball femoral part are reported in Figures 7.27 and 7.28

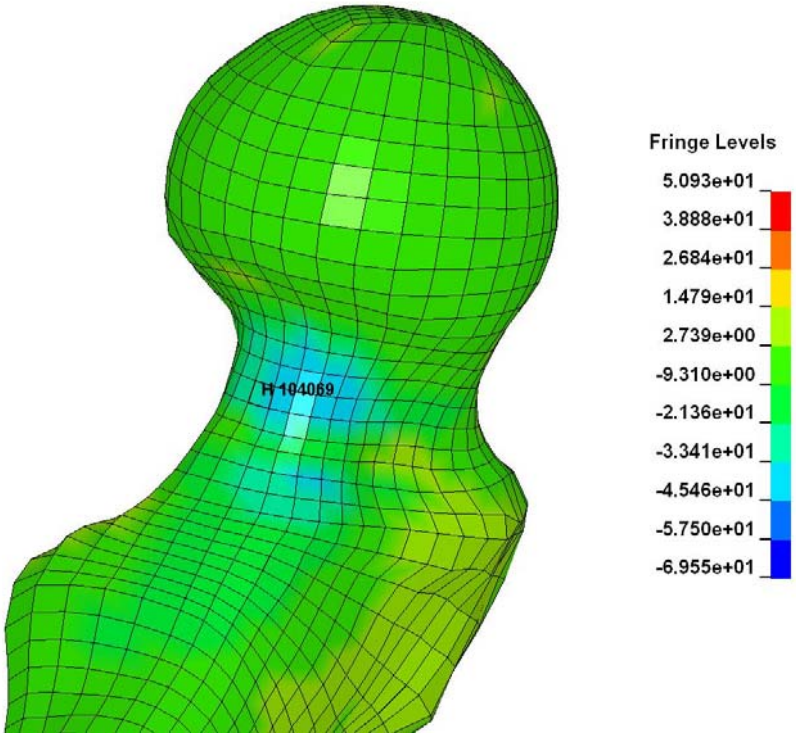

Figure 7.27. Transverse shear ultimate strength fringe plot for the femoral neck region.

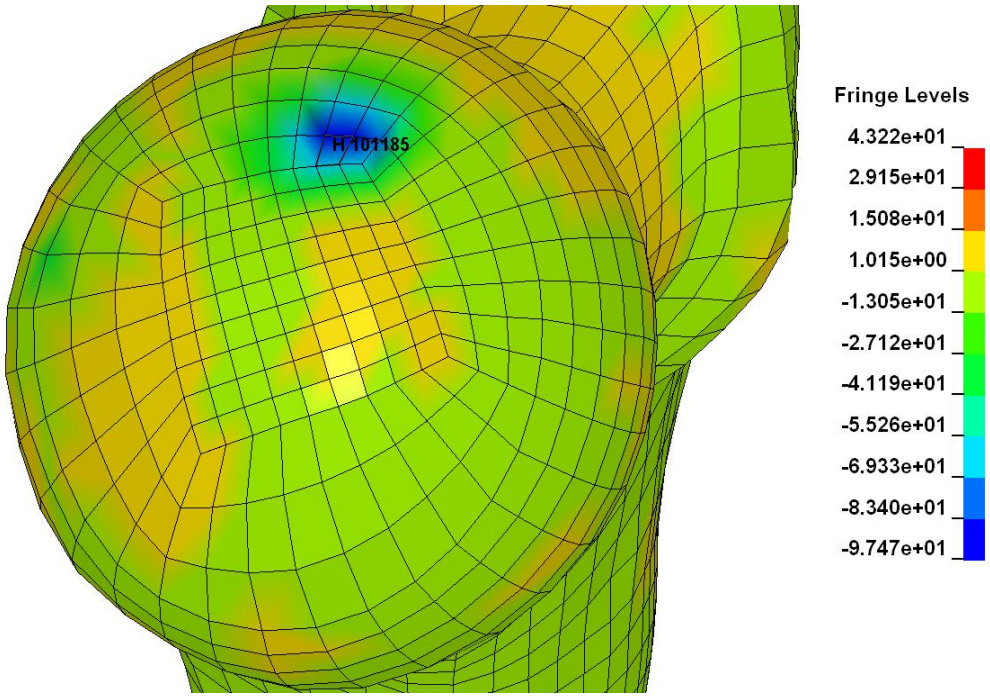

Figure 7.28. Transverse shear ultimate strength fringe plot for the femoral neck region.

7.3.8. Comments

The behavior of the femur force obtained from the FE simulations considering different angles of adduction prior to impact is shown in Figure 7.29.

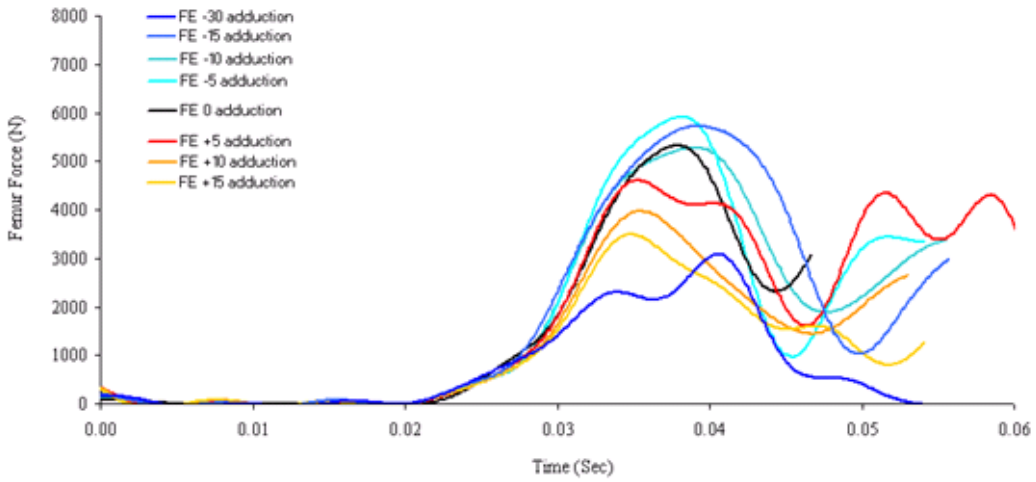

Figure 7.29. Comparison of local femur force behavior for different angles of adduction.

As can be seen more clearly from Figure 7.30, femur forces from the adducted thigh reach a peak which is lower than those obtained in the neutral position impact simulation. One of the reasons is certainly connected to the fact that for high angles of adduction it is more likely for the hip-joint to dislocate as consequence of a frontal impact. When the femoral head dislocates from the acetabular cup, it is no longer subjected to the compressive load condition that it would experience in its normal neutral position. Its load condition, however, is not dropped immediately to zero because the femoral bone is still connected to the ligaments which try to prevent the dislocation. So, in the unloading phase, the femur force behavior is less stiff with comparison to the neutral position, as appears clearly in Figure 7.24 (right). In the FE simulations, the hip joint dislocation happened for the 15 degrees thigh adduction impact. For the 5 and 10 degrees thigh adduction impact, the femoral ball did not dislocate: however, a decrease in femoral peak force can be explained by the fact that the femoral head, because of its initial condition, impacts towards the end of the acetabular cup wall, where the thickness of the cortical and trabecular parts of the

pelvis bone are smaller and easier to break. A fracture of the acetabular wall does not mean necessarily a consequent dislocation of the hip joint as will be explained later, but it certainly reduces the load condition of the femoral head.

Some of the curves reported in the graphs shows two peaks, or a tendency for a second peak, generally lower than the first. For those which were recorded during adducted thigh impact simulations, the explanation for this second peak is connected to a second different fracture mechanism occurring to the KTH. In fact, the first peak is related to the first KTH complex failure, which normally happens to the acetabular cup or to the femoral head. They are, however, only "partial" failures. After a certain decrease of the femoral axial force, the KTH reaches another "stable" position allowing the femoral force to increase again until a second, and this time, total fracture happens. This second fracture was found to always be a neck-trochanteric femur rupture in the FE simulations.

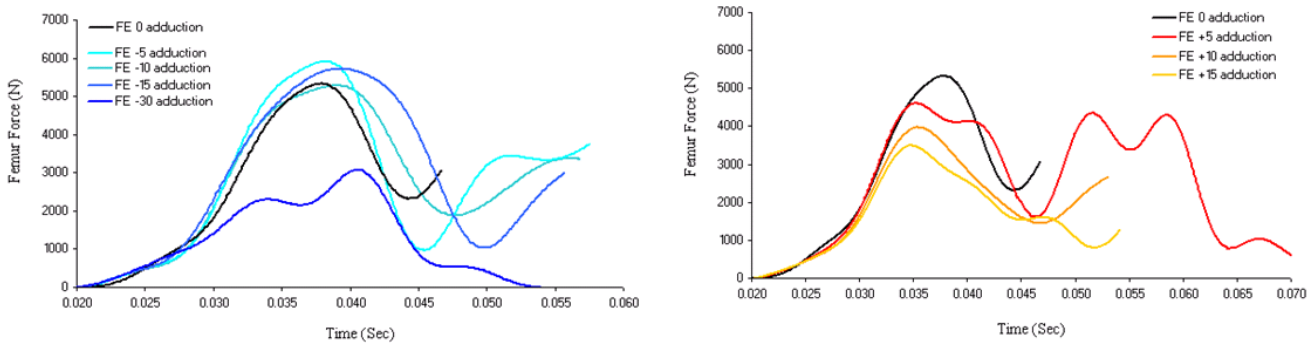

Figure 7.30. Comparison of local femur force behavior for angles of adduction between -30 and -5 degrees (left) and between +5 and +15 (right).

Similar comments can be made for the thigh abducted FE impact results. This time, however, the peak femoral force tends to be higher than the one from the neutral position impact. The reason is found in the initial anatomical position of the femoral head. Because of its abducted position, the femoral head is inserted deeply into the acetabular cup, closer to the thick cortical and trabecular pelvic region where the pelvis is harder to break than the thinner ends of the cup. Moreover, a frontal impact to an adducted thigh

allows for sliding and rotating of the femoral head inside the acetabular cup, during which time the particular loading conditions to the femur allow for increasing the force in the shaft before leading to a fracture. The only different behavior was found for a very high angle of adduction such as 30 degrees. In this case, a much lower peak force was observed with respect to the neutral position impact, at which a top femoral ball failure occurred. As expected, however, this fracture mechanism did not prevent a second increase of the femoral force, leading to a total rupture of the femoral neck.

Figure 7.31 shows the change as a percentage of femur force for an understanding of increasing or decreasing values according to the angles of adduction.

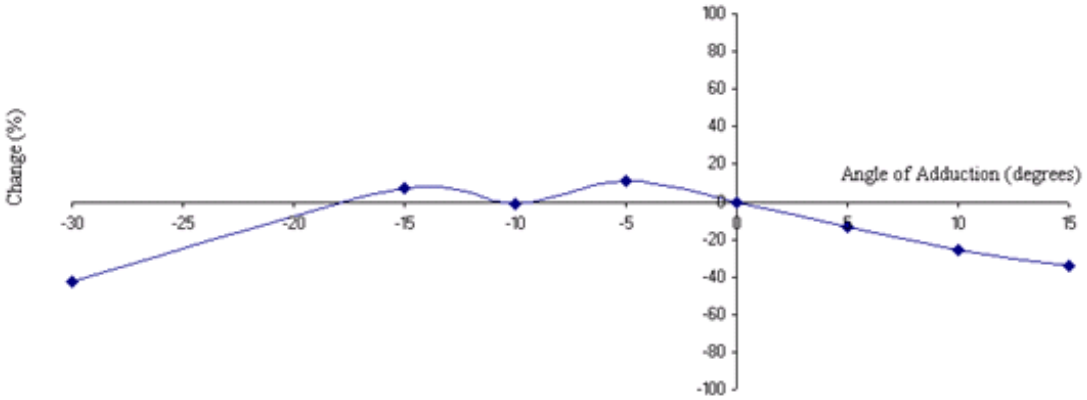

Figure 7.31. Femur force changes with respect to different angles of adduction.

It is very interesting to analyze and investigate fracture mechanisms at different initial angles of adduction. Generally, three different regions of the KTH were affected by failures during these FE simulations: the femoral trochanters, the femoral head and the acetabular cup of the pelvis. Figure 7.32 and Table 7.1 show the fracture initiation force values with respect to the peak forces recorded for each simulation. In this case, it is not explained where the first failure happened in the KTH complex. It is interesting to note that the neutral position appears to be the strongest position during a frontal impact.

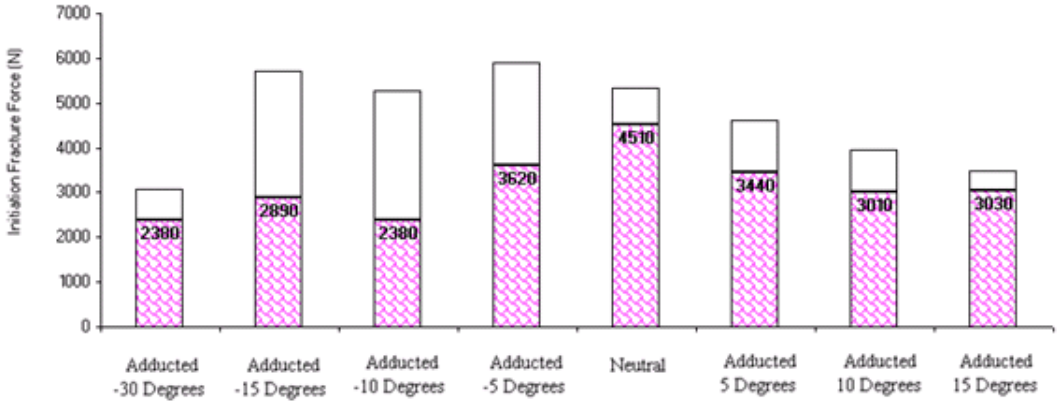

Figure 7.32. Fracture initiation force for different angles of adduction.

Table 7.1. Comparison of peak femur force and initiation femur force for different angles of adduction.

Flexion (Degrees)	Adduction (Degrees)	Peak Femur Force (kN)	First Fracture Force (kN)
0	-30	3074	2380
0	-15	5722	2890
0	-10	5282	2380
0	-5	5913	3620
0	0	5328	4510
0	5	4609	3440
0	10	3971	3010
0	15	3492	3030

Figures 7.33 to 7.36 and Table 7.2 show the fracture initiation force at different angles of adduction/abduction for each KTH region which experienced failure prior to the first peak femur axial force: the pelvis, the femoral neck and trochanters and the top femoral head. In fact, fractures of the pelvis are only failures of the acetabular cup. A summary of all types of fracture mechanisms for the adducted KTH is also shown in Figure 7.37 and Table 7.3.

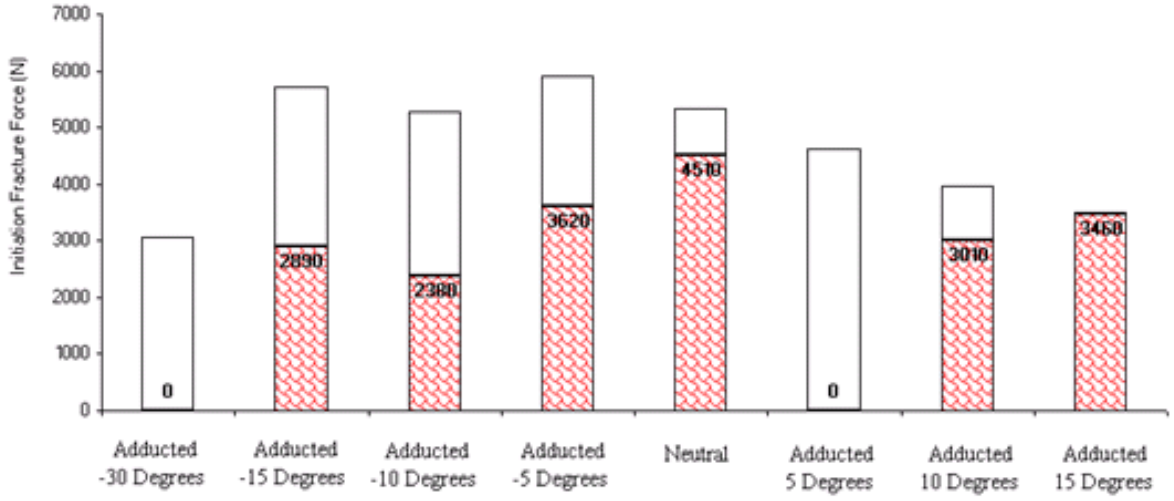

Figure 7.33. Fracture initiation force in the pelvis bone for different angles of adduction.

Table 7.2. Values for fracture initiation force for different types of failure mechanism at different angles of adduction.

Flexion (Degrees)	Adduction (Degrees)	Fracture Pelvis (N)	Fracture Top Ball Femur (N)	Fracture Femur (N)
0	-30	***2940***	2380	***2730***
0	-15	2890	5690	***5650***
0	-10	2380	4260	4990
0	-5	3620	4380	5700
0	0	4510	-	5300
0	5	-	3440	***4540***
0	10	3010	3010	***3520***
0	15	3460	3030	***1540***

Bold and Italic = fracture happened after peak femur force reached.

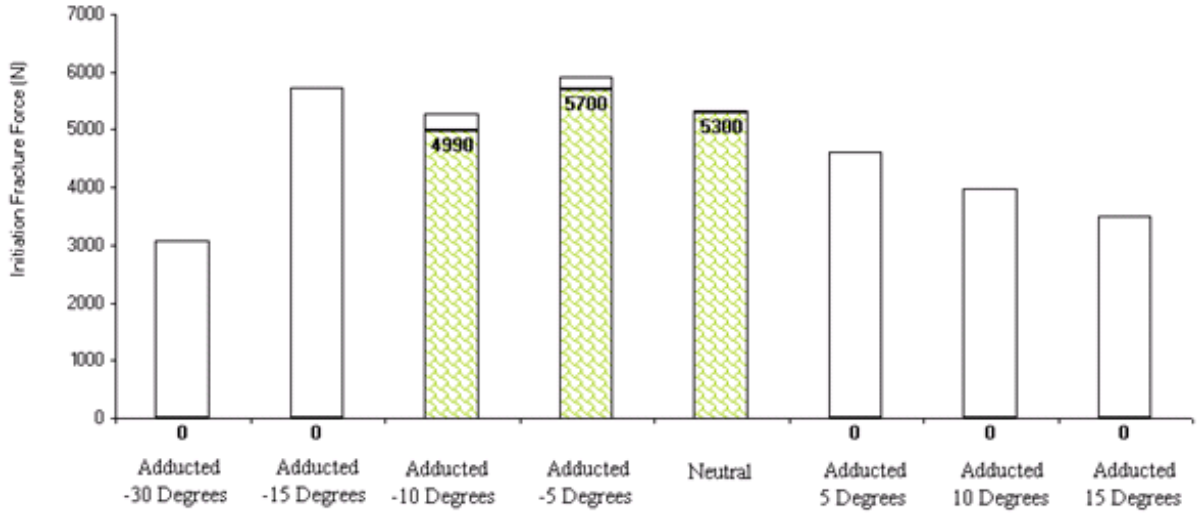

Figure 7.34. Fracture initiation force in the Femur Bone for different angles of adduction.

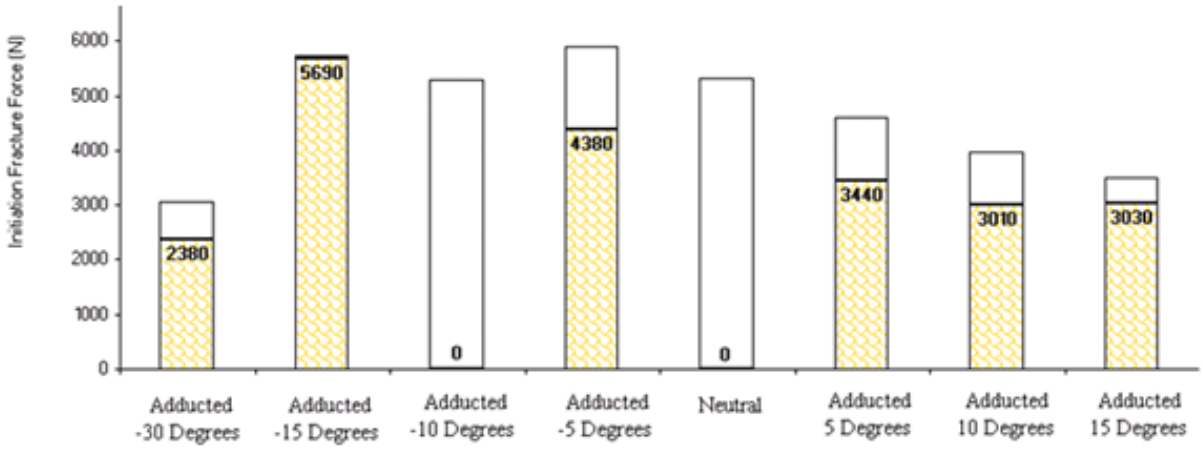

Figure 7.35. Fracture initiation force at the Top Femoral Ball bone for different angles of adduction.

It is very interesting to note that fractures to the acetabular cup and to the top femoral head happened in almost all simulations, before reaching the peak of the femoral force. On the other hand, only three out of eight cases reported femoral neck or trochanteric failure. Also, these three cases of femoral neck fracture occurred for neutral or abducted thigh positions. From these results it seems that the acetabular cup and the top femoral head seem to be the weakest regions of the KTH complex, when considering adduction positions. It must be said, at this point, that the fracture of the cortical acetabular cup is in any simulation smaller in dimensions than the one occurred to the trabecular part of the same region. This result is a little bit in contrast with the knowledge that the cancellous part of a bone is less stiff and weaker than the cortical part. The FE results suggest consequently that a revision of the mechanical trabecular properties of the pelvis bone is needed for a correct and realistic prediction of its failure mechanism. To have weaker trabecular properties would lead most probably to a clearer hip joint dislocation for the 15 degrees adduction FE simulation, and it might also permit a femoral head dislocation at smaller angles of thigh adduction. In fact, more correct geometrical properties for the capitis femoris ligament (the only connection between the femoral head and the acetabular cup) would probably help for a better and more realistic understanding of the hip joint dislocation mechanism.

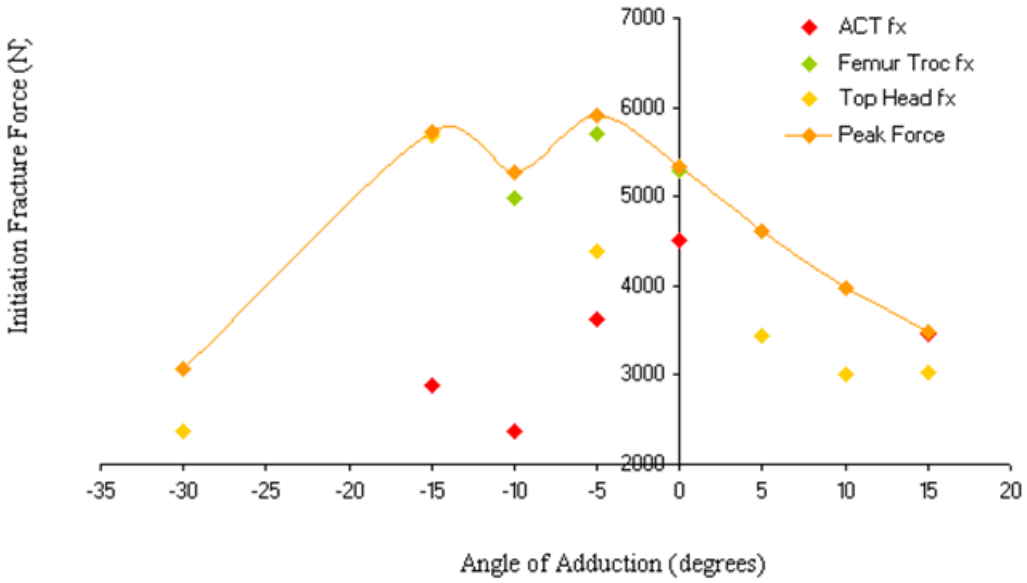

Figure 7.36. Fracture initiation force for different types of failure mechanism at different angles of adduction.

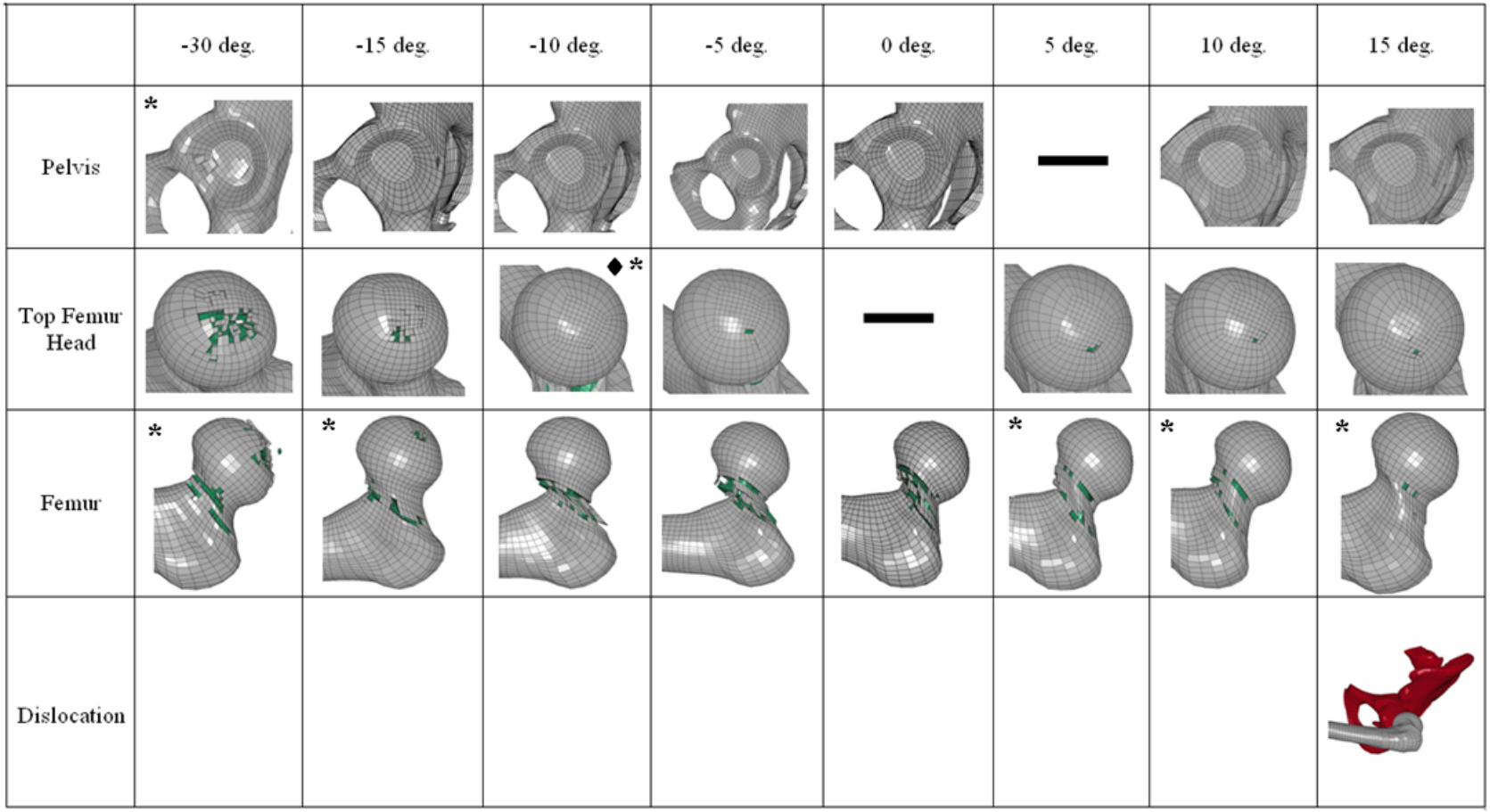

♦ = very small fracture
* = failure after peak of femur force

Figure 7.37. Summary of fracture mechanisms at different angles of adduction.

Table 7.3. Summary of fracture mechanisms at different angles of adduction.

Flexion (Degrees)	Adduction (Degrees)	Fracture Pelvis	Fracture Top Ball Femur	Fracture Femur	Notes
0	-30	Acetabular Cup	Top Ball Femur Rupture	Neck-Trochanter	
0	-15	Acetabular Cup, small	Top Ball Femur Rupture	Neck-Trochanter	
0	-10	Acetabular Cup, small	Top Ball Femur Rupture, very small	Neck-Trochanter	
0	-5	Acetabular Cup, small	Top Ball Femur Rupture	Neck-Trochanter	
0	0	Acetabular Cup, small	-	Neck-Trochanter	
0	5	-	Top Ball Femur Rupture	Neck-Trochanter	
0	10	Acetabular Cup	Top Ball Femur Rupture	Neck-Trochanter	
0	15	Acetabular Cup	Top Ball Femur Rupture	Neck	Hip Joint Dislocation

Another comparison that can be made with regards to the force of fracture for adducted KTH is reported in Figure 7.38. In this graph, the first fracture initiation force recorded during the neutral position impact simulation is compared to the failure initiation forces obtained in each adducted KTH impact.

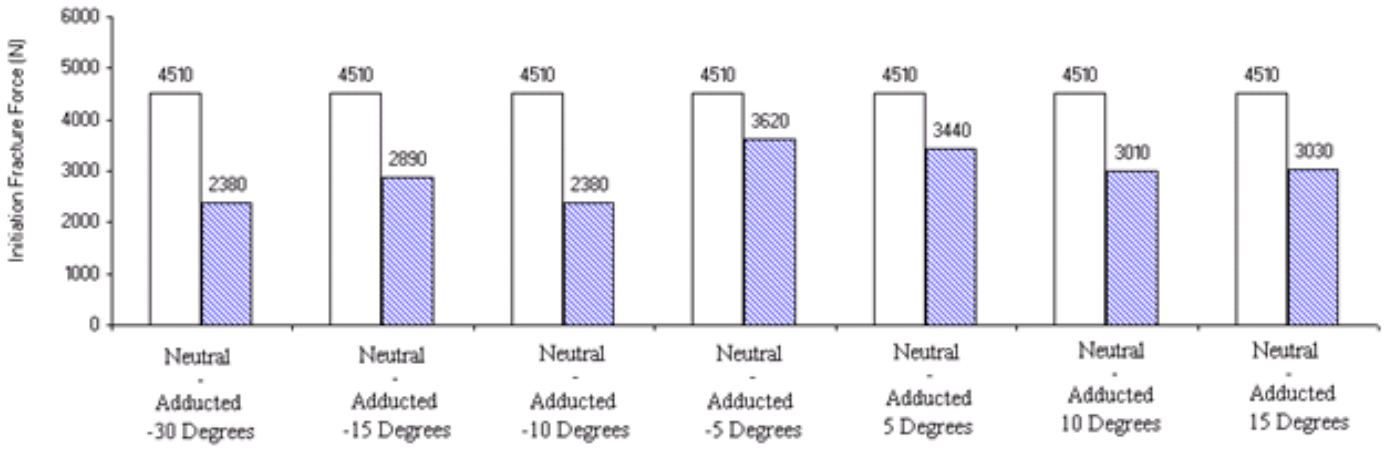

Figure 7.38. Fracture initiation comparison between neutral and out-of-position adducted KTH impact simulations.

Unfortunately, no tests were found with the same setup and load conditions in order to compare these FE simulation results to and proof their validity. The only research project found which closely proposed the same load conditions is a work conducted by Rupp (Rupp et al., 2004). He performed frontal impact tests to both neutral and 10-degree adducted lower limb pairs: the fracture initiation force in a 10-degree adducted KTH resulted to be about 20% lower than the one recorded for neutral position impact tests. With the FE simulations performed in this project, it is found that the difference in percentage of the failure initiation force between the neutral position and the 10-degree adducted impacts is about 30 percent. Consequently, the results obtained by the FE model can be considered acceptable, having also in mind that the test results come from empiric data which are affect by errors and are also derived by statistical analysis which could decrease the gap between the one-by-one comparison of KTH pairs, neutral and adducted. According to the different peak forces obtained by the FE simulations, probability of AIS2+ and AIS3+ were calculated following the same injury criteria that was already considered for the whole-body validation (Kuppa, 2001). They are reported in Table 7.4 and in Figures 7.39 and 7.40, where their probability is presented directly with respect to the initial angle of adduction considered.

Table 7.4. AIS2+ andAIS3+ values resulted for femoral forces observed at different angles of adduction.

Adduction (degrees)	Peak force (N)	AIS2+	AIS3+
-30	3.074	0.0148	0.0184
-15	5.722	0.0562	0.0425
-10	5.282	0.0452	0.0371
-5	5.913	0.0617	0.0451
0	5.328	0.0462	0.0376
5	4.609	0.0323	0.0300
10	3.971	0.0234	0.0245
15	3.492	0.0183	0.0210

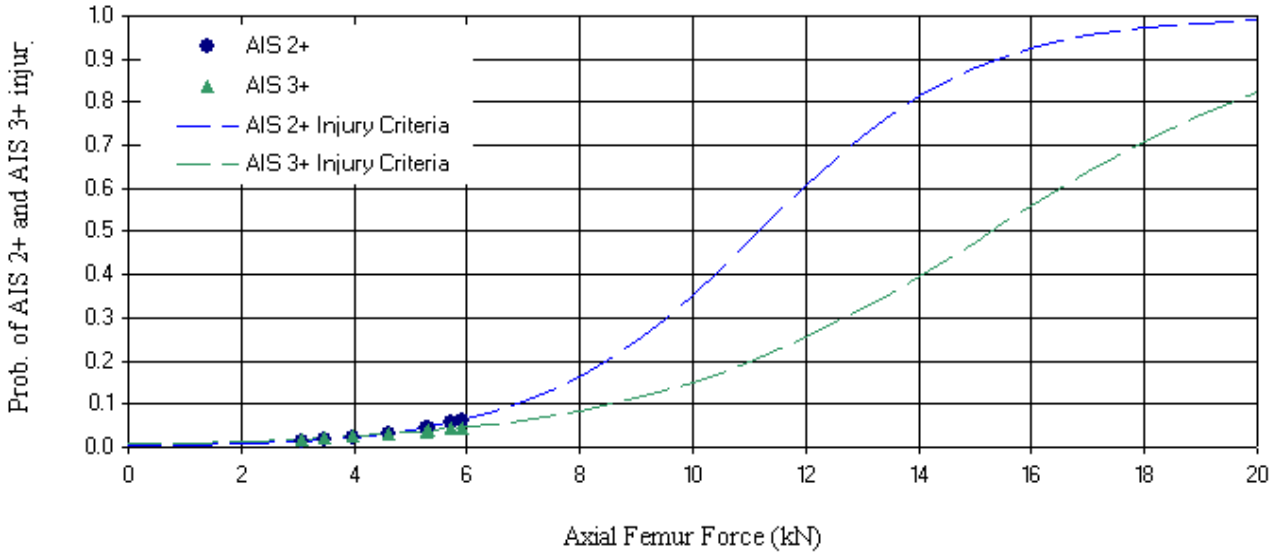

Figure 7.39. Probability of AIS2+ and AIS3+ knee-thigh-hip injuries for forces resulted at different angles of adduction.

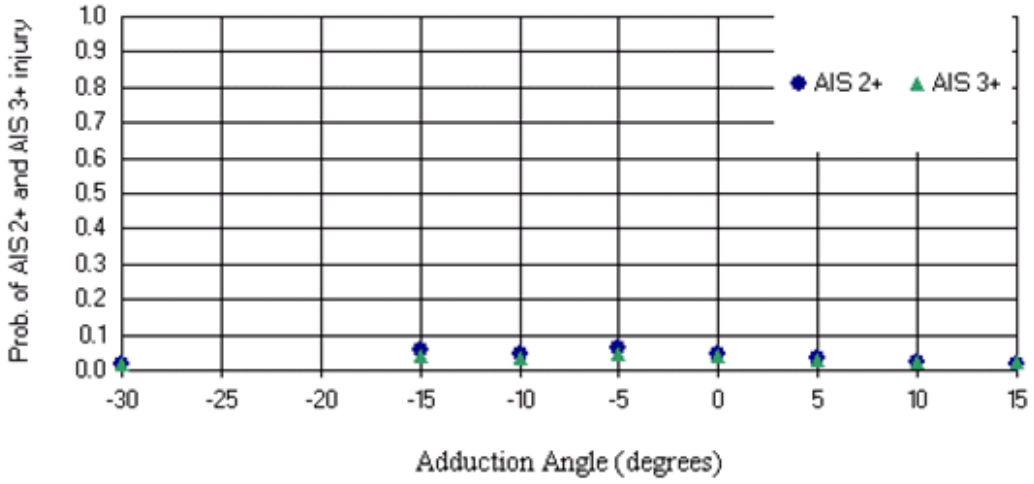

Figure 7.40. Probability of AIS2+ and AIS3+ knee-thigh-hip injuries compared at different angles of adduction.

From these graphs, it appears that a higher probability of KTH bone fracture occurs when the thigh is initially abducted, rather than adducted. These results confirm what was already previously found and discussed about failure mechanisms for an adducted KTH.

Ligaments fracture was not observed in any of the adduction/abduction FE simulations. It is very interesting to observe that in all adducted positions, a fracture of the femoral head occurred after the axial femoral force peak was reached. It seems that while the femoral head tried to dislocate from the acetabular cup, the hip joint ligaments pulled the femur back into the socket. At this point, looking at the FE simulations, fracture of the trochanteric-head region of the femur occurred. It is not known whether this femoral head fracture is related to avulsion failure of the iliofemoral or ischiofemoral joint ligaments, or if this is a rupture which happens with no relation to the ligaments dynamic and properties. At the moment, there are not, however, physical tests that could help understanding the right dynamic. It would be very interesting if impact KTH tests could be conducted with the scope of understanding the sequencing of the bones and soft tissue failures. Right now, fractures are investigated, but no sequence of failures is detected. Sensors or other opportune devices could be inserted in the cadaver specimens prior to

testing, with the aim to report the sequence of the fractures occurred during tests. FE KTH simulation results would be compared to the test outcomes: only at that point it will be possible to understand if the FE KTH impacts are predicting the right failure dynamic and the behavior of hip joint ligaments.

Kuppa proposed injury criteria and injury limits for 25% probability of AIS 2+ lower extremity injury for the 50th percentile adult male (Kuppa, 2001). For the KTH, the limit for 25% probability of AIS 2+ injury is set to a 9,040 N axial femur force. A 15-mm tibia-femur condyles relative displacement is defined as injury limit for the knee ligaments and a 5,060 N proximal tibia axial force is reported as 25% probability of AIS 2+ injury for the tibia plateau. (Kuppa, 2001) Results from FE simulations (i.e., impacts of the KTH and Viano tests reproduction) reproduced the same outcomes as for the knee ligament injury criteria. On the other end, axial impact results reported KTH bone fractures for a recorded axial femur force lower than 9,040 N, either for neutral and out-of-position KTH setups. These outcomes would suggest revising and lowering the threshold force for KTH failure mechanism. As far as the tibia plateau threshold force is concerned, problems were encountered when dealing with FE simulations trying to replicate the injury criteria. Bangelmaier et al. dynamically tested 12 matched pairs of cadaver isolated tibiofemoral joints, impacting them repeatedly until fracture was observed. The results were further analyzed to develop injury criteria for tibial plateau and condyle fractures. Bangelmaier tests setup was reproduced for simulations, but no gross fractures were obtained. (Bangelmaier, 1999) Only small failures of the knee condyles were observed but the tibial plateau was not affected by the impact at all. This particular response of the FE model can be explained by the fact that the mesh of the tibia was not remeshed and is probably too coarse for a realistic transmission of force from the tibial plateau to the femoral condyles. More likely, with a finer mesh definition for the tibia bone, the FE KTH model would be able to replicate also this third injury criteria considered.

7.3.9. Impact of the Lower Limb at 15 Degrees Thigh Flexion

7.3.9.1 Impact of the Lower Limb at 15 Degrees Thigh Flexion: Setup

The setup and the initial configuration for the impact simulation of the lower limb at 15 degrees of thigh flexion are shown in Figure 7.41

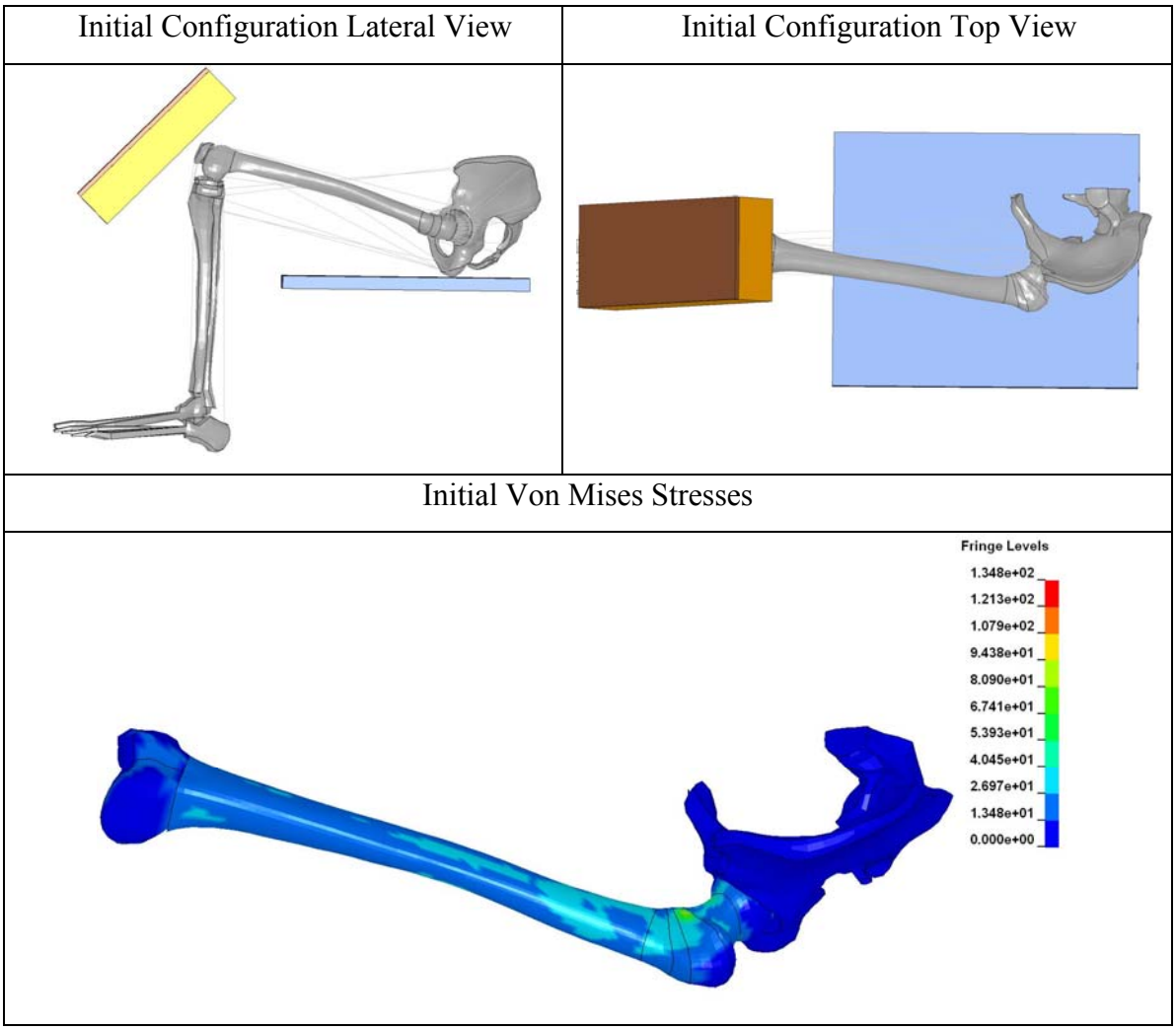

Figure 7.41. Initial configuration for the 15-degree thigh flexion impact simulation: lateral (top left) and top view (top right), and initial Von Mises stresses (bottom).

7.3.9.2 Impact of the Lower Limb at 15 Degrees Thigh Flexion: Results

The final configuration for the impact simulation of the lower limb at 15 degrees of thigh flexion is shown in Figure 7.42. The resulting peak femur force was observed to be 4,720 N.

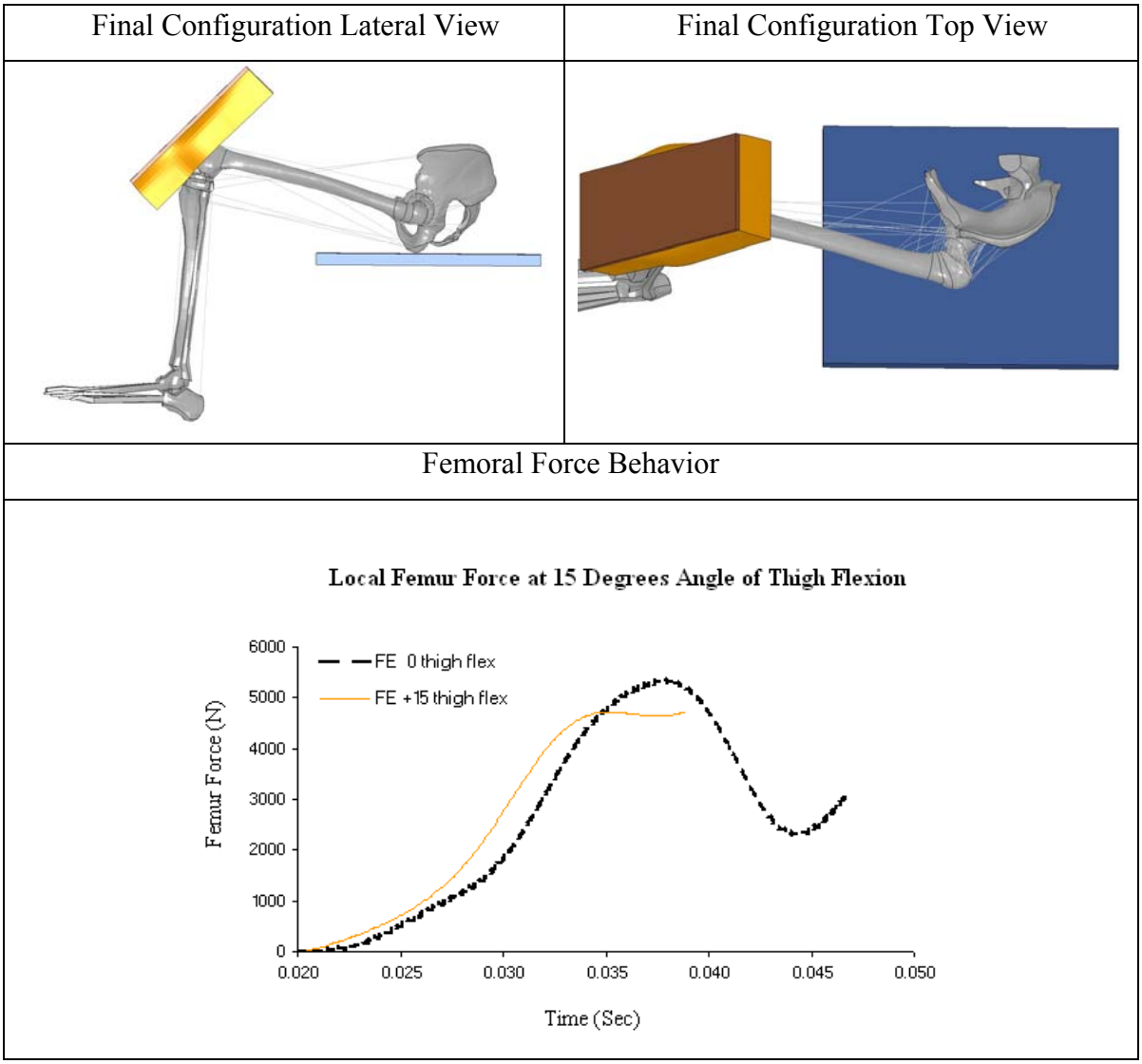

Figure 7.42. Final configuration for the 15-degree thigh flexion impact simulation: final configuration lateral view (top left) and top view (top right), and femoral force behavior (bottom).

The fracture mechanism for the KTH in the simulation of a 15-degree thigh flexion is shown in Figure 7.43.

Pelvis	Femur
—	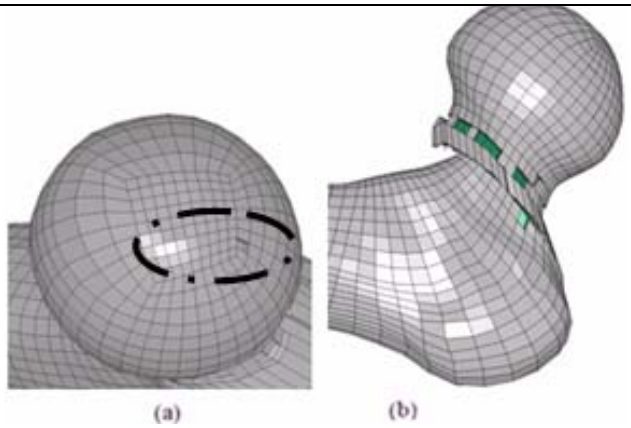

Figure 7.43. Bone fracture results for the 15-degree thigh flexion impact simulation: no failure for the pelvis bone (left), small fracture at the top femoral head (right (a)) and failure of the femur neck-trochanter (right (b)).

No pelvis failure was observed. A very small fracture to the top head of the femur was observed starting at 3,310 N. Failure to the femoral neck-trochanter initiated at 4,500 N. The femoral neck failed because elements reached the ultimate transverse shear strength, while the top of the femur ball fractured when elements reached the transverse shear ultimate strength.

7.3.10. Impact of the Lower Limb at 30 Degrees Thigh Flexion

7.3.10.1 Impact of the Lower Limb at 30 Degrees Thigh Flexion: Setup

The setup and the initial configuration for the impact simulation of the lower limb at 30 degrees of thigh flexion are shown in Figure 7.44.

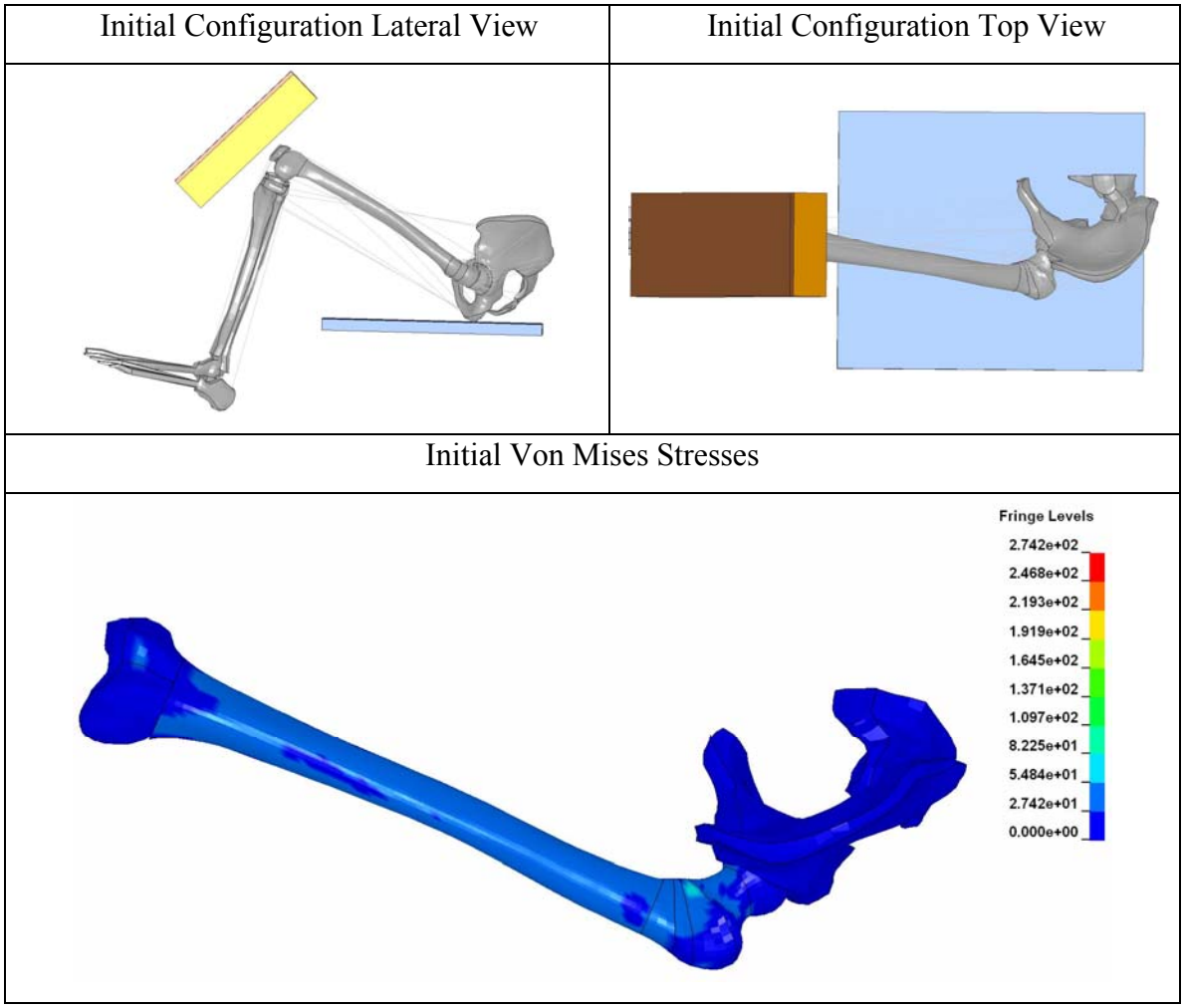

Figure 7.44. Initial configuration for the 30-degree thigh flexion impact simulation: lateral (top left) and top view (top right), and initial Von Mises stresses (bottom).

7.3.10.2 Impact of the Lower Limb at 30 Degrees Thigh Flexion: Results

The final configuration for the impact simulation of the lower limb at 30 degrees of thigh flexion is shown in Figure 7.45. The resulting peak femur force was observed to be 4,694 N.

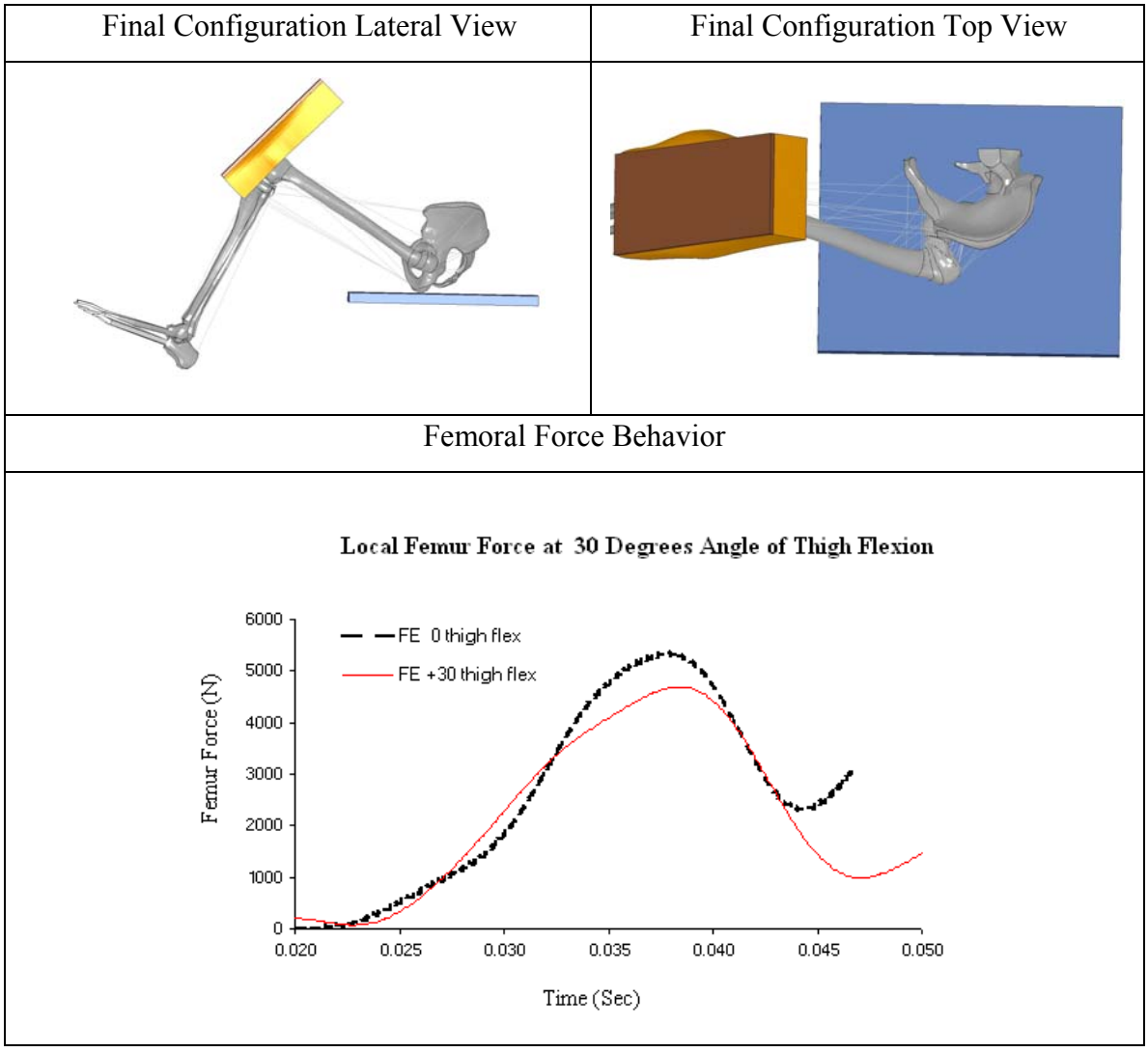

Figure 7.45. Final configuration for 30-degrees thigh flexion impact simulation: final configuration lateral view (top left) and top view (top right), and femoral force behavior (bottom).

The fracture mechanism for the KTH in the simulation of a 30-degree thigh flexion is reported in Figure 7.46.

Pelvis	Femur
	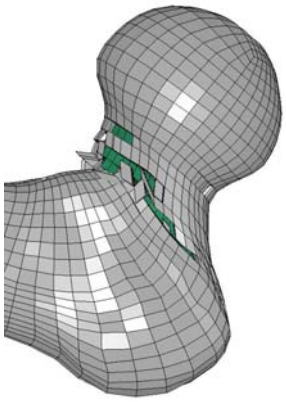

Figure 7.46. Bone fracture results for the 30-degree thigh flexion impact simulation: no failure for the pelvis bone (left), failure of the femur neck-trochanter (right).

No failures to the pelvis or to the top head of the femoral bone were observed. Fracture to the femoral neck-trochanter initiated at 4,530 N.
It was not clear which was the dominant reason for femoral neck elements failure.

7.3.11. Comments

The behavior of the femur force obtained from FE simulations considering different angles of thigh flexion prior to impact is reported in Figure 7.47.

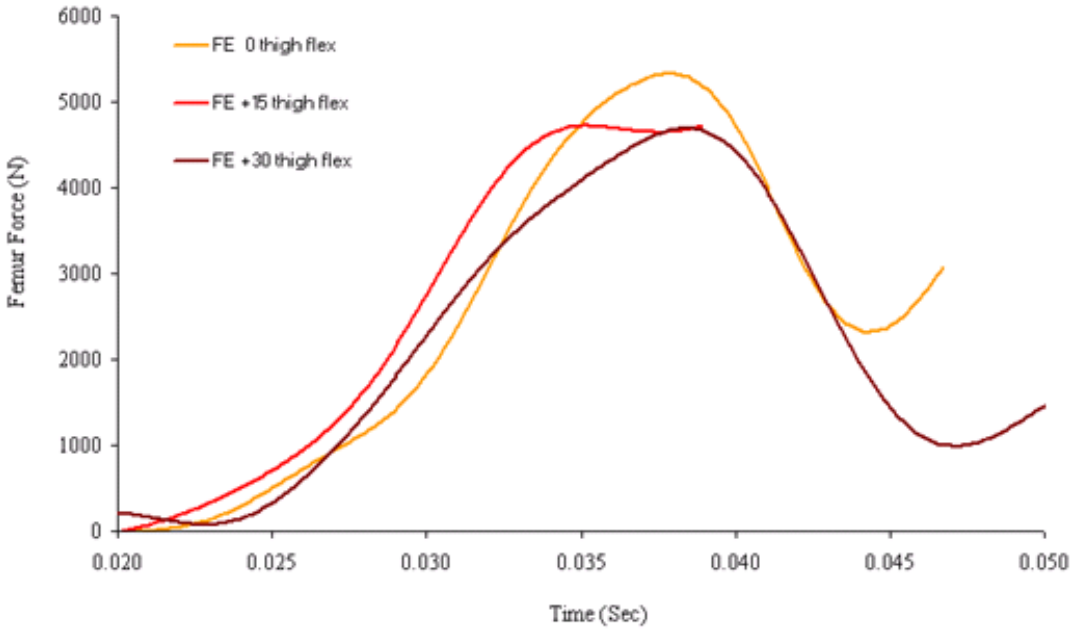

Figure 7.47. Comparison of local femur force behavior for different angles of thigh flexion.

Femur forces from flexed thigh have a peak which is lower than the one obtained by the neutral position impact simulation. The peak is always reached after failure of the femoral neck. As it can be seen from Figure 7.48, FE simulations results show that the change of the femur peak force due to a frontal impact for flexed thigh with respect to the neutral position does not really depend on the angle of thigh flexion.

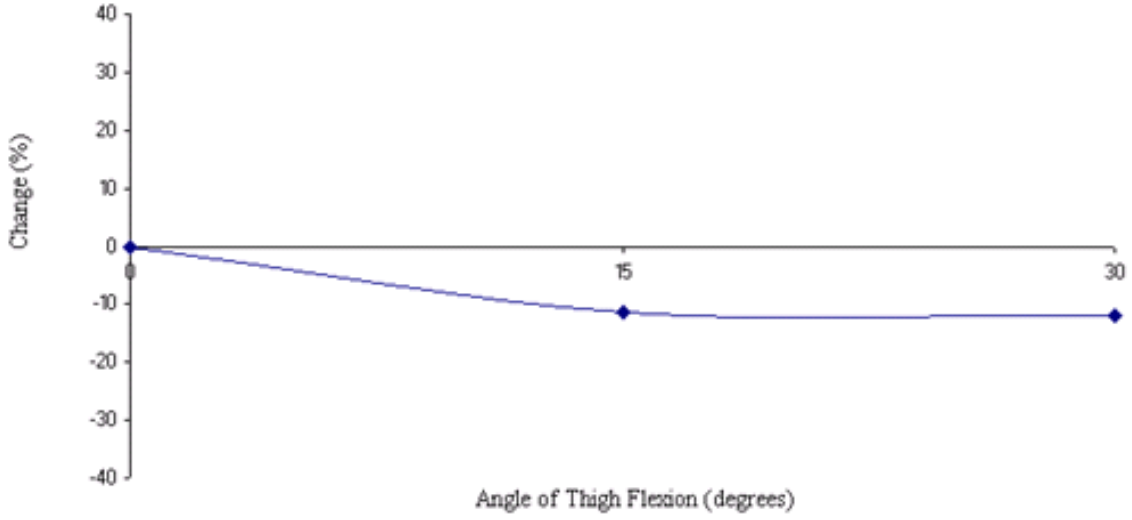

Figure 7.48. Femur force changes with respect to the NHTSA test value according to different angles of thigh flexion.

The KTH model appears weaker when the thigh is flexed than when it is loaded frontally at its neutral position.

In both simulations, the main region of the KTH which was affected by failures during impact was the femoral neck. It is interesting to note that the initiation fracture force for the femoral neck region was almost the same value for both the 15-degree and the 30-degree thigh flexion setup. In the 15-degree flexed simulation, however, a very small fracture occurred to the top of the femoral ball, prior the injury mechanism started for the neck region. Figure 7.49 and Table 7.5 shows the very first fracture initiation force for different angles of thigh flexion: considering the very small fracture happening to the top ball of the femur helps dropping the initiation fracture of the 15-degree flexion impact from 4,500 N, which is the failure force of the femoral neck, to 3,310 N, when actually the top femoral ball fracture begins. As far as the 30-degree thigh flexion is concerned, the initiation force, 4,530 N, is very similar to the initiation force for the neutral position, which is 4,510 N.

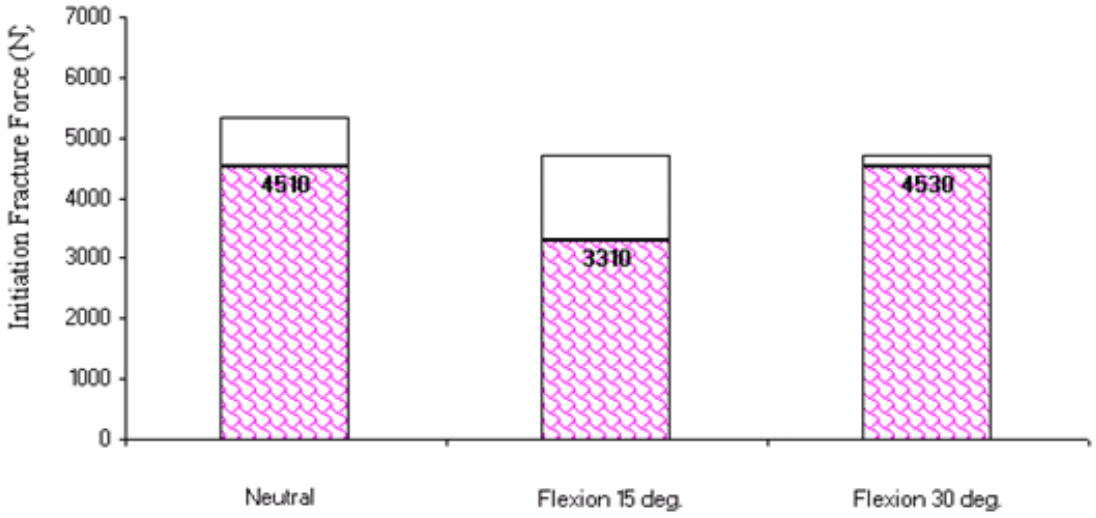

Figure 7.49. Fracture initiation force for different angles of thigh flexion.

Table 7.5. Comparison of peak femur force and initiation femur force for different angles of thigh flexion.

Flexion (Degrees)	Adduction (Degrees)	Peak Femur Force (kN)	First Fracture Force (kN)
0	0	5328	4510
15	0	4720	3310
30	0	4694	4530

Figures 7.50 to 7.53 and Table 7.6 report the fracture initiation force at different angles of thigh flexion for each KTH region which experienced failure prior to the achievement of the first peak force: the pelvis bone, the femoral neck and trochanters and

the top femoral ball. A summary of all types of fracture mechanisms for the adducted KTH is also reported in Figure 7.54 and Table 7.7.

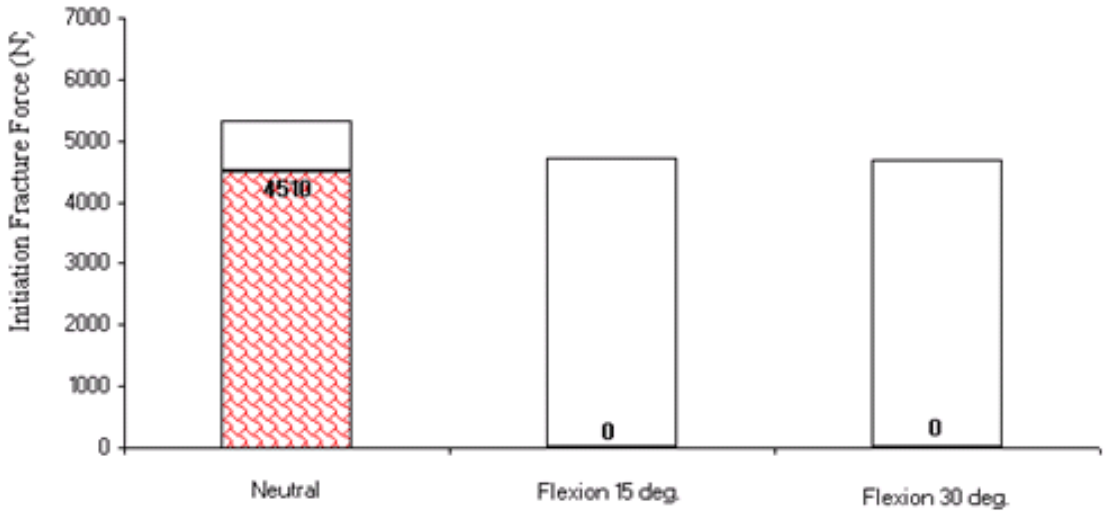

Figure 7.50. Fracture initiation force in the pelvis bone for different angles of thigh flexion.

Table 7.6. Values for fracture initiation force for different types of failure mechanism at different angles of thigh flexion.

Flexion (Degrees)	Adduction (Degrees)	Fracture Pelvis (N)	Fracture Top Ball Femur (N)	Fracture Femur (N)
0	0	4510	-	5300
15	0	-	3310	4500
30	0	-	-	4530

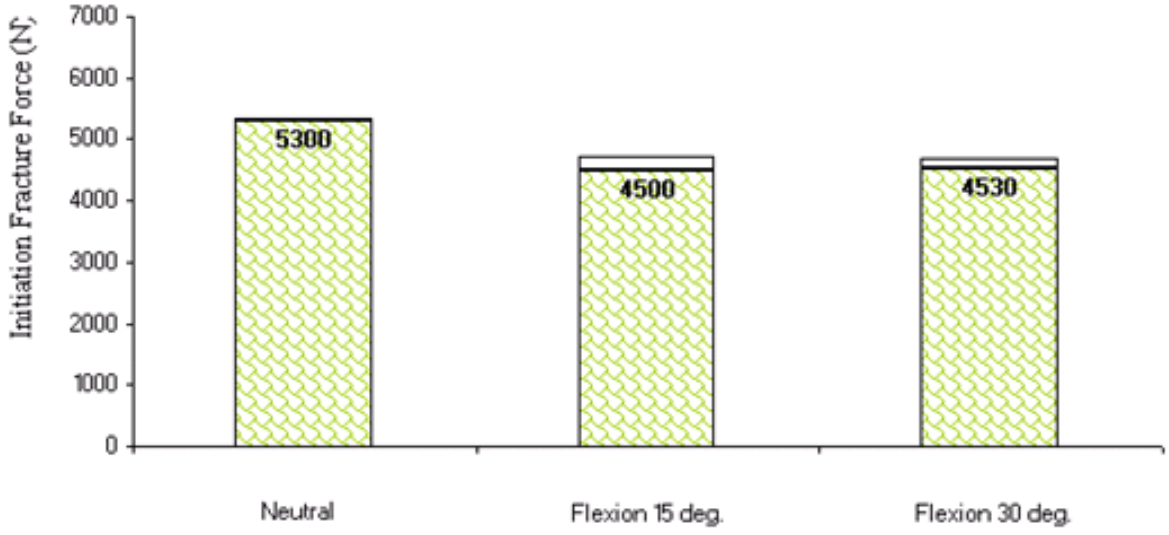

Figure 7.51. Fracture initiation force in the femur bone for different angles of thigh flexion.

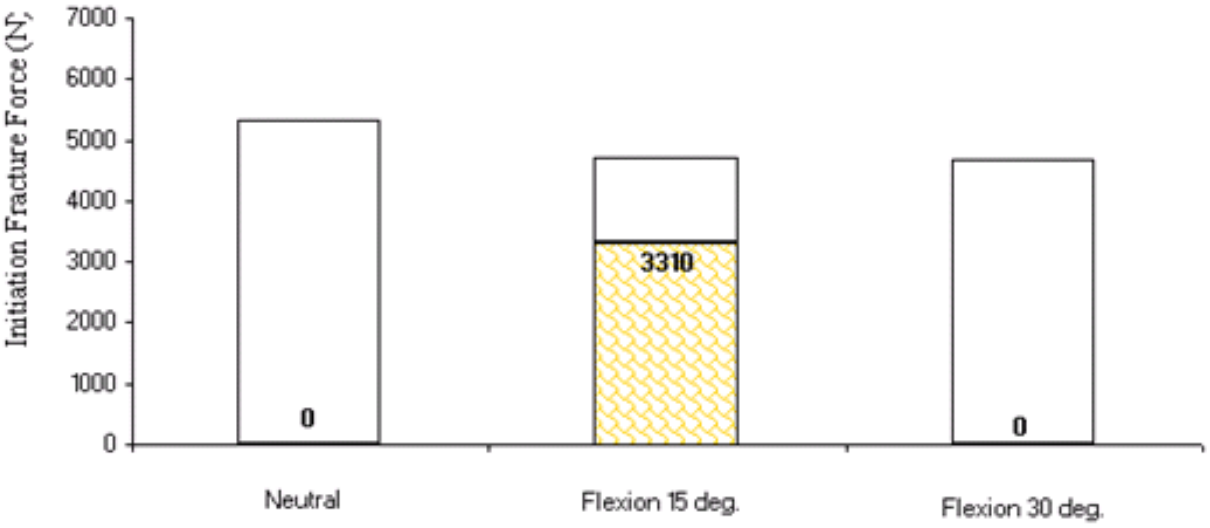

Figure 7.52. Fracture initiation force at the top femoral head bone for different angles of thigh flexion.

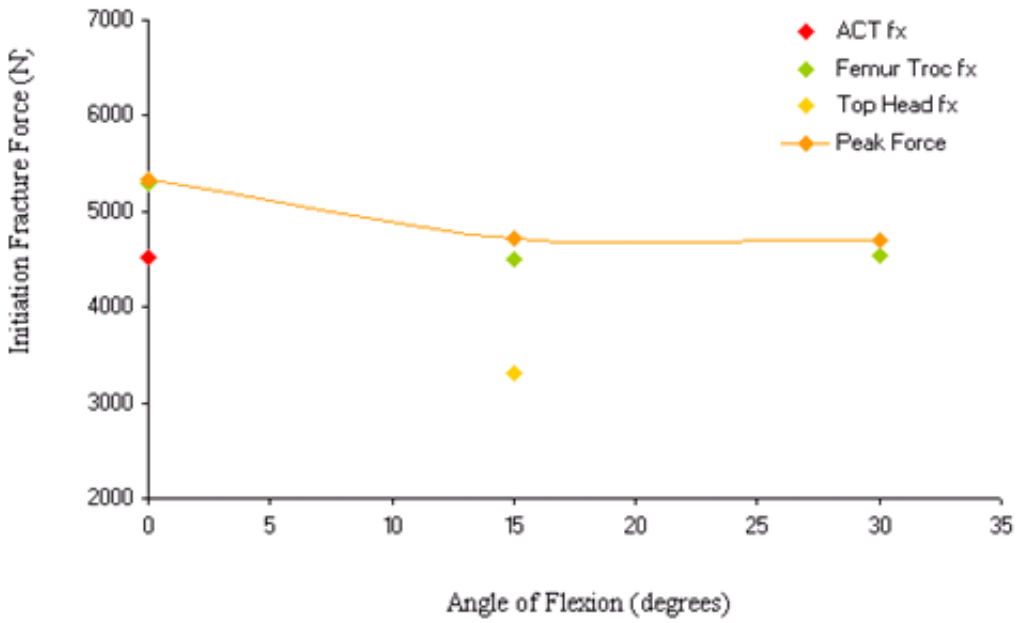

Figure 7.53. Fracture initiation force for different types of failure mechanism at different angles of thigh flexion.

Table 7.7. Summary of fracture mechanisms at different angles of thigh flexion.

Flexion (Degrees)	Adduction (Degrees)	Fracture Pelvis	Fracture Top Ball Femur	Fracture Femur
0	0	Acetabular Cup, small	-	Neck-Trochanter
15	0	-	Top Ball Femur Rupture, very small	Neck-Trochanter
30	0	-	-	Neck-Trochanter

	0 Flexion	15 Flexion	30 Flexion
Pelvis	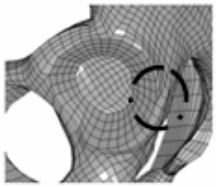	—	—
Top Femur Head	—	♦ 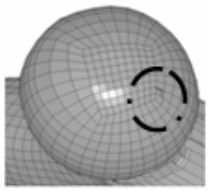	—
Femur	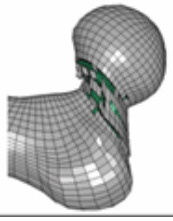	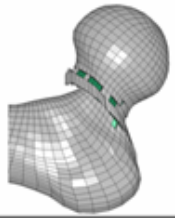	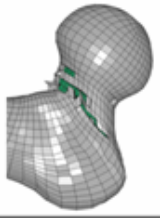

♦ = very small fracture

Figure 7.54. Summary of fracture mechanism for the thigh flexion impact simulations setup.

It is interesting to note that no fracture to the pelvis bone occurred for the thigh flexion impact simulations. It is not clear if the lack of acetabular cup failure in these cases is somehow related to the mechanical properties chosen for the pelvis. In fact, it was already discuss in the previous section that trabecular mechanical properties for the pelvis seemed to need a revision because the material appeared too hard to break. On the other hand, however, no failure of the cortical component of the pelvis happened. This could also suggest that the model is actually behaving properly and that the lack of failure mechanism for the pelvis region is just a realistic consequence of the particular initial position for the loading condition considered: the KTH, as conclusion, could behave strongly in the pelvic region.

Another comparison that can be made with regards to the force of fracture for flexed KTH is reported in Figure 7.55. In this graph, the first fracture initiation force recorded during the neutral position impact simulation is compared to the failure initiation forces obtained in each thigh flexed KTH impact.

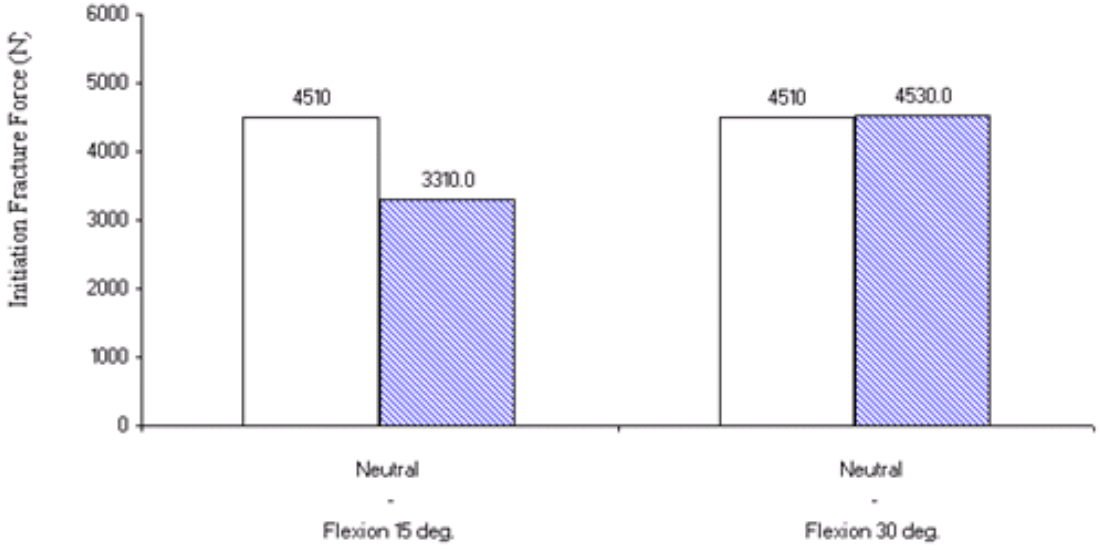

Figure 7.55. Fracture initiation comparison between neutral and out-of-position flexed KTH impact simulations.

The only research project found which closely proposed the same load conditions is a work conducted by Rupp (Rupp et al., 2004). He performed frontal impact tests to both neutral and 30-degree thigh flexed lower limb pairs: the fracture initiation force in a 30-degree thigh flexed KTH resulted to be about 30% lower than the one recorded for neutral position impact tests. With the FE simulations performed in this project, it is found that basically there was no difference in percentage of the failure initiation force between the neutral position and the 30-degree flexed impacts. Discussion about this result was already reported above. The comparison of the FE simulations results and the tests conducted by Rupp suggests that there is a high probability that the KTH FE model is not actually behaving realistically when subjected to this type of setup and loading conditions.

According to the different peak forces obtained by the FE simulations, probability of AIS2+ and AIS3+ were calculated following the same injury criteria that was already considered for the whole-body validation (Kuppa, 2001). They are reported in Table 7.4 and in Figures 7.56 and 7.57, where their probability is presented directly with respect to the initial angle of adduction considered.

Table 7.8. AIS2+ and AIS3+ values resulted for femoral forces observed at different angles of thigh flexion.

Flexion (degrees)	Peak force (N)	AIS2+	AIS3+
0	5.328	0.0462	0.0376
15	4.72	0.0341	0.0310
30	4.694	0.0337	0.0308

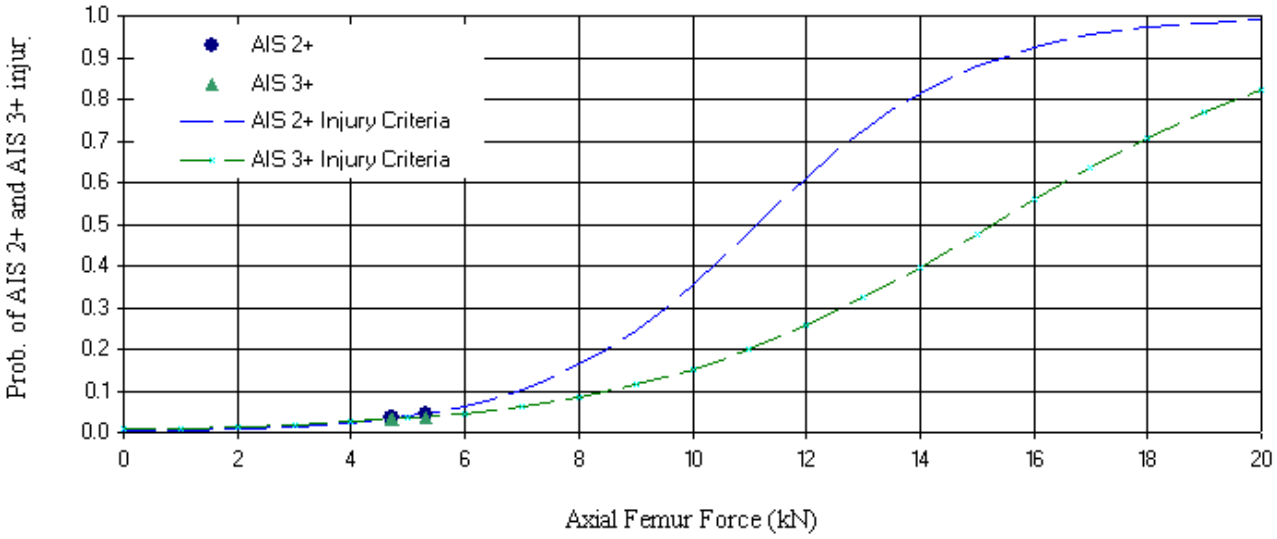

Figure 7.56. Probability of AIS2+ and AIS3+ knee-thigh-hip injuries for forces resulted at different angles of thigh flexion.

Figure 7.57. Probability of AIS2+ and AIS3+ knee-thigh-hip injuries compared at different angles of thigh flexion.

From these graphs, it appears that a lower probability of KTH bone fracture occurs when the thigh is initially flexed, rather than at neutral position. These results confirm what was already previously found and discussed about failure mechanisms for a flexed KTH.

Ligaments fracture was not observed in any of the flexed FE simulations.

7.4 Impact of the Lower Limb moved of more than One Angle from the Neutral Position

7.4.1. Impact of the Lower Limb at 15 Degrees Thigh Flexion and 15 Degrees Adduction

7.4.1.1 Impact of the Lower Limb at 15 Degrees Thigh Flexion and 15 Degrees Adduction: Setup

The setup and the initial configuration for the impact simulation of the lower limb at 15 degrees of thigh flexion and 15 degrees of adduction are shown in Figure 7.58.

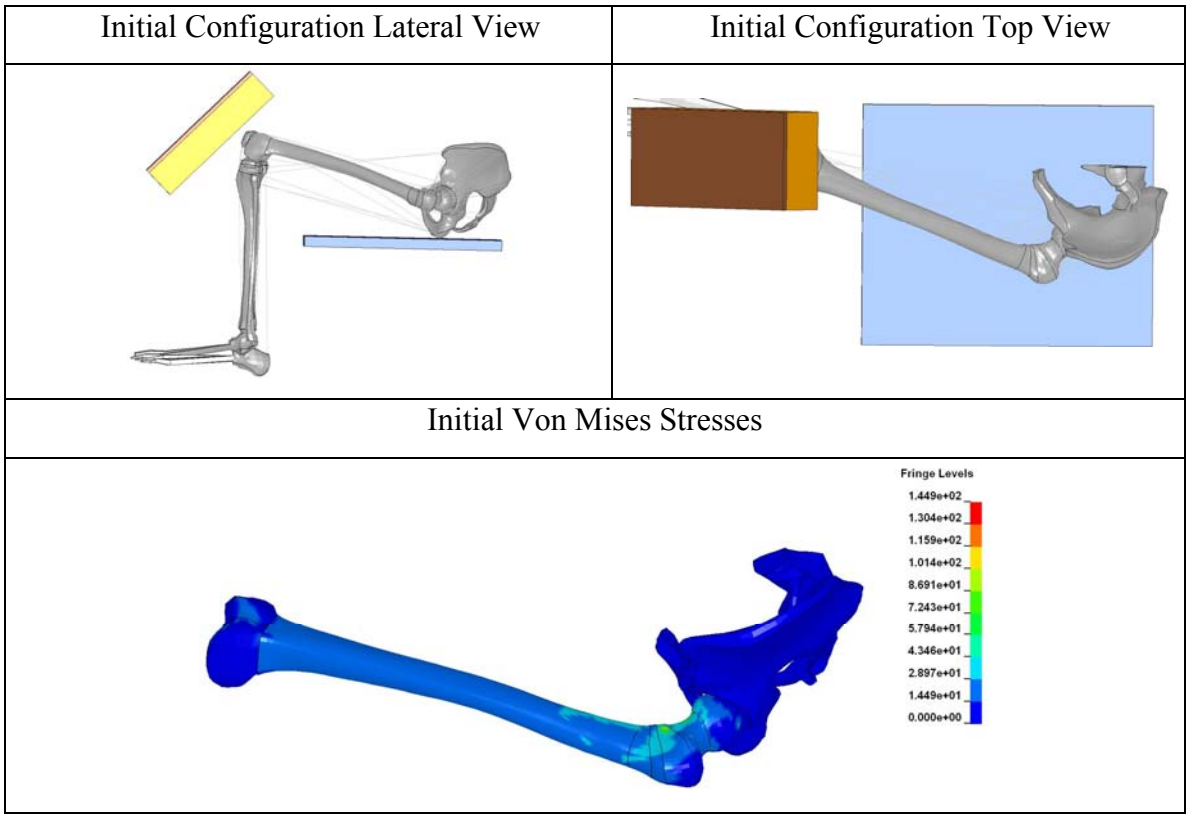

Figure 7.58. Initial configuration for the 15-degree thigh flexion and 15-degrees adduction impact simulation: lateral (top left) and top view (top right), and initial Von Mises stresses (bottom).

7.4.1.2 Impact of the Lower Limb at 15 Degrees Thigh Flexion and 15 Degrees Adduction: Results

The final configuration for the impact simulation of the lower limb at 15 degrees of thigh flexion and 15 degrees of adduction is shown in Figure 7.59. The resulting peak femur force was observed to be 2,865 N.

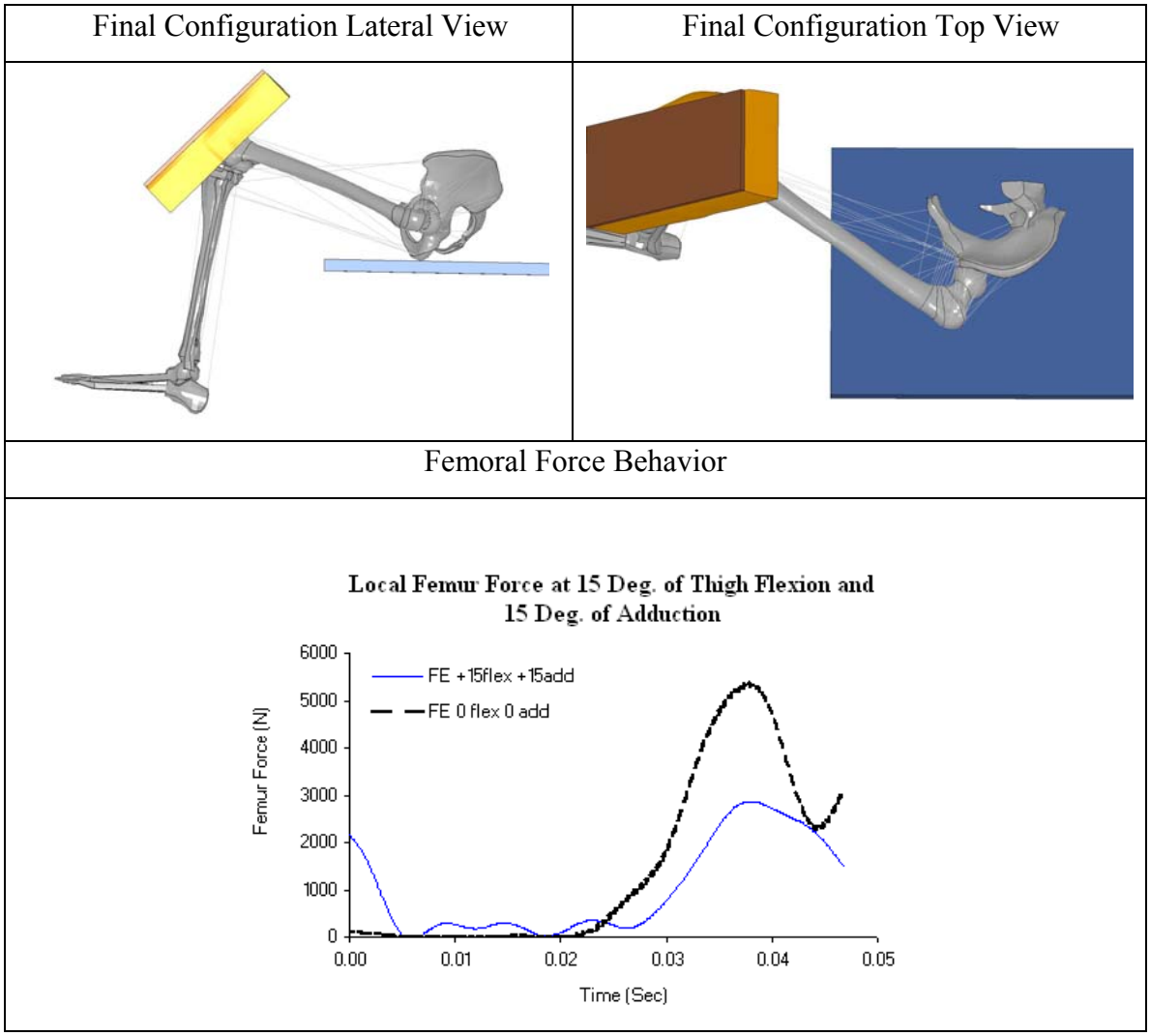

Figure 7.59. Final configuration for the 15-degree thigh flexion and 15-degrees adduction impact simulation: final configuration lateral view (top left) and top view (top right), and femoral force behavior (bottom).

The fracture mechanism for the KTH in the simulation of a 15-degree thigh flexion and 15-degree adduction is shown in Figure 7.60.

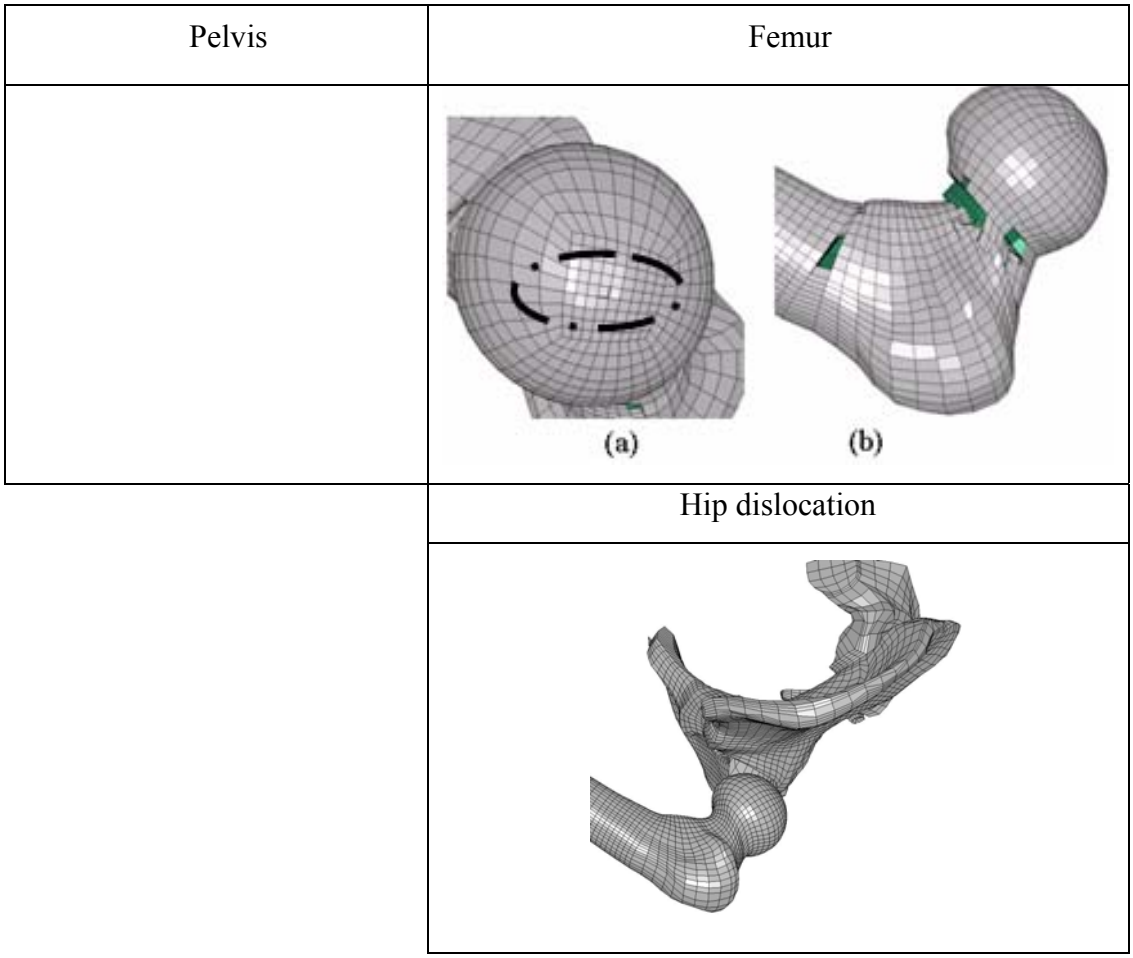

Figure 7.60. Bone fracture results for 15-degrees thigh flexion and 15-degrees adduction impact simulation: no rupture for the pelvis bone (top left) small fracture to the top femoral head (top right (a)), fracture to the femoral neck-trochanter and shaft (top right (b)), and dislocation of the hip joint before failure (bottom).

No rupture occurred for the pelvis bone. A hip dislocation was observed. After the dislocation occurred, fractures to the top-head femur and to the femoral head were observed, initiating at 2,620 N and at 2,520 N respectively. It was not clear which were the dominant reasons for femoral neck and top femoral ball elements failures.

7.4.2. Impact of the Lower Limb at 15 Degrees Thigh Flexion and -30 Degrees Adduction

7.4.2.1 Impact of the Lower Limb at 15 Degrees Thigh Flexion and -30 Degrees Adduction: Setup

The setup and the initial configuration for the impact simulation of the lower limb at 15 degrees of thigh flexion and -30 degrees of adduction are shown in Figure 7.61.

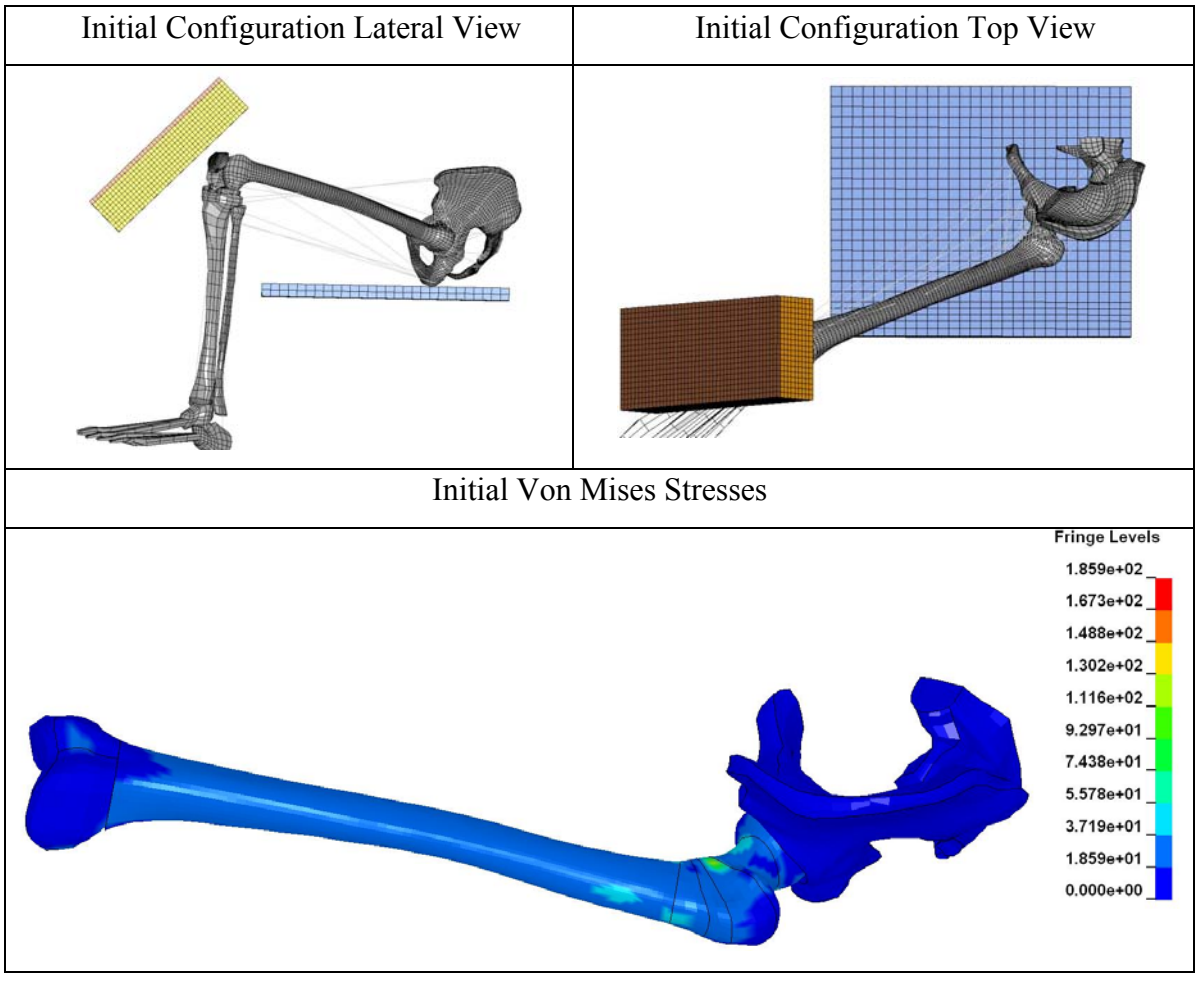

Figure 7.61. Initial configuration for the 15-degree thigh flexion and -30-degrees adduction impact simulation: lateral (top left) and top view (top right), and initial Von Mises stresses (bottom).

7.4.2.2 Impact of the Lower Limb at 15 Degrees Thigh Flexion and -30 Degrees Adduction: Results

The final configuration for the impact simulation of the lower limb at 15 degrees of thigh flexion and -30 degrees of adduction is shown in Figure 7.62. The resulting peak femur force was observed to be 2,514 N.

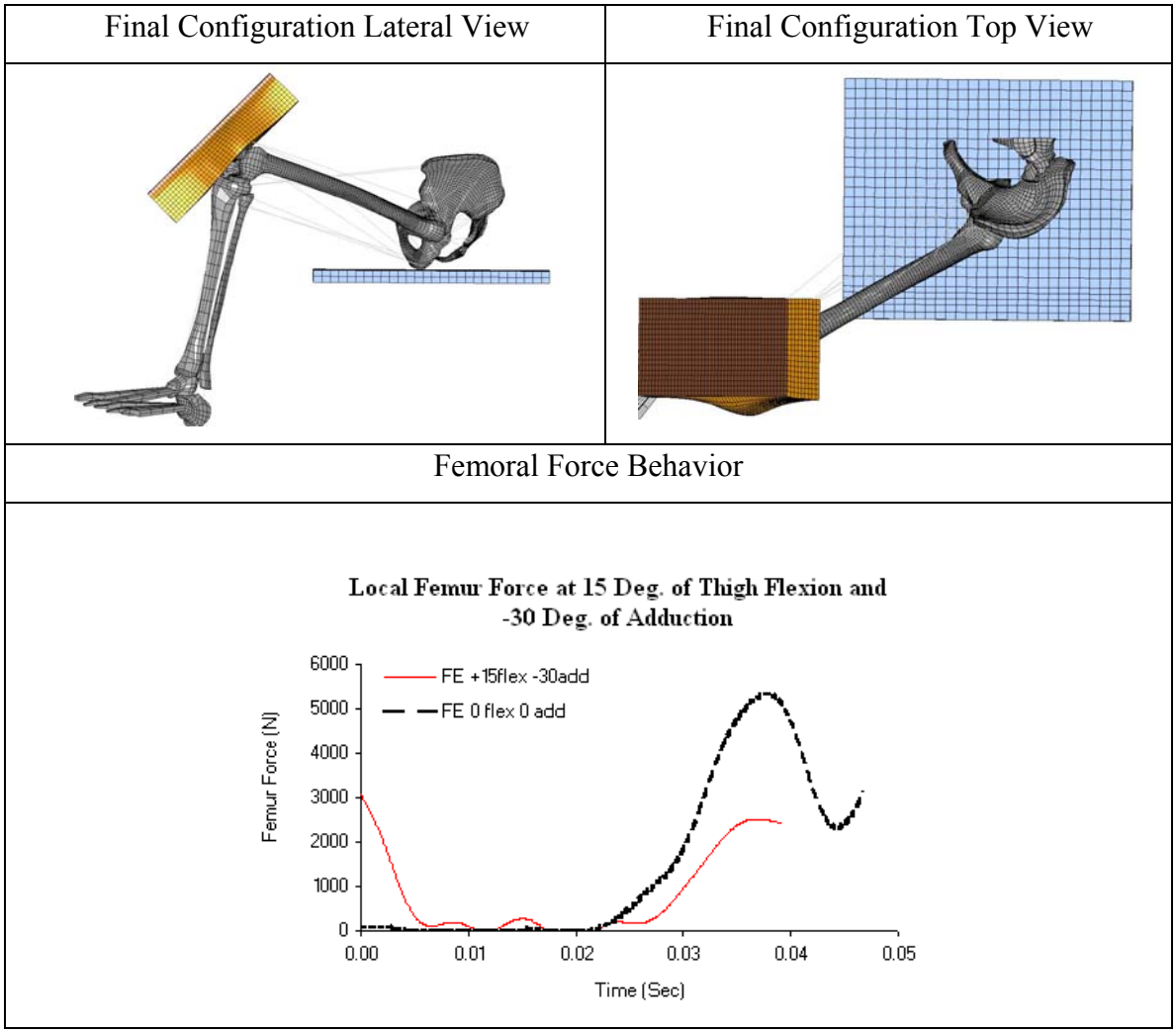

Figure 7.62. Final configuration for the 15-degree thigh flexion and -30-degrees adduction impact simulation: final configuration lateral view (top left) and top view (top right), and femoral force behavior (bottom).

The fracture mechanism for the KTH in the simulation of a 15-degree thigh flexion and -30-degree adduction is shown in Figure 7.63.

Pelvis	Femur
	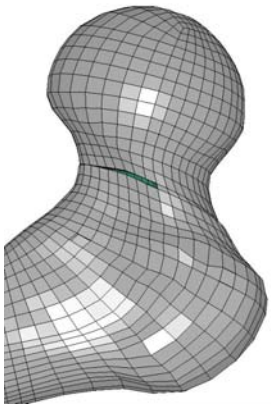

Figure 7.63. Bone fracture results for the 15-degree thigh flexion and -30-degree adduction impact simulation: no failure for the pelvis bone (left), fracture to the femur neck (right).

No rupture occurred for the pelvis bone. Fracture to femoral neck was observed, initiating at 2,460 N, after the femur force reached its peak.

It was not clear which was the dominant reason for femoral neck elements failure.

7.4.3. Impact of the Lower Limb at 30 Degrees Thigh Flexion and 15 Degrees Adduction

7.4.3.1 Impact of the Lower Limb at 30 Degrees Thigh Flexion and 15 Degrees Adduction: Setup

The setup and the initial configuration for the impact simulation of the lower limb at 30 degrees of thigh flexion and 15 degrees of adduction are shown in Figure 7.64.

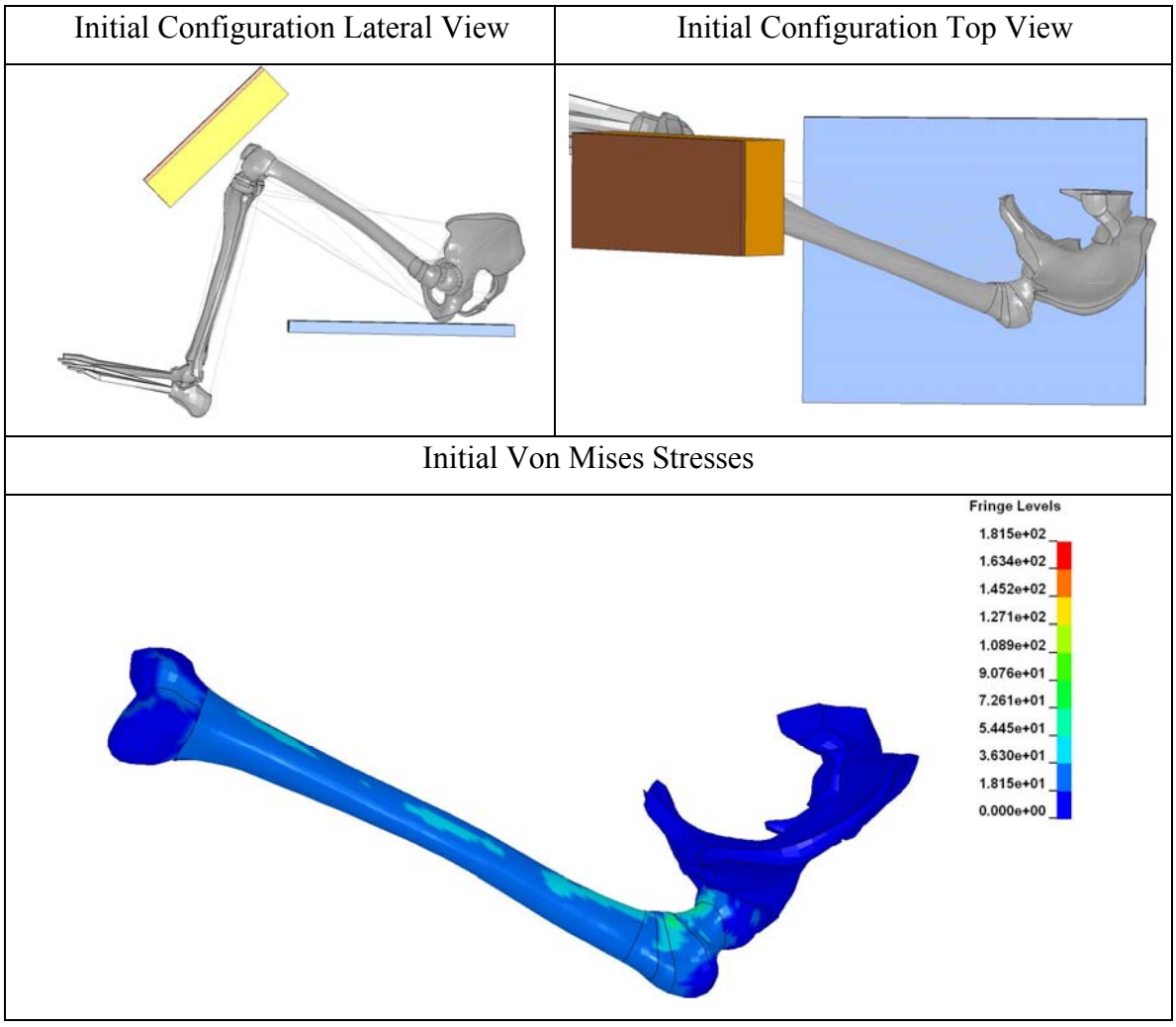

Figure 7.64. Initial configuration for the 30-degree thigh flexion and 15-degrees adduction impact simulation: lateral (top left) and top view (top right), and initial Von Mises stresses (bottom).

7.4.3.2 Impact of the Lower Limb at 30 Degrees Thigh Flexion and 15 Degrees Adduction: Results

The final configuration for the impact simulation of the lower limb at 30 degrees of thigh flexion and 15 degrees of adduction is shown in Figure 7.65. The resulting peak femur force was observed to be 3,271 N.

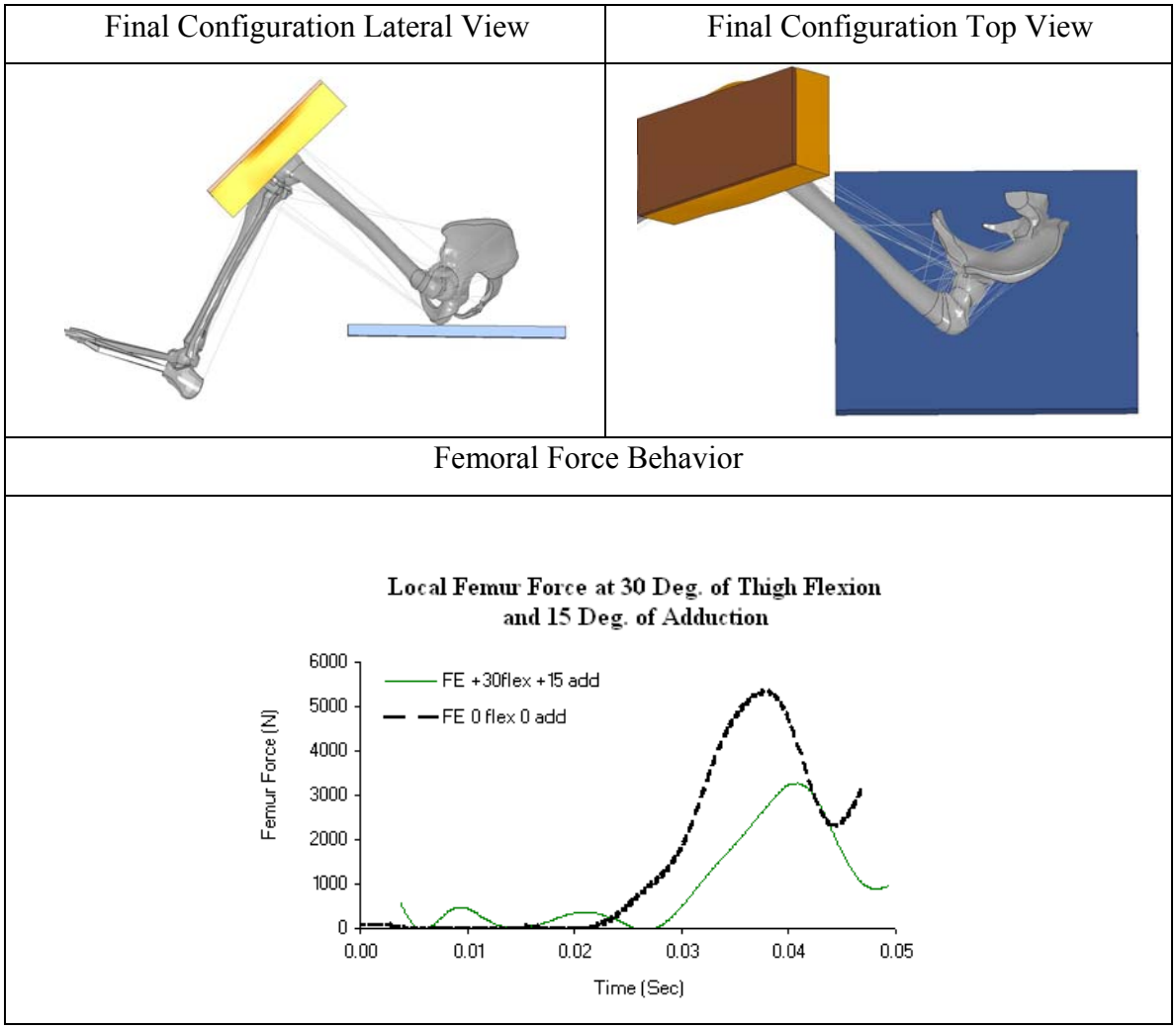

Figure 7.65. Final configuration for 30-degrees thigh flexion and 15-degrees adduction impact simulation: final configuration lateral view (top left) and top view (top right), and femoral force behavior (bottom).

The fracture mechanism for the KTH in the simulation of a 30-degree thigh flexion and 15-degree adduction is reported in Figure 7.66.

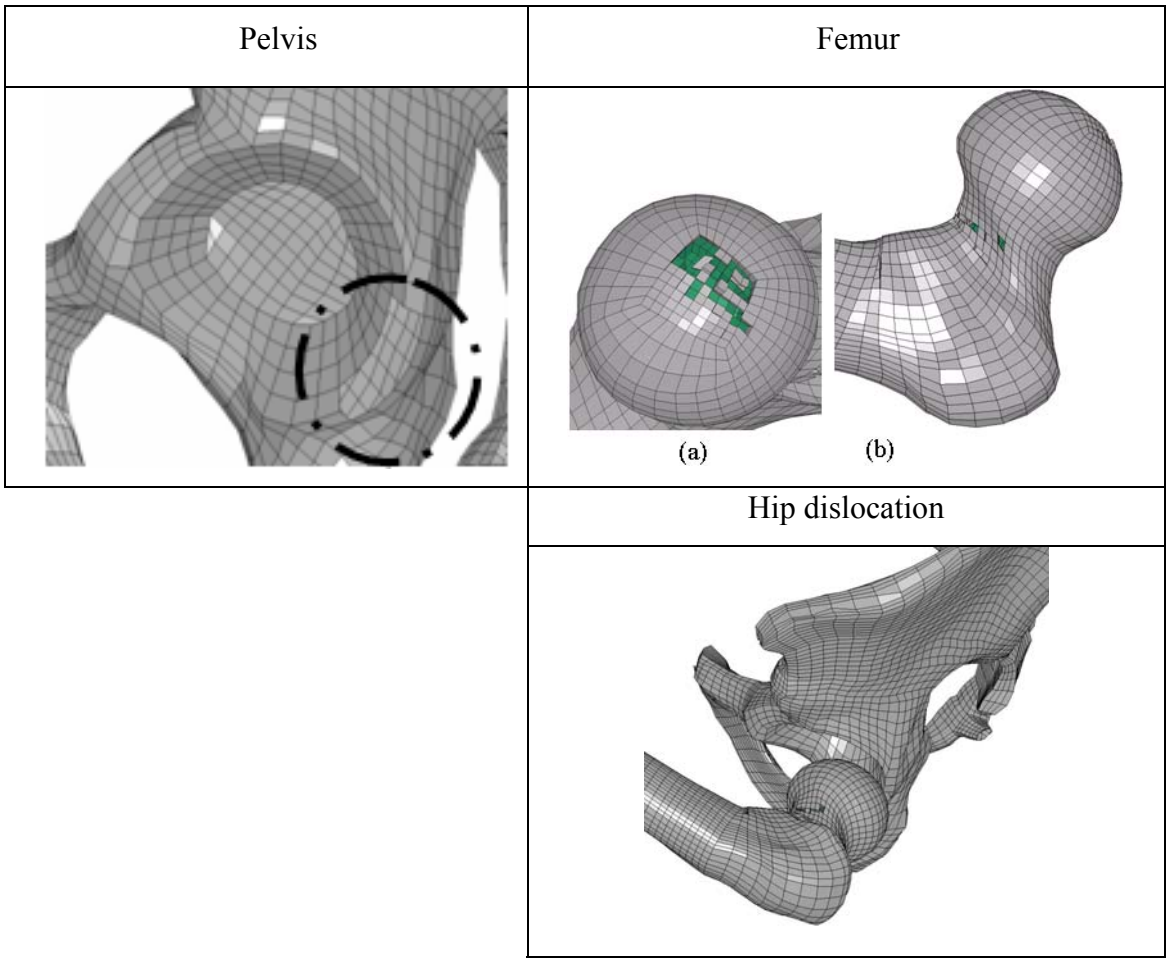

Figure 7.66. Bone fracture results for the 30-degree thigh flexion and 15-degree adduction impact simulation: rupture at the acetabular cup (top left), small fracture to the top femoral head (top right (a)), fracture to the femoral head-trochanter and shaft (top right (b)), and dislocation of the hip joint before failure (bottom).

A consistent acetabular cup rupture was observed starting at 3,010 N, and a top-head femur failure at 2,290 N. Also, fractures to the femoral neck and the lower trochanter-shaft region occurred initiating at 3,130 N.

It was not clear which were the dominant reasons for femoral neck and top femoral ball elements failures.

7.4.4. Impact of the Lower Limb at 30 Degrees Thigh Flexion and -30 Degrees Adduction

7.4.4.1 Impact of the Lower Limb at 30 Degrees Thigh Flexion and -30 Degrees Adduction: Setup

The setup and the initial configuration for the impact simulation of the lower limb at 30 degrees of thigh flexion and -30 degrees of adduction are shown in Figure 7.67.

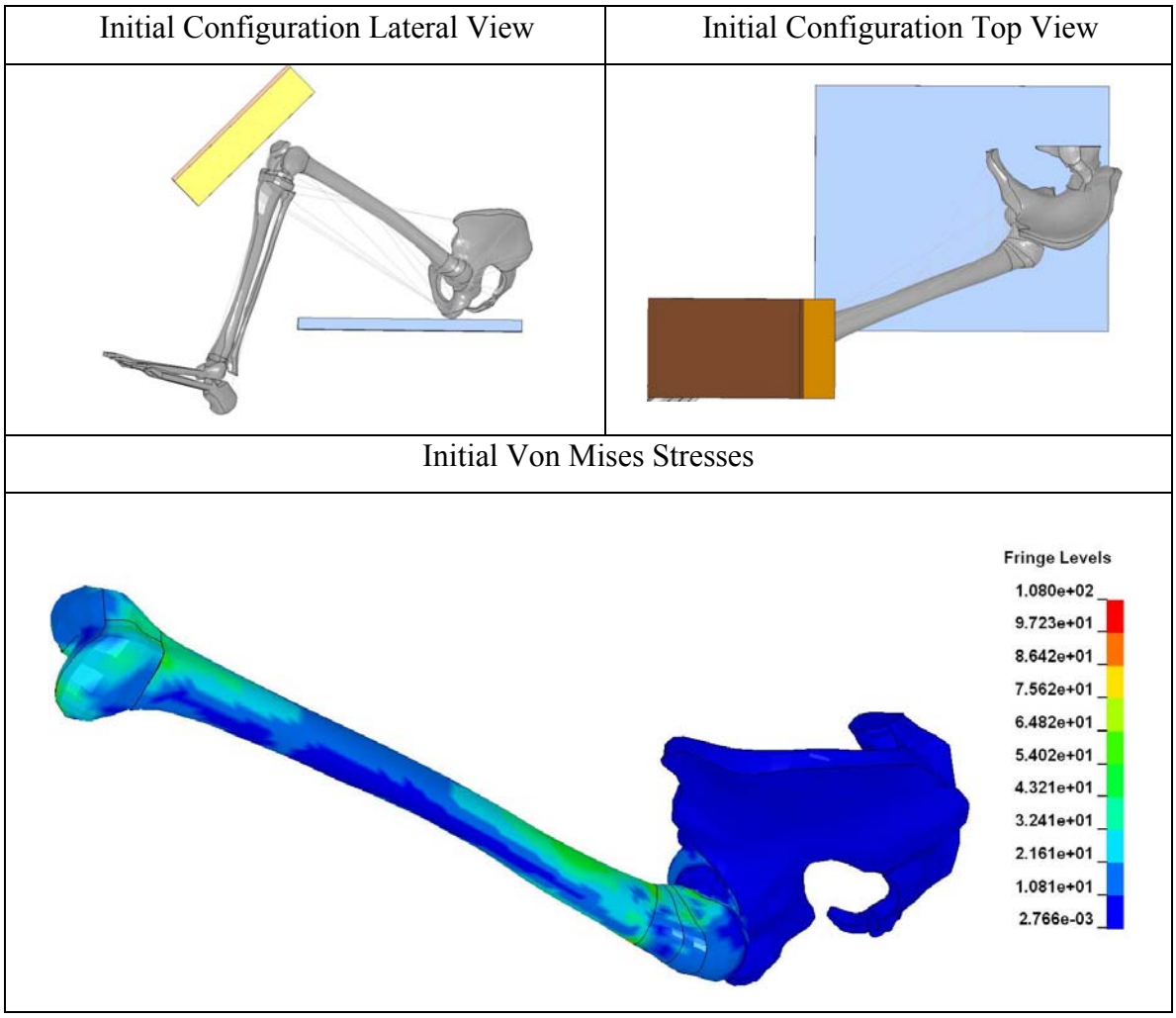

Figure 7.67. Initial configuration for the 30-degree thigh flexion and -30-degrees adduction impact simulation: lateral (top left) and top view (top right), and initial Von Mises stresses (bottom).

7.4.4.2 Impact of the Lower Limb at 30 Degrees Thigh Flexion and -30 Degrees Adduction: Results

The final configuration for the impact simulation of the lower limb at 30 degrees of thigh flexion and -30 degrees of adduction is shown in Figure 7.68. The resulting peak femur force was observed to be 3,207 N.

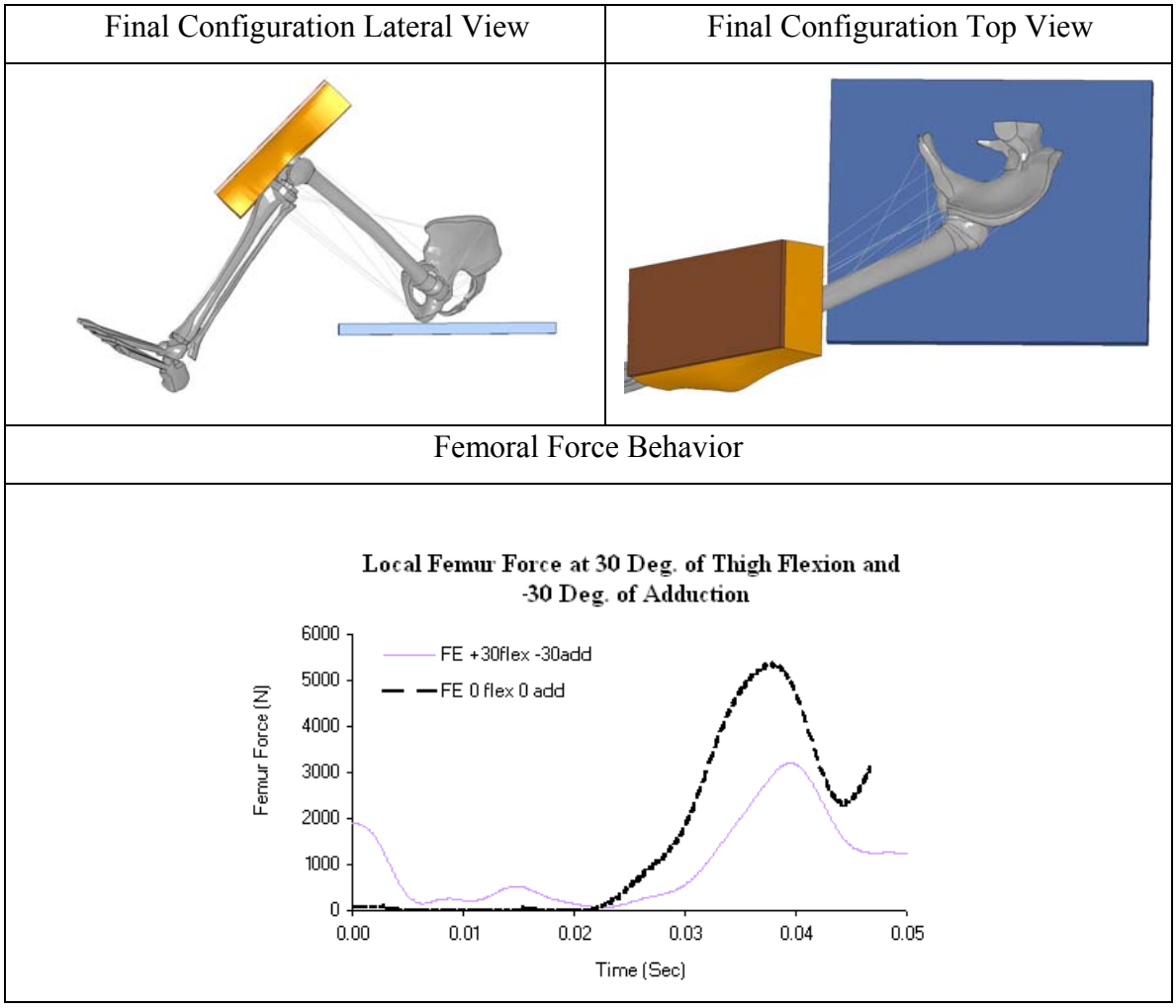

Figure 7.68. Final configuration for the 30-degree thigh flexion and -30-degree adduction impact simulation: final configuration lateral view (top left) and top view (top right), and femoral force behavior (bottom).

The fracture mechanism for the KTH in the simulation of a 30-degree thigh flexion and -30-degree adduction is reported in Figure 7.69.

Pelvis	Femur
	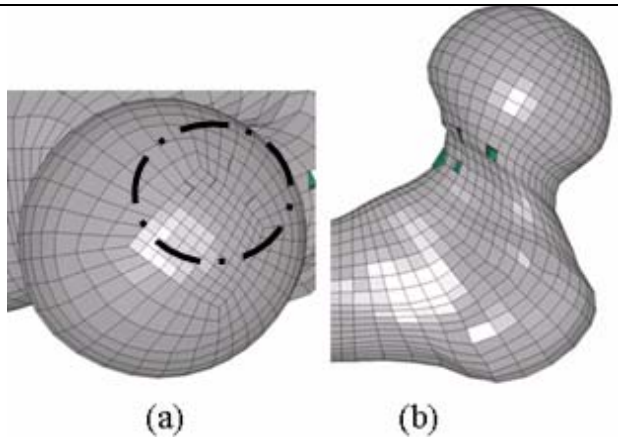 (a) (b)

Figure 7.69. Bone fracture results for the 30-degree thigh flexion and -30-degree adduction impact simulation: no rupture for the pelvis bone (left), small fractures at the top head of femur (right (a)) and failure of the femoral neck-trochanter (right (b)).

No rupture was observed for the pelvis bone. Fracture to the top femur occurred starting at 3,160 N. After the femur force reached its peak, a failure of the femoral neck was observed initiating at 3,180 N.

It was not clear which was the dominant reasons for femoral neck elements failure. The top of the femur ball fractured when elements reached the transverse shear ultimate strength.

7.4.5. Comments

The behavior of the femur force obtained from FE simulations considering different combinations of thigh flexion and adduction angles prior to impact is shown in Figure 7.70.

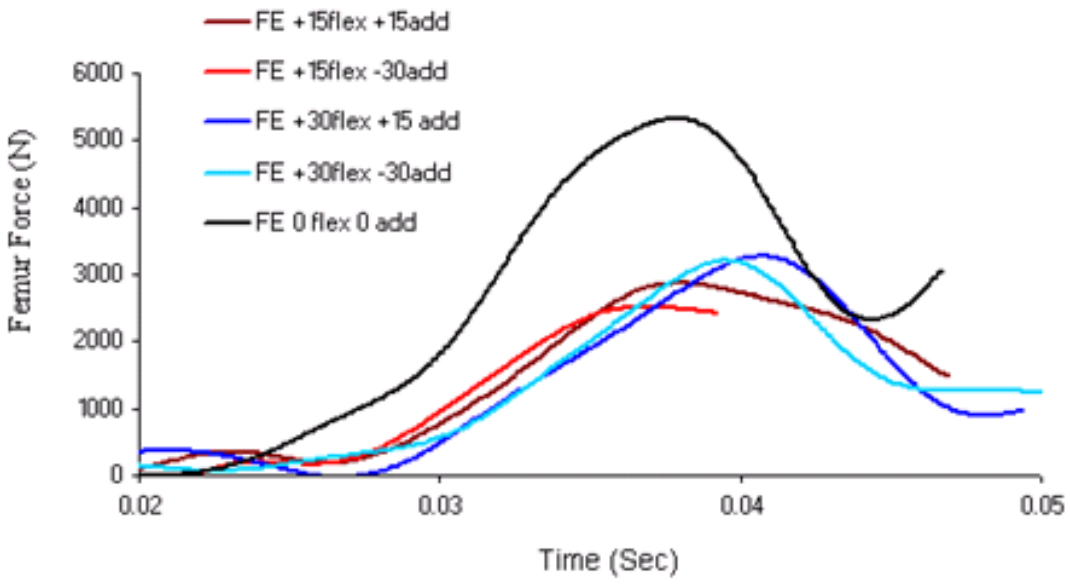

Figure 7.70. Comparison of local femur force behavior for different angles of thigh flexion and adduction.

Simulations involving a 30-degree thigh abducted appeared to be weaker than the one adducted 15 degrees, no matter which angle of thigh flexion was considered. It would be very interesting to compare these results to findings from tests with the same setup and loading configurations. Unfortunately, no tests were found in literature with these types of impact configuration. The results obtained, however, follow the general behavior found for the single-angle impacts setup. In fact, also in that case, femur force reached a lower peak when it came to a high angle of abduction prior to the frontal impact.

As it can be seen from Figures 7.71 and 7.72, FE simulations results show that the change of the femur peak force due to a frontal impact for flexed and adducted thigh with respect to the neutral position does not really depend on the angle of thigh flexion, but it does vary according to the adduction position. It would be necessary, however, to run more FE simulations with different combinations of angles of thigh flexion and adduction in order to have a more realistic and complete behavior of the femur force during these combined setups.

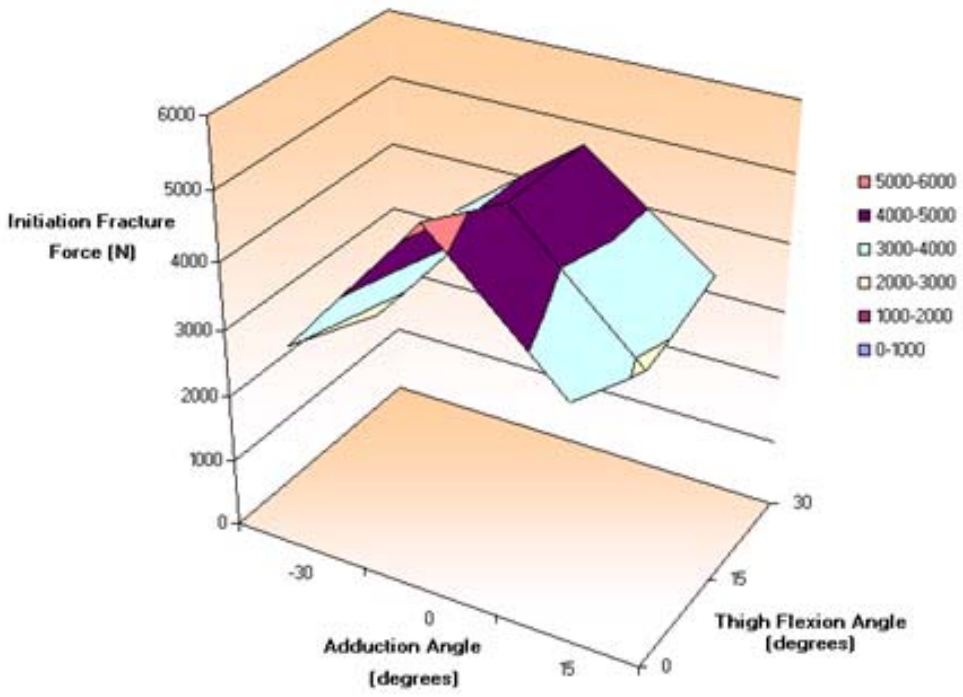

Figure 7.71. Peak force behavior during frontal impact depending on initial angles of adduction and thigh flexion, 3-D view.

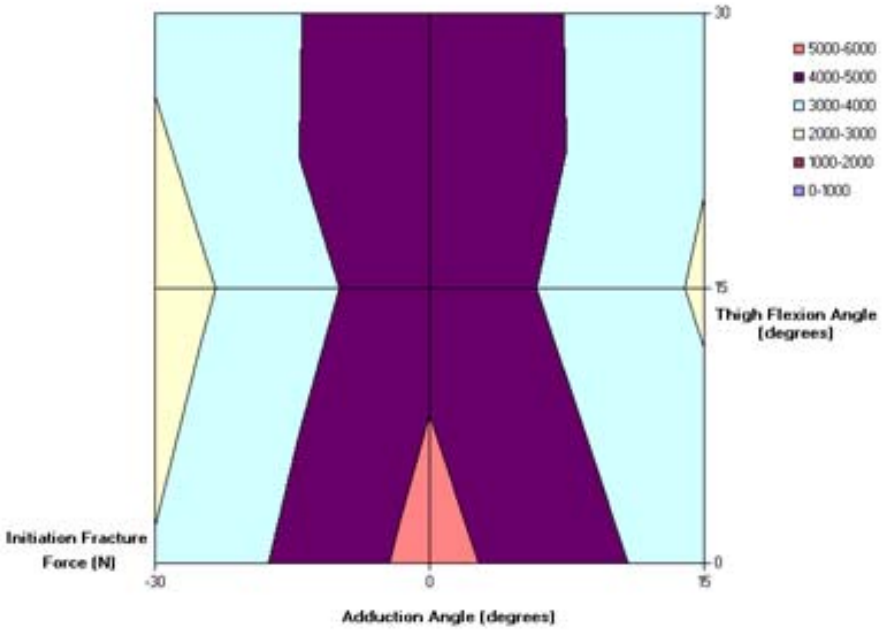

Figure 7.72. Peak force behavior during frontal impact depending on initial angles of adduction and thigh flexion, 2-D view.

From a failure mechanism point of view, the KTH model appears generally weaker when the thigh is flexed to a higher angle. In fact, Figure 7.73 shows that the only acetabular cup fracture registered in these FE simulations was for the 30-degree flexed and 15-degree adducted thigh setup. Small failures of the femoral head were recorded only in one of the 15-degree flexed thigh condition simulations. A relevant failure of this region was obtained only in one of the 30-degree flexed simulation condition.

In all simulations, the main region of the KTH which was affected by failures during impact was the femoral neck. It certainly appeared to be the weakest region of the KTH under combined loading conditions. It is interesting to note that fracture occurred to the higher femoral shaft in both simulations where the femur was initially adducted of 15 degrees. Dislocation of the hip joint happened for simulations with a 15-degree initial adduction angle.

	15 flex – 15 add	15 flex – -30 add	30 flex – 15 add	30 flex – -30 add
Pelvis			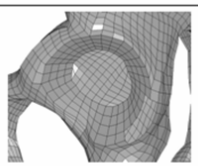	
Top Head Femur	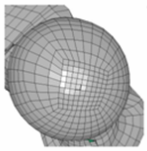 ♦ *		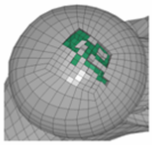	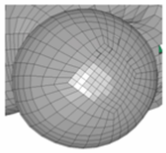 ♦
Femur	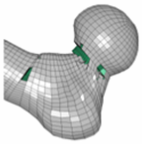 *	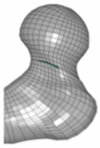 *	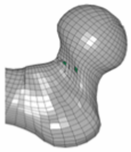	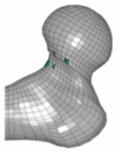 *
Dislocation	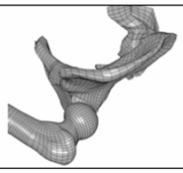		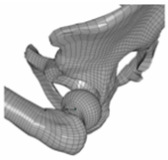	

♦ = very small fracture

* = failure after peak of femur force

Figure 7.73.. Summary of fracture mechanisms for combination of initial angles.

Table 7.5 shows the very first fracture initiation force for combination of angles of thigh flexion and adduction.

Table 7.9. Comparison of peak femur force and initiation femur force for different angles of thigh flexion.

Flexion (Degrees)	Adduction (Degrees)	Peak Femur (kN)	First Fracture (kN)
15	15	2865	***2520***
15	-30	2514	***2460***
30	15	3271	2290
30	-30	3207	3160

***Bold and Italic** = fracture happened after the peak femur force has reached.

Figures 7.74 to 7.76 and Table 7.10 report the fracture initiation force for each KTH region which experienced failure prior to the achievement of the first peak force: the pelvis bone, the femoral neck and trochanters and the top femoral ball. A summary of all types of fracture mechanisms for the adducted KTH is also reported in Table 7.11.

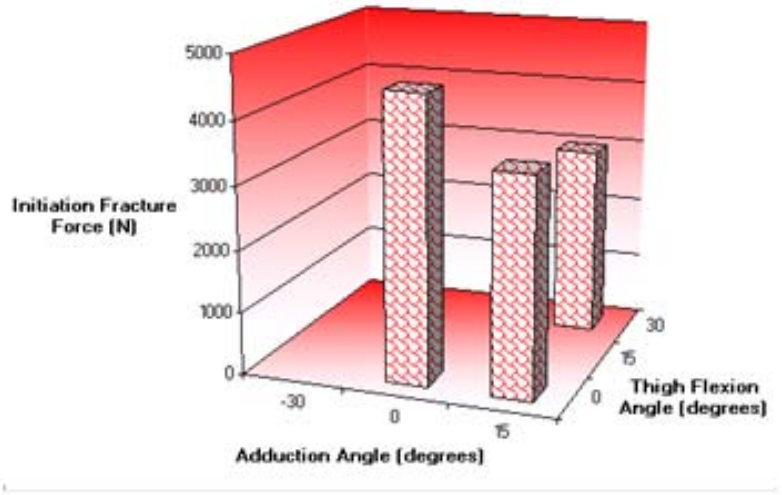

Figure 7.74. Fracture initiation force in the Pelvis bone for different angles of thigh flexion and adduction.

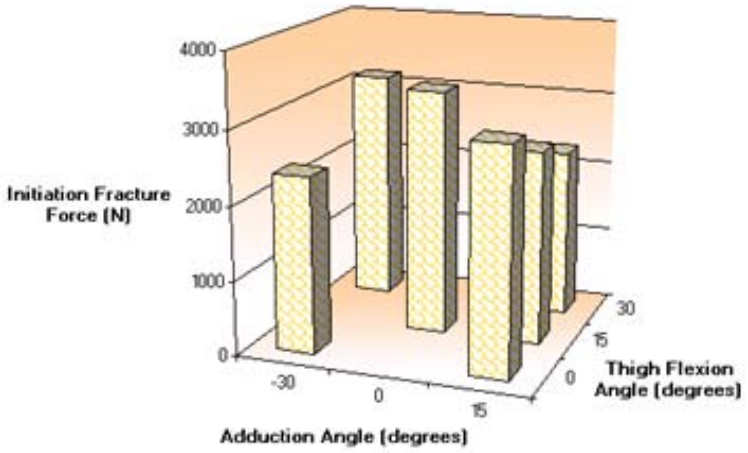

Figure 7.75. Fracture initiation force at the Top Femoral Ball bone for different angles of thigh flexion and adduction.

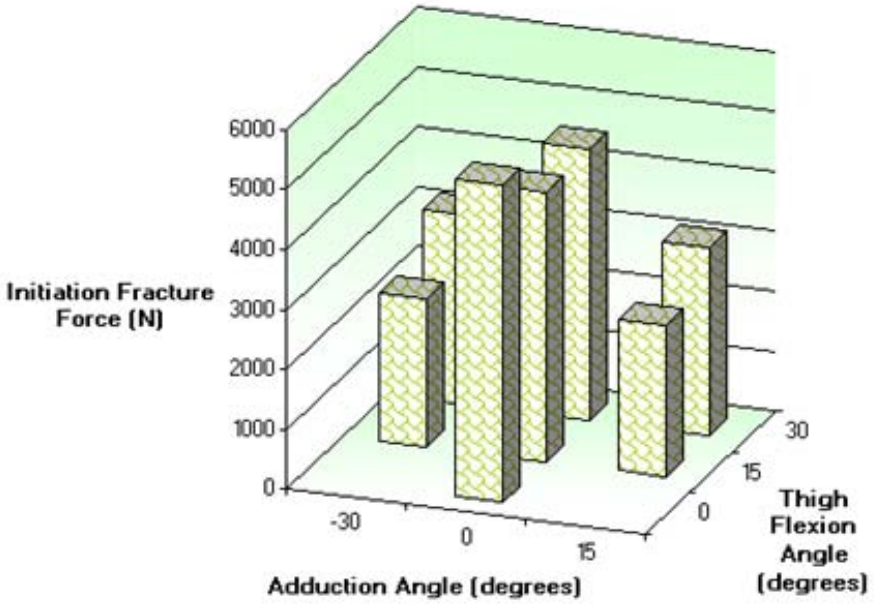

Figure 7.76. Fracture initiation force in the Femur Bone for different angles of thigh flexion and adduction.

Table 7.10. Values for fracture initiation force for different types of failure mechanism at different angles of thigh flexion.

Flexion (Degrees)	Adduction (Degrees)	Fracture Pelvis (N)	Fracture Top Ball Femur (N)	Fracture Femur (N)
15	15	-	***2620***	***2520***
15	-30	-	-	***2460***
30	15	3010	2290	3130
30	-30	-	3160	***3180***

****Bold and Italic*** = fracture happened after the peak femur force has reached.

Table 7.11. Summary of fracture mechanisms at different angles of thigh flexion.

Flexion (Degrees)	Adduction (Degrees)	Fracture Pelvis	Fracture Top Ball Femur	Fracture Femur	Notes
15	15	-	Top Ball Femur Rupture, very small	Neck and Shaft	Hip Joint Dislocation
15	-30	-	-	Neck	-
30	15	Acetabular Cup	Top Ball Femur Rupture	Neck and Shaft	Hip Joint Dislocation
30	-30	-	Top Ball Femur Rupture, small	Neck	-

According to the different peak forces obtained by the FE simulations, probability of AIS2+ and AIS3+ were calculated following the same injury criteria that was already considered for the whole-body validation (Kuppa, 2001).
They are reported in Table 7.12 and 7.13 and in Figures 7.77 and 7.78, where their probability is presented directly with respect to the initial angle of thigh flexion and adduction considered.

Table 7.12. AIS2+ values resulted for femoral forces observed after frontal impact with the KTH at different initial angles of thigh flexion and adduction.

AIS+2	adduction		
flexion	-30	0	15
0	0.014808	0.04624	0.01833
15	0.011111	0.03415	0.0133
30	0.015851	0.0337	0.01638

Table 7.13. AIS3+ values resulted for femoral forces observed after frontal impact with the KTH at different initial angles of thigh flexion and adduction.

AIS+3	adduction		
flexion	-30	0	15
0	0.01839	0.03759	0.02102
15	0.015369	0.03105	0.0172
30	0.019189	0.03079	0.01959

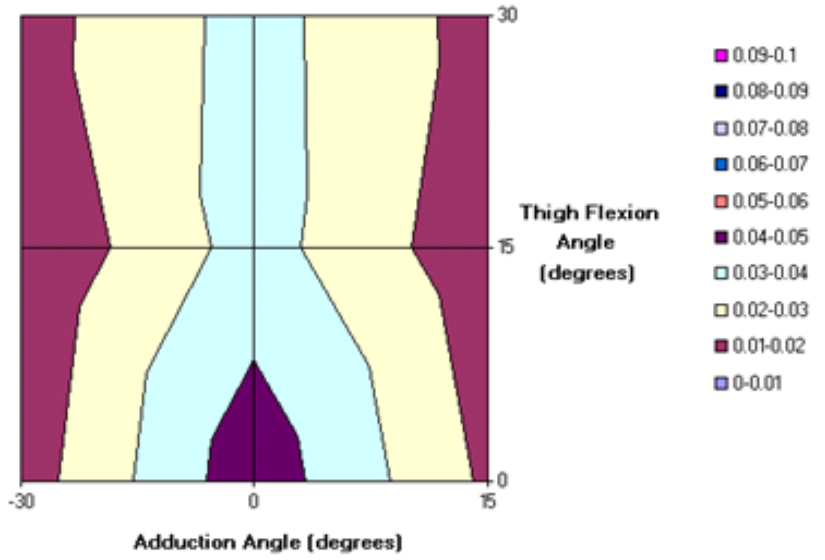

Figure 7.77. Probability of AIS2+ knee-thigh-hip injuries for femur forces resulted after frontal impact with the KTH at different initial angles of thigh flexion and adduction.

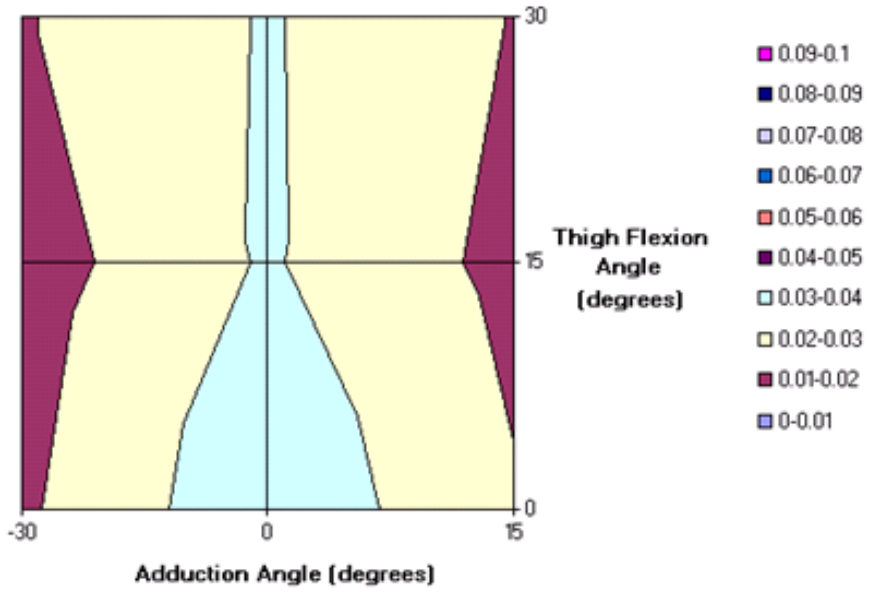

Figure 7.78. Probability of AIS3+ knee-thigh-hip injuries for femur forces resulted after frontal impact with the KTH at different initial angles of thigh flexion and adduction.

From these graphs, it seems that probability of KTH bone fracture is not greatly affected by the angle of thigh flexion. On the other hand, it appears that it is more likely to have a lower probability of KTH bone injury when the thigh is either adducted or abducted to a relative high angle. These results confirm what was already previously found and discussed about failure mechanisms for a combined adducted-flexed KTH complex.

Ligaments fracture was not observed in any of the out-of-position KTH FE simulations. Similar comments as those reported for adducted FE simulations could be considered.

VIII. Conclusions and Further Research

A finite element model of the Knee-Thigh-Hip of a 50th percentile male was developed with the purpose of investigating and predicting failure mechanisms in this body region during a frontal car crash. The LLNL lower extremity model was used as a starting point although many changes were applied to this initial model. Finer meshes of the femur, pelvis, and patella bones were developed and different geometrical modeling for trabecular and cortical parts of the femur and the pelvis were performed. Bones were modeled with non-isotropic composite material models and stress-based failure properties were applied. Bone materials were validated by comparing simulations to three different types of axial impact tests of bones conducted by Rupp in order to validate the mechanical properties chosen for representation of the pelvis, the femoral head and the femoral condyles.

Ligaments and muscles were represented as discrete elements with an anatomically correct consideration of their origins and insertion sites in the bones. Only passive properties of muscles were initially considered. Inertial properties of the lower limb were taken into account by adding nodal masses to each bone of the lower extremities. The whole model with inclusion of soft tissue, passive muscles and ligaments was validated by comparing FE simulations to a whole cadaver sled test conducted by Rupp. The two main parameters considered for comparison between the test and FE simulation results were the femoral axial force and the failure mechanism observed. There were many uncertainties about the physical test setup. As a consequence, parametric simulations of the FE model were performed with respect to the knee-bolster spacing, the location on the femur where the axial force was measured and the initial angles of adduction, thigh flexion and knee extension. Results showed that the femur axial force is noticeably influenced by small changes of the parameters considered while the KTH fracture mechanism was nearly always the same that observed in the cadaver sled test.

After validation, the model was further improved by including dynamic failure properties for the ligaments and a more realistic method for simulating the patella dynamics during movements. This was accomplished through the representation of the patellar tendon with use of seatbelt material and sliprings. Active muscle properties were also included in the model in order to replicate different types of lower limb movements and for a further understanding of role of active muscles in KTH fracture mechanisms during braking or other actions prior to a frontal crash.

Simulations of frontal impacts with a dashboard were run with the lower limb at different positions of either thigh flexion or adduction and with a combination of these two angles. Failure mechanisms of the KTH and the behavior of the axial femoral force were investigated for these different types of scenarios. Results were acceptable and encouraging when compared to findings in the literature, replicating failures of different parts of the femur and the pelvis bones, or dislocation of the hip joint according to the initial position of the lower leg prior to impact.

From some simulations results, however, it looks like that trabecular part of the pelvis is too stiff for fracture. Apparently, the values chosen for the ultimate strength properties for this bone are too high. A wider range of properties values from literature must be investigated to find the best ultimate strength properties for this part of the KTH.

Moreover, it is known from literature that cortical pelvis thickness varies according to the location on the bone and could be significantly different. In order to replicate the mechanical responses of pelvis for any general load application, it would be useful to use the correct local thickness of the cortical bone since this could influence the local strength of the material.

Results found during frontal impacts simulations with the KTH model at different initial angles of adduction and thigh flexion were compared to results obtained by Rupp et al. performed dynamical impact tests at the same initial conditions. (Rupp, 2004) Fracture initiation force results were very similar when compared to 10 degree adduction test setup. However, dissimilarities in fracture initiation force results were found for the thigh flexion test setups. Impact simulations for different initial angles of thigh flexion should be investigated in more detail from an anatomical point of view. This dissimilarity may be

another consequence of the simplified representation of mechanical and ultimate properties of the pelvis in the correct KTH model.

Ligaments fracture was not observed in the out-of-position KTH FE simulations. Femoral head fractures, however, reported with impacts of adducted KTH, could be related to avulsion failures of the ischiofemoral and iliofemoral ligaments. It would be very interesting if impact KTH tests equipped with sensors could be conducted with the scope of understanding the sequencing of the bones and soft tissue failures. At that point, it would be possible to compare tests and FE results for validation of the FE KTH impacts failure dynamic outcomes and hip joint ligament behavior.

The KTH model was able to replicate the same injury criteria for ligament failure defined by Viano. (Viano, 1978) It suggested, however, lowering the actual axial femur force threshold for fractures in the knee-thigh-hip, since fractures in the KTH were experienced at a femur force less than the actual used 9,040 N limit, both in neutral and in out-of-position KTH axial impacts. Unfortunately, FE coarse mesh of the tibia plateau did not allow reproducing Bangelmaier tests for replication or definition of injury criteria for the tibia and condyles region.

Further research could be addressed to a range of more realistic vehicle interior geometries to investigate the response of the KTH according to various scenarios. Moreover, KTH fracture mechanisms can be investigated and compared to previous findings when introducing use of seatbelts, airbag and improved knee-bolsters.

IX. REFERENCES

AAFP: American Academy of Family Physicians (2008), "Strong medicine for America", www.aafp.org, February 6 2008.

Agarwal, G.C., Golltieb, GL, (1977), "Oscillation of the human ankle joint in response to applied sinusoidal torque on the foot," *J. Physiol.,* Vol. 268, pp. 151-176.

Aidely, D.J., (1971) "The Physiology of Excitable Cells," Cambridge Univ. Press, London, U.K.

Aigner, M., and Heegaard, J., (1999) "One-dimensional quasi-static continuum model of muscle contraction as a distributed control system," Center for Turbulence Research.

Alexander, R. McN., Bennet-Clark, H.C., (1977) "Storage of elastic strain energy in muscle and other tissues," *Nature,* Vol. 265, pp. 114-117.

Anatomy, (2008) www2.ma.psu.edu/~pt/renee384/anatomy.htm, February 6 2008.

Anderson, M., "Biomechanics of Hip Joint Capsule, (2002) " Internal Report for Project COME 10: 3D Visualization of Joints from *MRI Data*.

Anderson, A.E., Peters, C.L., Tuttle, B.D., and Weiss, J.A., (2005) "Subject-specific finite element model of the pelvis: development, validation and sensitivity studies", ASME, Vol. 127, pp. 364-373.

Bach, T.M., O1apman, A.E. and Calvert, T. W., (1983) "Mechanical resonance of the human body during voluntary oscillations about the ankle joint," *J. Biomech*. Vol. 16, pp. 85-90.

Bagley, A.M., (1987) “Analysis of human response to slow isokinetic movement,” *M.S. Thesis*, Arizona State University.

Bangelmaier, et al., (1999) "Axial Compressive Load Response of the 90o Flexed Human Tibiafemoral Joint," Paper No. 99SC08, *43rd Stapp Car Crash Conference*.

Barbenel, JC., Evans JH, and Finlay JB, (1973) ”Stress-strain-time relations for soft connective tissues.” In: Kenedi, editor. “*Perspectives in Biomedical Engineering*,” New York: McMillan; 165–172.

Beillas P., Papaioannou G., Tashman S., and Yang K.H., (2004) “A new method to investigate in vivo knee behaviour using a finite element model of the lower limb”, *Journal of Biomechanics* 37, pp.1019-1030.

Bhavikati, S.S., (2004) “Finite element analysis.”, New Age International Publishers.

Bingham, DN., and Dehoff PH., (1979) “A constitutive equation for the canine anterior cruciate ligament,” *ASME J Biomech Eng*; Vol. 101, pp. 15–22.

Blincoe LJ, Seay AG, Zaloshnja E, Miller TR, Romano EO, Luchter S, and Spicer RS. (2002) “The Economic Impact of Motor Vehicle Crashes 2000.” DOT HS 809-446. Washington, DC: Department of Transportation.

Bonifasi Lista, C., (2003) “Multiaxial Viscoelastic Properties of Human Medial Collateral Ligament,” *MS Thesis*, Department of Bioengineering, University of Utah.

Crisco JJ., Moore, D.C>, McGovern, R.D., (2002) “Strain-rate sensitivity of the rabbit MCL diminishes at traumatic loading rates.”, *Journal of Biomechanics*, Vol. 35, pp. 1379-1385.

Decraemer, WF., Maes MA, Vanhuyse VJ, Vanpeperstraete P., (1980) "A nonlinear viscoelastic constitutive equation for soft biological tissues based upon a structural model," *J Biomechanics,* 13:559–564.

Dehoff, PH., (1978) "On the nonlinear viscoelastic behaviour of soft biological tissues," *J Biomechanics*; 11:35–40.

DiMasi, F.P., Eppinger, R., and Marcus J., (1991) "3-D anatomic brain model for relating cortical strains to automobile crash loading.", *Proceedings 13th International Experimental Safety Vehicle Conference*, Paper No. 91-58-0-11, DOT.

Dischinger PC, Burgess AR, Cushing BM, et al:, (1994) "Lower extremity trauma in vehicular front seat occupants.", . In Proceedings of the 4th Annual Injury Prevention through Biomechanics Symposium, Detroit, Wayne State University, pp.29-42.

Dischinger PC, Kerns TJ, and Kufera JA., (1995) "Lower extremity fractures in motor vehicle collisions: the role of driver gender and height.", Accid Anal. And Prev. 27(4):601-606.

edmunds.com, (2007), "Safety tips", www.edmunds.com/.../articles/105394/article.html, December 3, 2007

Farnese, R., (2006) "A finite element model of the 50th percentile male human hip ligaments for impact loadings." *Thesis*. Politecnico di Milano, Milano, Italia.

France, E.P., Paulos, L.E., Abbott, P.J., et al., (1987) "Failure characteristics of the medial collateral ligament of the knee: effect of high strain rate.", *Aviation, Space and Environmental Medicine*, Vol.58, pp. 488.

Frisen, M., Magi M., Sonnerup L., and Viidik A., (1969) "A rheological analysis of soft collagenous tissue. Part I: theoretical considerations," *J Biomechanic*s, 2:13-20.

Fung, Y.C., (1993) "Biomechanics: Mechanical Properties of Living Tissues, " 2nd ed. Springer-Verlag, New York.

Garnier, K.B., et al., (1999) "Mechanical characterization in shear of human femoral cancellous bone: torsion and shear tests.", *Medical Engineering & Physics*, Vol. 21, pp. 641-649.

Goldstein, S., Frankeburg, E., and Kuhn, J., (1993) "Biomechanics of bone.", in "*Accidental injury: biomechanics and prevention*." Springer-Verlag, New York, pp. 198-223.

Gray, H., (1918) "Anatomy of the Human Body.", http://www.bartleby.com/107

Hall, B.K., (1992) "Bone: a treatise.", CRC Press.

Hewitt, J.D., Glisson, R.R., Guilak, F., and Vail, T.P., (2002) "The mechanical properties of the human hip capsule ligaments", Journal of Arthroplasty, Vol. 17(1), pp. 82-89.

Holden, JA, Cristoffel T., (1986) "A Course on Motor Vehicle Trauma: Instructors Guide-Final Users Manual." DOT/OST/P-34/86-050. Washington, DC: Department of Transportation.

Huelke, D., et al., (1991) "Lower Extremity Injuries in Frontal Crashes: Injuries, Locations, AIS, and Contacts*", SAE Paper No. 910811*.

Hyde, A. S., (1992) “Chapter Five: Crash Injuries Of The Extremities”, in *Crash Injuries: How and Why They Happen: A Primer for Anyone Who Cares About People in Cars*, Society of Automotive Engineers.

ICB Dent, (2008) “Mechanical properties of bone”, *www.feppd.org* , February 14, 2008.

Kennedy, E.A., et al., (2004) “Lateral and posterior dynamic bending of the mid-shaft femur: fracture risk curves for the adult population.”, *Stapp Car Crash Journal*, Vol. 48, pp. 27-51.

King, A., and Chou, C.C., (1975) “Mathematical modeling, simulation and experimental testing of biomechanical system crash response.”, *AIAA 11th Annual Meeting and Technical Display*, also in: 1976 *Journal of Biomechanics*, pp. 301-317.

Kleinberger, M., (1993) “Application of finite element techniques to the study of cervical spine mechanics.”, *Proceedings 37th Stapp Car Crash Conference*, SAE Paper No. 933131, SAE, Warrendale, Pennsylvania.

Koch, (1917) “The Laws of Bone Architecture.”, *Am. Jour. of Anat*., 21.

Kuppa, S., Wang, J., Eppinger, R. and Haffner, M., (2001) “Lower Extremity Injuries and Associated Injury Criteria.”, *Proceedings of the Seventeenth International Technical Conference on the Enhanced Safety of Vehicles*, Amsterdam.

Kuppa, S., (2002) “An Overview of the Knee-Thigh-Hip Injuries in Frontal Crashes in the United States,” National Highway Traffic Safety Administration, *ISSI*; 416 USA.

Lakes, R.S., Vanderby, R., (1999) “Interrelation of creep and relaxation: a modeling approach for ligaments,” *J Biomech. Engineering*, Vol. 121, pp. 612-615.

Lanir, Y., (1980) “A microstructure model for the rheology of mammalian tendon,” *ASME J Biomech Eng,* 102:332–339.

Lawrence Nordhoff Jr., (2004):”Chapter 14. Crash Speeds and Injury Risk: Epidemiologic and Forensic Considerations”, in *Motor Vehicle Collision Injuries: Biomechanics, Diagnosis, and Management*, Second Edition, Jones & Bartlett Publishers.

Lewis, P.R., Molz, F.J., Schmidke, S.Z., and Bidez, M.W., (1996) “A NASS-based investigation of pelvic injury within the motor vehicle crash environment”, *SAE Paper No. 962419*. Warrendale, PA: Society of Automotive Engineers.

LSTC (Livermore Software Technology Corporation), (2003) “LS-DYNA, KEYWORD USER’S MANUAL”, version 970.

LSTC (Livermore Software Technology Corporation), (2007a) “LS-DYNA, KEYWORD USER’S MANUAL”, version 971.

LSTC (Livermore Software Technology Corporation), (2007b) “LsPrePost user’s manual”, version 2.2.

Luchter, S., (1995) “Long Term Consequences of Lower Extremity Injuries”, *Proceedings of the International Conference on Pelvic and Lower Extremity Injuries*, Washington D.C., December.

Lydon, C., Crisco, J.J., Panjabi, M., and Galloway, M., (1995) “Effect of elongation rate on the failure properties of the rabbit anterior cruciate ligament”, *Clinical Biomechanics*, Vol. 10, pp. 428-433.

MacKenzie, E., et al., (1996) “The Development of the Functional Capacity Index”, *Journal of Trauma*, Vol. 41, No. 5, pp. 799-807.

Mass of body segment, (2005) Pathobiomechanics and Pathokinesiology, www.biomech.ftvs.cuni.cz, April 25 2005.

McGowan, C., (1999) "A practical guide to vertebrate mechanism.", Cambridge University Press.

MedicineNet.com, (2008), February 6 2008.

Merk Manuals. Online Medical Library, (2008) "Fractures", www.merck.com/mmpe/print/sec21/ch309/ch309b.html, April 11, 2008.

Mertz, et al., (1989) "Size, Weigth and Biomedical Impact Response Requirements for Adult Size Small Female and Large Male Dummies.", *SAE Paper No. 890756*, SAE International Congress and Exposition.

NHTSA, http://www-nrd.nhtsa.dot.gov/database/nrd-51/asp/QueryTestTable.asp, 2005.

Monma, H., and Sugita, T., (2001) "Is the mechanism of traumatic posterior dislocation of the hip a brake pedal injury rather than a dashboard injury?", *Injury*, Vol. 32(3), pp. 221-222.

Muscle Atlas, (2008) University of Washington Radiology, www.rad.washington.edu, February 5 2008.

Nahum, A.M., and Melvin, J., (2002) "Accidentally Injury: biomechanics and prevention", Springer.

Netter, F.H., Dalley II, A.F., (1997) "Atlas of Human Anatomy," Second Edition, Novartis.

NHTSA, U.S. Department of Transportation, (2002a)"Traffic safety Facts, 2002". National Center for statistics and Analysis, DOT HS 809 612. Washington, DC: Department of Transportation.

NHTSA, U.S. Department of Transportation, (2002b) "Traffic safety Facts, 2001: A Compilation of Motor Vehicle Crash Data from the Fatality Analysis Reporting System and the General Estimates System". DOT HS 809 484. Washington, DC: Department of Transportation.

Niebur, G.L., et al., (2002) "Biaxial failure behavior of bovine tibial trabecular bone.", *Journal of biomechanical engineering*, Vol. 124.

Olivetti, N., (2006) "Development of a Hill's model of the human knee-thigh-hip region for frontal car crash simulations.", *Thesis*. Politecnico di Milano, Milano, Italia.

Ore, L., et al., (1993) "Accident Investigation and Impairment Study of Lower Extremity Injury", *SAE Paper No. 930096*.

OrthoMeditec. Our Joint Success, (2008) "Orthopedic Trauma: Medical Background", www.orthomeditec.com/medical_background.htm, February 12 2008.

Pattimore, D., et al., (1991) "The Nature and cause of Lower Limb Injuries in Car Crashes", *35th Stapp Car Crash Conference, SAE Paper No. 912901*.

Peck, L. (2007) "Dynamic Failure Properties of the Porcine Medial Collateral Ligament: Predicting Human Injury in High Speed Frontal Automotive Collisions.", *Master Thesis*. Worcester Polytechnic Institute, Worcester, MA, USA.

Perfect, S.A., Weiss, J.A., and Schauer, D.A., (1997) "Finite Element Modeling of the Human Anatomic Pelvis and Leg. ", *Final Report*, NHTSA.

Pike, J.A. (1990) “Automotive Safety: Anatomy, Injury, Testing, and Regulation.”, Warrendale, PA: Society of Automotive Engineers.

Pilkey WD, Sieveka EM, Crandall JR, and Klopp G. (1994) “The influence of foot placement and vehicular intrusion on occupant lower limb injury in full-frontal and frontal-offset crashes”, Paper No. 94 S4 W31, presented at the *International ESV Conference*.

Pioletti, DP., Rakotomanana LR, Benvenuti JF, and Leyvraz PF, (1998) “Viscoelastic constitutive law in large deformations: applications to human knee ligaments and tendons,” *J Biomechanics*; Vol. 31, pp. 753–757.

Pioletti, DP., and Rakotomanana LR, (2000) “Non-linear viscoelastic laws for soft biological tissue,” *Eur. J. Mech. A/Solids* Vol. 19, pp. 749-759.

Plank, G., and Eppinger, R., (1989) “Computed dynamic response of the human thorax from a finite element model.”, *Proceedings 12th International Experimental Safety Vehicle Conference*, pp. 665-672, DOT.

Polgar K., Viceconti M., and O’Connor J.J., (2000) “A comparison between automatically generated linear and parabolic tetrahedral when used to mesh a human femur”, *Journal of Engineering in Medecine*.

Puso, M.A., and Weiss, J.A., (1997) “Finite element implementation of anisotropic quasilinear viscoelasticity using a discrete spectrum approximation,” *ASME Journal of Biomechanical Engineering*.

Ray, M. H., (1996) "Repeatability of Full-Scale Crash Tests and a Criteria for Validating Finite Element Simulations," *Transportation Research Record No. 1528*, Transportation Research Board, Washington, D.C.

Read, K., et al., (2002) "Physical and Psychosocial Outcomes Following Motor Vehicle Related Lower Extremity Injury", *Proceedings of the AAAM Conference*.

Renaudin, F., Guillemot, H., LaVaste, F., Skalii, W., LeSage, F., and Pecheux, C., (1993) "A 3-D finite element model of pelvis in side impact.", *Proceedings 37th Stapp Car Crash Conference*, SAE Paper No. 933130, SAE, Warrendale, Pennsylvania.

Ruan, J.S., Khalil, T.B>, and King, A.I., (1993) "Finite element modeling of direct head impact.", *Proceedings 37th Stapp Car Crash Conference*, SAE, Warrendale, Pennsylvania.

Rupp JA , (2002) "'Test Report No. NB0221', Discretionary Cooperative Agreement in Support of Biomechanical Research – KTH Injury Investigations. The University of Michigan Transportation Research Institute (UMTRI)", Ann Arbor, MI.

Rupp, J.D., Reed, M.P., Jeffreys, T.A., and Schneider, L.W., (2003a) "Effects of the hip posture on the frontal impact tolerance of the human hip joint.", Paper No. 2003-22-0002, *Stapp Car Crash Journal*,; 21-34.

Rupp JA ,'(2003b) Test Reports NB336L/R-NB337R-NB338R-from NB342Rthrough NB345R-NB447R-448RR-NB450L', Discretionary Cooperative Agreement in Support of Biomechanical Research - KTH Injury Investigations, The University of Michigan Transportation Research Institute (UMTRI), Ann Arbor, MI.

Rupp JA, (2003c) 'Test Reports NB337L-NB341L/R-NB342R-NB343L-NB345L-NB447R-NB448L', Discretionary Cooperative Agreement in Support of Biomechanical Research - KTH Injury Investigations, The University of Michigan Transportation Research Institute (UMTRI), Ann Arbor, MI.

Rupp JA, (2003d) 'Test Reports NB450L-NB341L/R', Discretionary Cooperative Agreement in Support of Biomechanical Research - KTH Injury Investigations, The University of Michigan Transportation Research Institute (UMTRI), Ann Arbor, MI.

Rupp, J.D., and Schneider L.W., (2000) "Injuries to the hip joint in frontal motor-vehicle crashes: biomechanical and real-world perspectives", Orthopedic Clinics of North America, 35, pp. 493-504.

Savio L, Woo Y., et al., "Injury and Repair of Ligaments and Tendons," *Annu. Rev. Biomed. Eng.*, 02:83–118.

Sochor, M.R., Faust, D.P., Wang, S.C., and Schneider, L.W., (2003) "knee, thigh, and hip injury patterns for drivers and right front passengers in frontal impacts.", *SAE Paper 2003-01-0164*, SP-1784. Warrendale, PA: Society of Automotive Engineers; pp.101-109.

Tencer A, Kaufman R, Ryan K, Grossman D, Henley B, Mann F, Mock C, Rivara F, Wang S, Augenstein J, Hoyt D, and Eastman B., (2002) " Femur fractures in relatively low speed frontal crashes : the possible role of muscle forces," *Accident Analysis and Prevention,* 34, pp 1-11.

Teresinski, G., (2005) "Chapter 10: Injuries of the Thigh, Knee, and Ankle as Reconstructive Factors in Road Traffic Accidents" in *Forensic Medicine of the Lower Extremity. Human Identification and Trauma Analysis of the Thigh, Leg, and Foot*, Humana Press.

Truesdell, C., and Noll, W., (1992) "The Non-Linear Field Theories of Mechanics," Springer-Verlag, New York.

Tschoegl, N.W, (1989) " The Phenomenological Theory of Linear Viscoelastic Behavior", Springer-Verlag, New York.

Turner, C.H., and Burr, D.B., (1993) “Basic biomechanical measurement of bone: a tutorial” Pergamon press.
UMTRI: (University of Michigan Transportation Research Institute), (2002) “NHTSA Test Report NB0221”, UMTRI/DOT - DTNH22-99-H-17000 UMTRI.

Valle, L., (2005) “A reconstruction procedure for non-continuously fractured tibia: numerical and experimental evaluation.”, *Thesis*. Politecnico di Milano, Milano, Italia.

Viano, D.C., et al., (1978) “Bolster Impacts to the Knee and Tibia of Human Cadavers and an Anthropomorphic Dummy.”, *Proceedings of the Twenty-Second Stapp Car Crash Conference*, SAE Paper No. 780896.

Viceconti M., Casali M., Massari B., Cristofolini L., Bassini S., and Toni A., (1996) “The ‘standardized femur program’ proposal for a reference geometry to be used for the creation of finite element models of the femur.”, *Journal of Biomechanics* 29 (9), p. 1241.

Viidik, A., and Ekholm, R., (1968a) “Light and electron microscopic studies of collagen fibers under strain,” *Z Anat Entwickl Gesch* , Vol. 127, pp.154–164..

Viidik, A., (1968b) “A rheological model for uncalcified parallel-fibred collagenous tissue,” *J Biomechanics,* Vol. 1, pp.3-11.

Weiss, J.A., and Gardiner, J.C., (2001) “Computational Modeling of Ligament Mechanics,” Critical Reviews™ in *Biomedical Engineering*, Vol. 29(4), pp. 1-70.

Winters, J.M., (1988) “Improvements within the A.V. Hill model structure: strength and limitations,” *Proc. IEEE Eng. Med. Biol*., pp. 559-560, New Orleans.

Woo, SL-Y, Peterson, R.H., Ohland, K.J., et al., (1990) “The effects of strain rate on the properties of the medial collateral ligament in skeletally immature and mature rabbits: a

biomechanical and histological study.", *Journal of Orthopaedic Research*, Vol.8, pp. 712-721.

Woo, S.L.-Y., An, K.-N., Arnoczky, S.P., Wayne, J.S., Fithian, D.C.,and Myers, B.S., (1994) "Anatomy, biology, and biomechanics of tendon, ligament and meniscus," Simon SR, editor, *Orthopaedic Basic Science*, American Academy of Orthopaedic Surgeons, 47-74.

Xerogeanes, J.W., Fox, R.J., et al., (1998) "A functional comparison of animal anterior cruciate ligament models to the human anterior cruciate ligament.", *Annals of Biomedical Engineering*, Vol. 26, pp. 345-352.

Yoganandan, N., Cusick, J.F., Pintar, F.A., and Rao, R.D., (2001) "Whiplash injury determination with conventional spine imaging and cryomicrotomy.", *Spine*, Vol. 26(22), pp. 2443-2448.

Zatsiorsky, V.M., and Seluyanov V.N., (1983) "The mass and inertia characteristics of the main segments of the human body," *Matsui, H., Kobayashi,K., Biomechanics. Champaign*, Vol. 8, pp. 1152–1159.

APPENDIX A

Matlab Routines

- Matlab routine for calculation of solid element stresses when imposing two different movements to the leg.

- Matlab routine for calculation of shell elements stresses when imposing two different movements to the leg.

Matlab routine for calculation of solid elements stresses when imposing two different movements to the leg.

```
 1
 2 %
 3 % Matlab Program to sum the values of the stresses
 4 % for solid elements for two different movements.
 5 %
 6 %
 7 clear
 8 format long
 9 %
10 % I open my files obtained from "dynain" in LSDYNA (fopen)
11 %
12 in1 = fopen('Flex15_solid.txt','r');
13 in2 = fopen('Abd40_solid.txt','r');
14 %
15 % I create Matrixes were to stored the data read from the opened files (fopen)
16 %
17 in_m = fopen('Matrix_Final_solid.txt','wt'); % "in_m" is a scalar MATLAB integer
18 %
19 % I scan all the files, till the end of them
20 %
21 while (~feof(in1)  &&  ~feof(in2))
22
23            a1 = fscanf(in1,'%10d %10d %10d %10d %10d\n', [5 1]);
24            a1 = a1';
25
26            a2 = fscanf(in2,'%10d %10d %10d %10d %10d\n', [5 1]);
27            a2 = a2';
28
29            b1 = fscanf(in1,'%16f %16f %16f %16f %16f\n', [5 1]);
30            b1 = b1';
31
32            b2 = fscanf(in2,'%16f %16f %16f %16f %16f\n', [5 1]);
33            b2 = b2';
34
35                 btot=b1+b2;
36
37            c1 = fscanf(in1,'%16f %16f %16f\n', [3 1]);
38            c1 = c1';
39
40            c2 = fscanf(in2,'%16f %16f %16f\n', [3 1]);
41            c2 = c2';
42
43                  ctot=c1+c2;
44
45                                        fprintf(in_m,'%10d %9d %9d %9d %9d\n',a1');
46                                        fprintf(in_m,'%16f %15f %15f %15f %15f\n',btot');
47                                        fprintf(in_m,'%16f %15f %15f\n',ctot');
48 end
49
50            fclose(in1);
51            fclose(in2);
52            fclose(in_m);
53
54 fprintf ('Command Executed: please, read the files \n');
55
```

Matlab routine for calculation of shell elements stresses when imposing two different movements to the leg.

```
%
%
% Matlab Program to sum the values of the stresses
% for shell elements for two different movements.
%
%
clear all
format long
%
% I open my files obtained from "dynain" in LSDYNA (fopen)
%
in1 = fopen('Flex15_shell.txt','r');
in2 = fopen('Abd40_shell.txt','r');
%
% I create Matrixes were to stored the data read from the opened files (fopen)
%
in_m = fopen('Matrix_Final_shell.txt','wt'); % "in_m" is a scalar MATLAB integer
%
% I scan all the files, till the end of them
%
while (~feof(in1)  &&  ~feof(in2))

           a1 = fscanf(in1,'%10d %10d %10d %10d\n', [4 1]);
           a1 = a1';

           a2 = fscanf(in2,'%10d %10d %10d %10d\n', [4 1]);
           a2 = a2';

           b1 = fscanf(in1,'%10f %10f %10f %10f %10f %10f %10f %10f\n', [8 1]);
           b1 = b1';

           b2 = fscanf(in2,'%10f %10f %10f %10f %10f %10f %10f %10f\n', [8 1]);
           b2 = b2';
                btot=b1+b2;

           c1 = fscanf(in1,'%10f %10f %10f %10f %10f %10f %10f %10f\n', [8 1]);
           c1 = c1';

           c2 = fscanf(in2,'%10f %10f %10f %10f %10f %10f %10f %10f\n', [8 1]);
           c2 = c2';
                 ctot=c1+c2;
                                    fprintf(in_m,'%10d %9d %9d %9d\n',a1');
                                    fprintf(in_m,'%10f %9f %9f %9f %9f %9f %9f %9f\n',btot');
                                    fprintf(in_m,'%10f %9f %9f %9f %9f %9f %9f %9f\n',ctot');
end
           fclose(in1);
           fclose(in2);
           fclose(in_m);

fprintf ('Command Executed: please, read the files \n');


```